Global travel time tomography
with 3-D reference models

Maisha Amaru

Global travel time tomography
with 3-D reference models

Globale reistijdentomografie
met 3-D referentiemodellen

(met een samenvatting in het Nederlands)

Globale Laufzeittomographie
mit 3-D Referenzmodellen

(mit einer Zusammenfassung in deutscher Sprache)

PROEFSCHRIFT

TER VERKRIJGING VAN DE GRAAD VAN DOCTOR
AAN DE UNIVERSITEIT UTRECHT
OP GEZAG VAN DE RECTOR MAGNIFICUS, PROF. DR. W.H. GISPEN,
INGEVOLGE HET BESLUIT VAN HET COLLEGE VOOR PROMOTIES
IN HET OPENBAAR TE VERDEDIGEN
OP WOENSDAG 31 JANUARI 2007 DES MIDDAGS TE 4.15 UUR

DOOR

Maisha Lara Amaru

geboren op 02 juni 1977, te Neuwied, Duitsland

Promotor: Prof. Dr. W. Spakman
Co-promotor: Dr. A. Villaseñor

The Earth has music for those who listen.
William Shakespeare

Contents

Chapter 1

Introduction

1.1 Global Tomography

Knowledge of the Earth's interior is essential for the understanding of processes observed at the surface such as volcanism, seismicity, plate movements, vertical movements or variations of the geomagnetic field. But as direct probing of the deep interior remains impossible, indirect observations have to be used to gain information on the Earth's mantle and core. Mantle rocks, which were brought up to the surface give indications on the composition, temperature and pressure distribution of localized regions in the mantle. On a long wavelength scale, gravity measurements can provide information on the density distribution of mantle material and geomagnetic observations of the past and present field give insight into dynamic processes in the outer core. With magnetotelluric measurements, a long wavelength 3-D image of electric conductivity related to varying rock properties in the upper mantle can be determined. Finally, seismic tomography presents a powerful tool to image the present state of seismic velocity heterogeneities within the Earth's crust, mantle and core on a variety of scales as seismic wave propagation is influenced by the material along the waves' paths through the Earth.

Focussing now solely on seismology, velocity information can be obtained from various types of seismological data: P- and S-wave arrival times of phases traveling through the Earth's crust, mantle and core have been used by many authors to derive global compressional and shear velocity models (e.g. Zhou, 1996; Grand *et al.*, 1997; van der Hilst *et al.*, 1997; Obayashi and Fukao, 1997; Bijwaard *et al.*, 1998; Kennett *et al.*, 1998; Vasco and Johnson, 1998; Bijwaard and Spakman, 2000; Boschi and Dziewonski, 2000; Kárason and van der Hilst, 2001; Zhao, 2001; Grand, 2002; Kennett and Gorbatov, 2004; Lei and Zhao, 2006). Furthermore, a new class of travel time tomography models is evolving which takes into account the finite frequency of body waves by incorporating Fresnel kernels (Montelli *et al.*, 2004a, 2004b) as theory states that the infinite frequency approximation of ray theory can cause imaged velocity anomalies to be reduced in amplitude and laterally blurred in their extent (Dahlen, 2004). However, as this method requires knowledge of the frequency content of the picked phases and as travel time data sets of long period body waves are up to now

comparatively small, resolution is lower (≈ 200 km / $1.8°$, Montelli *et al.*, 2004b) than can be reached with regular travel time tomography. Travel time tomography based on ray theory leads to highly detailed images of velocity structures in the Earth with a maximum lateral resolution of approximately $0.6°$ for global P models and $1.8°$ for global S models. Local tomography dealing with very small study volumes is able to produce even better resolved models but only for limited regions. However, the main shortcoming of travel time tomography is that ray coverage is particularly low where earthquakes and stations are sparse as in the upper mantle beneath oceans or cratons and therefore cannot provide good models of these areas.

In contrast, inversion of surface wave group and phase velocity measurements results in velocity models of the upper mantle (e.g., Shapiro and Ritzwoller, 2002; Boschi *et al.*, 2004) with a sufficient ray coverage also in other regions where only few earthquakes are observed or a sparse network exists. But the model resolution is only at best on the order of $3.0°$ which is too low for imaging, for example, the narrow outlines of subducted slabs.

Normal mode splitting functions contain structural information on very long wavelength features up to spherical harmonic degree 8 (lateral sensitivity comparable to $\approx 23° \times 23°$ cells) but unlike surface waves and most body wave phase types their informational content covers the entire Earth's interior. Global models with this type of data were amongst other authors produced by Resovsky and Ritzwoller (1999), Ishii and Tromp (2001) and Beghein *et al.* (2002).

Other researchers invert waveforms of body and surface waves (e.g., Li and Romanowicz, 1996; Mégnin and Romanowicz, 2000) to derive global shear velocity models up to degree 24 (comparable to $\approx 8° \times 8°$ cells).

To overcome the problem that different types of seismological data image only certain parts of the Earth many authors employ mixed data sets consisting of surface wave dispersion, normal mode splitting functions, long period waveforms and absolute as well as differential travel time data (Su *et al.*, 1994; Masters *et al.*, 1996; Ekström and Dziewonski, 1998; Liu and Dziewonski, 1998; Ritsema *et al.*, 1999; Masters *et al.*, 2000; Gu *et al.*, 2001). However, due to the amount and type of data, mainly long wavelength models are obtained with these data sets.

In this thesis, advantage is taken of the various types of seismological observations in a different approach: To obtain a model that shows the high-resolution features of travel time tomography, the data set is improved by adding new, accurate arrival times. Furthermore, the gaps in ray coverage are implicitly filled by applying reference velocity models based on different seismological data sets not used for inversion here.

Among problems that all types of tomographic inversions inherently have in common are a) that the reference model has to be close to the real Earth due to linearization of the mathematical problem and b) that model amplitudes are reduced due to regularization during inversion which is required because of the ill-posedness of the problem. The effect of the nonlinearity of the tomography equations has been addressed in global travel time tomography, for example, by Bijwaard and Spakman (2000) and Widiyantoro *et al.* (2000). These authors account for ray bending due to 3-D heterogeneities by alternating tomographic inversion steps with 3-D ray tracing to improve the prediction of travel times and 3-D raypaths. The decrease of model amplitudes due to regularization of the inversion can partly be remedied by avoiding

12

overparameterization of the model. Therefore earlier studies have either used mixed data sets as described in the previous paragraph resulting in sufficient sampling in all regions of interest or by using an irregular grid parameterization dependent on data sampling or model characteristics (e.g., Abers and Roecker, 1991; Bijwaard *et al.*, 1998; Kárason and van der Hilst, 2000; Sambridge and Faletič, 2003).

The aim of this thesis is to establish improved models of 3-D velocity structures within the crust and mantle by employing a more extensive data set and by using 3-D starting models based on complementary seismic data. Overall, improved tomography models of the Earth's crust and mantle may provide further insight into the tectonic/geodynamic evolution of the Earth and a better understanding of the geodynamic processes within it. Besides that, an improved velocity model allows for a better travel time prediction and therefore more accurate event locations, which is also a step towards creating a seismological reference model of the Earth.

1.2 Data Set

Travel time tomography models can be improved on a regional scale by incorporating accurate arrival times of body waves which have not been used before to fill, in particular, gaps in ray coverage in the upper mantle. Sources of such data sets are archives of data centers (e.g. ORFEUS[1], ANSS[2]) which store the waveforms but do not process them further, bulletins which contain arrival times that were not reported to the ISC[3] (e.g. Euro-Mediterranean bulletin, Godey *et al.*, 2006) or temporary experiments with spatially dense station arrays which mainly use either relative teleseismic travel time residuals or local absolute travel times (e.g. EIFEL (Ritter *et al.*, 2000), MIDSEA (van der Lee *et al.*, 2001), SVEKALAPKO (Bock and the SVEKALAPKO Seismic Tomography Working Group, 2001), TOR (Gregersen *et al.*, 2002)). As part of this thesis, such high-accuracy data sets were picked with a semi-automated picking software (Sandoval *et al.*, 2004a) and obtained from other groups for stations in Europe and North America and afterwards combined with the latest travel time data set of Engdahl et al. (1998) for subsequent usage in global travel time tomography. Additionally, to better constrain the lower mantle, core phases were employed as they were not used in previous studies which applied the same tomography algorithm. Core phases have also been used by other authors to investigate the lower mantle and core with global travel time tomography (e.g. Obayashi and Fukao, 1997; Vasco and Johnson, 1998; Boschi and Dziewonski, 2000; Kárason and van der Hilst, 2001; Lei and Zhao, 2006).

1.3 Method

Tomography models can be improved by starting from a velocity model that gives a more realistic representation of the Earth's crust and mantle instead of the commonly used 1-D spherically symmetric reference models. Therefore, in this study a 3-D reference model from

---

[1] Observatories and Research Facilities for European Seismology
[2] Advanced National Seismic System, U.S. Geological Survey
[3] International Seismological Centre

surface wave tomography is used for the uppermost mantle which contains also a detailed crustal model and a long wavelength shear velocity model based on a mixed data set as described above is incorporated for the rest of the mantle. The new reference model deviates significantly from the 1-D model in which the earthquakes were originally located. Therefore, the earthquakes are relocated prior to the tomographic inversion in the 3-D reference model to obtain consistency between the new reference model, travel time predictions and earthquake locations and to thereby also avoid baseline shifts in the residuals. In contrast, in previous studies working with 3-D reference models (e.g. Bijwaard and Spakman, 2000; Widiyantoro *et al.*, 2000) this step was omitted assuming that changes in event parameters are small enough to be neglected which may not be justified

To take into account the nonlinearity of the tomography problem and the underestimation of model amplitudes due to ill-posedness, the tomography with 3-D reference models is taken even further here. A modified 3-D reference model is set up that utilizes 3-D velocity models based on independent long period data sets in regions of low ray coverage with short period P-waves and replaces them by a tomography model based solely on P travel times otherwise. Before replacement with this travel time tomography model, the model amplitudes are enhanced to counteract their underestimation due to regularization. Yet in order not to affect the model misfit only the null space part of the model is used. By using this combined 3-D reference model, the nonlinearity of the problem is better taken into account as ray paths and travel times are adjusted according to this new model which gives a better representation of the Earth's velocity field as "seen" by short period P waves than the previous 3-D reference model.

1.4 Thesis Outline

In Chapter 2, the basic theory of travel time tomography based on ray theory and our implementation is reviewed. Furthermore, the parameterization used as well as the applied damping procedures are described. Chapter 3 contains a regional study of the uppermost mantle beneath Europe. It represents an orientation on the main theme of this thesis demonstrating the effect of 3-D reference models on a small data set and regionally restricted model. In Chapter 4, the picking of the new arrival times for Europe is described and the resulting picks are presented with a quality estimate. Chapter 5 deals with the extension of the tomographic method for the use of different 3-D reference models and accounting for the difference in source parameters due to the change of reference model. Furthermore, these models are compared to a global tomography model using a 1-D reference model. Chapter 6 provides a description of new details that could be derived from the improved tomography model also including the Euro-Mediterranean bulletins (Godey *et al.*, 2006) as additional data and Chapter 7 gives an interpretation of the new model beneath western North America including the additional data from stations in that region. In Chapter 8, the improvement of travel time prediction and earthquake location with the new tomography model is shown and differences to the relocations of Engdahl *et al.* (1998) are discussed. Finally, in Chapter 9 the main results of this study are summarized.

Chapter 2

Methodology

In this chapter, a summary of the basic theory of travel time tomography is given based on the derivations and descriptions of Spakman and Nolet (1988), Spakman (1993), Bijwaard (1999) and Spakman and Bijwaard (2001).

2.1 Linearized seismic tomography

In travel time tomography, observed arrival times of seismic waves are compared to theoretical times predicted by a reference velocity model to obtain seismic velocity variations within the Earth with respect to the reference model. The basic observation thereby consists of the arrival time affected by a reading error (= $t_{\text{arrival}} + \epsilon$). The observed arrival time t_{arrival} is composed of the real travel time $T_x(s)$ of the wavefront, travel time effects Δt_s due to station elevation and instrument response and the real origin time $t_{x(\text{origin})}$

$$t_{\text{arrival}} = T_x(s) + \Delta t_s + t_{x(\text{origin})} \tag{2.1}$$

where $T_x(s)$ depends on the Earth's slowness field (the reciprocal of the seismic wave speed), using the true earthquake location x. The slowness field s is unknown in equation 2.1. However, reference models inferred from seismological observations exist as the standard 1-D Earth models of Jeffreys and Bullen (1940), PREM (Dziewonski and Anderson, 1981), IASP91 (Kennett and Engdahl, 1991) or ak135 (Kennett *et al.*, 1995) which can be used to compute the travel time for these reference models. To obtain a better prediction of the travel times, the spherically symmetric reference models can be replaced by more realistic velocity models which vary in three dimensions. Independent of the exact type of reference model used, the computation of the predicted arrival times is given as

$$t^0_{\text{arrival}} = T^0_{x_0}(s_0) + t^0_{x_0(\text{origin})} \tag{2.2}$$

where the index "0" denotes reference model quantities, $T^0_{x_0}$ is the predicted travel time starting from the reference source location x_0 along the linearized ray path in the reference model, s_0 is the slowness of the reference model and $t^0_{x_0(\text{origin})}$ is the origin time computed in the reference model. These reference model quantities are obtained from an earthquake location

procedure where the arrival time observations are used as constraints after correction for the Earth's ellipticity (Kennett and Gudmundsson, 1996). Arrival times of some special phases (e.g. pP, pwP) require an additional bounce point topography/bathymetry correction. Also, generally an earthquake will be mislocated with respect to its true position as a result of the observational errors, of possibly insufficient data constraints, and of the slowness difference between the true Earth and the reference Earth, the slowness anomaly.

The delay time, which will be used to obtain velocity variations in a tomographic inversion, is defined as the difference of observed and predicted arrival time

$$d = t_{\text{arrival}} - t^0_{\text{arrival}} + \epsilon \tag{2.3}$$

Replacing the arrival times by the expressions derived in equation 2.1 and 2.2 gives the delay d as

$$d = T_x(s) - T^0_{x_0}(s_0) + \Delta t_s + \underbrace{t_x - t_{x_0}}_{\Delta t_x} + \epsilon \tag{2.4}$$

where Δt_x contains the timing error due to source mislocation as a result of the slowness anomaly field $s - s_0$ and ϵ describes the observational errors (e.g. picking errors, phase misidentifications, remaining location errors).

In the high-frequency approximation seismic wave propagation theory reduces to seismic ray theory. In this approximation travel times are computed by integration of the slowness along the ray path:

$$T_x(s) = \int_L s \, dl \qquad \text{with} \qquad L = L(s) \tag{2.5}$$

where L is the ray path and dl the ray segment.

$$T^0_{x_0}(s_0) = \int_{L_0} s_0 \, dl_0 \qquad \text{with} \qquad L_0 = L_0(s_0) \tag{2.6}$$

L_0 is the ray path in the reference model and dl_0 is the ray segment.

Substitution of the travel time integral in the delay time equation gives:

$$d = \int_L s \, dl - \int_{L_0} s_0 \, dl_0 + \Delta t_x + \Delta t_s + \epsilon \tag{2.7}$$

If the difference between the actual Earth and the reference model is sufficiently small, the first travel time integral is linearized using Fermat's Principle. Applying Fermat's Principle effectively results in replacing L by L_0 and requires accounting for the spatial event mislocation $x - x_0$. The effect of the mislocation on the travel time is approximated by a Taylor expansion of the travel time around the reference source x_0. This leads to the delay time equation

$$d = \int_{L_0} (s - s_0) \, dl_0 + (\mathbf{x} - \mathbf{x_0}) \cdot \nabla_0 T^0 + \Delta t_x + \Delta t_s + \epsilon \tag{2.8}$$

which is the forward equation of travel time tomography based on ray theory. In a tomographic analysis, a large set of delay times equation 2.8 derived from many source-station combinations is inverted for estimates of the slowness anomaly field $s - s_0$, the event mislocations $\mathbf{x} - \mathbf{x}_0$, origin time errors Δt_x and the station static terms Δt_s.

2.2 Parameterization and forward (observation) equation

To convert a set of equations 2.8 into a matrix-vector equation for inversion, the piecewise continuous slowness field $\Delta s = s - s_0$ has to be parameterized. Among various methods, which exist for the parameterization, here the irregular cell representation of Spakman and Bijwaard (2001) is chosen. The volume of interest is initially divided into a regular grid of non-overlapping conical cells of a basic (=smallest) cell size. To make the cells independent of their geographical position on the globe, they are constructed in such a way that they have equal surface areas at given depth. Laterally, the size of the basic cells is set dependent on the maximum expected horizontal resolution (smallest detail). The investigated volume is discretized by layers with cells of constant thickness, where the layer thickness varies with depth and is defined to fit cell layers between the first-order seismic discontinuities contained in the reference model and to accommodate the expected resolution with depth. Subsequently, further regular grids are defined with cells which have a bigger lateral extension and are multiples of the basic cells. As a constraint for the cell size on the final irregular grid, the hitcount, i.e. the number of rays crossing a cell, is used and a hitcount threshold is defined. The hitcount is computed on each of the regular grids and the smallest cell size is determined, for which the hitcount is still above the threshold. Thus, the final irregular grid cells are all sampled by a comparable number of rays in regions of sufficient ray coverage. Effectively, the irregular grid results from an optimization procedure which adapts cell volume to obtain more or less equal hitcount in cells. Figure 2.1 shows an example of an equal surface area grid and an irregular grid.

The basic cells are represented by orthonormal cell functions b_j (normalized by $V_j^{-1/2}$ with V_j as volume of cell b_j) which are used to construct the non-overlapping, irregular grid cells c_k:

$$c_k = \sum_{j=1}^{N_b} P_{kj} b_j \tag{2.9}$$

where N_b is the number of basic cells and P_{kj} is the projection coefficient which is zero except when b_j is part of c_k.

The slowness anomaly field Δs ($= s - s_0$) can then be parameterized as follows:

$$\Delta s = \sum_{k=1}^{N} \Delta s_k c_k + \Delta s_p \tag{2.10}$$

where c_k represents the orthonormal cell function, Δs_k the projection coefficient, N the number of irregular cells in the volume and Δs_p the projection error. The projection error reflects the accuracy of the parameterization and will be small/negligible for a sufficiently

17

detailed parameterization (cf. Spakman, 1991).

The arc length l_{ik}^c in the irregular cells c_k is given by the projection of the arc length in the basic cells l_{ij}^b:

$$l_{ik}^c = \sum_{j=1}^{N_b} P'_{kj} l_{ij}^b \tag{2.11}$$

with P'_{kj} as projection coefficient which is one if the basic cell b_j is part of the irregular cell c_k and zero otherwise.

Using this discretization, the travel time difference for the i-th ray is calculated to

$$d_i \approx \sum_{k=1}^{N} \Delta s_k l_{ik}^c + \sum_{l=1}^{4} \Delta x_l g_{il} + \Delta \sigma_m l_{im} + \epsilon_i \tag{2.12}$$

where l_{ik}^c represents the length of the i-th ray in the k-th irregular cell, $\Delta \mathbf{x} = \mathbf{x} - \mathbf{x}_0$, g_{il} describes the elements of $\nabla_0 T^0$ (now including the source time error), $\Delta \sigma_m$ represents the unknown slowness error of the m-th station, (l_{im}) is the identity matrix and ϵ_i contains all errors and signal not accounted for by the previous terms.

The described approximations lead to the observation equation

$$\mathbf{d} = \mathbf{A} \cdot \mathbf{m} + \epsilon \tag{2.13}$$

with $\mathbf{A} = (l_{ik}, g_{il}, l_{im})^T$, $\mathbf{m} = (\Delta s_k, \Delta x_l, \Delta \sigma_m)^T$, $\mathbf{d}$ as data vector with the observed travel time residuals and ϵ as the error vector.

Equation 2.13 forms a system of inconsistent linear equations, usually ill-conditioned as a result of insufficient data, that are to be inverted to obtain a model.

2.3 Inversion and regularization

Due to data inconsistency and usual rank deficiency of $\mathbf{A}$, a unique solution of 2.13 does not exist. To deal with data inconsistency a measure of data fit, that determines how well model predictions approximate the real data, is required for selecting a solution (or a range of solutions in case of rank deficiency). In large size inverse problems, the usual strategy is to find the best-fitting model in the least squares sense, i.e. the model that gives the smallest sum of the squared differences between the observed data vector and its prediction computed from the model. The least square criterion is implemented as follows:

In equation 2.13, the data are first weighted by the data covariance $\mathbf{C}_d$ and next the minimization of $\epsilon^T \mathbf{C}_d^{-1} \epsilon$ is performed, or equivalently the minimization of the cost function

$$\Phi(\mathbf{m}) = (\mathbf{d} - \mathbf{Am})^T \mathbf{C}_d^{-1} (\mathbf{d} - \mathbf{Am}) \tag{2.14}$$

This results in the weighted least squares solution:

$$\mathbf{m} = (\mathbf{A}^T \mathbf{C}_d^{-1} \mathbf{A})^{-1} \mathbf{A}^T \mathbf{C}_d^{-1} \mathbf{d} \tag{2.15}$$
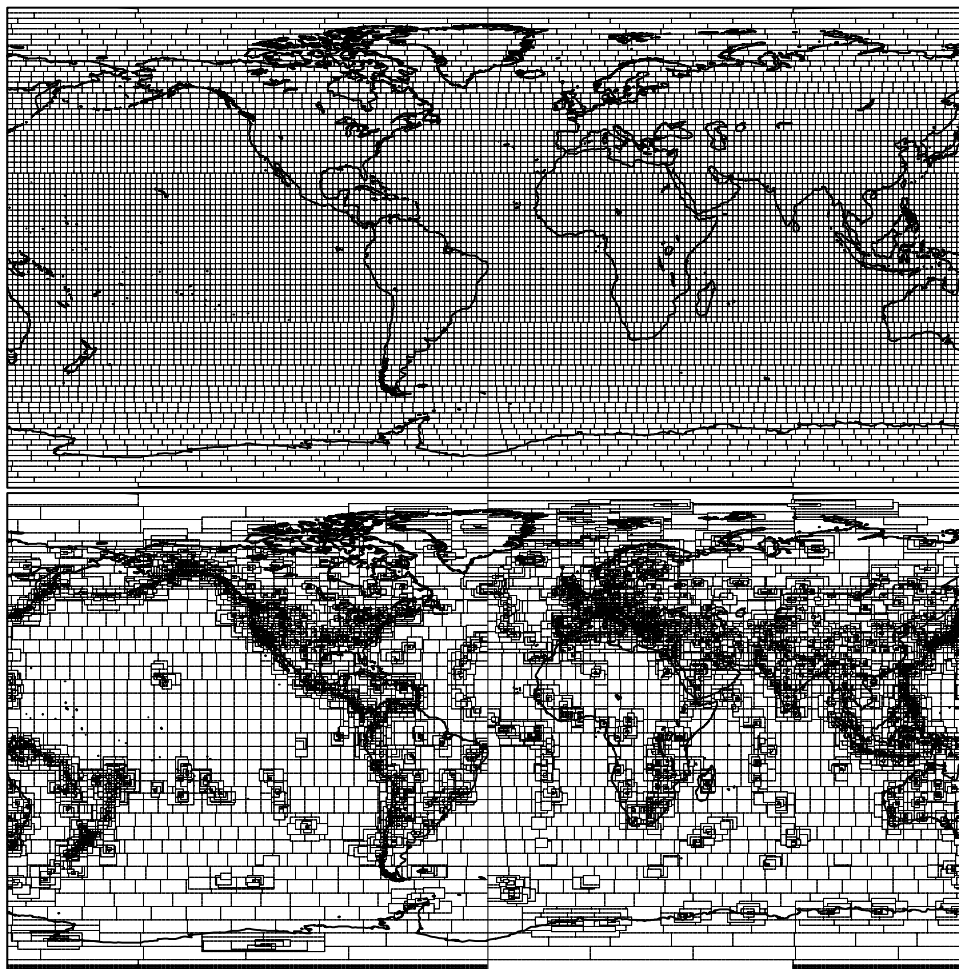
Figure 2.1: Example of two types of grid parameterizations for the topmost layer of the model. On the top, a regular $2.0° \times 2.0°$ grid with cells of equal surface area is displayed where the number of cells per latitude decreases from the equator towards the poles. On the bottom, an irregular grid is shown varying in cell size from $0.5° \times 0.5°$ to $5.0° \times 5.0°$. The cell size is reduced noticeably in areas with a large number of stations and/or earthquakes as it depends on the hitcount (i.e. the number of rays that traverse each cell).

Clearly, the least squares solution can only be computed if $(\mathbf{A}^T\mathbf{C}_d^{-1}\mathbf{A})^{-1}$ exists, i.e. for (numerically) overdetermined equations. In tomography this occurs only in exceptional cases. More often $\mathbf{A}$ has zero eigenvalues (there is no unique solution) and/or $\mathbf{A}$ is ill-conditioned. Very small eigenvalues exist due to, for instance, a dominance of nearly parallel ray paths sampling a model region. As a result of ill-conditioning, small errors in the data can lead to large amplitude errors in the model. The usual remedy to deal with rank deficiency and ill-conditioning is to resort to regularized least squares by extending the cost function with a term $\lambda^2\mathbf{m}^T\mathbf{C}^T\mathbf{Cm}$ that imposes amplitude, roughness and/or smoothness constraints on the model. This results in the following cost function:

$$\Phi(\mathbf{m}) = (\mathbf{d} - \mathbf{Am})^T\mathbf{C}_d^{-1}(\mathbf{d} - \mathbf{Am}) + \lambda^2\mathbf{m}^T\mathbf{C}^T\mathbf{Cm} \tag{2.16}$$

Minimization of Φ gives:

$$\mathbf{m} = \left[\mathbf{A}^T\mathbf{C}_d^{-1}\mathbf{A} + \lambda^2\mathbf{C}^T\mathbf{C}\right]^{-1}\mathbf{A}^T\mathbf{C}_d^{-1}\mathbf{d} \tag{2.17}$$

where λ is a tuning parameter which controls the trade-off between minimizing the data misfit and finding the minimum of the scaled model norm. $\mathbf{C}$ is a matrix imposing model amplitude damping if $\mathbf{C}$ is the identity matrix and smoothing if $\mathbf{C}$ is a second derivative finite difference operator. A model with reduced roughness is obtained by taking a first derivative operator. As derivative operators have non-trivial null spaces, they are often combined with amplitude damping for a complete regularization.

This formulation of the regularized weighted least squares inversion is equivalent to finding the normal least squares solution of the following equation:

$$\begin{pmatrix} \mathbf{C}_d^{-1/2}\mathbf{A} \\ \lambda\mathbf{C} \end{pmatrix}\mathbf{m} = \begin{pmatrix} \mathbf{C}_d^{-1/2}\mathbf{d} \\ 0 \end{pmatrix} \tag{2.18}$$

Station statics and mislocation parameters are associated with much smaller singular values of $\mathbf{A}$ than the slowness parameters of cells. Also, in our irregular model parameterization small cells, placed in mantle regions where we expect resolution for small detail, are usually associated with systematically smaller singular values than large cells which are placed in regions where only larger scale structure can be imaged. To balance the singular value spectrum of $\mathbf{A}$, (i.e. to relatively raise the singular values associated with small cells, mislocation and station parameters) a parameter scaling matrix $\mathbf{S}$ is implemented depending on cell size and hitcount, or parameter type. This leads to the following equation:

$$\begin{pmatrix} \mathbf{C}_d^{-1/2}\mathbf{A} \\ \lambda\mathbf{C} \end{pmatrix}\mathbf{S}^{-\frac{1}{2}}\mathbf{m}' = \begin{pmatrix} \mathbf{C}_d^{-1/2}\mathbf{d} \\ 0 \end{pmatrix} \tag{2.19}$$

with $(S_{jj}) = h_jV_j$ and h_j and V_j as hitcount and cell volume respectively and $\mathbf{m}' = \mathbf{S}^{\frac{1}{2}}\mathbf{m}$ as scaled model vector. The diagonal elements of $\mathbf{S}$ pertaining to mislocation, origin time error, and station static parameters are taken such that they scale these parameters to an expected slowness anomaly amplitude. The model parameter scaling is beneficial in case eq. 2.18 is to be solved with truncated Singular Value Decomposition (SVD) or with iterative solvers (e.g. conjugate gradients) which are stopped before formal convergence has been achieved.

Many types of solvers exist to compute the inverse matrix. Singular Value Decomposition (applied to eq. 2.19 and delivering as solution eq. 2.17, unless truncated SVD is used) requires full storage of the matrix and data-related matrices and is only applicable to relatively small inverse problems. For larger model sizes than SVD can deal with, the inverse matrix of eq. 2.17 can still be computed, for example, with Cholesky decomposition. Examples of inversions computed with SVD or Cholesky decomposition are studies by Ritsema *et al.* (1999) and Boschi (2003) respectively. Huge inverse problems dealing with a very large number of data (millions) and model parameters (hundreds of thousands), can presently only be solved with iterative solvers (e.g. conjugate gradient methods) which, when stopped before formal convergence, compute an approximate solution of (2.17). Throughout this thesis, the tomographic inversion is performed with the iterative conjugate gradient algorithm LSQR of Paige and Saunders (1982) which is applied to (2.19) and in full convergence yields solution (2.17), or an approximation when stopped before full convergence. LSQR resembles in the early iterations SVD (e.g. van der Sluis and van der Vorst, 1987) where the solution is constructed starting with the components associated with the highest singular values. Stopping the algorithm before formal convergence occurs has a comparable damping effect as truncated SVD.

2.4 Assessment of model quality

The quality of a solution is defined by data fit, spatial resolution and model covariance. A drawback of iterative techniques like LSQR is that only a solution and corresponding data fit are computed. Although approximate methods for finding resolution and covariance in huge inversions have been proposed (Nolet *et al.*, 1999, 2001; Yao *et al.*, 1999, 2001), it is practically not yet possible to obtain these exactly.

Spatial resolution is defined as follows: Let $\mathbf{m}_{true}$ be the true cell slowness anomaly field. The corresponding true data are defined as $\mathbf{d}_{true} = \mathbf{A}\mathbf{m}_{true}$. They are different from the real data $\mathbf{d}$ by an error ϵ which includes observational errors, effects of parameterization, linearization and other theoretical approximations. Writing (2.17) as

$$\mathbf{m} = \mathbf{G}\mathbf{d} \tag{2.20}$$

with $\mathbf{G}$ being the generalized inverse of $\mathbf{A}$ and

$$\mathbf{d} = \quad \mathbf{d}_{true} \quad +\epsilon \tag{2.21}$$
$$= \quad \mathbf{A}\mathbf{m}_{true} \quad +\epsilon \tag{2.22}$$

we find

$$\mathbf{m} = \mathbf{R}\mathbf{m}_{true} + \mathbf{G}\epsilon \tag{2.23}$$

where $\mathbf{R} = \mathbf{G}\mathbf{A}$ is the resolution kernel. $\mathbf{R}$ describes how the true cell model is mapped into the solution $\mathbf{m}$ and the term $\mathbf{G}\epsilon$ shows how errors/bias in the data map into the solution.

When the resolution matrix $\mathbf{R}$ cannot be explicitly computed (as in our inversions), sensitivity tests with synthetic slowness models can be conducted to implicitly obtain knowledge of $\mathbf{R}$

21

(Spakman and Nolet, 1988). As $\mathbf{m} = \mathbf{R}\mathbf{m}_{true}$ is a linear equation, one can invent a synthetic model $\mathbf{m}_{true}$, compute synthetic data

$$\mathbf{d}_{true} = \mathbf{A}\mathbf{m}_{true} \tag{2.24}$$

and solve

$$\mathbf{d}_{true} = \mathbf{A}\mathbf{m}_s \tag{2.25}$$

for the tomographic recovery $\mathbf{m}_s$ of the synthetic model to make inferences about $\mathbf{R}$ by comparison of $\mathbf{m}_s$ and $\mathbf{m}_{true}$. However, synthetic slowness anomaly models can only be designed to detect lack of resolution. When the synthetic model $\mathbf{m}_{true}$ is entirely in the null space of $\mathbf{A}$, it will be in the null space of $\mathbf{R}$ and $\mathbf{m}_s$ will only contain zeros. Conversely, when a particular synthetic model happens to be entirely in the range of $\mathbf{A}$, then the model will be recovered completely by tomography and one might be inclined to infer perfect resolution. However, Leveque *et al.* (1993) demonstrated that while a specific synthetic model is recovered, other synthetic models for the same region, but with different dominant structural wavelengths, can still be entirely in the nullspace. To ensure detection of lack of resolution it is therefore necessary to perform sensitivity tests with a large variety of synthetic models, particularly of different structural wavelength content (e.g. Bijwaard *et al.*, 1998). If, for a particular mantle region, no appreciable lack of resolution is detected for a wide variety of synthetic models, i.e. all models are well recovered, then this observation is taken as a measure of high resolution at the wavelengths used, although formally there is still a possibility that resolution is lacking.

The only synthetic model that leads to equivocal interpretations is an overall zero anomaly model except for one cell with a non-zero amplitude – a spike. The tomographic imaging of this model leads effectively to the computation of a column of the resolution kernel. As computing $\mathbf{m}_s$ requires an inversion with LSQR similar to the real data inversion, it is not feasible to reconstruct $\mathbf{R}$ from such synthetic tests when the model consists of a large number of parameters ($\sim 10^5$). A more efficient test, related to a single spike test, was designed by Spakman and Nolet (1988) where the synthetic model contains a 3-D network of spatially well separated spikes. The recovery of this synthetic model shows immediately lack of amplitude recovery of single cells and allows for detection of directional anomaly smearing. In this thesis, the spike tests will be conducted for a variety of spike sizes to assess lack of resolution.

Model covariance, i.e. amplitude errors and their correlations, cannot be formally computed, although the error correlations are implicitly contained in the resolution kernel. The effect of data errors on the solution amplitudes (i.e. the term $\mathbf{G}\epsilon$) is assessed by taking a randomly permuted version $\mathbf{d}_p$ of the data vector $\mathbf{d}$ for ϵ and solving $\mathbf{d}_p = \mathbf{A}\mathbf{m}$ (Spakman, 1991). This random data vector has the same bulk statistics (average, standard deviation, and higher order moments) as the real data vector. In this test, however, all correlation between the real data and their associated ray paths (the matrix $\mathbf{A}$) is destroyed and the permuted data vector $\mathbf{d}_p$ represents an upper limit of data noise. A good outcome of this noise test is a model with low amplitudes and only random amplitude variations. A poor outcome would be if imaged amplitudes and structural wavelengths are comparable to those in the model obtained from inverting the real data which would signal that data and ray paths are not correlated.

Chapter 3

Travel time tomography of the uppermost mantle beneath Europe

We have obtained a detailed P and S model of the uppermost mantle beneath Europe using regional travel time data based on the ISC and NEIC bulletins from the years $1964 - 2000$. Because of the data selection and the ray path distribution, our analysis is comparable to Pn tomography. However, the usual approximations of that method are not required here as we use a method that is also suited for global travel time tomography. Tests show that anomalies with horizontal dimensions of 45 km$\times$45 km and 90 km$\times$90 km can be reconstructed in the P model and the S model respectively. Realistic features are not only imaged for the uppermost mantle but also for the crust. High seismic velocities are found for regions of old oceanic lithosphere (e.g. Black Sea, Eastern Mediterranean basin). In contrast, tectonically active regions such as the Alps are imaged by low velocities as well as regions that are influenced by back arc spreading and volcanism (e.g.Tyrrhenian basin or Alboran basin). Also, the Trans-European Suture Zone, separating the East European platform with its high velocities from the tectonically younger western part of Europe, is well imaged.

3.1   Introduction

Seismic tomography has been used for a long time to study the velocity properties of the crust and mantle and to identify tectonic and geological structures. The obtained velocity models can serve as a starting point for tectonic interpretations and as background models for detailed local studies. They also allow for a more precise prediction of travel times and earthquake locations than standard 1-D models (e.g. JB (Jeffreys and Bullen, 1940), PREM (Dziewonski and Anderson, 1981) or ak135 (Kennett *et al.*, 1995)). The last aspect plays, for example, an important role for seismic monitoring in the context of the Comprehensive Nuclear-Test-Ban-Treaty (CTBT). Velocity models have been published for Europe using different data sets and techniques as travel time tomography (e.g. Spakman *et al.*, 1993; Hearn and Ni, 1994; Bijwaard and Spakman, 2000; Ritzwoller *et al.*, 2002a; Piromallo and Morelli, 2003), surface wave tomography (e.g. Ritzwoller and Levshin, 1998; Villaseñor *et al.*, 2001) and

waveform inversion (e.g. Snieder, 1988; Zielhuis and Nolet, 1994; Marquering and Snieder, 1996). Also, many more local tomography studies exist (see Chapter 4 or Piromallo and Morelli (2003) for a review).

The main purpose of this study is to retrieve a detailed model of the uppermost mantle below Europe that bridges the gap between global and local models using regional P and S travel times. Particularly for regional S-waves, only few detailed models exist for Europe (e.g. Bijwaard, 1999). To obtain a better model, regional travel times for this study are taken from an updated version of the relocated earthquake data set of Engdahl *et al.* (1998), which is based on the ISC and NEIC bulletins.

Moreover, improvements are made in the methodology. Because of the data selection and the ray path distribution, our technique is comparable to Pn tomography. However, the usual approximations of Pn tomography (see e.g. Ritzwoller *et al.*, 2002a) are not required here as a tomographic method is applied that is also used for global tomography (Bijwaard *et al.*, 1998). This method uses, for instance, an irregular grid parameterization (Spakman and Bijwaard, 2001), which enables a finer discretization in regions of high ray coverage. To further improve the model, a 3-D reference model is used to take varying Moho depths and regional changes of velocity properties into account (e.g. oceanic or continental crust).

3.2 Data

Travel times are taken from the updated relocated earthquake data set of Engdahl *et al.* (1998) of the years 1964 to 2000 (E.R. Engdahl, pers. comm., hereafter referred to as EHB data). This new version was extended with data from 1995 to 2000 and includes particularly more regional data (i.e. with an epicentral distance $< 28°$) than the original data set as a result of less restrictive selection criteria. While for the original data set events were selected, which had an open azimuth (= largest azimuthal sector without a seismic station) $\leq 180°$ using only teleseismic stations, now events are selected, which have a secondary azimuthal gap (= largest open azimuth filled by a single station) $\leq 180°$ not only using stations at teleseismic but also at regional distances. While the original data set contained in total 7 million P phases and 1 million S phases, the new data set contains 14 million P phases and 3 million S phases. Besides the European mainland we have included Iceland and Spitzbergen and limited the epicenter and station locations to $50°W - 60°E$ in longitude and $20°N - 80°N$ in latitude. From this data set, the P and S phases are chosen which have an epicentral distance of less than $14°$. The travel time residuals corrected for station elevation and Earth's ellipticity and computed with respect to the 1-D velocity model ak135 (Kennett *et al.*, 1995), are restricted to ±7.5 s and the maximum source depth is set to 200 km. The resulting subset contains 1.5 million P-wave travel times from 60,000 events registered at 1,500 stations and 500,000 S-wave travel times from 55,000 events recorded at 1,400 stations.

In Figure 3.1, an overview of the epicenter locations is presented. The majority of earthquakes is concentrated along plate boundaries and fault zones, particularly in the Mediterranean region (e.g. Greece and Turkey). The phase distribution of the selected data set is displayed in Figure 3.2. Most of the phases have epicentral distances of less than $3°$ in the new data set while the distribution is almost constant in the original data set. The total number of selected phases increased approximately by a factor of 15 for P and 100 for S phases.
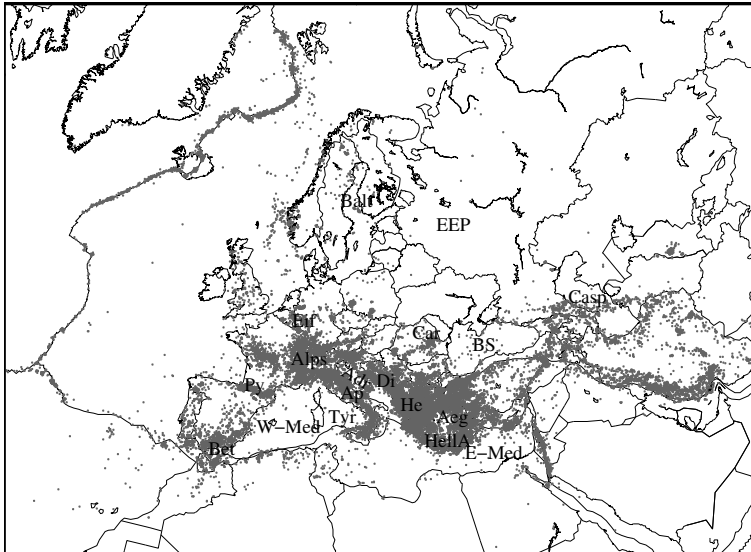
Figure 3.1: Map of the epicenter locations (gray dots) contained in the data selection. The gray shading indicates the topography, plate boundaries are displayed according to Bird (2003). Abbreviations: Adr – Adriatic Sea, Balt - Baltic shield, Bet – Betics, BS – Black Sea, Car – Carpathians, Casp – Caspian Sea, Di – Dinarides, EEP – East European platform, Eif – Eifel, E-Med – Eastern Mediterranean, He – Hellenides, HellA – Hellenic Arc, Py – Pyrenees, Tyr – Tyrrhenian Sea, W-Med – Western Mediterranean.

The standard deviation of the residuals varies between 1.21 s and 1.92 s for P phases and between 1.63 s and 3.15 s for S phases. Figure 3.3 shows the standard deviation as a function of epicentral distance.

3.3   Method

In travel time tomography, observed travel times of waves are compared to theoretical travel times that are calculated with a reference velocity model. The residuals with respect to the reference travel times are used to compute a 3-D velocity model for the analyzed region. Pn tomography usually assumes that P-waves travel as head waves just below the Moho and only the 2-D (horizontal) distribution of the Pn velocities in that layer is calculated. The variations in crustal structure are not included in the model, so terms must be incorporated that correct for the crustal legs at the station and the event site (e.g. Hearn and Ni, 1994; Ritzwoller *et al.*, 2002a). The method used here, which is also suited for global tomography studies, does not require these approximations because the rays are traced along their entire path.

25
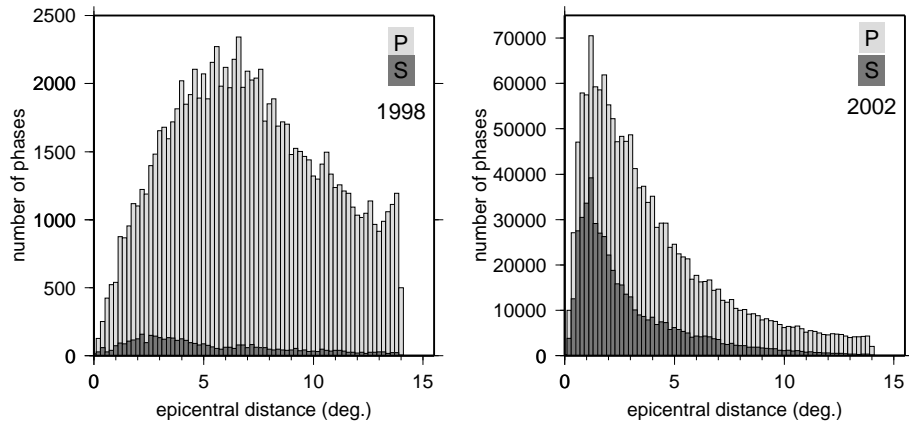
Figure 3.2: Phase distribution of P (light gray) and S (dark gray) phases with respect to the epicentral distance for the original (left) and the updated (right) EHB data set. Note the different vertical axes for the two data sets.
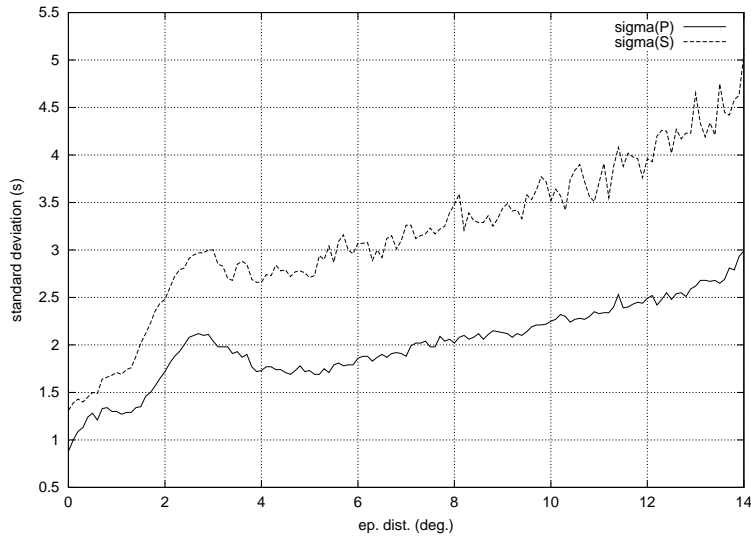
Figure 3.3: Standard deviation of the travel time residuals with respect to the epicentral distance.

3.3.1 Tomography with a 1-D reference/starting model

First, we carry out the tomographic inversion with a 1-D reference model to see the influence of the new regional travel time data alone and to compare the tomography model to other

26

studies which use the original EHB data set (e.g. Bijwaard *et al.*, 1998). The theoretical travel times are computed with the method of Buland and Chapman (1983) using the 1-D reference model ak135 and the according ray paths are determined with a ray shooting method. The obtained travel time residuals and ray paths are then used to set up the data vector and the inversion matrix respectively (see Chapter 2 for details). We perform the tomographic inversion iteratively with the LSQR algorithm of Paige and Saunders (1982) using ak135 as reference model and regularizing the solution with a second-derivative and a weak amplitude damping.

3.3.2 Tomography with a 3-D reference/starting model

Second, since the crust is highly heterogeneous and strongly variable in thickness, it is important in nonlinear tomography to use a starting model that takes the 3-D heterogeneities of the crust in account. Therefore, a 3-D reference model is set up which uses CRUST2.0 (http://mahi.uscd.edu/Gabi/rem.html), a refined version of CRUST 5.1 (Mooney *et al.*, 1998), in the crust and in the uppermost mantle, between the Moho and 200 km depth, laterally varying, depth-averaged velocities of CUB1.1 (Shapiro and Ritzwoller, 2002; Ritzwoller *et al.*, 2002b) are employed. CRUST2.0 is based on regionalization, i.e. it assigns average profiles for various types of crustal structures to $2.0° \times 2.0°$ cells for the whole globe. CUB1.1 is based on surface wave tomography using phase and group velocities of Love and Rayleigh waves.

A 3-D ray tracing through this 3-D model is performed for the selected event-station pairs of the EHB data set with the 3-D raytracer of Bijwaard and Spakman (1999a). This algorithm is based on the perturbation theory developed by Snieder and Sambridge (1992) and Pulliam and Snieder (1996). It takes an initial ray (computed in a 1-D model) and searches nearby paths which have minimum travel times in the 3-D velocity field.

The travel time residuals are then calculated as the difference between the observed travel times of the new EHB data set and the theoretical 3-D travel times. A relocation of the events in the 3-D model is not done as we only use a subset ($\Delta < 14°$) of the data for each event. Therefore, the earthquake locations are assumed to be fixed. The matrix-vector equation (containing the 3-D ray paths and travel time residuals) is inverted with the same method as before but now with the combination of CRUST2.0 and CUB1.1 as reference model.

3.3.3 Parameterization

Various methods exist to parameterize the investigated medium. Here, a method developed by Spakman and Bijwaard (2001) is applied, where the medium is parameterized by a grid with cells of irregular sizes. First, regular grids of several sizes (here $0.4°$, $0.8°$ and $1.2°$) are set up and the hitcount of each cell (i.e. the number of rays crossing a cell) is computed. The regular grid cells have equal surface areas and their thickness is chosen according to the layering of ak135. The hitcount is then used as a constraint to determine the cell sizes in the irregular grid in a way that the variation of the hitcount between neighbouring cells is minimal. Using an irregular grid has the advantage that each unknown is sampled by approximately the same number of data in regions of sufficient ray coverage. Therefore, less damping is needed to
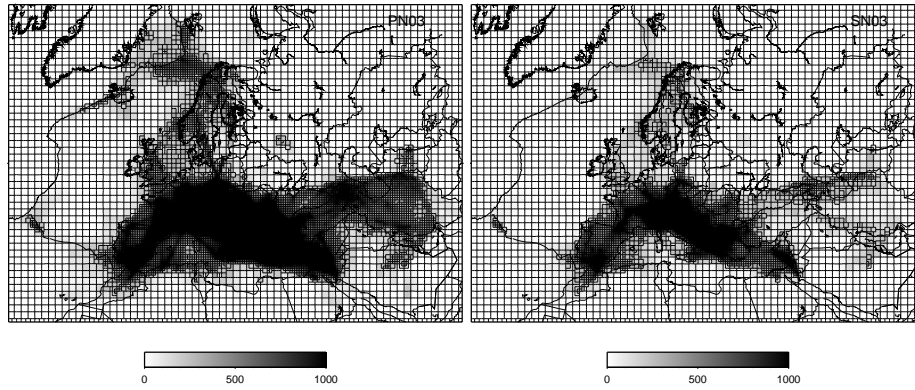
Figure 3.4: Hitcount map for the P- (left) and S-wave coverage (right) at 45 km depth overlaid by the irregular grid.

regularize the inversion. Furthermore, the computation time is significantly decreased. For the P model, for example, there are 650,000 unknowns on the $0.4° \times 0.4°$ grid while there are only 60,000 on the irregular grid. For the S model, the number of unknowns decreases to 50,000. In Figure 3.4, the hitcount of P- and S-waves overlaid by the irregular grid cells is displayed for the best sampled layer (35–55 km).

3.4   Model Resolution and Sensitivity Estimates

As stations and events are not equally distributed over the investigated region, the resolution of the velocity model varies spatially. The non-uniform illumination is clearly indicated in the hitcount maps. For example, there is a very low ray coverage in the Atlantic due to a concentration of the epicenters along the Mid-Atlantic ridge and a lack of stations within regional distance of the epicenters. Also for the East European platform there is a low ray coverage due to a low number of earthquakes and seismic stations.

Resolution can only be estimated since formal computation of the resolution matrix is too time consuming due to the large number of parameters. Instead, tests are performed with synthetic models (Spakman and Nolet, 1988) to find the minimum size of anomalies that can be reconstructed and to detect lack of resolution (see Chapter 2 for details). These tests are also useful to find the appropriate basic cell sizes. The synthetic model for these tests contains spikes of 5% amplitude with respect to the 1-D reference model and alternating sign of the anomaly. The spikes are well separated with a distance of at least twice the spike size in longitudinal direction, once the spike size in latitudinal direction and one layer in depth between them. Theoretical travel times are then calculated and Gaussian distributed noise on the order of 0.5 s is added to the data to perform an inversion comparable to the real data inversion. The geometry of the 1-D rays is used and the resulting matrix-vector

equation inverted. In Figure 3.5, an example of such a spike test is shown at 45 km depth with spikes of $0.8° \times 0.8°$. The best ray coverage, independent of the wave type, is found in the layer between 35 km and 55 km, which is the layer directly below the Moho in the 1-D model ak135. Because of the data selection that contains mainly Pn/Sn phases, this layer is expected to be the best sampled. A sufficient ray coverage is also found for the layers between 20 km – 35 km and 55 km – 75 km. For the P model, spikes of $0.4° \times 0.4°$ can be reconstructed while for the S model, only spikes of a minimum size of $0.8° \times 0.8°$.
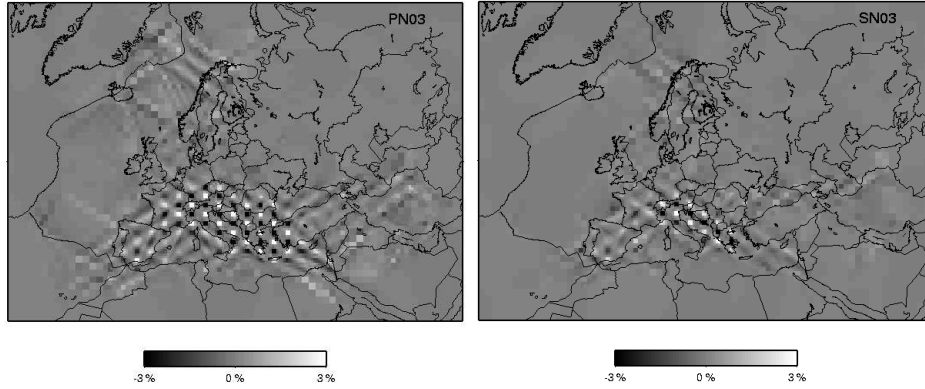
Figure 3.5: Spike tests for the P model (left) and the S model (right) at 45 km depth with spikes of $0.8° \times 0.8°$. The grayscales give the amplitude of the velocity anomalies.

To estimate the uncertainty of the velocity model caused by errors in the observed arrival times, the data vector is permuted randomly while keeping the order of the matrix rows (rays) as for the original data vector (Spakman and Nolet, 1988). In this case, the inversion model is expected to show random anomaly patterns of low amplitude if there are no correlations between delay times and ray paths. An example of such a test is given in Figure 3.6. In general, a random model is found in regions of good ray coverage with low amplitudes. Only poorly sampled regions, as for example north of Iceland in the S model, show systematic anomalies of higher amplitude ($\approx 1\%$). Thus, the amplitude uncertainties can be expected to be very low for the P model while they are higher for the S model.

Another way to test the sensitivity (not shown) is to use random noise (e.g. Gaussian distributed noise) as data vector and perform the inversion for this vector. Since the standard deviation of all selected residuals of the observed P data set is 1.84 s, the width of the Gauss function is chosen accordingly. The resulting model shows low amplitude anomalies ($\lesssim 0.5\%$) and is random for the P model, which means that the noise is uncorrelated and of low level. Unlike the permuted-data test, using Gaussian noise does, however, not test for the effects of systematic data noise.
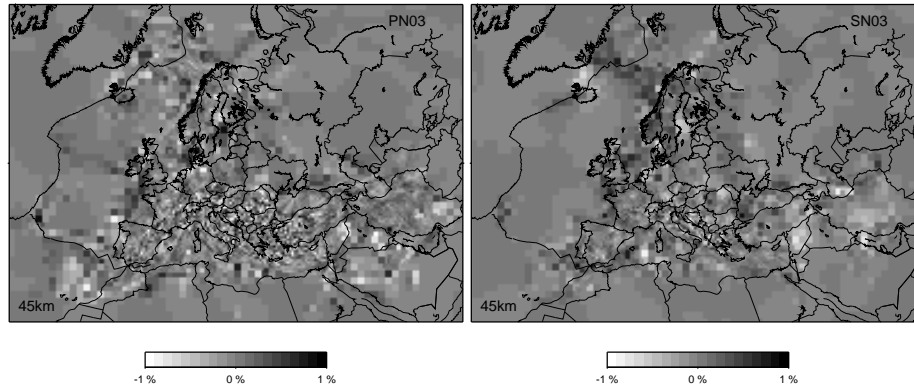
Figure 3.6: Test with a randomly permuted data vector for the P model (left) and the S model (right) at 45 km depth.

3.5 Results

3.5.1 Tomography with a 1-D reference model

The results of the tomography for ak135 as initial model are presented in Figure 3.7. Many tectonic regions can be identified in the P-wave and S-wave velocity models. Generally, the S model shows more positive velocity anomalies (with respect to ak135) than the P model. This shift towards higher velocities is caused by the fact that ak135 is too slow for S-waves in the crust/uppermost mantle. Therefore, in Figure 3.7 the S model is displayed with respect to ak135 increased by 1% of its velocity.

At 28 km depth (which is the lower crust in ak135), low-velocity anomalies dominate the P model. The anomalies associated with mountain ranges (Alps, Pyrenees, Apennines, Dinarides) are narrow and of large amplitudes. Other low-velocity anomalies are found beneath the Eifel, the Tyrrhenian basin and the Turkish-Iranian plateau, which are broader and have in absolute terms a lower amplitude at this depth than the anomalies found under mountain ranges.

At 45 km depths also both types of low-velocity anomalies are present due to crustal and mantle features but the mantle anomalies are now broader than before and have higher amplitudes. Furthermore, high-velocity anomalies can be associated with cratons as the East European platform or stable parts of Iberia and France. High-velocity anomalies are also found beneath basins such as the Eastern Mediterranean or the South Caspian basin.

Even though ak135 is too slow in the uppermost mantle for S waves, many features described above for the P model could be imaged as well with the S model but with a lower resolution as there are less S residuals. Velocities that were left unchanged in the inversion and therefore contain the velocities of ak135 (3.85 km/s at 28 km and 4.48 km/s at 45 km depth) as below parts of the East European craton appear in Figure 3.7 as weak low velocity anomalies as an effect of the increased reference velocity chosen for display (3.89 km/s and 4.53 km/s

30

respectively).

Taking into account the results of the permuted data tests, the average error of model amplitudes amounts to less than 10% and 15% respectively for the P and S velocity anomalies.
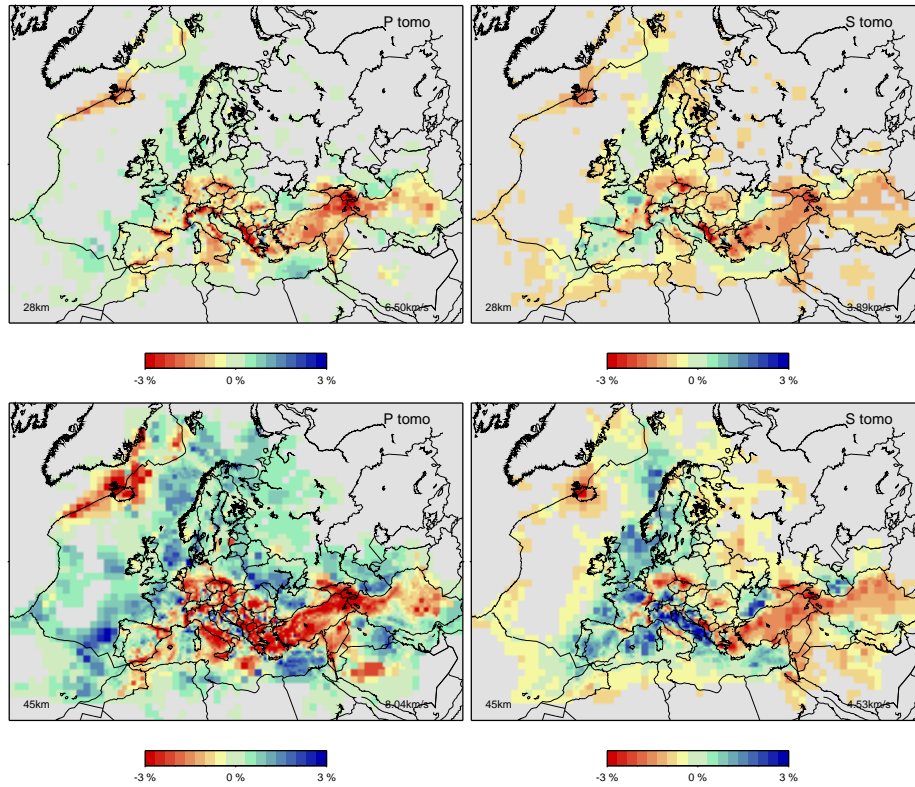
Figure 3.7: Results of the tomographic inversion for the P model (left) and the S model (right) at 28 km depth (top) and 45 km depth (bottom). The velocity anomalies are given with respect to the 1-D velocity model ak135 for P as indicated by the number on the lower right of each figure and with respect to $1.01 \times v_s(ak135)$ for S. Gray are the regions without crossing rays.

3.5.2 Tomography with a 3-D reference model

The 3-D model combined of CRUST2.0 and CUB1.1 is now used as reference model for the inversion. The results of the inversion with reference to this model are clearly different from the results of the inversion with ak135 as reference model. They are shown in Figure 3.8 and 3.9 with respect to the average velocity of the appropriate layer and with respect to the 3-D reference model. Generally, the inversion of the S residuals shows less deviations from

31

the reference model than the P inversion as there are less S travel times and therefore less resolving power in the data but also since the 3-D S reference model provides a better representation of shear velocities in some regions.

The velocities of the P model (see Fig. 3.8) are in the middle and lower crust significantly higher than ak135. For instance, the P-wave velocity between 20 km and 35 km in ak135 is only 6.50 km/s, while the average velocity of that layer is 7.07 km/s in the 3-D inversion model. Similar to the results of the inversion with ak135 as reference model, the obtained anomalies can be related to tectonic units. Low velocity anomalies are observed along mountain ranges (e.g. Betics, Alps, Dinarides) best seen in the difference between the inversion and reference model resulting, for example, in a finer outline of the western edge of the Alps. Furthermore, reduced velocities are obtained beneath the Western Mediterranean, in particular beneath Corsica and Sardinia. But also in the Eastern Mediterranean velocities are reduced indicating that they are not as high as would have been expected from the reference model. Velocities beneath the Turkish-Iranian plateau are almost unchanged as the reference model already explains travel time deviations well in that region. Also beneath the East European platform few differences exist between reference and inversion model due to either a good representation of velocities in the reference model or due to a lack of resolving power of the travel time residuals in that area.

Mostly lower velocities than in ak135 are found for the layer between 35 km and 55 km (on average $v_p = 7.81$ km/s while in ak135 $v_p = 8.04$ km/s). In this layer the reference model is a combination of the long wavelength structures in CUB1.1 (e.g. Atlantic) and CRUST2.0 (East European platform). Furthermore, the observed features of the inversion model at this depth show many similarities to the model obtained with ak135 as reference. The velocities beneath Iceland and further along the Mid-Atlantic ridge are greatly decreased compared to the reference model. The Western Mediterranean Sea shows also lower than average velocities while they are higher than average for the Eastern Mediterranean (as in the inversion model using ak135 as starting model). Orogenic belts as the Alps, Pyrenees or Dinarides are well reconstructed in this model. At 45 km depth, low velocities are found in the P and S model as in the inversion model using ak135 as starting model. The Adriatic plate is imaged by high velocities. Velocities beneath the East European platform are slightly increased in the inversion model indicating that even though this region still contains crustal material at this depth it is faster than would be expected from the reference model.

The S inversion model shows features which are very similar to those obtained in the P inversion. However, fewer regions display changes from the reference model. Deviations are in particular the reduced velocities of the western edge of the Alps, the Hellenic Arc and Iceland. Furthermore, higher velocities than in the reference model are observed beneath the Adriatic basin and beneath Spain. These differences are also observed at 45 km depth but now with stronger amplitudes. Besides that, low velocities are also observed north of Iceland and in the Western Mediterranean basin enhancing the difference between western and eastern basin as in the P inversion models.

3.6 Discussion and Conclusions

The main purpose of this study was to create a high-resolution image of the uppermost mantle and the crust. To obtain such an image, a tomographic inversion for P-wave and S-wave travel times of regional earthquakes was applied. In the following, the most important features of the new model are described and briefly discussed.

Negative velocity perturbations are found for the Mid-Atlantic ridge, where they reflect the spreading of the Atlantic. However, the low velocities beneath Iceland in the P and S model are not only caused by the opening of the Atlantic, but also by a plume (e.g. Wolfe *et al.*, 1997; Shen *et al.*, 1998; Bijwaard and Spakman, 1999b; Allen *et al.*, 2002).

Furthermore, the whole Turkish-Iranian plateau is imaged by low velocities that have also been stated by other researchers who applied Pn tomography (Hearn and Ni, 1994; Ritzwoller *et al.*, 2002a) and in other earlier mantle tomography studies (e.g. Spakman *et al.*, 1993). The anomaly can be interpreted as hot or partially molten material (Hearn and Ni, 1994; Ritzwoller *et al.*, 2002a) as the high temperatures can be explained by the back arc extensional setting of the region during the collision of the Arabian and the Eurasian plate (Dercourt et al., 1986). Alternatively, recent studies by Sengör *et al.* (2003) and Keskin (2003) show that the high temperatures and therefore low velocities can be ascribed to steepening and detachment of the Neo-Tethys slab beneath Eastern Turkey followed by rising of hot asthenosphere material.

Orogenic regions (e.g. Alps, Carpathians, Hellenides and Pyrenees) and back-arc basins (Tyrrhenian basin, Aegean) are also characterized by low velocities.

A comparison of the low-velocity anomalies at 45 km depth in our model to those in the surface wave tomography model of Boschi *et al.* (2004) shows a good agreement of anomalies on a larger scale in the Alpine-Carpathian belt, the Tyrrhenian basin and the Aegean even though features in our model have sharper outlines.

In regions with oceanic lithosphere (Black Sea, South Caspian basin and Eastern Mediterranean basin), positive velocity perturbations are obtained in this study. But while the Eastern Mediterranean basin is imaged by high-velocity anomalies in our model, low velocities are found in the surface wave tomography model of Boschi *et al.* (2004) and only turn into positive perturbations at greater depths. The differences are most likely caused by the fact that the travel time tomography is better resolved at 45 km depth. Also, high velocities are obtained for both, travel time tomography and surface wave tomography models, beneath stable parts of Spain and France and beneath cratonic regions (Baltic shield, East European platform, only for the use of a 1-D reference model for travel time tomography as in the 3-D reference model this region is still considered as crust). However, the Trans-European Suture Zone, which separates the East European platform from the younger parts of Central Europe is imaged in less detail in the surface wave tomography than in our model.

The use of a 3-D reference model instead of a 1-D reference model results, independently of the applied reference model, in P and S tomography models that show the main tectonic features as observed for use of a 1-D reference model. Yet, in regions of low resolution mainly the reference model is re-obtained, besides regions where the reference model already gives a good representation of the velocity heterogeneities.

On the whole, we have obtained high-resolution P and S velocity models for the crust and the uppermost mantle showing new details of the tectonic structures beneath Europe. The higher

resolution is due to the use of a larger, reprocessed data set. Also, unlike in earlier Pn tomography studies, we traced the rays along their entire path as they can undergo rapid velocity changes in the crust. Nevertheless, since we used only regional data, vertical structures like subducted slabs are not imaged with our model.

Figure 3.8: Displayed is on the top the 3-D reference model derived from CRUST2.0 and CUB1.1 and in the middle the results of the P-inversion. The velocity anomalies are given with respect to the average velocity of each layer (see number at the bottom right of the figures). Illustrated on the bottom is the difference between the reference and the inversion model. All models are shown at 28 km depth (left) and 45 km depth (right).

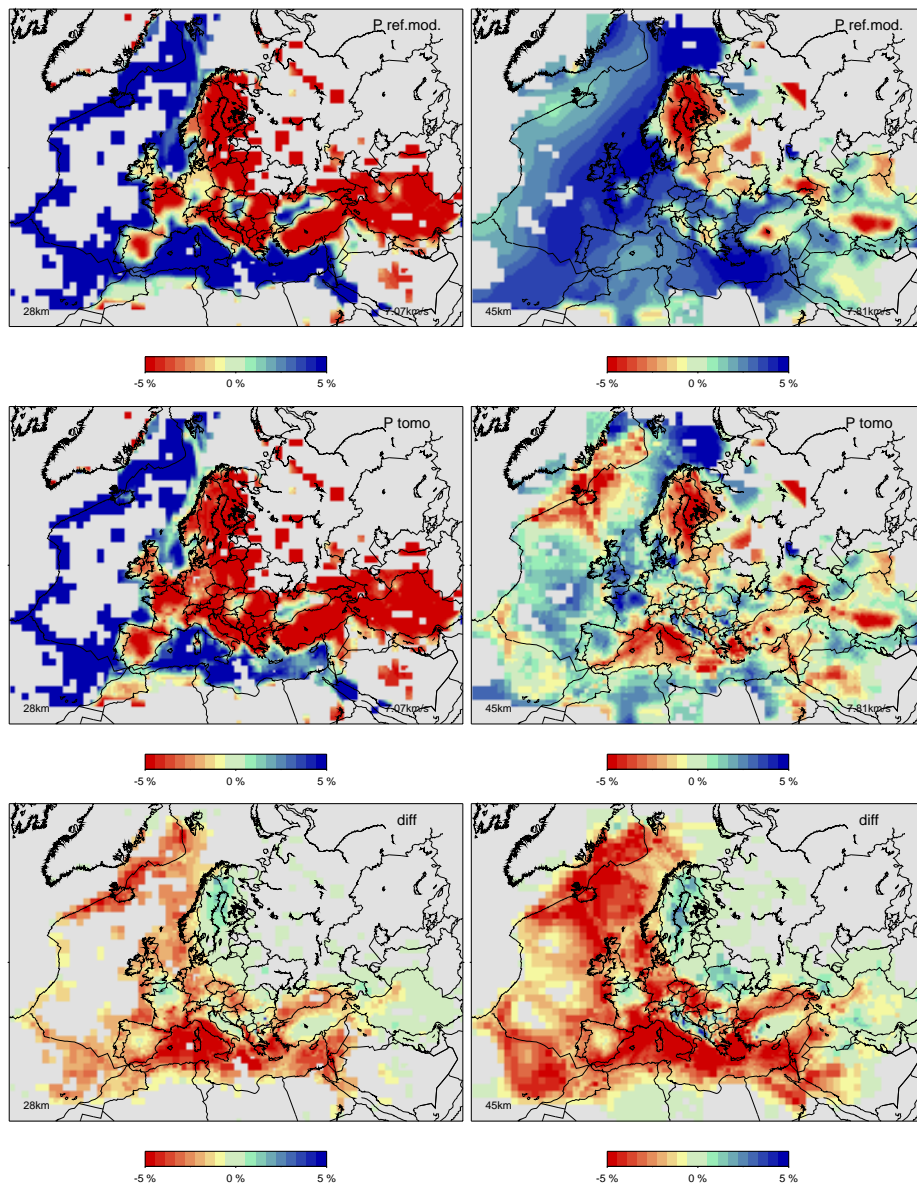**Figure 3.9:** Displayed is on the top the 3-D reference model derived from CRUST2.0 and CUB1.1 and in the middle the results of the S-inversion. The velocity anomalies are given with respect to the average velocity of each layer (see number at the bottom right of the figures). Illustrated on the bottom is the difference between the reference and the inversion model. All models are shown at 28 km depth (left) and 45 km depth (right).
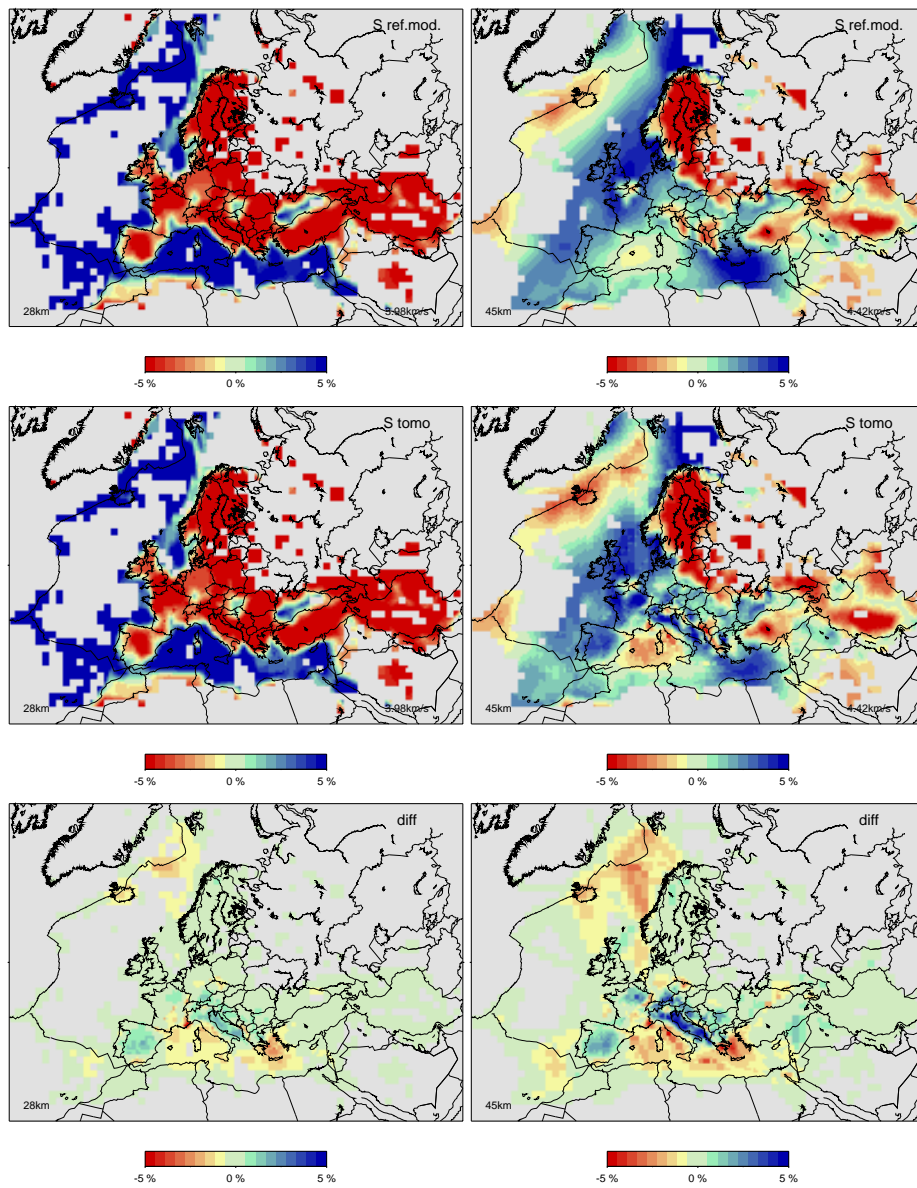
Chapter 4

A new absolute arrival time data set for Europe

The main aim of this study is to create a data set of accurate absolute arrival times for stations in Europe which do not report to the ISC (International Seismological Centre). Waveforms were obtained from data centers and temporary experiments and an automatic picking method was applied to determine absolute arrival times for first and later arriving P and S phases. 86,600 arrival times were picked whose distribution of residuals shows generally low standard deviations. Furthermore, mean teleseismic station residuals reflect the properties of the underlying crust and uppermost mantle. Comparison to ISC data for matching event-station-phase combinations also confirms the good quality of the new absolute arrival time picks. Most importantly, this data set complements the ISC data as it fills regional data gaps in Europe.

4.1   Introduction

Arrival times are routinely reported by many seismological networks to the ISC, resulting in bulletins of millions of arrival times since 1964. Clearly, a wealth of information can be gained from these data regarding the Earth's interior, for example, by application of travel time tomography. However, the reporting stations are not distributed equally over the globe therefore leaving gaps, in particular, in the oceans and stable cratonic regions. Furthermore, the quality of these data, which are mostly handpicked, varies greatly (Röhm *et al.*, 1999).

Besides stations included in arrival time bulletins, a large number of seismic stations exist whose waveforms are not used routinely but are sent to data centers for digital storage. For many events included in these waveforms, arrival times were either not picked at all or only with limitations (e.g. a restricted period in time or limited epicentral distance range).

Another valuable source of data is provided by temporary experiments. To fill the geographical gaps, many regional experiments were carried out during the last 15 to 20 years where spatially dense temporary networks were placed in the field for several months. Often, arrival times for events registered at those arrays were only picked relatively. That means, not the

arrival time of a phase onset was determined but the arrival time of the first maximum or minimum after the onset. This procedure has the advantage that observational errors due to high noise levels can be reduced but as a major disadvantage, arrival times are only obtained with respect to the unknown mean network arrival time for a specific event. Therefore, they cannot be used for event relocation or to obtain absolute velocity information on the crust and mantle below the array. Consequently, obtaining arrival times for events recorded at such stations which do not report arrival times to the ISC can provide new detailed information for high-resolution travel time tomography.

Besides using additional stations, the picks should also be of a consistent good quality as erroneous picks will affect or overprint velocity structures which would otherwise be imaged in travel time tomography. Generally, hand picks are considered to give the best quality but for large data sets this approach is not feasible. However, advanced automatic picking techniques can be applied when many waveforms are recorded for a single event which provide very accurate picks.

The aim of this study is to present such a data set of absolute arrival times for Europe. This data set provides high quality picks of previously unused waveforms and can, for instance, be combined with the ISC arrival times for travel time tomography. To ensure a good picking quality for a large number of waveforms we apply a recently developed two-step automatic phase picker. With our approach, we focus on Europe where many temporary experiments have taken place and where data centers provide a large source of additional waveforms from various digital networks in Europe.

4.2   Data

During the past 15 years large teleseismic experiments were conducted in Europe where spatially dense seismograph arrays were placed in the field for several months. Data from such experiments were obtained as waveforms from the CALIXTO, EIFEL, MIDSEA, SVEKA-LAPKO, and TOR experiment. Another data collection (named "Leeds" data set hereafter) was provided by the University of Leeds, UK (Arrowsmith, 2003) and the ORFEUS (Observatories and Research Facilities for EUropean Seismology) data center forms a further important source of waveforms. A map of all station locations is displayed in Figure 4.1.

4.2.1   Leeds Data Set

This waveform collection comprises 150 stations from the BGS (British Geological Survey), DIAS (Dublin Institute for Advanced Studies) and LDG (Laboratoire de Détection et de Géophysiqe, France) seismic networks. Many of these stations did not report arrival times to the ISC on a regular basis. The data set contains registrations from the period 1993-2001. It was used so far only for classic teleseismic travel time tomography with relative arrival time picks (Arrowsmith, 2003; Arrowsmith *et al.*, 2005) to investigate the relation between asthenosphere, lithosphere and crust beneath the British Isles. We used the waveforms as provided to us by S. Arrowsmith (pers. comm.).

4.2.2 CALIXTO

The CALIXTO (Carpathian Arc LIthosphere X-TOmography) experiment was carried out to investigate the lithosphere/asthenosphere structure of the Vrancea zone (southeast Carpathians) known for its strong and localized seismicity. From May 1999 to November 1999, 110 mobile stations were placed in the field in Romania. The data set was supplemented by registrations from 18 permanent stations in Romania (see Wenzel *et al.* (1998) for details). Among the published tomography studies about the CALIXTO experiment are teleseismic P tomography studies using relative travel time residuals (Martin and Ritter, 2005; Martin *et al.*, 2006), an upper crustal absolute P tomography (Landes *et al.*, 2004) and a study using handpicked absolute P arrival times by Weidle *et al.* (2005). However, absolute arrival times were neither picked for S waves nor for the entire set of local and regional events.

4.2.3 EIFEL

The EIFEL project was conducted to investigate the Quarternary volcanism in the Eifel and a possible mantle plume as its origin. Between November 1997 and June 1998, 158 stations were operated in the Eifel and surrounding regions. Ritter *et al.* (2000) give an overview of the experiment. Among studies about this experiment are a receiver function study (Grunewald *et al.*, 2001), a teleseismic P tomography (Ritter *et al.*, 2001) and a teleseismic S tomography study (Keyser *et al.*, 2002) both using relative travel time residuals.

4.2.4 MIDSEA

The MIDSEA (Mantle Investigation of the Deep Suture between Eurasia and Africa) project was performed to fill gaps in the Mediterranean area where no broadband registrations existed before and should therefore improve images of the lithosphere and mantle beneath the Mediterranean region (van der Lee *et al.*, 2001). Registrations from 10 stations were available via ORFEUS. These stations had been placed in the field for 1–2 years during the period June 1999 – May 2002. Among studies about this project are a receiver function study (van der Meijde *et al.*, 2003), a surface wave tomography study (Marone *et al.*, 2003) and a shear wave splitting analysis (Schmid *et al.*, 2004). For this data set, absolute arrival times were not picked.

4.2.5 SVEKALAPKO

The SVEKALAPKO (SVEcofennian-KArelian-LAPland-KOla) project was carried out in Finland with the aim to get a better understanding of the formation of the oldest continents, namely the core of the Karelian province of Archean age (2.6 Ga). 128 mobile stations were placed in the field from August 1998 to May 1999. The data set was completed by registrations from 15 permanent stations (see Bock and the SVEKALAPKO Seismic Tomography Working Group (2001) for experiment details). Among studies about this experiment are a receiver function study (Alinaghi *et al.*, 2003), a teleseismic P tomography study (Sandoval *et al.*, 2003, 2004b), a surface wave tomography study (Bruneton *et al.*, 2004) and a local

tomography study (Yliniemi *et al.*, 2004). Only for the local study, absolute arrival times were used.

4.2.6 TOR

For the TOR (Teleseismic Tomography across the Tornquist Zone in Germany–Denmark–Sweden) experiment, 120 stations were placed in South Sweden, Denmark and North Germany from October 1996 to April 1997 to image the Tornquist zone, that separates the Baltic shield from the younger (Phanerozoic) parts of Central Europe, in greater detail than before. Many studies already exist for this experiment using a range of seismological methods. Besides an overview of the experiment given by Gregersen *et al.* (2002), among the studies are a teleseismic P tomography (Arlitt *et al.*, 1999), non-linear P and S tomography studies (Shomali *et al.*, 2006; Voss *et al.*, 2006), receiver function studies (Gossler *et al.*, 1999; Wilde-Piórko *et al.*, 2002; Alinaghi *et al.*, 2003) and anisotropy analyses (Wylegalla and TOR Working Group, 1999; Plomerova and TOR Working Group, 2002). However, none of the named studies used absolute travel times.

4.2.7 ORFEUS

The ORFEUS Data Center provides the biggest data set particularly picked for our study. Their archive contains registrations from the years 1988 to 2000 for stations of the European digital seismometer network of which approximately half of the stations did either not report at all or at least not regularly to the ISC.

4.3 Method

The data described above were obtained from the individual sources as waveform registrations. Since the main interest of this study are the arrival times, those waveforms were processed further. They were either obtained already sorted by events or if necessary the events were selected from the EHB catalog (Engdahl *et al.*, 1998), a reprocessed version of the ISC bulletins, using within Europe earthquakes with $m_b > 4.5$ and for teleseismic events earthquakes with $m_b > 5.5$. As the seismograms were provided in various data formats, they were converted by us to the common format SAC (Goldstein *et al.*, 2003). Since the stations were equipped with different types of sensors, which are sensitive in different frequency ranges, the registrations were restituted to simulate the short period WWSSN (World Wide Standardized Seismographic Network) sensor with a dominant frequency around 1 Hz. Besides P-wave arrivals for events in all distance ranges, also S-wave arrivals were picked for the CALIXTO data set. In those cases, the registrations were restituted with a Wiechert sensor with a dominant frequency of 0.1 Hz and continuing high amplification towards higher frequencies to account for the lower frequencies of S-waves. As a next step, the waveforms were bandpass filtered according to the epicentral distance of the registered phase and the phase type (cf. Sandoval *et al.*, 2004a). Theoretical travel times were computed for all registrations in the Earth reference model ak135 (Kennett *et al.*, 1995) to choose appropriate time windows for the travel time picking.
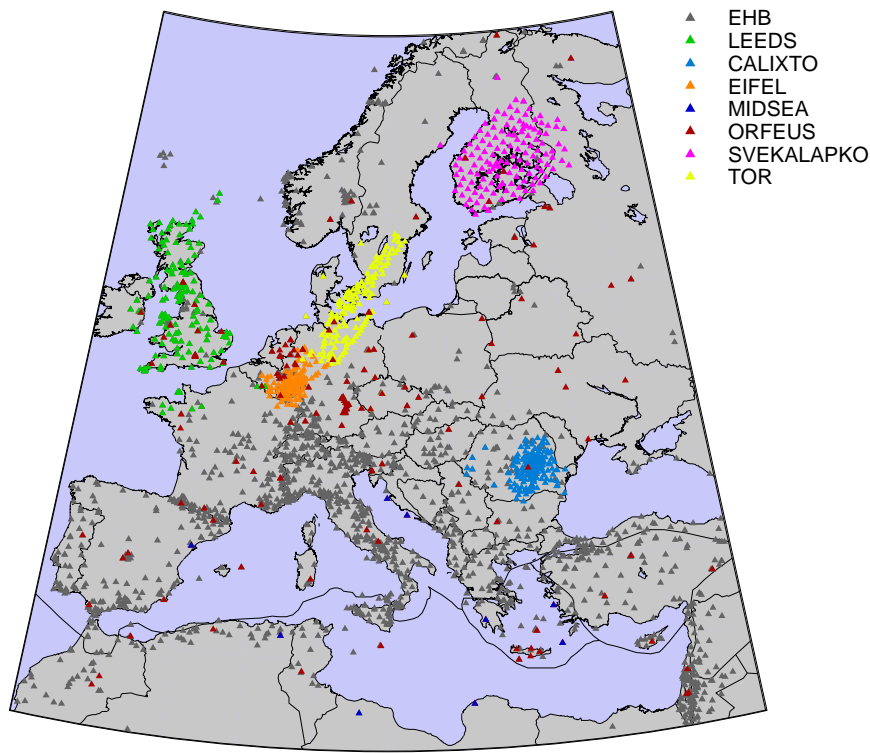
Figure 4.1: Station locations. The different colours denote to which network/data source the stations belong.

Because of the large number of waveforms, hand-picking was not feasible anymore. Therefore, the picking of the arrival times was carried out with a semi-automated picking software developed by Sandoval *et al.* (2004a). The picking was performed per event with a two-step algorithm to ensure a good picking quality. First, the STA/LTA algorithm of Earle and Shearer (1994) was applied. This algorithm is based on a short-term-average to long-term-average ratio taken along an envelope function of the seismogram and returns the absolute arrival time as a result. Then, the picks were grouped regionally and a reference station with a high signal-to-noise ratio was selected manually for each region. The reference waveforms were cross-correlated with each other for consistency between the regions. Afterwards, the

waveforms within each region were cross-correlated with the reference station to improve the STA/LTA pick. This method was applied for picking of the CALIXTO, EIFEL, SVEKA-LAPKO and TOR experiments.

Later on, the procedure was refined as it required input from the user to choose the reference waveforms which would have been too time-consuming for larger data sets. Additionally, as grouping by equally sized subregions is not the optimum approach for wide-spread station locations as the ORFEUS stations, a cluster analysis was performed to group the stations. Instead of cross-correlation an adaptive stacking method based on the algorithm of Rawlinson and Kennett (2004) was applied to each cluster as this method is more robust concerning waveform variability than cross-correlation techniques. With this method, all waveforms were initially aligned with respect to their theoretical travel time and stacked. They were shifted with respect to the stack to iteratively maximize the stack. As a result, the travel time residual of each phase relative to its theoretical travel time was obtained and an error estimate was computed via the misfit between the individual waveforms and the stacked signal. Subsequently, the STA/LTA picker was applied to the stacked waveform to obtain an accurate pick of the phase onset and finally absolute arrival times were computed for each station from the combination of STA/LTA pick and relative station residuals. The refined method was applied to the ORFEUS, MIDSEA and Leeds data sets.

Such methods work well if the waveforms within a group/cluster are similar to each other but work less well if waveforms change rapidly with distance as can be the case for example for local events. Then, the picker allows for user input to pick the arrival times by hand.

4.4   Results

In total, 86580 absolute arrival time picks were obtained with an estimated picking error of 0.10–0.20 s. Table 4.1 gives a more detailed overview of the number of picks. All residuals used and displayed in this study are computed with respect to ak135. As is shown in Figure 4.2, the residuals (observed – theoretical travel time) are centered around -0.13 s with a standard deviation of 1.05 s appropriate for a data set that contains information about many different geological settings. The solid black line in Figure 4.2 represents the best fitting Gaussian curve with a standard deviation of 0.67 s. Towards bigger residuals, the observed data do not follow a normal distribution but show a broader tail. This effect is mainly attributed to errors in the data set (for example event mislocation or picking errors) but also to 3-D velocity structures along the ray path (e.g. Röhm, 1999; Pulliam *et al.*, 1993).

Generally, rays from teleseismic events recorded at a dense station array take approximately the same path through the Earth except for the part directly beneath the array. Therefore, their travel time differences for each event reflect the velocity differences of the crust and lithosphere beneath the array. Two examples which indicate the high quality of the obtained picks are illustrated in Figure 4.3. On the left, an event in the Afghanistan-Tajikistan border region registered at the EIFEL array is displayed. It shows highest residuals in the center of the array and west of it (as the wavefront arrives from the east) indicating the lower velocities directly beneath the Eifel. On the right, the obtained travel time residuals for an event in Japan registered at the TOR array are shown. A transition can be observed from negative

Data Set	Picks	Events	Distance Range
Leeds	5237 (P)	64	28°– 162°
CALIXTO	4078 (P)	210	0°– 158°
	1484 (SV)	100	0°– 86°
	1564 (SH)	101	0°– 88°
EIFEL	6288 (P)	90	5°– 164°
MIDSEA	739 (P)	256	0°– 160°
ORFEUS	56686 (P)	2056	0°– 178°
SVEKALAPKO	5606 (P)	102	20°– 148°
TOR	4898 (P)	111	2°– 160°

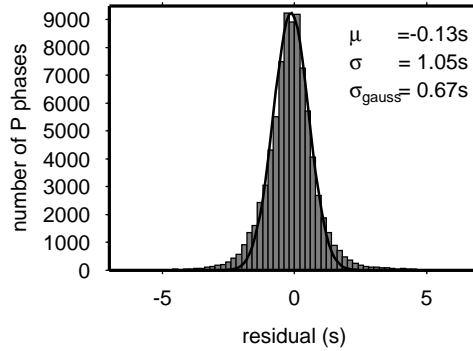**Table 4.1:** Summary of the obtained arrival time picks.

Figure 4.2: Histogram of the P residuals (with respect to ak135) for the newly picked data. The solid line indicates the best fitting Gaussian function.

residuals in the north due to the high velocities of the Baltic shield across the Tornquist zone to higher residuals related to the slower velocities of the younger parts of central Europe.

Since the automatic picker works best for teleseismic events, even though data for all distance ranges were picked, for the remainder of this paper, focus will be on arrival times obtained for teleseismic events ($\Delta > 28°$). Computing the mean of all teleseismic residuals obtained at a single station will mainly reflect the regional velocity variations underneath the stations as for a wide azimuthal coverage of epicentral regions source effects and contributions of the paths further away from the station will diminish. In Figure 4.4, the mean teleseismic station residuals of the new data and their standard deviations are presented (upper and lower right respectively). For comparison, the mean teleseismic residuals and standard deviations of the ISC bulletins are displayed on the upper and lower left.

Negative residuals are found beneath the SVEKALAPKO array and the northern part of the TOR array reflecting the high velocities of the Baltic shield. The residuals become positive at the southern part of the TOR array due to the lower velocities of the underlying lithosphere.
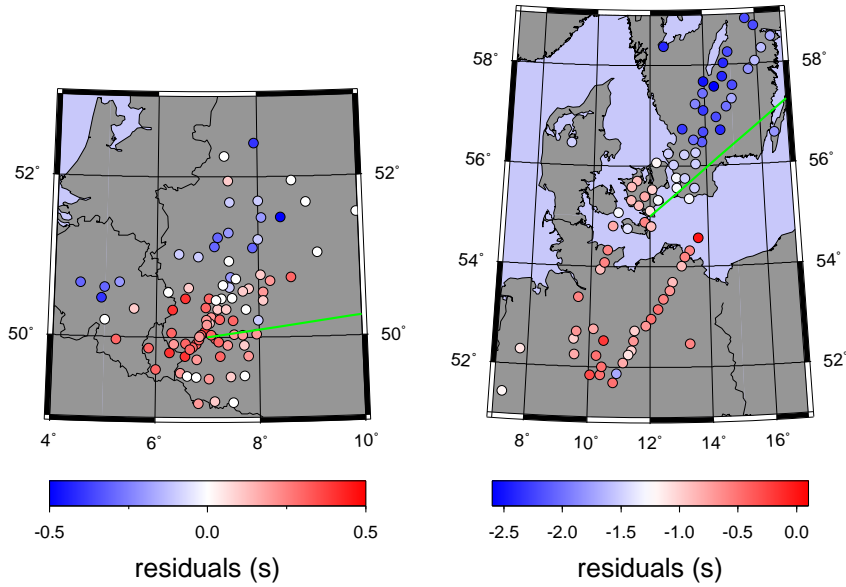
Figure 4.3: Example of residuals (with respect to ak135) obtained for the EIFEL (left) and TOR array (right) for an event in the Afghanistan-Tajikistan border region (30 May 1998 06:22:31.1, 37.141°N, 70.094°E, z = 35.2 km, m_b = 5.7) and Japan (19 October 1996 14:44:41.75, 31.911°N, 131.574°E, z = 18 km, m_b = 6.2) respectively. The green line indicates the direction of incidence of the wavefront.

The Eifel region shows only in the central part slightly positive residuals (on average) related with the lower velocities underneath it but otherwise negative velocities due to higher velocities in the surrounding crust and lithosphere (particularly to the north and northeast). For the British data set, generally small residuals are found with the most negative residuals in the Central Highlands region possibly caused by high velocities of remnants of a subducted oceanic plate (Arrowsmith, 2003, and reference therein). The CALIXTO array shows positive residuals in the bend zone of the southeast Carpathians and in the Transylvanian and Focsani basins. Negative residuals are found towards the northeast on the East European Platform, the east and in the southwestern part of the seismic array (west of the Intra-Moesian fault). Overall, 50 of the 160 stations in the ORFEUS archive did not report arrival times to the ISC, in particular NARS stations (Network of Autonomously Recording Seismographs, see e.g. Paulssen *et al.* (1990, 2000)) and about 40 more stations either reported only local and regional arrival times to the ISC or not for the entire period of operation. Picking of arrival times from the rest of the stations did not consume much extra time due to the applied picking method. The ORFEUS stations on the East European Platform display negative residuals due to the fast velocities of the old cratonic material beneath it while for example the stations in the Netherlands show positive residuals.

A comparison of the new data with the mean teleseismic residuals of the EHB catalog (orig-

inating from the ISC bulletins) shows similarities but due to the locally denser station distribution regional variations can be seen in more detail as for example across the Tornquist zone.

The standard deviation of the new teleseismic residuals are generally low around 0.5–0.7 s except for regions where the residuals show a strong azimuthal dependence (e.g. TOR - many events either from north-northeast along array direction or perpendicular to the array from east-southeast, CALIXTO - complex tectonic structure due to collisional setting, deep sediment basins) or concerning the highest standard deviations where only few teleseismic arrival time picks with greater variation exist. Nevertheless, the scatter of residuals is much lower than for most of the ISC data indicating the high quality of the data set.

As a final inspection of the new picks, identical teleseismic event-station-phase pairs were retrieved from the EHB catalog and compared to the new picks. Approximately 17,000 such pairs could be found mainly from the ORFEUS catalog but also for stations of the other data sets. As displayed in Figure 4.5, the new residuals are on average 0.09 s faster with a standard deviation of 0.77 s for the difference between the residuals. The picking error of the ISC data can then be estimated since the difference in residuals corresponds to the difference in picking errors:

$$d_{ISC} = d + \epsilon_{ISC} \tag{4.1}$$

$$d_{NEW} = d + \epsilon_{NEW} \tag{4.2}$$

$$\Rightarrow d_{ISC} - d_{NEW} = \epsilon_{ISC} - \epsilon_{NEW} \tag{4.3}$$

where d_{ISC} and d_{NEW} denote the individual, observed travel time residuals, d is the residual without picking errors, ϵ_{ISC} and ϵ_{NEW} are the picking errors.

With a picking error on the order of 0.15 s for the newly picked data, a standard deviation of 0.77 s for the distribution of $\epsilon_{ISC} - \epsilon_{NEW}$ measurements and under the assumption of Gaussian error propagation, the picking errors in the ISC data amount to approximately 0.75 s. This value is larger but still in agreement with the estimate of Gudmundsson *et al.* (1990) of $\sigma \approx 0.5$ s for random errors in teleseismic ISC residuals.

4.5 Conclusions

The main objective of this study was to obtain accurate arrival time picks for stations within Europe which did not report to the ISC and to fill data gaps in regions with few stations. Waveforms were provided by spatially dense temporary arrays and data centers in Europe. These waveforms were then preprocessed and absolute arrival times picked with the automatic phase picker of Sandoval *et al.* (2004a). Analyses of the picks show their high quality and that they contain significant information on the geologic properties of crust and uppermost mantle directly beneath the stations. Therefore, the new data set can be combined with the ISC data for global travel time tomography to obtain a high-resolution velocity model of crust and mantle beneath Europe in particular beneath the dense station arrays. Furthermore, this study shows where lack of data/stations is still greatest (e.g. parts of East Europe or Scandinavia). For future research, valuable information could also be gained from near real time picking of the VEBSN (Virtual European Broadband Seismograph Network) as gradually more waveforms become available in near real time for stations which do not report to

the ISC so far.

The new arrival time picks will be made available via anonymous ftp on ftp://terra.geo.uu.nl/-people/amaru/.

4.6   Acknowledgments
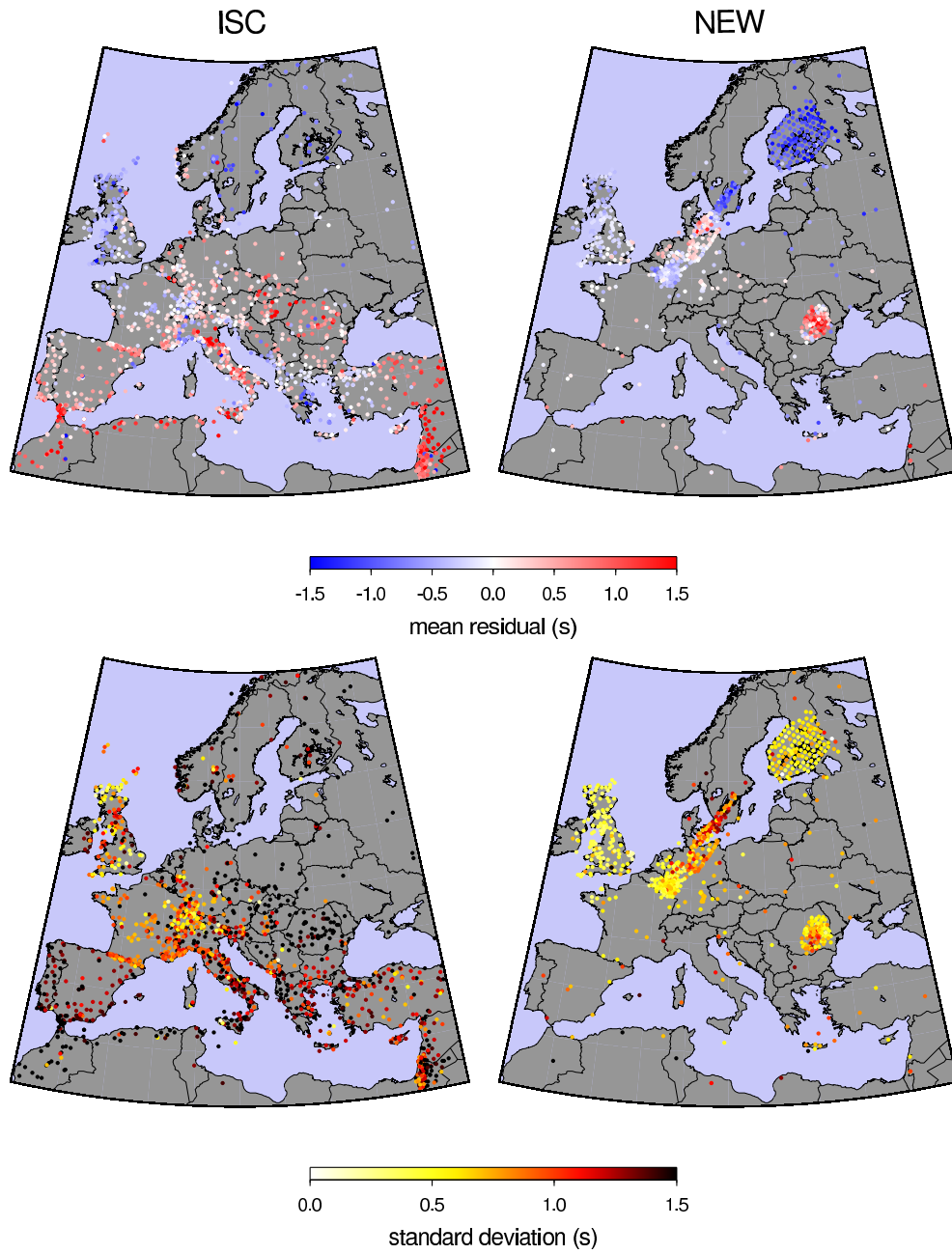
Figure 4.4: Mean teleseismic travel time residuals per station for the EHB data set (upper left) and the new data (upper right) and standard deviation per station for the EHB data set (lower left) and the new data (lower right). All residuals are computed with respect to the reference model ak135.
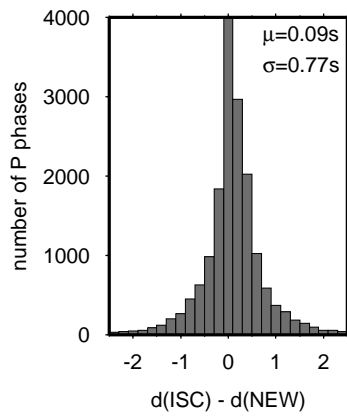
Figure 4.5: Histogram of the differences between residuals of the EHB data set and the newly picked arrival time data set for matching station-event-phase combinations.

48

Chapter 5

Travel Time Tomography With 3-D Reference Models

In global travel time tomography usually one-dimensional (1-D) reference models are used with respect to which the forward tomographic problem is linearized. This leads to delay times, ray path geometry, earthquake hypocenters and origin times which are computed for the 1-D reference model. The delay time is the basic datum for tomographic inversion in which it is back-projected along reference model ray paths into the 3-D seismic wave speed of the Earth's interior. As a result of insufficient data the tomographic inverse problem is underdetermined which leads to tomographic models biased towards the reference model.

In this study, the dependence of a tomographic model on the reference model is investigated for the particular case of global travel time tomography. For this purpose we perform tomographic analyses with three different reference models, one 1-D model and two 3-D models. The 1-D model (ak135) has been used in various global studies and serves both to provide the link to earlier studies and to provide a comparison to our experiments with 3-D reference models. The first 3-D reference model we use is constructed from recent mantle tomography models which are based on long period seismic data and independent inversion techniques. These models provide a long wavelength background of mantle structure. The second 3-D reference model is an adaptation of the first reference model where we included the detailed structure imaged with short period data in the well resolved parts of the mantle.

Prior to tomographic inversion, earthquakes are relocated in the 3-D reference model using a grid search technique and 3-D ray tracing. This also provides the linearization of the forward problem with respect to the 3-D reference model and results in a delay time data set which is consistent with the reference model.

We observe that in well resolved mantle volumes the imaged structure is independent of the reference model which supports the actual existence of imaged mantle anomalies and gives independent credit to the resolving power of the large set of short period travel time data used. In poorly resolved regions the different tomographic models prove to be reference model dependent. An important outcome of our experiments is a new tomographic model that combines in a consistent way the structure imaged with short period travel times with the

structure imaged with long period data (long period S wave data, surface waves and normal modes). This model is specifically useful, for example, for applications in forward modeling of seismic wave propagation, regional and global event location, mantle dynamics studies and analysis of the Earth's gravity field.

5.1 Introduction

Global travel time tomography is a well established and powerful tool to image the seismic velocity properties of the Earth's crust and mantle in detail. To retain computational feasibility and reduce mathematical complexity, simplifications are made in the process of creating a tomographic model. Regarding mathematical complexity, seismic tomography is a nonlinear inverse problem as a result of the dependence of ray geometry (or Fresnel zone in finite-frequency tomography) on the seismic wave speed and of seismic travel times on earthquake location. The forward problem is, however, always linearized with respect to properties of a reference model of seismic wave speed. In the ray approximation, Fermat's stationarity principle is invoked to replace the true ray path by the ray path in the reference model and changes of travel time as a result of event mislocation are approximated by a first order Taylor expansion of the travel time with respect to small changes in the source location (e.g. Spakman *et al.*, 1993). The quality of these approximations depends on the quality of the reference model in the sense of being already a close approximation of the seismic wave speed structure of the Earth. What close means in this respect has not been thoroughly investigated but experiments by van der Hilst and Spakman (1989) and Spakman *et al.* (1993) demonstrate that changing the reference model for mantle tomography significantly affects the tomographic model. This effect is also well known from local tomographic studies of the crust (e.g. Kissling *et al.*, 1994).

In global travel time tomography usually 1-D reference models are used in which wave speed only varies with depth. Different 1-D reference models exist (relating to different data types or subsets of global data) and several of these have been used as reference models in tomographic research as they already give a good approximation of the velocity distribution in the Earth. Nevertheless, lateral variations exist within the Earth being strongest in the crust and uppermost mantle. These 3-D heterogeneities obviously affect the travel times of waves and can also significantly modify the paths which rays take through the Earth (e.g. oceanic versus continental crust). Therefore, in many tomography studies corrections are applied to account for such 3-D structure. For example, in local teleseismic travel time tomography it has become standard procedure to correct travel times for crustal 3-D velocity structure beneath a seismometer array and afterwards fix crustal velocities in the inversion process (e.g. Sandoval *et al.*, 2003; Martin and Ritter, 2005). As another approach, heterogeneities in the crust can be included by forcing of the tomographic inverse model towards an assumed 3-D crustal model (Li *et al.*, 2006). This, however, neglects ray-bending effects.

By performing 3-D ray tracing, ray path geometry can be made consistent with 3-D structure obtained during inversion. This has been applied in various local and regional tomography studies (e.g. Papazachos and Nolet, 1997; Sandoval *et al.*, 2003) besides a few global nonlinear tomography studies (Bijwaard and Spakman, 2000; Widiyantoro *et al.*, 2000). So far, only Widiyantoro *et al.* (2000) have started directly from a 3-D reference model for their

tomographic inversions of 400,000 S-wave travel times.

In this study we will perform global tomographic experiments starting from different types of reference models (1-D and 3-D). Our aim is three-fold:

1. to investigate the dependence of global tomography models on the reference model used (1-D or 3-D reference models)

2. to create a tomographic model that combines the information contained in short period travel time data with that of long period seismic data

3. to relocate a large earthquake data set to account for the 3-D heterogeneities contained in the 3-D reference model

The scientific rationale underlying these three goals will be described in the following:

5.1.1   The dependence of global tomography on the reference model used

Even if a data set provides a perfectly resolved tomographic model, the linearizations and other theoretical simplifications made in the forward problem (e.g. adopting ray theory) may still produce spurious and biased results in the tomographic model. Data are back-projected along the wrong seismic ray paths (approximations of the real ray paths), and the seismic rays used generally start from the wrong source location. Effectively, these approximations cause inconsistency between the observations and forward model properties and translate implicitly into (correlated) data noise which may be mapped as spurious seismic wave speed anomalies or bias results both spatially and in imaged amplitudes (e.g. van der Hilst and Spakman, 1989; Spakman *et al.*, 1993). After a tomographic model has been obtained it can be used as a reference model for a subsequent forward modeling and inversion step in which 3-D ray tracing effectively provides linearization with respect to 3-D mantle structure imaged in the previous inversion step (Bijwaard and Spakman, 2000; Widiyantoro *et al.*, 2000). This may remove part of the bias but can only be expected to remove it completely if the ray set used provides near perfect spatial resolution. Yet, perfect resolution does not exist in global mantle tomography owing to the strongly non-uniform global distribution of earthquakes and seismological stations. As a result, (large) parts of the mantle are not well sampled leading to a poor resolution and a biased or spurious model. These parts of the model are mostly determined by the regularization used in the inverse problem. The regularization determines how properties of the reference model blend into the tomographic model. Rays that are traced through these parts of the model cannot converge to the real ray geometry and as a result the final tomographic model depends on the reference (starting) model. The only way to assess the dependence of the final model on the starting model is by experimenting with different starting models. In this study we present global tomography models based on 1-D and 3-D reference models, to assess the effects which different starting points may have on tomographic results.

5.1.2 Creating a tomographic model that combines the information contained in short period travel time data with that of long period seismic data

Depending on data type (short period travel time picks, long period travel times determined from waveform correlation, surface waves or normal modes), on tomographic technique (parameterization with spherical harmonic basis functions versus parameterization with local basis functions) and on regularization techniques (amplitude damping and/or derivative damping), distinctly different mantle models have been created although special regularization techniques can be used to improve similarity between models.

Models based on classical arrival time picks of short period P-waves and parameterized with local basis functions (e.g. conical cells) generally contain large, poorly resolved mantle volumes for which insufficient data exist to reliably image structure, for example, in the upper mantle below oceans, particularly in the southern hemisphere. When using the same data in conjunction with a parameterization with global basis functions (spherical harmonics) these data gaps are implicitly interpolated in the model space by virtue of the global nature of the basis functions. Boschi and Dziewonski (1999) offered reconciliation of both approaches by combining a cell parameterization with regularization based on first derivative damping. By its nature however, first derivative regularization interpolates (and extrapolates) in model space, particularly, in regions of few or no data constraints. These interpolated parts of the model remain, however, in the null space of the tomographic problem.

Tomography based on local parameterizations is particularly useful to exploit the resolving power of short period P-wave data in well sampled mantle regions (e.g. van der Hilst *et al.*, 1997; Bijwaard *et al.*, 1998) while tomography using global spherical harmonic basis functions is useful in conjunction with data with a relatively low sensitivity for the detail ($\lesssim$ 200 km) of mantle structure such as normal modes, surface waves, and carefully selected long period S-wave or P-wave data (e.g. Li and Romanowicz, 1996; Ekström and Dziewonski, 1998; Ritsema *et al.*, 1999). Unlike travel time tomography models, such models are based on a more uniform sampling of mantle structure albeit at large wavelength (e.g. laterally 500-1000 km or larger). Long period data are largely complementary in sensitivity for mantle structure compared to the sensitivity of short period data, and in part complementary in spatial sampling of the mantle. A combined inversion of short period travel time data with long period data would be beneficial to arrive at a more complete structural model of the mantle.

In this study, we choose for a hybrid approach to reach this goal by taking independent (in data and technique) tomographic models based on long period data as reference models for tomographic inversion of short period P-wave data. In this way, the partly complementary structural information contained in long period data is already contained in the background of our experiments, and will (hopefully) be more focused in regions where the short period travel time data may prove to have superior resolving power for structural detail.

5.1.3 Nonlinear earthquake location in 3-D models of mantle structure

Standard, earthquakes are located in 1-D reference models (e.g. ISC, NEIC procedures). The procedure developed by Engdahl *et al.* (1998) particularly advocates the use of modern 1-D

reference models and empirical station corrections to, at least partially, account for effects of near-station crust and mantle structure. As noted earlier, tomographic models based on travel times (derived from earthquake location in 1-D models) show that large parts of the mantle are insufficiently resolved owing to lack of data. Travel time models based on local parameterization and using local regularization suggest that the resolving power of the short period P-wave data for the very long wavelength content of mantle structure may not be strong. Models constructed from long period data (including surface waves and normal modes) do, however, indicate the presence of very long wavelength mantle structure. One possibility for explaining this difference between models is that during earthquake location (part of) the signal belonging to long wavelength heterogeneity is mapped into a hypocenter mislocation depending on the global or regional station network involved for each event. A way around this potential problem is relocation of earthquakes in long wavelength tomography models. In this way, our procedure of using 3-D reference models requires 3-D location of the earthquakes prior to tomographic inversion in the 3-D reference model, which will also account for effects on the location of the far-field long wavelength structure of the mantle.

In summary, we anticipate that 3-D ray tracing and nonlinear earthquake location in a realistic 3-D reference model prior to tomographic inversion provide a better starting point for inversion than a simple 1-D reference model could. Independent of this, our hybrid approach of using long wavelength tomography models of Earth structure, which are constructed from long period data, as 3-D starting models for short-period travel time tomography will blend the structural information implicitly contained in short period data with that obtained from inversions of long period data. This leads to a more complete model than either approach by itself can deliver at present.

5.2 Data

5.2.1 EHB catalog

The main data source for travel time tomography is a reprocessed and updated version of the International Seismological Centre (ISC) bulletins extended with travel times from the National Earthquake Information Center (NEIC) of the U.S. Geological Survey for the most recent events (Engdahl *et al.*, 1998). This database will be referred to hereafter as EHB catalog. The latest version of this database contains earthquake observations for the period 1964–2004 including over 445,000 events for 27.4 mill. first and later arriving phases. The processing of Engdahl *et al.* (1998) comprised a phase re-identification, theoretical travel time calculation in the reference model ak135 (Kennett *et al.*, 1995) and source relocation involving corrections for crust and mantle heterogeneity. From that catalog, 7.9 mill. regional P arrivals, 9.7 mill. teleseismic P, pP and pwP arrivals and 1.5 mill. PcP, PKPab, PKPbc, PKPdf and PKiKP phases were selected for the global P tomography of this study. The selection criteria for epicentral distance and travel time residual range are given in Table 5.1. The precision of the P phases was estimated following the method of Gudmundsson *et al.* (1990). This method uses ray bundles of teleseismic phases with decreasing width to extrapolate the standard deviation of ray bundles with zero width, which is presumed to be the upper limit of

errors in the data. For the phases selected from the EHB catalog for $25° - 100°$ distance this error is estimated to be 0.65 s.

5.2.2 Euro-Mediterranean bulletin

The Euro-Mediterranean bulletin of the Euro-Mediterranean Seismological Centre (EMSC) provides the second data set used in this study. Like the EHB catalog, this bulletin contains a collection of travel time observations but only from local networks in the Euro-Mediterranean region (Godey *et al.*, 2006). Well constrained earthquakes in this catalog were relocated by the EMSC. However, if existent, the corresponding EHB location is used here instead of the EMSC locations. Otherwise, the events are relocated in ak135 including empirical regional travel time corrections for consistency with the EHB catalog following the approach of Engdahl *et al.* (1998) and using the relocation method described in Section 5.3. From the resulting EMSC subset, 155,000 travel time residuals from 14,000 events were selected using the selection criteria given in Table 5.1. Following the method of Gudmundsson *et al.* (1990), here the upper limit of random data errors was estimated to be 0.68 s.

5.2.3 Newly picked data for stations in Europe

Additionally, temporary experiments in Europe (CALIXTO (Wenzel *et al.*, 1998), EIFEL (Ritter *et al.*, 2000), MIDSEA (van der Lee *et al.*, 2001), SVEKALAPKO (Bock and the SVEKALAPKO Seismic Tomography Working Group, 2001), TOR (Gregersen *et al.*, 2002)), the ORFEUS archives (Observatories and Research Facilities for European Seismology) and a data collection from Leeds University, UK (Arrowsmith, 2003) form another source of data for travel time tomography. The data from these stations were obtained as waveforms, pre-processed and picked with the automatic picking method of Sandoval *et al.* (2004a). This procedure resulted in a total of 83,500 P-wave travel times (see also Chapter 4). The picking errors were estimated within the picking algorithm to be approximately 0.15 s. The obtained travel times were later on combined with the Euro-Mediterranean bulletin and EHB catalog data using the same selection criteria as for the EHB catalog.

5.2.4 Newly picked data for stations in North America

Furthermore, in North America many of the data registered and stored by the Advanced National Seismic Network (ANSS), the Incorporated Research Institutions for Seismology (IRIS), the Canadian National Seismic Network (CNSN), the Southern California Earthquake Data Center (SCEDC) and the NARS-Baja project (Trampert *et al.*, 2003) are not reported to the ISC on a regular basis. Data from these sources were obtained for 2002–2004 and build the fourth subset used here. Originally, the data set was acquired and picked by Sandoval *et al.* (2004a) as part of an investigation of the lithosphere and mantle beneath North America. It was obtained using the same processing as for the European data set and contains 120,000 P-wave picks for 486 events. As for the newly picked data for stations in Europe, the picking error is expected to be on the order of 0.15 s since they were obtained with the same picking method. Again, the same selection criteria as for the EHB catalog were applied.

phase type	epicentral distance	residual range
P	$\leq 25°$	± 7.5 s
P	$> 25°$	± 3.5 s
pP, pwP (focal depth ≥ 35 km)	$25° - 100°$	± 3.5 s
PcP	$25° - 40°, 47° - 70°$	± 3.5 s
PKiKP, PKPdf	$110° - 140°$	± 3.5 s
PKPab, PKPbc, PKPdf	$\geq 150°$	± 3.5 s

Table 5.1: Selection criteria for the different phase types used for tomography.

5.3 Tomographic method

In seismic tomography, travel time residuals, i.e. the difference between observed arrival times and the corresponding reference model arrival times, are used to invert for 3-D velocity variations with respect to the reference model. In the high-frequency approximation, the Fresnel zone collapses into a seismic ray and seismic wave propagation theory reduces to seismic ray theory. In this approximation travel times are computed by integration of the slowness along the ray path resulting in the following delay time equation:

$$d = \underbrace{\int_L s \, dl}_{T_x(s)} - \underbrace{\int_{L_0} s_0 \, dl_0}_{T_{x_0}^0(s_0)} + \Delta t_x + \Delta t_s + \epsilon \tag{5.1}$$

where d represents the delay/travel time residual, the first and second integral describe the computation of the "true" and predicted travel times $T_x(s)$ and $T_{x_0}^0(s_0)$ respectively with L as ray path through the Earth starting at the true earthquake location x, L_0 as ray path in the reference model starting at the reference location x_0, dl and dl_0 are the ray segments, s is the Earth's slowness field and s_0 is the slowness field of the reference model. Δt_x contains the timing error due to source mislocation as a result of the slowness anomaly field $s - s_0$, Δt_s contains travel time effects due to station elevation and instrument response and ϵ describes the observational errors (e.g. picking errors or phase misidentification, remaining location errors). Equation 5.1 holds for any adopted reference model.

The first integral of equation 5.1 is linearized under the assumptions that the ray path in the reference model is sufficiently close to the actual ray path in the Earth ($L \approx L_0$) and that the reference earthquake locations are sufficiently close to the real locations. The effect of the spatial earthquake mislocation on the travel time is approximated by a Taylor expansion of the travel time around the reference source x_0. This leads to the forward equation of travel time tomography based on ray theory:

$$d = \int_{L_0} (s - s_0) \, dl_0 + (\mathbf{x} - \mathbf{x}_0) \cdot \nabla_0 T_{x_0}^0 + \Delta t_x + \Delta t_s + \epsilon \tag{5.2}$$

In a tomographic analysis, a large set of delay time equations 5.2 derived from many source-station combinations is discretized and inverted for estimates of the slowness anomaly field

$s - s_0$, event mislocations $\mathbf{x} - \mathbf{x}_0$, origin time errors Δt_x and the station statics term Δt_s. Following the approach of Bijwaard *et al.* (1998), composite rays are used instead of single rays for the EHB and EMSC data where a composite ray is built from single rays of the same phase type which are recorded at the same station and originate from the same event cluster (defined by volumes of $0.3° \times 0.3° \times dz$ with volume thickness dz increasing from 15 km at the surface to 40 km at 660 km depth). In this way, the number of data for inversion is reduced and at the same time the signal-to-noise ratio increased. The data are weighted prior to inversion by the spread of the individual delay times within the respective ray bundle to account for the difference in ray bundle size.

$$W_{rb}^{-1} = \sqrt{\frac{\sum_{i=1}^{N}(\overline{dt} - dt_i)^2}{N}} \qquad (5.3)$$

where W_{rb} represents the ray bundle weight, dt_i is the delay of ray i and $\overline{dt}$ is the average delay of the ray bundle. The weights were restricted to one order of magnitude.

For the newly picked data (Section 5.2.3 and 5.2.4), this approach is not used as their quality is expected to be higher. Instead, single rays with large weight are used. The resulting data vector contains 10.4 million residuals from originally 19.4 million single residuals.

The Earth is parameterized by an irregular grid of non-overlapping cells according to the method of Spakman and Bijwaard (2001) where the cell size depends on the number of rays crossing a cell. The horizontal cell size varies in crust and mantle between $0.5° \times 0.5°$ and $10.0° \times 10.0°$ with an increasing layer thickness from the crust (10 km) to the lower mantle (200 km). The inner and outer core are both parameterized by a single layer with cells of $10° \times 10°$ to allow for core structure but simultaneously prevent large model variations. The irregular grid is constructed from 8 035 000 cells of $0.5° \times 0.5°$ which are projected using a hitcount constraint onto 604 000 non-overlapping irregular cells. The irregular cell approach mostly reduces overparameterization thereby improving the conditioning of the inversion matrix while retaining the possibility to resolve structure at small scales ($0.5°$) where allowed by the data.

The tomographic inversion itself is performed iteratively with the LSQR algorithm of Paige and Saunders (1982). Simultaneously with the inversion for cell slowness anomalies, we invert for event cluster mislocations and station corrections. A second-derivative damping is applied to regularize the solution of the inversion and to obtain a smooth model. Additionally, for inversion with 3-D reference models an amplitude damping is applied to suppress large model excursions particularly in the crust and directly beneath it. The model parameters are scaled for inversion dependent on cell size and hitcount to emphasize small cells and weigh down cells with very high hitcounts in the lower mantle following the approach of Bijwaard *et al.* (1998):

$$\begin{pmatrix} \mathbf{C}_d^{-1/2}\mathbf{A} \\ \lambda\mathbf{C} \end{pmatrix} \mathbf{S}^{-\frac{1}{2}}\mathbf{m}' = \begin{pmatrix} \mathbf{C}_d^{-1/2}\mathbf{d} \\ 0 \end{pmatrix} \qquad (5.4)$$

where $\mathbf{A}$ contains the ray path segments, relocation and station coefficients, $\mathbf{C}_d$ represents the data covariance matrix, λ is a damping factor controlling the trade-off between data misfit and model norm/smoothness varying between 1000 and 7000, $\mathbf{C}$ is the matrix of damping

coefficients, $\mathbf{S}$ the scaling matrix with $(S_{jj}) = h_j V_j$ and h_j and V_j are hitcount and cell volume respectively, $\mathbf{m}' = \mathbf{S}^{\frac{1}{2}}\mathbf{m}$ is the scaled model vector $\mathbf{m}$ and $\mathbf{d}$ the data vector consisting of the travel time residuals.

5.3.1 Reference Models

1-D reference model

The radial model ak135 by Kennett *et al.* (1995), which has served as reference model in many other studies, is used as the 1-D reference model. The basic data set of travel time delays and earthquake locations is already consistent with this reference model. The tomographic model computed with respect to ak135 is hereafter called P06.

Long wavelength 3-D reference model

We constructed a 3-D reference model from two global tomography models determined from long period data. The CUB2.0 model (Ritzwoller *et al.*, 2002b) covers the crust and uppermost mantle and is combined with the model S20RTS (Ritsema *et al.*, 1999) in the deeper mantle. The CUB model is based on broadband surface wave group and phase velocity measurements and implicitly contains a global crustal model since it uses CRUST2.0 (Bassin *et al.*, 2000) in the background. The P velocities are taken as provided by this model. Between 200 and 300 km, the model S20RTS is smoothly blend in using a depth-weighted average of both models. S20RTS is based on Rayleigh wave phase velocity measurements, shear wave travel times and normal mode splitting measurements. Since S20RTS is a shear velocity model, it is converted to P velocities using the depth-dependent $d \ln v_s / d \ln v_p$ values of Bolton and Masters (2001) which range from 1.345 in the upper mantle to 3.45 in the lowermost mantle. In the Earth's core the 1-D reference model ak135 is used. The reference model is called CUB+S20RTS with which we compute two tomographic models: P06_CS obtained without a priori 3-D relocation of earthquakes, and P06_CSloc which is obtained starting from 3-D relocated events in the reference model CUB+S20RTS. Raypaths and travel time predictions in the reference models are obtained with 3-D raytracing (Bijwaard and Spakman, 1999a).

Hybrid 3-D reference model

It is well known that velocity anomaly amplitudes are systematically underestimated in travel time tomography as a result of reduced resolution, regularization, and incomplete convergence of the LSQR algorithm. Sensitivity tests with synthetic models demonstrate that in many regions recovered amplitudes are on the order of 50-70% of the synthetic amplitudes while the synthetic velocity patterns can still be well reconstructed. The amplitude loss cannot be recovered by inversion (it is in the null space) but amplitude enhancement can be made as part of the reference model. For this purpose (and for another reason discussed in section 5.5.3) a 3-D reference model is constructed that combines the better-resolved part of model P06 with reference model CUB+S20RTS. Prior to this combination the amplitudes of P06 are

first uniformly enhanced by a factor 2. Next, to correct for amplified amplitudes that would affect the data fit we only retain the part of the amplification that is located in the null space of the inverse problem. This part can be determined with the null space shuttle of Deal and Nolet (1996). The resulting model P06$^+$ is blended with reference model CUB+S20RTS leading to the new reference model CUB+S20RTS+P06$^+$. The reference model construction is implemented along the following lines: The tomographic inverse problem in which ak135 is used as reference model leads to the solution $\boldsymbol{x}_{P06}$ and is described by the following equation

$$\boldsymbol{A}\boldsymbol{x}_{P06} = \boldsymbol{d} \tag{5.5}$$

where $\boldsymbol{A}$ contains the ray path segments in each grid cell and $\boldsymbol{d}$ is the data vector. The difference between the amplified tomography model $\boldsymbol{x}_{amp}$ ($= 2\boldsymbol{x}_{P06}$) and the obtained model $\boldsymbol{x}_{P06}$ is

$$\Delta\boldsymbol{x} = \boldsymbol{x}_{amp} - \boldsymbol{x}_{P06} \tag{5.6}$$

The part of $\Delta\boldsymbol{x}$ which lies in the null space of $\boldsymbol{A}$ (i.e. $\Delta\boldsymbol{x}_{null}$) can be found by applying the null space shuttle of Deal and Nolet (1996): Let $\boldsymbol{h}$ be defined as

$$\boldsymbol{h} = \boldsymbol{A}\Delta\boldsymbol{x} \tag{5.7}$$

and $\Delta\boldsymbol{x}$ be the sum of the components lying in the range ($\Delta\boldsymbol{x}_{range}$) and in the null space ($\Delta\boldsymbol{x}_{null}$) of $\boldsymbol{A}$ such that

$$\Delta\boldsymbol{x} = \Delta\boldsymbol{x}_{range} + \Delta\boldsymbol{x}_{null} \tag{5.8}$$

Then inversion of

$$\boldsymbol{A}\Delta\boldsymbol{x} = \boldsymbol{A}(\Delta\boldsymbol{x}_{range} + \Delta\boldsymbol{x}_{null}) = \boldsymbol{h} \tag{5.9}$$

will give an estimate of $\Delta\boldsymbol{x}_{range}$ as $\boldsymbol{A}\Delta\boldsymbol{x}_{null} = \boldsymbol{0}$ by definition, so that the final amplified model (using eq. 5.8 to obtain $\Delta\boldsymbol{x_{null}}$)

$$\boldsymbol{x}_{P06^+} = \boldsymbol{x}_{P06} + \Delta\boldsymbol{x}_{null} \tag{5.10}$$

does not affect the data misfit since

$$\boldsymbol{A}\boldsymbol{x}_{P06^+} = \boldsymbol{A}\boldsymbol{x}_{P06} + \underbrace{\boldsymbol{A}\Delta\boldsymbol{x}_{null}}_{=0} = \boldsymbol{d} \tag{5.11}$$

The final, amplified model P06$^+$ is then combined with CUB+S20RTS applying a hitcount-dependent criterion where the hitcount is the number of rays crossing a cell. For cells with a hitcount greater than 500/1000/2000 in the upper/mid/lower mantle P06$^+$ is used. A gradual transition from P06$^+$ to CUB+S20RTS is achieved by using a hitcount-weighted average of both models in an intermediate hitcount range. For cells with a hitcount lower than 100/200/400 in the upper/mid/lower mantle CUB+S20RTS is used. Also, to ensure a smooth transition between P06 and CUB+S20RTS, the combined model is smoothed taking into account the adjacent cells in latitude and longitude direction. In the Earth's core the 1-D

reference model ak135 is used. With respect to reference model CUB+S20RTS+P06$^+$ we compute two tomographic models: P06_3D obtained without a priori 3-D relocation of earthquakes, and P06_3Dloc which is obtained starting from 3-D relocated events in the reference model CUB+S20RTS+P06$^+$. Again, raypaths and travel time predictions in the reference model are computed with 3-D raytracing.

5.3.2 Relocation

In the only other global tomography study using 3-D reference models of Widiyantoro *et al.* (2000), relocation of earthquakes in the actual reference model is neglected. Yet, to establish complete consistency between source parameters, travel times and the reference model, it is necessary to relocate the events in the 3-D reference models. The relocation procedure is based on the grid search method of Sambridge and Kennett (1986). Using the ak135 (EHB) location as starting point, the grid search is performed around this location. Initially, a grid of 2 km node spacing is used which is subsequently refined to 1 km node spacing. The grid nodes are supplied with theoretical travel times of the 3-D reference model using the ray tracing method of Bijwaard and Spakman (1999a).

From an analysis of the distributions of epicenter, depth and origin time shifts with respect to the original EHB locations, we discarded the 2% of relocations with the largest shifts in the tails of the respective distributions to avoid erroneous relocations. The rejected relocations consist mainly of events which are only regionally constrained or where only few arrival times could be used. Thus, for relocation in CUB+S20RTS 426,000 out of 450,000 earthquake relocations were accepted, for the rest we kept the original EHB location. For relocation with CUB+S20RTS+P06$^+$ 434,000 relocations were accepted. The differing numbers of accepted relocations and generally smaller relocation vectors for CUB+S20RTS+P06$^+$ indicate that CUB+S20RTS+P06$^+$ explains travel times better than CUB+S20RTS.

In summary, five tomographic models will be determined:

- P06 with respect to the 1-D reference model ak135

- P06_CS with respect to CUB+S20RTS but without 3-D relocation of events prior to inversion, i.e. 3-D ray tracing starts from ak135-locations

- P06_CSloc with respect to CUB+S20RTS with 3-D relocation in this reference model prior to inversion

- P06_3D with respect to CUB+S20RTS+P06$^+$ but without 3-D relocation of the events

- P06_3Dloc with respect to CUB+S20RTS+P06$^+$ and with 3-D relocation of the events prior to inversion

5.4 Model Resolution and Variance Estimates

Before analyzing and comparing the resulting tomography models, the spatial and amplitude errors of these models are estimated. As stations and events are not equally distributed over
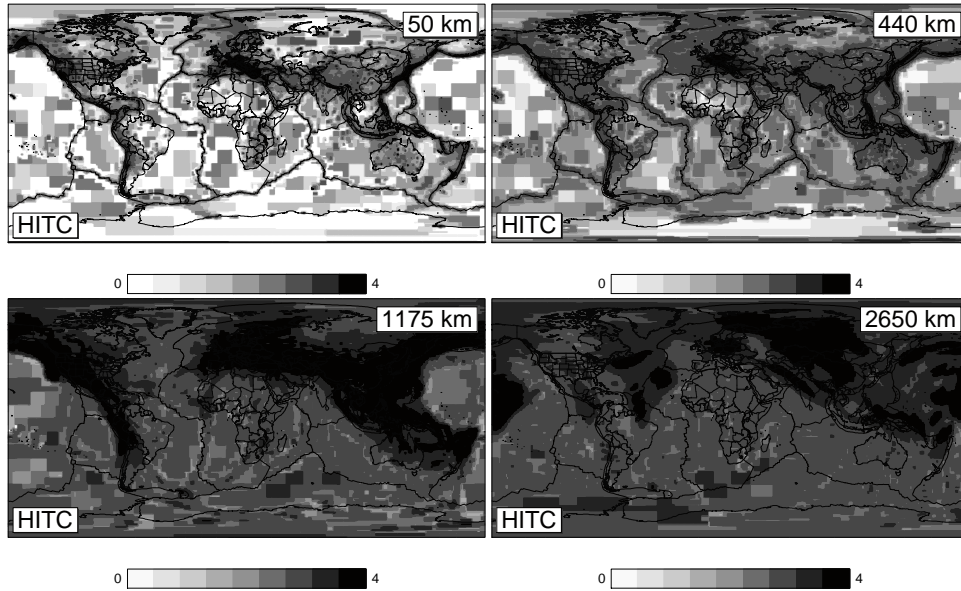
Figure 5.1: Logarithmic hitcount (i.e. number of rays crossing a cell) at 50 km, 440 km, 1175 km and 2650 km depths.

the Earth, the resolution of the velocity models varies spatially. The former fact is clearly indicated in the hitcount maps (Fig. 5.1). For example, ray coverage in the uppermost mantle is low beneath the oceans and cratons due to a low number of earthquakes and seismic stations.

The computation of the formal resolution matrix is practically excluded due to the large number of parameters, therefore tests are performed with synthetic models (Spakman and Nolet, 1988) to find the minimum size of anomalies that can be reconstructed and to detect lack of resolution. The synthetic models for these tests contain well separated spikes of $\pm 5\%$ amplitude with respect to the reference model with a distance of at least once the spike size in all directions between them and being shifted laterally with depth. The spike models are generated on an equal surface area grid and subsequently projected onto the irregular grid. Theoretical travel times are then calculated and Gaussian distributed noise with a standard deviation of ± 0.5 s is added to the data. The spike amplitudes of $\pm 5\%$ are large compared to the overall seismic P-anomaly values typically imaged (few percent in the upper mantle, less than 1% in the lower mantle). We have adopted these synthetic amplitudes because they lead to a signal-to-noise ratio of the synthetic delays, which is comparable to that of the real data when Gaussian noise is added to the synthetic delays with a standard deviation of 0.5 s (comparable to data noise). We aim at a similar signal-to-noise-ratio because we want to mimic the inversion of real data as closely as possible. The reason why much larger synthetic amplitudes are needed to obtain a similar signal-to-noise ratio lies in the different structural character of real Earth structure and of the synthetic models used. Synthetic delays are acquired along rays that sample the alternating pattern of spike amplitudes where positive and negative contributions to the synthetic delay cancel for a large part along most ray paths. In
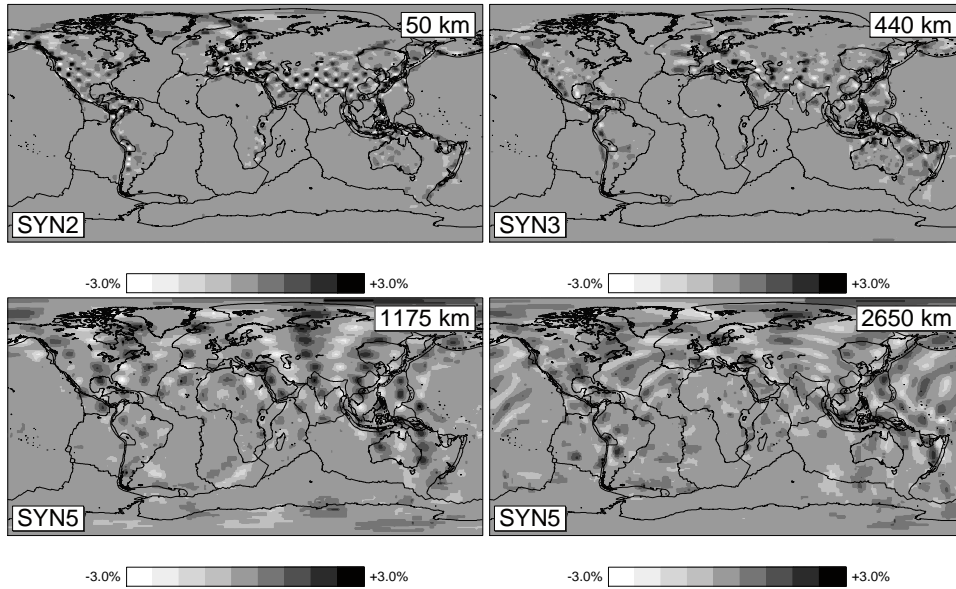
Figure 5.2: Spike tests for a cell size of 2°× 2° at 50 km depth, 3°× 3° at 440 km depth, 5°× 5° at 1175 km depth and 5°× 5° at 2650 km depth. The grayscales give the amplitude of the velocity anomalies.

this sense, the alternating spike model is typically a model that lies close to, and in practice usually partly in, the null space.

Earlier work (Bijwaard and Spakman, 2000) and our own experiments have shown that sensitivity test results, when using ray paths in a 1-D model or when using ray paths in 3-D models, only differ in small local detail which cannot be easily quantified as being a significant local improvement or degradation of spatial resolution. We are mainly interested in the more global effects of using different starting models for travel time tomography and have observed that the tomography models are not differently resolved on larger spatial scales, irrespective of the reference model used. For this reason we have concentrated on conducting sensitivity tests with the ray path set as computed in the 1-D ak135 reference model. The fact that spatial resolution on larger spatial scales is highly comparable between models renders resolution as less discriminative for comparison of results on global scales.

In Figure 5.2, 5.3 and the appendix of this thesis (Fig. A.1 to A.10), examples of such spike tests are shown at various depths with spikes of different sizes increasing with depth as the spatial resolution decreases with depth. While in the best resolved regions of the uppermost mantle anomalies of 0.5°×0.5° horizontally can be reconstructed, in the lowermost mantle only anomalies of 3.0°×3.0° to 4.0°×4.0° and bigger can be imaged (Figure 5.3). Furthermore, resolution is generally poor below oceans, in particular, in the southern hemisphere and in the lowermost mantle stronger lateral smearing is observed than at shallower depth.
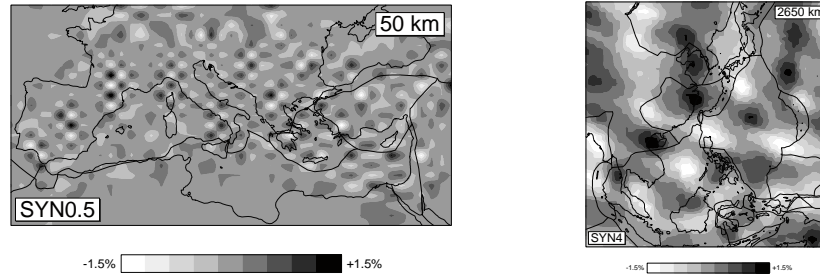
Figure 5.3: Blow-ups of spike tests for a cell size of $0.5° \times 0.5°$ beneath Europe at 50 km depth and $4° \times 4°$ beneath southeast Asia at 2650 km depth. The grayscales give the amplitude of the velocity anomalies.

To estimate the uncertainty of the velocity model caused by errors in the observed travel times, various methods can be applied, for example, using Gaussian distributed noise as data vector while keeping the original matrix for inversion (not performed here). As another test, the data vector can be permuted randomly before performing the inversion keeping again the same inversion matrix as for the original data vector (Spakman, 1991). This test also serves to investigate the correlation between data and ray paths where one would expect that the resulting model shows random anomalies of low amplitude if there are no correlations between delay times and ray paths. An example of such a test is given in Figure 5.4. In general, a random model with low amplitudes ($\approx 0.2 - 0.3\%$) is found in regions of good ray coverage. Only poorly sampled regions, as for example the Northern Atlantic at 50 km depth, display systematic anomalies of higher amplitude ($\approx 1\%$).

Data variance reduction obtained from the inversions ranges between 44.7% and 75.0% depending on how well the respective reference model already predicts the travel times (see Table 5.2). However, the inversions result in standard deviations of the weighted composite residuals between 1.44 to 1.58 for all models. The largest standard deviations are found for CUB+S20RTS as starting model while they are comparable for ak135 and CUB+S20RTS+P06$^+$ as starting models (taking into account that during 3-D ray tracing in the 3-D reference models noise on the order of 0.1 s is added to the residuals (Bijwaard and Spakman, 1999a)).

As a further analysis of model properties, the mean anomaly and the respective root-mean-square (RMS) values are computed for each layer and cells with a hitcount greater than 1000 (Fig. 5.5). The biggest model amplitudes are found in the crust and upper mantle. In particular, the models which implicitly contain CRUST2.0 display large average velocity perturbations in the crust with respect to ak135. On average, positive values are observed in the upper mantle in CUB+S20RTS and the according inversion models P06_CS and P06_CSloc as those models are dominated by high-velocity anomalies in regions sampled by short period P waves in the upper mantle while they are negative in the other models below 200 km depth. The mean values reduce to less than $\pm 0.2\%$ in the mid and lower mantle. For comparison, the mean velocity perturbations of the permuted data vector test are displayed which are close
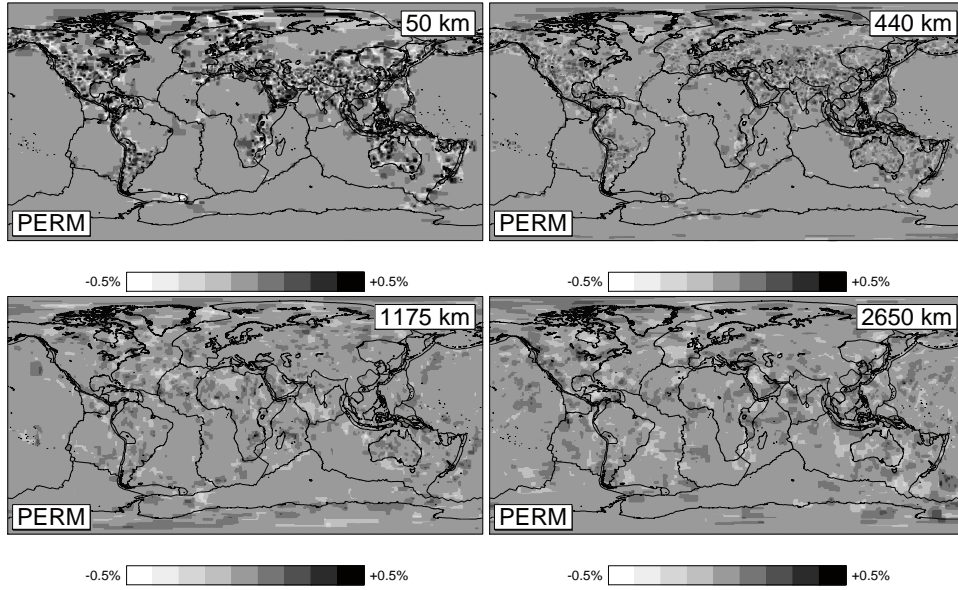
62

Figure 5.4: Sensitivity test with a randomly permuted data vector at 50 km, 440 km, 1175 km and 2650 km depth.

	variance reduction from inversion	mean residual $\pm\sigma$ relative to the start. model before inversion	mean residual $\pm\sigma$ relative to the start. model after inversion
P06	52.1%	0.07 ± 2.08	0.01 ± 1.44
P06_CSx	75.0%	1.30 ± 3.04	0.00 ± 1.52
P06_CSlocx	61.6%	0.11 ± 2.55	0.00 ± 1.58
P06_3Dx	62.0%	-0.66 ± 2.40	0.00 ± 1.48
P06_3Dlocx	44.7%	-0.14 ± 1.99	0.00 ± 1.48

Table 5.2: Data variance reduction from inversion of all models and the mean $\pm$ standard deviation of the weighted composite residuals with respect to the starting model before and after inversion.

to 0% throughout the mantle.

High RMS values are found in the models with a 3-D reference model, in particular, for the inversion models P06_3D and P06_3Dloc. RMS values below the Moho reduce from ≈2.5% to 0.5%-0.7% at the 660 km discontinuity. In the mid and lower mantle, they are smaller with 0.1%-0.3% increasing again in the lowermost mantle. The model of the permuted data vector test contains RMS values of $\approx 0.25\%$ at the top, reducing to $\approx 0.2\%$ in the upper mantle and to $< 0.1\%$ in the lower mantle. This RMS profile resulting from the permuted data test provides an upper bound for the amplitude errors since the data are treated as errors in this test while true data errors are smaller.

5.5 Results

We focus on the tomographic models P06, P06_CSloc, and P06_3Dloc which are all obtained from inverting data sets (delays, ray paths, and hypocenters) that are consistent with the reference models used (ak135, CUB+S20RTS, and CUB+S20RTS+P06$^+$, respectively). For display and interpretation purposes all models are displayed with respect to reference model ak135. Using a different reference model for display than the starting model for inversion proves useful for interpretation of crust and mantle structures (e.g. Kissling and Spakman, 1996). Two other models are shown, P06_CSlocx and P06_3Dlocx, which constitute the actual inversion results with respect to the reference models CUB+S20RTS and CUB+S20RTS+P06$^+$, respectively, and show explicitly how and where the reference model is changed.

5.5.1 Tomography with respect to a 1-D reference model – P06

The first model (P06) will serve as a standard to which all other models will be compared to illustrate the effect of using a 3-D reference model. As the aim of this study is to investigate the dependence of global tomography on the reference model (e.g. relocation in the reference model, type of model used) we will present the main anomalies found in the tomography models only briefly. The information contained in the travel time residuals is easiest observed in the model P06 obtained with ak135 as reference model. In Figures 5.7 and 5.13, it is displayed in the top row at 50 km, 185 km, 440 km, 1175 km, 1900 km and 2650 km depth.

Interpretations can be given according to studies by Grand *et al.* (1997), Bijwaard *et al.* (1998), Bijwaard and Spakman (1999b), Goes *et al.* (1999), Rangin *et al.* (1999), van der Voo *et al.* (1999) and Montelli *et al.* (2006). In the upper mantle high-velocity anomalies are related to subducted slabs as, for example, along the Tonga-Kermadec trench (see also Fig. 5.8) or beneath southeast Asia (see also Fig. 5.9). Continental shields and cratons in the upper mantle are also imaged by high-velocity anomalies (e.g. the Canadian Shield or East European platform in Fig. 5.7 at 50 km, 185 km), while low-velocity anomalies are associated with tectonically active regions such as mountain ranges (e.g. Alps, North American Cordillera), back-arc basins (e.g. Western Mediterranean basin) or rifting/spreading centers (Mid-Atlantic ridge, Red Sea). Furthermore, low-velocity anomalies can be related to higher
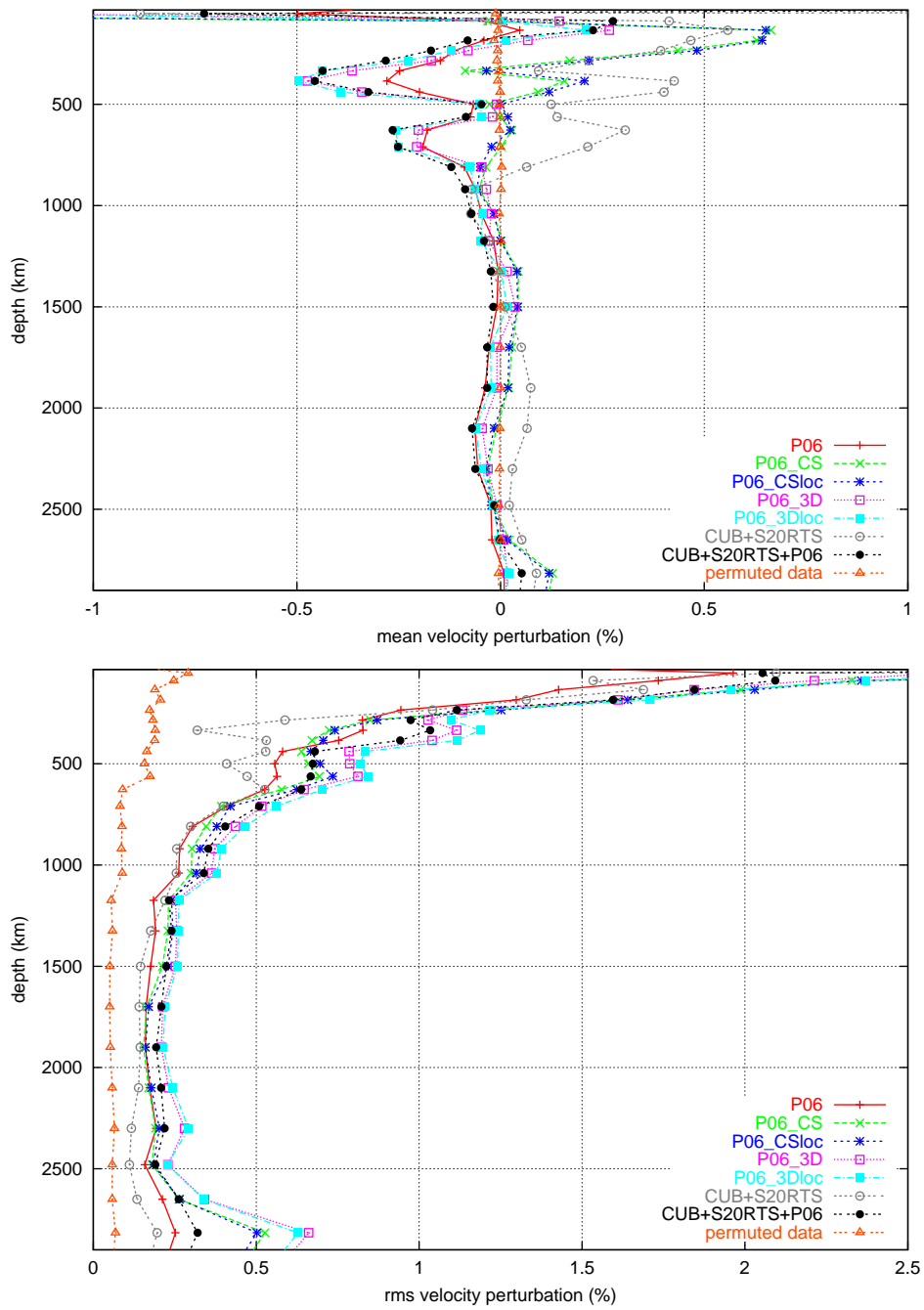
Figure 5.5: Depth-dependent laterally averaged velocity perturbation (top) and root-mean-square values (bottom) with respect to ak135 of the different models for regions sampled by more than 1000 rays.
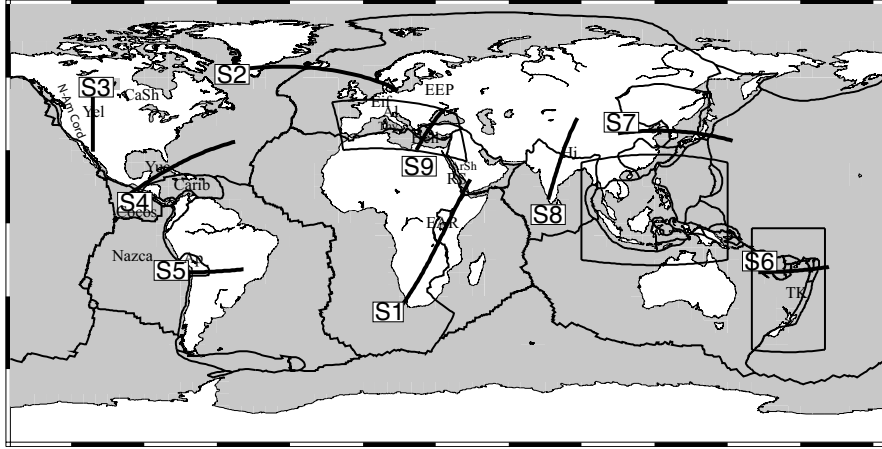
Figure 5.6: Location of the regions mentioned in the text, blow-ups (Figs. 5.8 to 5.10 and vertical cross-sections (Fig. 5.14). Abbreviations: Al - Alps, Ap - Altiplano, ArSh - Arabian Shield, CaSh - Canadian Shield, Carib - Caribbean plate, EAR - East African rift, EEP - East European platform, Eif - Eifel, Hi - Himalaya, N-Am Cord. - North American Cordillera, RS - Red Sea, Thy - Tyrrhenian Basin, TK - Tonga-Kermadec trench, Yel - Yellowstone, Yuc - Yucatan Basin. Plate boundaries after Bird (2003).

than average mantle temperatures in regions of presumed hot upwellings or plumes (e.g. Iceland, Eifel).

In the lower mantle, high-velocity anomalies represent remnants of subducted slabs as, for instance, at 1175 km depth the north-south oriented anomaly beneath the Americas related to the subduction of the Farallon plate or the west-east directed anomaly across Eurasia due to the subduction of the Tethys ocean. Low-velocity anomalies in the lower mantle, which are also observed at shallower depth, image plumes and hot upwellings as, for example, the low-velocity anomaly beneath the East African rift system or in Central Europe.

Besides that, undersampled regions can easily be detected in this model as they obtain $\pm 0\%$ velocity perturbations in the inversion.

5.5.2 Tomography with respect to the 3-D reference model CUB+S20RTS – model P06_CSloc

Figure 5.7 displays results for selected depths (figure columns) of models P06 (first row), P06_CSloc (second row), the actual inversion result P06_CSlocx (third row), and the reference model CUB+S20RTS (last row). The model P06_CSloc is the tomographic model obtained with CUB+S20RTS as starting model displayed with respect to ak135 and P06_CSlocx is the same model but displayed with respect to CUB+S20RTS.

In the crustal layers (not shown) only little information can be gained from the data except for a few regions in Europe, Japan or northwestern America where many stations and events exist. Therefore, in the crust the results are dominated by the reference model (CUB2.0 which

incorporates the crustal model CRUST2.0). Through event relocation and 3-D ray tracing in the reference model prior to inversion, ray path geometry and predicted travel times are still affected by the crustal heterogeneity (Bijwaard and Spakman, 1999a), which changes e.g. crustal entry/exit angles of rays and which has a global effect on ray geometry (i.e. with respect to rays in ak135).

At 50 km (Fig. 5.7) the resolving power of the travel time data set becomes apparent. At this depth, model resolution is mostly provided by uppermost mantle grazing Pn waves. P06_CSlocx (third row) shows explicitly where the reference model is changed. At 50 km, this solution mostly adds negative anomalies to the reference model, lowering the generally positive reference amplitudes found in many oceanic regions. Conversely, in the continental areas the solution tends to add small-amplitude positive anomalies to the reference model. Comparison to the P06 model explains that all these changes only occur where the travel time data indeed sample the uppermost mantle. Most of the oceanic areas and cores of continental regions retain reference model velocities for lack of ray sampling. Still, the inversion offers a good means to integrate seismic velocity information based on surface wave inversion (the reference model) with that obtained from travel time inversions.

A first glance at a depth of 185 km suggests great similarity between the reference model and P06_CSloc. On the global scale the changes are subtle but important as evidenced by the solution P06_CSlocx (third row) that, in many regions, shows narrow high-velocity variations and effectively adds the image of subducted slab to the reference model. This is even more convincing in cross-sectional view or mapview blow-ups (e.g. Figs 5.8, 5.9, 5.10, 5.14, discussed later). Apart from subduction zones, more complex variations in wave speed are required by the data in the European-Mediterranean region, the Tethys belt, southeast Asia and for instance under North America. For these regions and subduction zones the reference model is completely changed, attesting to the resolving power of the travel time data, and the model P06_CSloc resembles closely model P06.

Deeper in the mantle, where S20RTS provides the reference model, the amplitudes of the solution P06_CSlocx are more of the order of reference model wave speeds and the mantle volume sampled by seismic rays becomes much larger. Models P06 and P06_CSloc are quite similar in regions of good resolution. Differences between the two models occur mostly below oceanic areas where ray sampling is low and the data therefore have reduced resolving power to change the reference model. The depth-layer at 1175 km provides an illustration of these effects. Here, the 3-D reference model provides, although on a larger wavelength scale (smoother), a similar representation of the positive anomalies associated with subduction of the Tethys and Farallon oceans under Eurasia and the Americas, respectively. The solution P06_CSlocx looks rather random in structure but in fact focuses the reference model in these mantle subduction regions strongly towards P06 giving credit to the resolving power of the data set at this depth. Also below Africa, South America, and the north Atlantic, the reference model is strongly changed, focusing the "African super plume" (Ritsema *et al.*, 1999) in the former region, and focusing the "Iceland plume" (Bijwaard and Spakman, 1999b) in the latter.

Around all these regions a transition occurs toward reference model anomalies which are only exclusively found beneath the NE Pacific and SW Atlantic. Similar observations can be made for the layer at 1900 km where again the reference model is being focused toward

P06 and which demonstrates that the tomographic models P06 and P06_CSloc are relatively independent of the reference models in most regions.

Occasionally the inversion with respect to the 3-D reference model produces totally new anomalies that are neither found (or suggested) in P06 nor in the 3-D reference model. An example is the positive anomaly north of the Fiji region in the SW Pacific at a depth of 2650 km. This anomaly occurs in a region of moderate resolution. Other examples of strong focusing of barely visible, low-amplitude structures in P06 or in the reference model, are the positive anomalies in the Tonga region, in the Indian ocean, the SE Pacific, South America and the SW Atlantic region. Redistribution of teleseismic ray geometry in the 3-D model with respect to ak135 is largest in the deepest mantle and may lead to visibility and focusing of hitherto undiscovered structure.

5.5.3 Inversion with respect to the alternative 3-D reference model CUB-+S20RTS+P06$^+$ – model P06_3Dloc

As the results have shown so far, in regions of good resolution (according to the sensitivity tests) the tomographic models are very similar independent of the reference model used. In regions of very low resolution the models mostly reflect the reference model. There is an intermediate range where the solution is reference model dependent due to the spatially variable but limited resolving power of the data. In these regions P06_CSloc is a mix between the 3-D reference model and model P06 and there is no obvious reason why one would prefer one specific solution. With the construction of reference model CUB+S20RTS+P06$^+$ we have chosen to replace the intermediate and well-resolved regions with P06$^+$, an amplitude-enhanced version of P06. With this choice we accept to bias the solution in these mantle volumes toward a solution based on ak135. By construction, P06$^+$ contains larger anomaly amplitudes than P06 due to model amplification in the null space but its features are generally similar in regions of good resolution. As P06$^+$ replaces CUB+S20RTS in regions sampled by most rays, we can also account better, through 3-D ray tracing, for the non-linearity of the inverse problem resulting from small-scale high-amplitude velocity heterogeneity (e.g. slabs). In Figures 5.11 and 5.12, two mapview sections are displayed showing the effect of anomaly amplification at 440 km depth under northwestern America and at 1900 km depth beneath southeast Asia. The part of the model amplification that lies in the null space is generally less than half the amplitude of P06.

Figure 5.13 displays the inversion results of model P06_3Dloc (in the same format as Figure 5.7). At first instance one might expect that the solution P06_3Dlocx would only give rise to moderate changes of the reference model because CUB+S20RTS+P06$^+$ already combines the best from inversion model P06 with reference model CUB+S20RTS. Furthermore, amplitude amplifications in P06$^+$ are retained to the null space, hence data insensitive. Instead, although less pronounced than in solution P06_CSlocx (Fig 5.7), we observe changes with substantial amplitude and spatial variation. The reason must be found in the fact that the null space shuttle experiment leading to P06$^+$ was performed with ak135 as a reference and that in less well-sampled regions CUB+S20RTS is employed. After construction of the reference model CUB+S20RTS+P06$^+$, all events have been relocated prior to inversion using 3-D ray
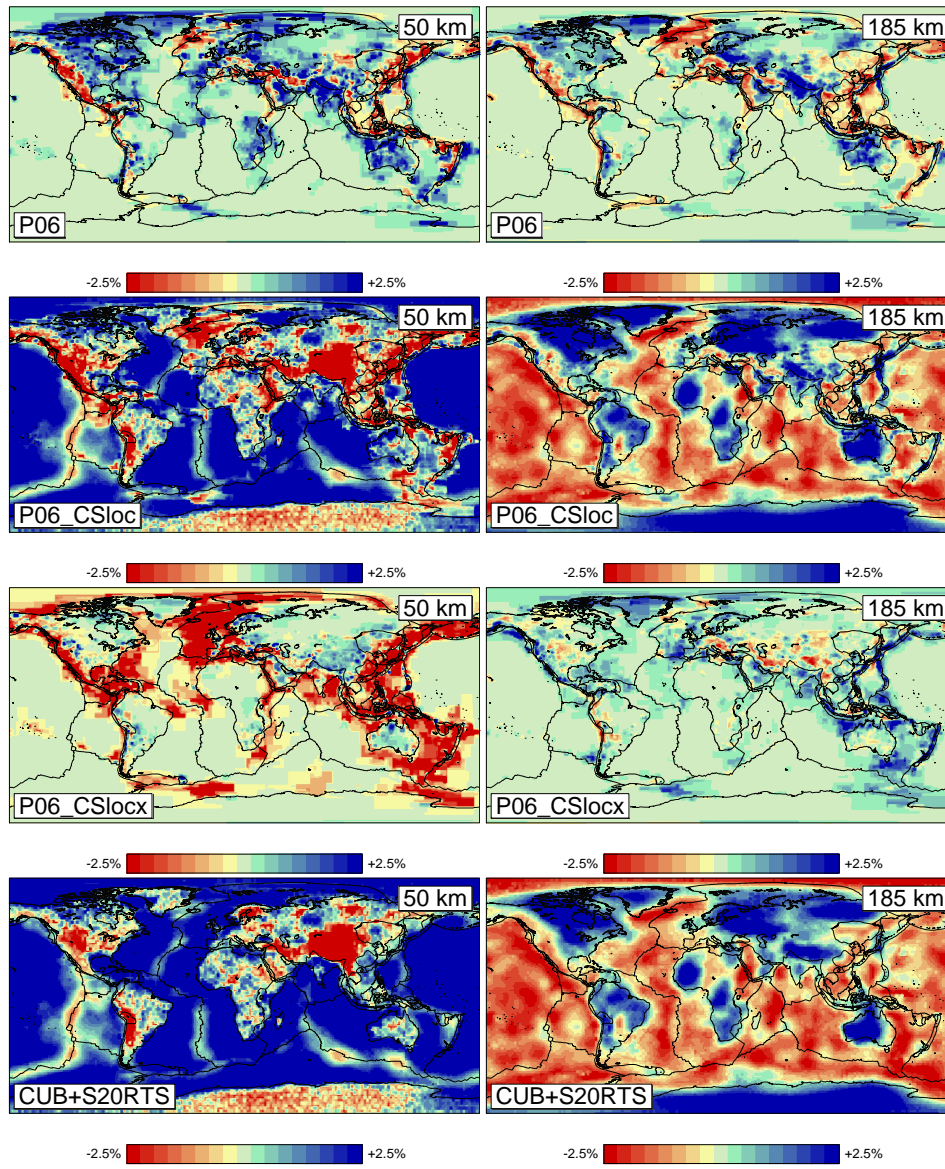
Figure 5.7: Tomography model P06 using ak135 as starting model (top), P06_CSloc using CUB+S20RTS as starting model displayed with respect to ak135 (second from top), P06_CSlocx using CUB+S20RTS as starting model displayed with respect to CUB+S20RTS (third from top) and the model CUB+S20RTS itself (bottom) displayed as velocity perturbations with respect to ak135. Shown are horizontal slices through the models at 50 km (left) and 185 km depth (right).
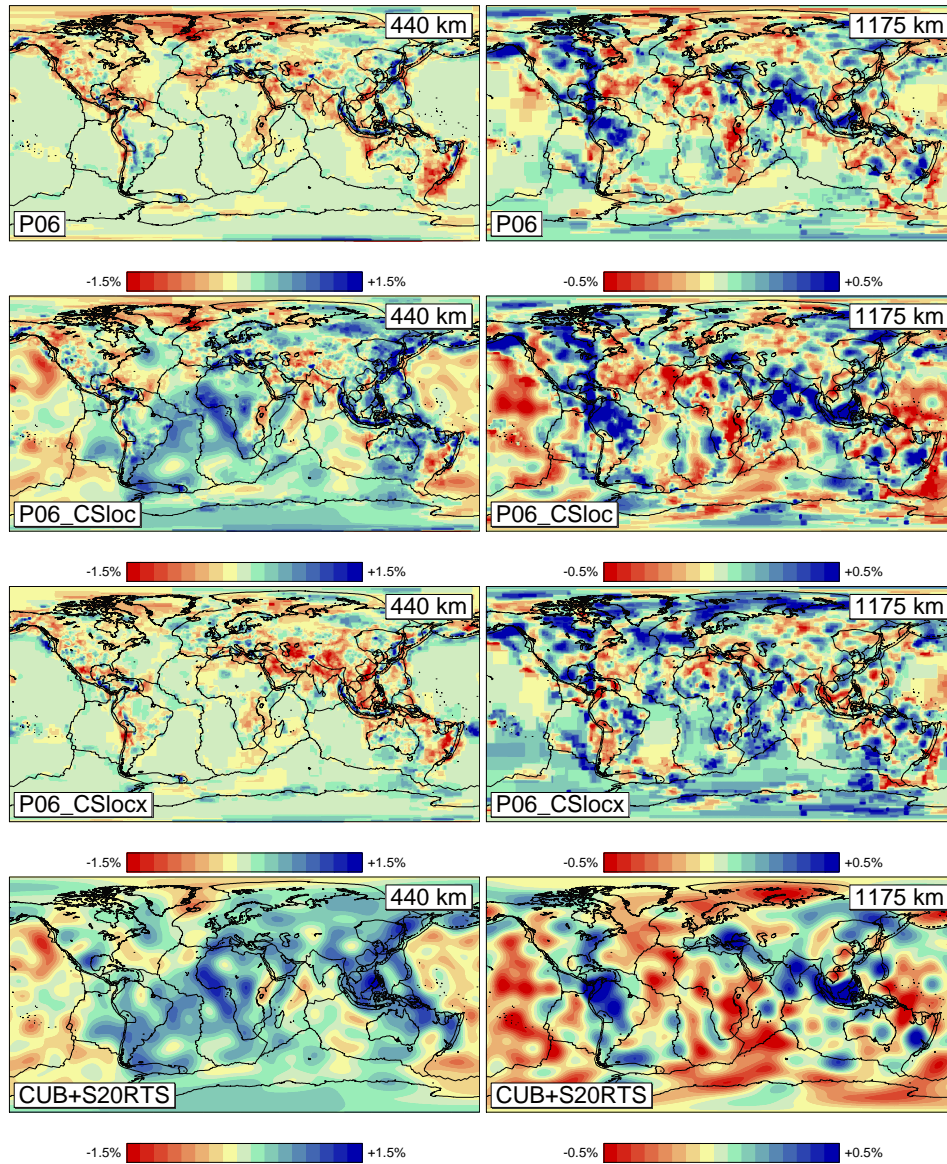
Figure 5.7: (Continued). Horizontal slices through the models at 440 km (left) and 1175 km depth (right).
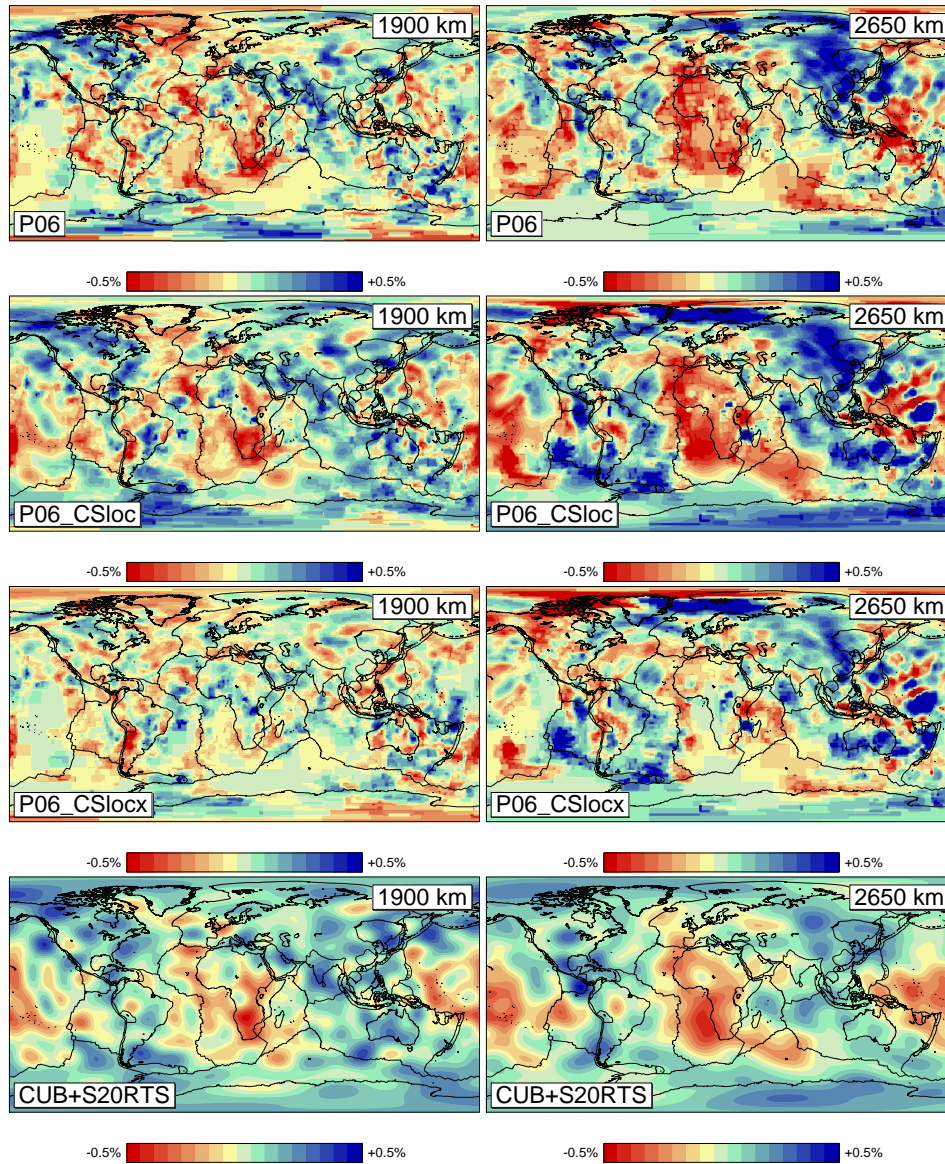
Figure 5.7: (Continued). Horizontal slices through the models at 1900 km (left) and 2650 km depths (right).
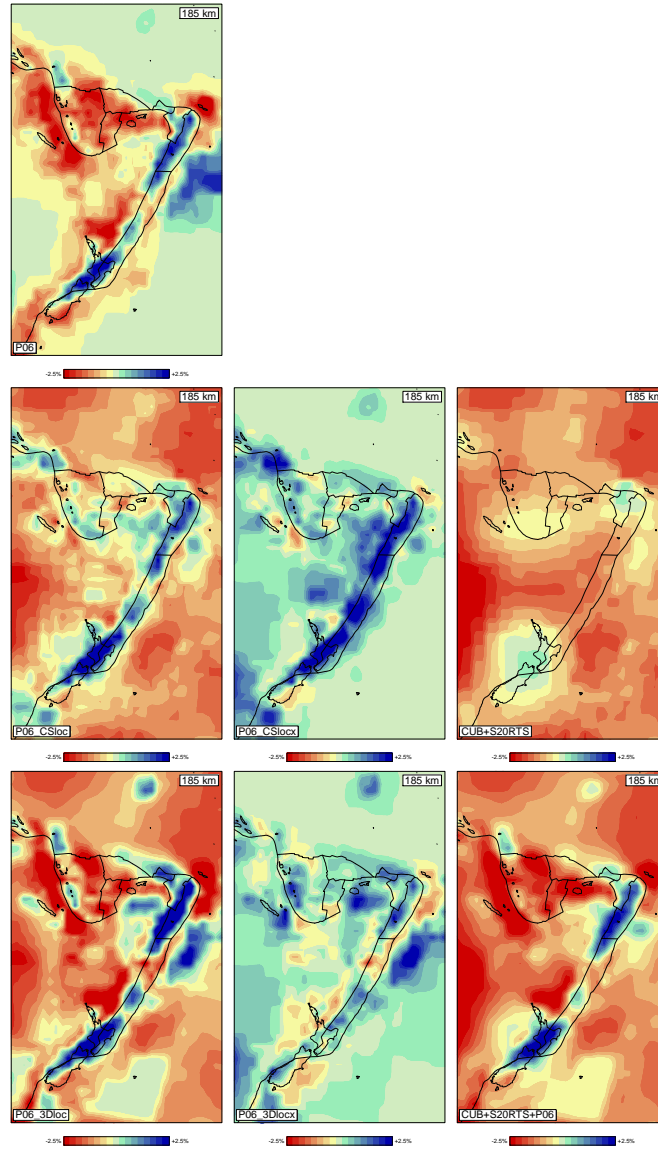
Figure 5.8: Model section at 185 km depth beneath the Tonga-Kermadec region. Tomography model P06 using ak135 as starting model (top), P06_CSloc using CUB+S20RTS as starting model displayed with respect to ak135 (middle row, left column), P06_CSlocx using CUB+S20RTS as starting model displayed with respect to CUB+S20RTS (middle column and row) and the model CUB+S20RTS itself (middle row, right column) displayed as velocity perturbation with respect to ak135. P06_3Dloc using CUB+S20RTS+P06$^+$ as starting model displayed with respect to ak135 (bottom row, left column), P06_3Dlocx using CUB+S20RTS+P06$^+$ as starting model displayed with respect to CUB+S20RTS+P06$^+$ (bottom row, middle column) and the model CUB+S20RTS+P06$^+$ itself (bottom row, right column) displayed as velocity perturbation with respect to ak135.
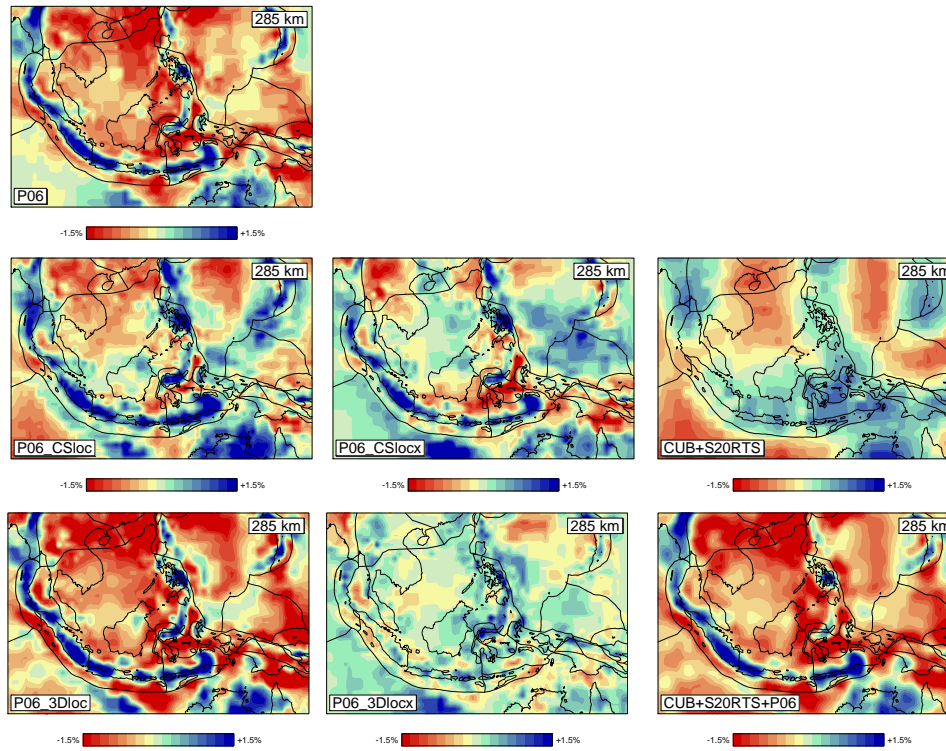
Figure 5.9: Model section at 285 km depth beneath southeast Asia. Models as in Figure 5.8.
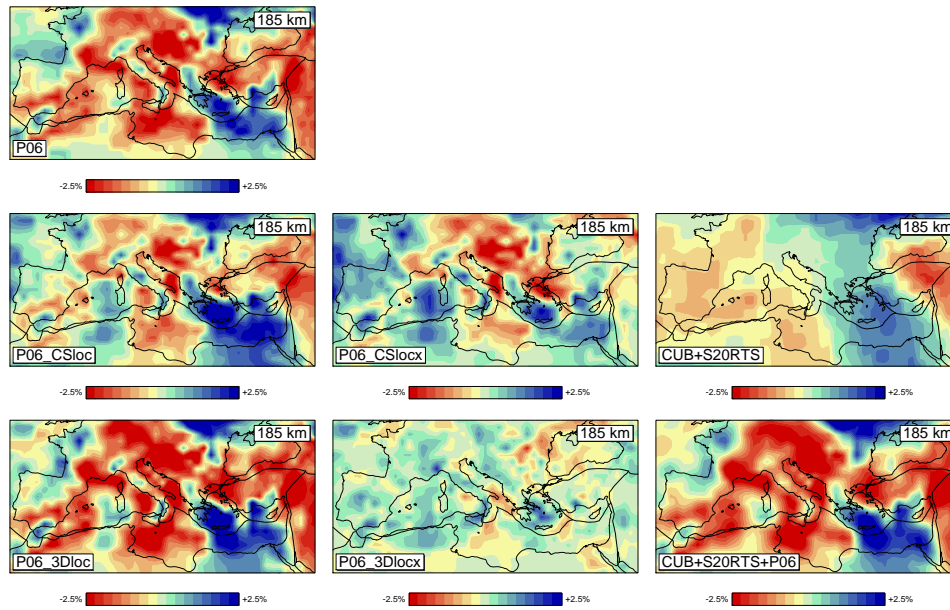
Figure 5.10: Model section at 185 km depth beneath the Europe-Mediterranean region. Models as in Figure 5.8.

tracing and leading to new delay times and 3-D ray paths. Hence, the amplitude amplifications are not necessarily completely lying in the null space of the current inverse problem and are subject to change. In contrast to ray tracing in reference model CUB+S20RTS, ray paths are now also traced through detailed 3-D heterogeneity, for example, in subduction regions which leads to focusing of slab structure and enhanced heterogeneity contrasts in model P06_3Dloc. These observations are similar to those of Bijwaard and Spakman (2000). Still, we should expect that the increased anomaly contrasts generally observed for P06_3Dloc compared to P06_CSloc are also partly contained in the null space as long as these are also present in the reference model.

At 50 km, P06_3Dlocx requires comparable corrections as P06_CSlocx which is understandable because in most of the affected regions the reference models CUB+S20RTS and CUB-+S20RTS+P06$^+$ are the same. At 185 km of depth we notice a similar global effect but subtle differences exist which can only be observed in blow-ups of the models as given for some regions in Figures 5.8-5.10. These figures show invariably that, irrespective of already enhanced velocity contrasts between slab and ambient mantle contained in reference model CUB+S20RTS+P06$^+$, the inversion result P06_3Dlocx continuous to enhance these contrasts leading to even more focusing of structure as required by the travel time data. In the first part of the lower mantle, e.g. 1175 km depth, the correction P06_3Dlocx to the reference model tends to further focus the huge positive anomalies associated with Farallon and Tethys subduction and the low-velocity heterogeneity under eastern Africa. At 1900 km, the corrections are relatively smooth but do lead to enhancement of amplitudes and structure with respect to the reference model and also with respect to solution P06_CSloc. In the deepest mantle (2650 km), new structure is introduced under Europe and the Tonga-Fiji regions, while also under the Americas amplification of anomalies can be observed. At this depth, the difference in reference models in the lower hemisphere, where the resolving power of the data is relatively low, leads particularly to differences between the tomographic models P06_CSloc and P06_3Dloc.

5.5.4 Vertical cross sections

Differences and possible improvements of the presented inversion models can also be observed in vertical cross-sections (Figure 5.14), for which the locations are indicated in Figure 5.6. Starting with a section across East Africa (S1) where Ritsema *et al.* (1999) interpreted a hot upwelling in their model, we observe that this upwelling, being however narrower in mapview (see Fig. 5.7 and 5.13), is also retrieved with the travel time data.

While little velocity structure is imaged in S20RTS beneath Iceland (S2) in the mantle below 1800 km, all three travel time tomography models show low velocities originating at the base of the mantle as was imaged before by Bijwaard and Spakman (1999b).

It is still a question under debate if volcanism beneath Yellowstone is fed by a deep mantle plume and seismic tomography does not provide models yet which would allow a definite statement. However, independent of the applied reference model a low-velocity anomaly is imaged down to the core-mantle boundary to the south of Yellowstone (S3). It is most coherent in the upper 1400 km depth while between 1400 km and 1800 km depth a weak anomaly or respectively no anomaly at all is imaged.

Narrow outlines of the subducted Cocos plate beneath the Yucatan Basin (S4) are visible and the use of 3-D reference models increases the amplitudes of the tomography models below the 660 km discontinuity.

The subduction of the Nazca plate beneath South America (S5) looks similar in all travel time tomography models and shows that the subducted material accumulates in a vertical column in the lower mantle while S20RTS shows comparatively little detail in the lower mantle. The subduction zone in P06_CSloc is slightly broadened in the uppermost mantle while the data have enough resolving power otherwise to avoid overprinting by the reference model.

A cross-section of the Pacific plate subducting underneath the Australian plate at the Tonga trench (S6) shows for all tomography models the high-velocity structure of the subducted slab and in all sections it is visible that the slab penetrates the 660 km discontinuity. Again, the difference between the inversion models relates to the dependence on the reference model.

The subduction of the Pacific plate beneath Eurasia below Japan (S7) is very well resolved in all tomography models due to the large amount of data available.

The collision of the Indian plate with Eurasia (S8) displays many similarities in all tomography models despite the fact that CUB+S20RTS only shows one positive "blob", which again supports the reliability of the obtained models.

As a last example, the subduction of the African plate beneath Eurasia along the Hellenic arc is displayed (S9). Again, all three tomography models agree well with each other while CUB+S20RTS contains much less details. Evidently, the slab continues in all inversion models into the lower mantle.

In summary, these cross-sections demonstrate the resolving power of the travel time data set leading to imaging of comparable structures independent of the reference model.

5.5.5 Effects of relocation on tomography with 3-D reference models

Event relocation prior to tomography has several effects on tomography. When the EHB event location is used for computation of theoretical travel times in the 3-D reference models, baseline shifts occur as the mean velocity per layer of the 3-D reference models is not equal to ak135 at the according depth (see Fig 5.5). Relocation in the respective reference model removes this baseline shift of travel time residuals and reduces the scatter of the residuals (see Table 5.3, Figure 5.15). The residuals of the EHB catalog which originate from event location in model ak135 using regionalized heterogeneity corrections by Engdahl *et al.* (1998) show a narrow distribution centered around 0 s. In contrast, the residuals computed with respect to CUB+S20RTS for EHB locations exhibit a broader distribution due to the 3-D variations of the model and a baseline shift of 0.73 s appears as CUB+S20RTS is particularly in the upper mantle dominated by high-velocity anomalies (with respect to ak135). Relocating the events in CUB+S20RTS removes this baseline shift centering the residuals around 0.07 s and narrows the distribution. Also the travel time residuals computed for the final reference model CUB+S20RTS+P06$^+$ but starting from the EHB locations show a baseline shift although smaller (in absolute terms) than for CUB+S20RTS and negative (-0.36 s). Relocation centers the baseline shift around -0.04 s and the scatter in the residuals is even smaller than for ak135 indicating a better travel time prediction. Consequently, to establish consistency between source parameters and travel time residuals, a relocation is mandatory.

76

	mean residual (s)	standard deviation (s)
AK135 (EHB)	-0.01	1.37
CUB+S20RTS	0.73	1.87
CUB+S20RTS,loc	0.07	1.66
CUB+S20RTS+P06$^+$	-0.36	1.49
CUB+S20RTS+P06$^+$,loc	-0.04	1.28

Table 5.3: The mean $\pm$ standard deviations of the unweighted, single travel time residuals computed for the different reference models without and with earthquake relocation in the respective reference model (see also Fig. 5.15).

Other observations concern the tomographic inversion for velocity perturbations and simultaneous inversion for event cluster relocations and station corrections.

The difference between the models with and without a priori relocation shows that the largest changes appear in the crust and the uppermost mantle where most earthquakes are located. In particular in subduction zones, velocities increase when a relocation is performed beforehand resulting in more focussed slab anomalies (see, for example, the Sunda subduction zone at 90 km depth in Fig. 5.16). Deeper in the mantle, differences are less systematic but still velocity contrasts such as below Australia (Fig. 5.17) at 1175 km depth are enhanced. In the lowermost mantle, only few changes are observed.

Station corrections, which are obtained as part of the inversion, correlate well with average station residuals before inversion. Furthermore, the corrections are regionally systematic. Thus, they mainly serve to remove average station delays, most likely related to the (crustal) velocity structure beneath the stations not accounted for by the reference and tomography models. Relocation prior to inversion results in particular for the model CUB+S20RTS in smaller station corrections indicating that the inconsistency between travel times and source parameters without a priori relocation is partially compensated by increased station corrections.

Also, simultaneously with the inversion for 3-D velocity variations, event cluster relocation terms are obtained for the composite residuals. However, they are of limited value since they were determined without S and sP phases and represent entire clusters of earthquakes. The direction of the relocation vectors is regionally systematic and depending on the used reference model with a trade-off between hypocenter depth and origin time corrections as observed in previous studies (e.g. Bijwaard *et al.*, 1998).

5.6 Discussion and Conclusions

We have conducted mantle tomography experiments with 1-D and 3-D reference models inverting a very large data set of P-wave travel times. Using distinctly different reference models implies inverting distinctly different delay time data sets, as reference model predictions of travel times are different. Reference model independent wave speed structure could be retrieved for large mantle regions where, according to sensitivity tests, spatial resolution is good to moderate. In other regions mantle structure inverted from the travel time information

blended with the reference model velocities or the reference model was found unchanged. The first 3-D reference model was composed from CUB2.0 in the crust and uppermost mantle overlying S20RTS in the deeper mantle. Interestingly, after 3-D location of all events in the reference model it proved that travel time predictions are worse than in the 1-D model ak135 (Table 5.3). This is surprising since both CUB2.0 and S20RTS are tomographic models derived from long period data and are assumed to give a better representation of mantle structure than a simple 1-D model. Improved locations combined with improved mantle structure should basically lead to a better travel time prediction (smaller delay times). We have not yet traced the reasons for this. Possible reasons can be that: (1) the locations in ak135 were performed using station corrections related to station elevation, crust and mantle heterogeneity (Engdahl *et al.*, 1998) while we did not use that in our location procedure, (2) the long wavelength models image different seismic velocities or have stronger amplitudes than in the real mantle as a result of insufficient damping during inversion (high-variance models), (3) the conversion between P and S velocity anomalies with the scaling factors of Bolton and Masters (2001) is not appropriate at all depths or more likely (4) the long wavelength models lack short wavelength structures (e.g. subducted slabs) which significantly affect travel times.

The best performing reference model in terms of travel time prediction is CUB+S20RTS+P06$^+$ although the difference with ak135 is small. Travel time predictions in the resulting inversion model P06_3Dloc (see Chapter 8) also demonstrates that this model predicts travel times better than ak135. Irrespective of the different statistics of the input data for inversion, still highly comparable models could be found with acceptable normalized data misfit (Table 5.2). The additional data error resulting from 3-D ray tracing, which we estimate to be of the order of 0.1 s, presumably slightly increases the misfit relative to that achieved in the P06 inversion and also increases the standard deviation prior to inversion.
 Basically we have obtained the following results:

1. A new tomographic model P06 is computed relative to reference model ak135 and based on much more data than before.

2. Using an internally consistent procedure involving 3-D ray tracing, 3-D earthquake relocation and tomographic inversion, we have combined mantle structure obtained from short period travel time inversion with the structure imaged in long wavelength tomography based on long period data. This leads to two totally new mantle models, P06_CSloc and P06_3Dloc, of which we prefer the latter because it includes travel time and ray geometrical effects associated with strong amplitude and short-wave length heterogeneity (e.g. slabs) in the well resolved part of the mantle. P06_3Dloc also predicts travel times better than ak135.

3. We have demonstrated that short period P-wave delay times contain sufficient resolving power to completely replace, in well resolved mantle volumes, the high-amplitude long wavelength structure as obtained by inversion of long period data. A similar observation was made by Widiyantoro *et al.* (2000) from their inversions of S-wave travel times.

4. By using different reference models as starting point for inversion we have shown that, in the well-resolved mantle volumes, imaged structure is independent of the reference

model used which supports the actual existence of imaged structure.

5. Reference model dependence of inversion results occurs in regions where tomographic models (considerably) disagree and model quality thus depends on the quality of the reference model.

6. With relocation prior to tomography using a 3-D reference model, generally velocity contrasts across subduction zones are enhanced allowing for a better separation of effects of source location from velocity heterogeneities.

Apart from regional details, all models have comparable spatial resolution as they are basically obtained from the same data set and, on a global scale, fairly similar ray geometry. Discrimination between these models should be made on account of the quality of travel time data prediction. The statistical significance of usually small changes in data fit relies on precise knowledge of data errors which is unfortunately mostly absent for the huge data set of mostly hand-picked data.

The models P06_CSloc and P06_3Dloc can serve as global reference models for earthquake location and waveform modeling, as back ground models for regional tomography, as starting models for global travel time or waveform tomography, as background for regional seismotectonic studies, or may prove useful in studies of mantle dynamics and the gravity field of the Earth.

Overall, our preferred model is the model P06_3Dloc as it shows low data misfits comparable to P06 after inversion (see Tbl. 5.2), was obtained with raytracing in a detailed 3-D reference model and furthermore implicitly contains realistic lateral velocity anomalies in regions that are not well sampled by short period P waves.
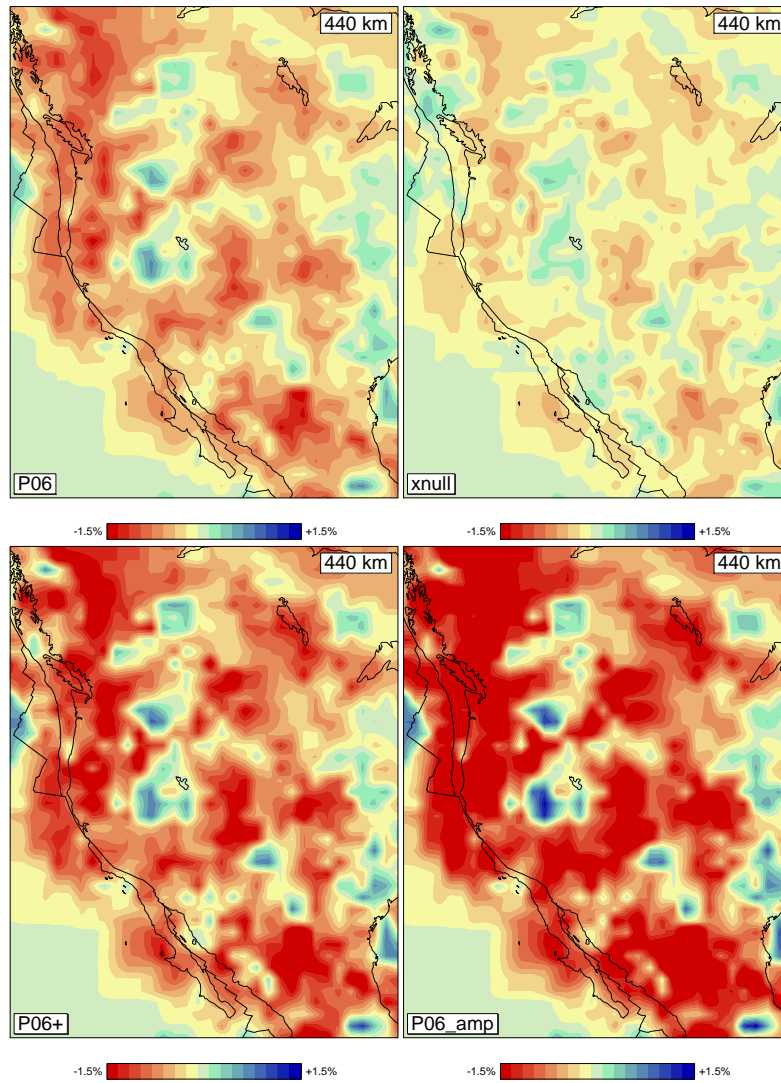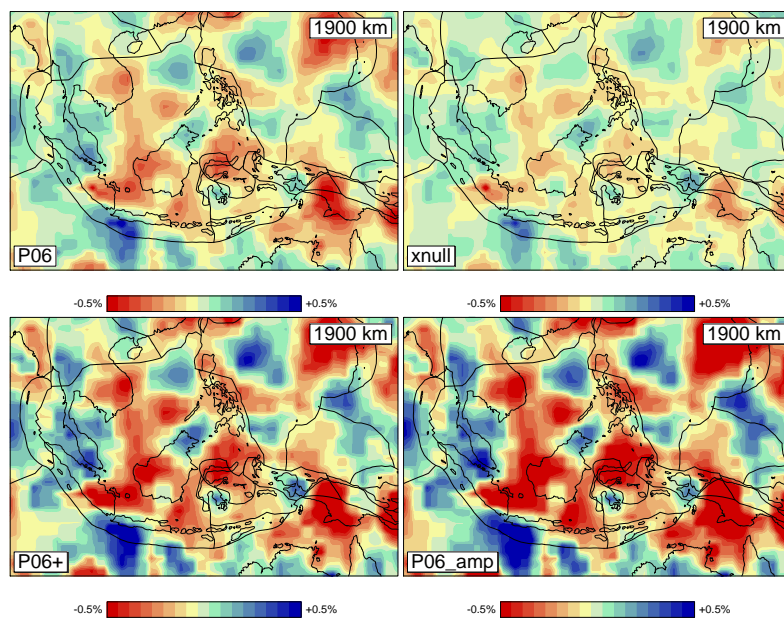
5.7   Acknowledgments

Figure 5.11: Model section at 440 km depth beneath western North America. Tomography model P06 using ak135 as starting model (top, left), xnull (top, right) is the model part $\boldsymbol{\Delta x}_{null}$ of the amplification that lies in the null space of $\mathbf{A}$, P06$^+$ (bottom, left) is the model P06+$\boldsymbol{\Delta x}_{null}$ and P06_amp (bottom, right) is the model P06 amplified by a factor of 2.
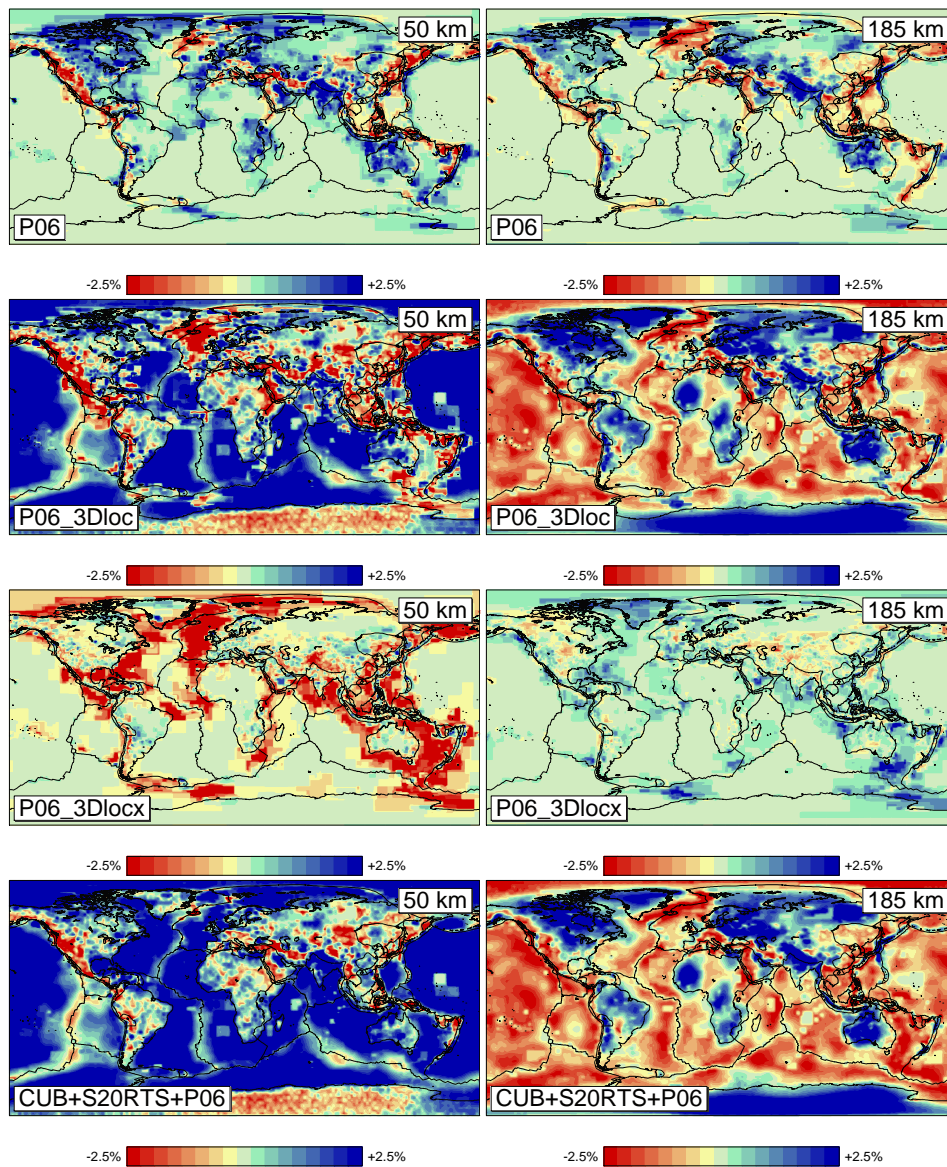
Figure 5.12: Model section at 1900 km depth beneath southeast Asia. Tomography model P06 using ak135 as starting model (top, left), xnull (top, right) is the model part $\Delta\boldsymbol{x}_{null}$ of the amplification that lies in the null space of $\mathbf{A}$, P06$^+$ (bottom, left) is the model P06 $+\Delta\boldsymbol{x}_{null}$ and P06_amp (bottom, right) is the model P06 amplified by a factor of 2.

Figure 5.13: Tomography model P06 using ak135 as starting model (top), P06_3Dloc using CUB+S20RTS+P06[+] as starting model displayed with respect to ak135 (second from top), P06_3Dlocx using CUB+S20RTS+P06[+] as starting model displayed with respect to CUB+S20RTS+P06[+] (third from top) and the model CUB+S20RTS+P06[+] itself (bottom) displayed as velocity perturbations with respect to ak135. Shown are horizontal slices through the models at 50 km (left) and 185 km depth (right).
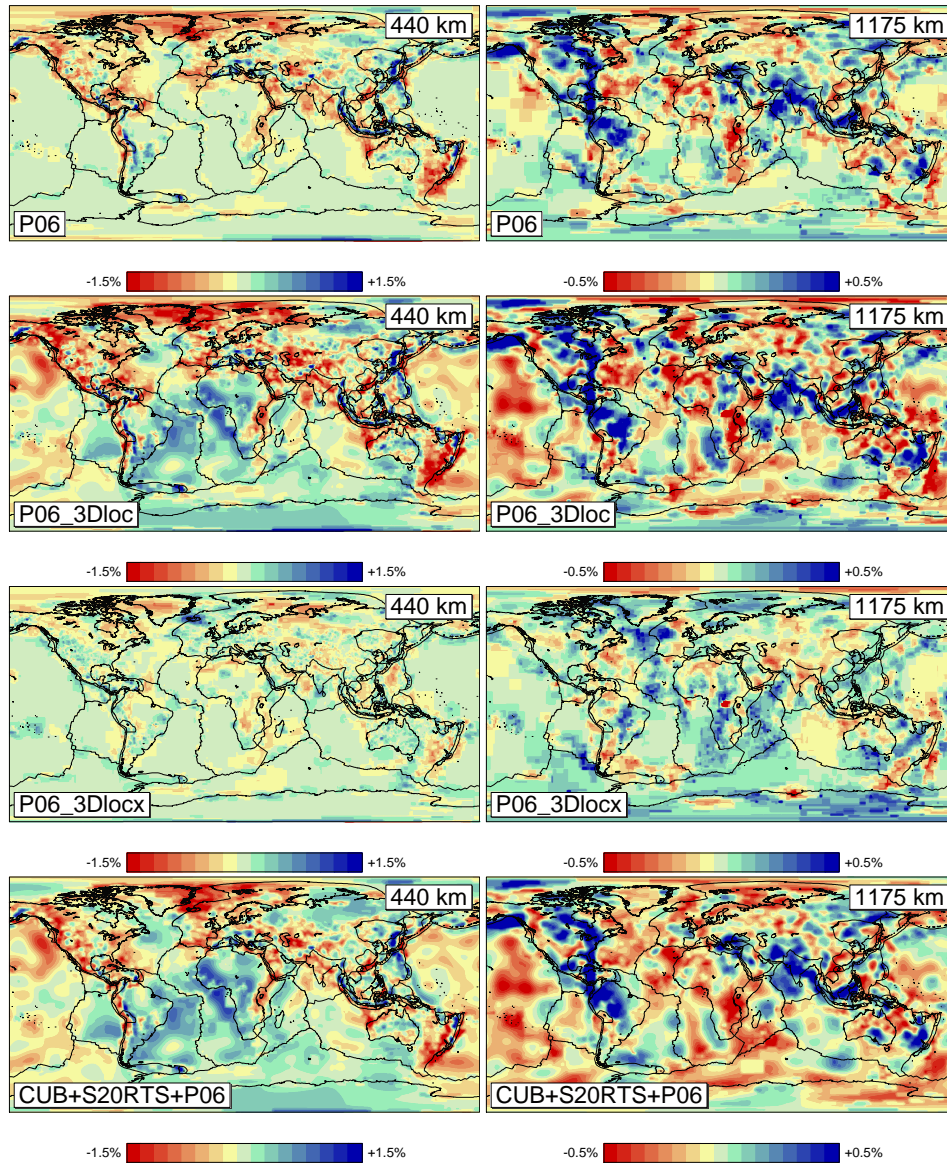
82

Figure 5.13: (Continued). Horizontal slices through the models at 440 km (left) and 1175 km depth (right).
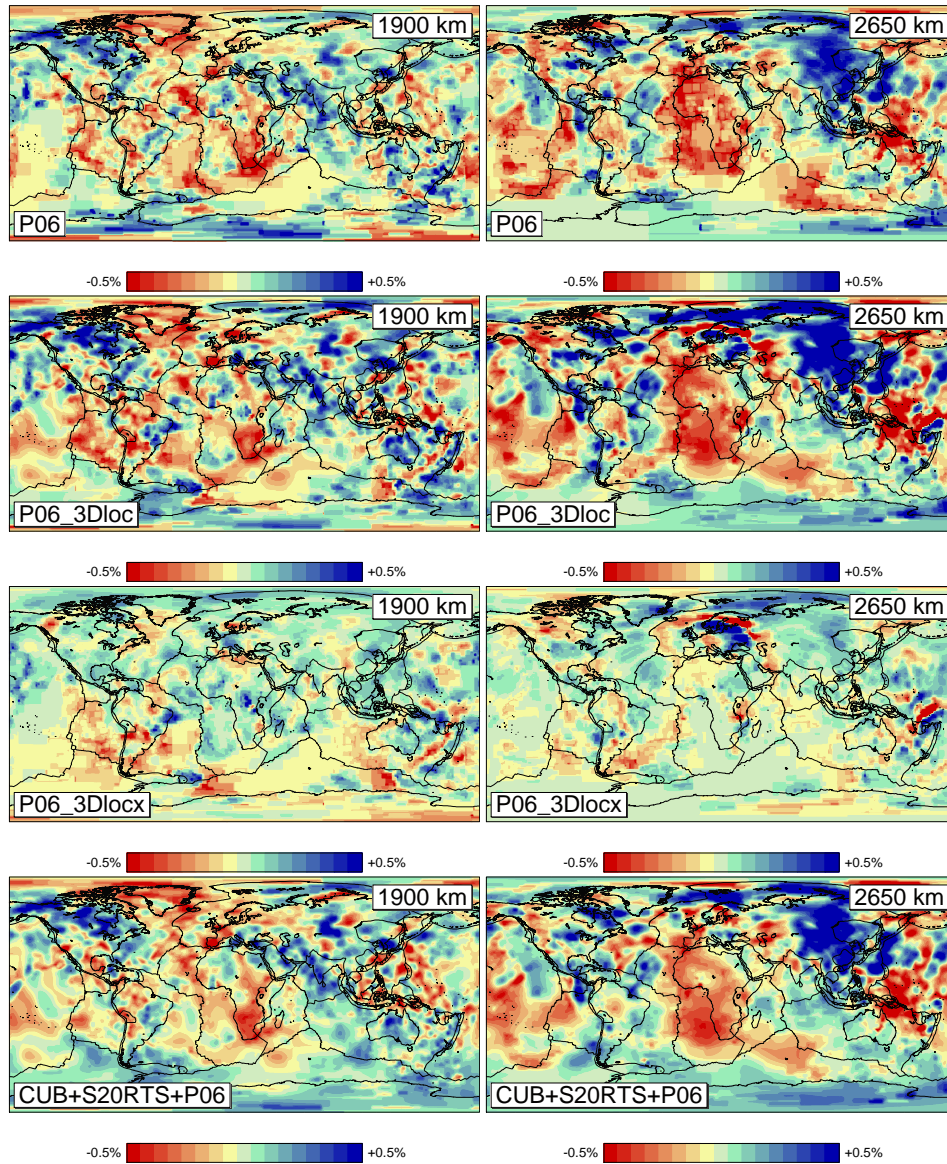
Figure 5.13: (Continued). Horizontal slices through the models at 1900 km (left) and 2650 km depth (right).
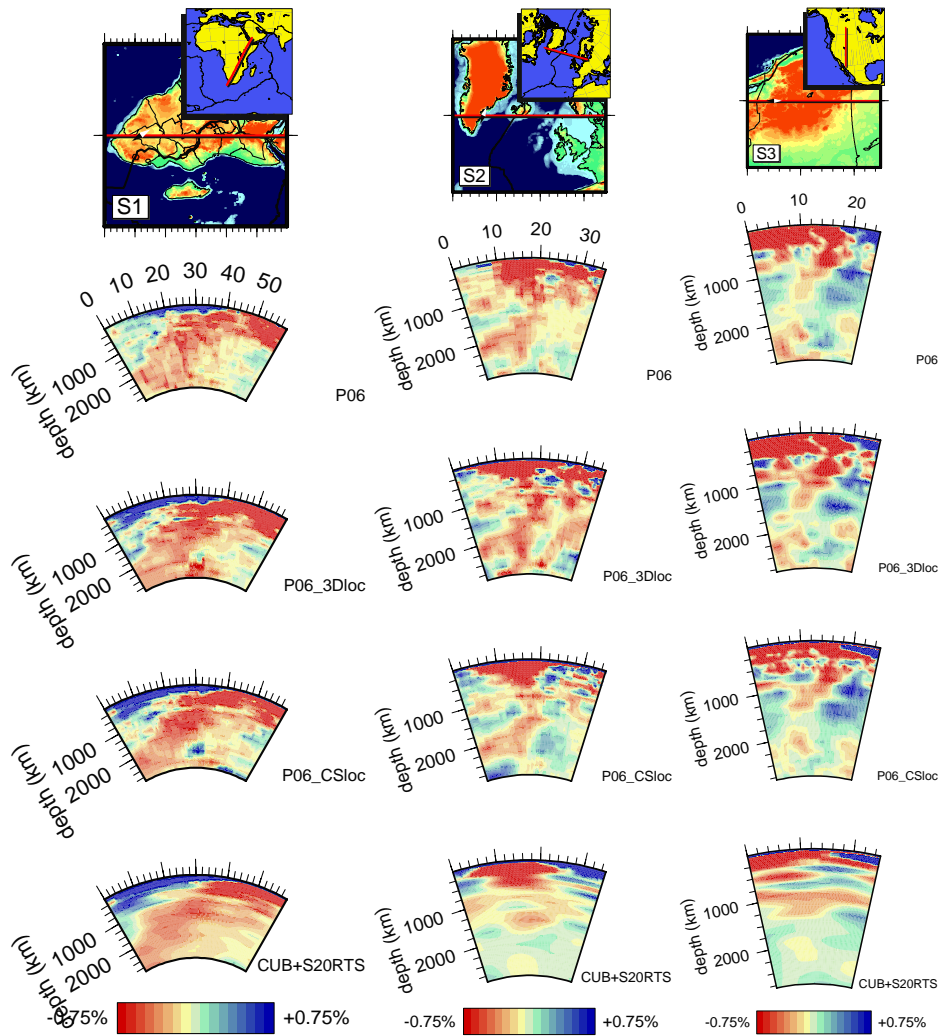
Figure 5.14: Vertical cross-sections displayed with respect to ak135 through the tomography models below East Africa (S1), Iceland (S2) and Northwest America (S3) for the tomography models using ak135 (top), CUB+S20RTS+P06$^+$ (second from top), CUB+S02RTS (third from top) as reference model and the reference model CUB+S20RTS itself (bottom).
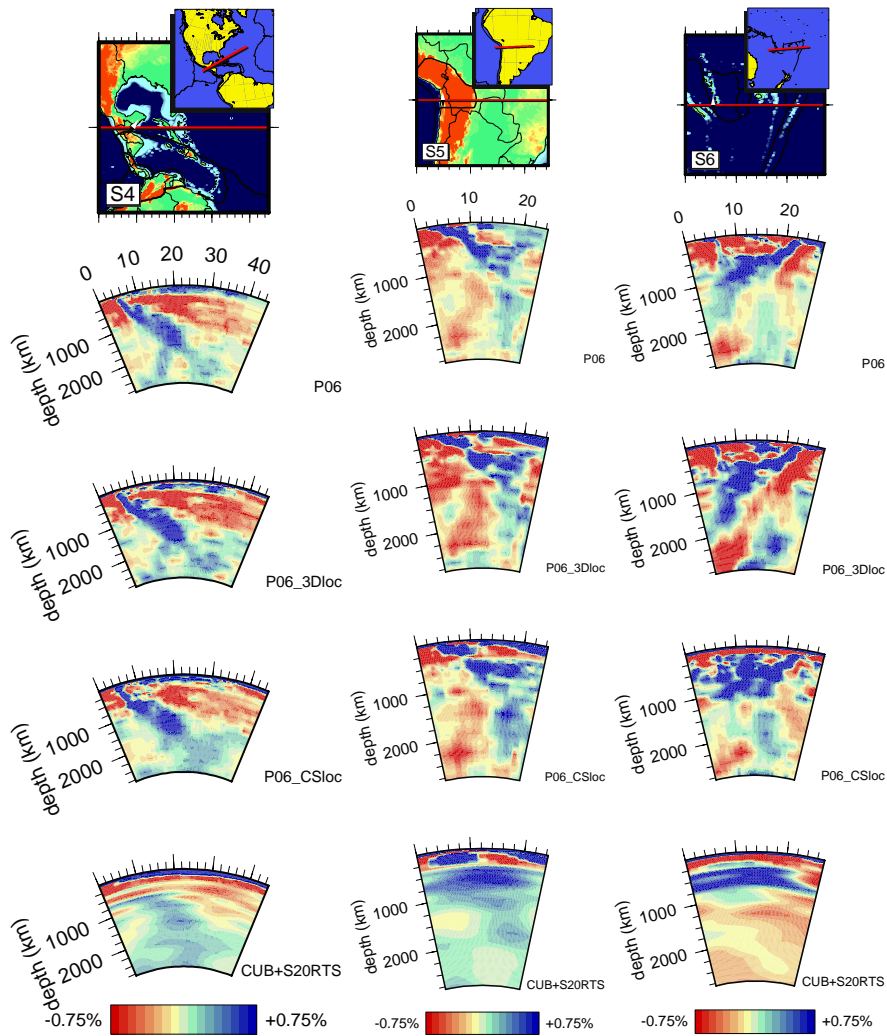
Figure 5.14: (Continued). Vertical cross-sections through the tomography models below the Carribean plate (S4), the Altiplano plate (S5) and Tonga (S6).
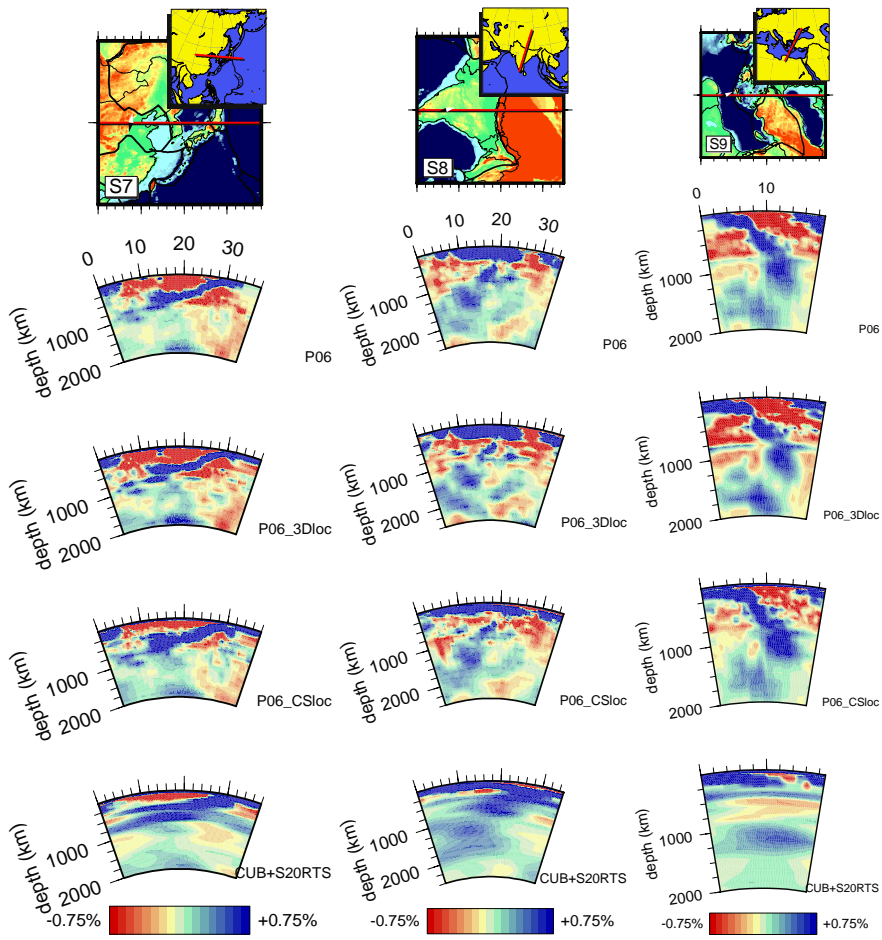
Figure 5.14: (Continued). Vertical cross-sections through the tomography models below Japan (S7), across the Himalaya (S8) and the Hellenic Arc (S9).
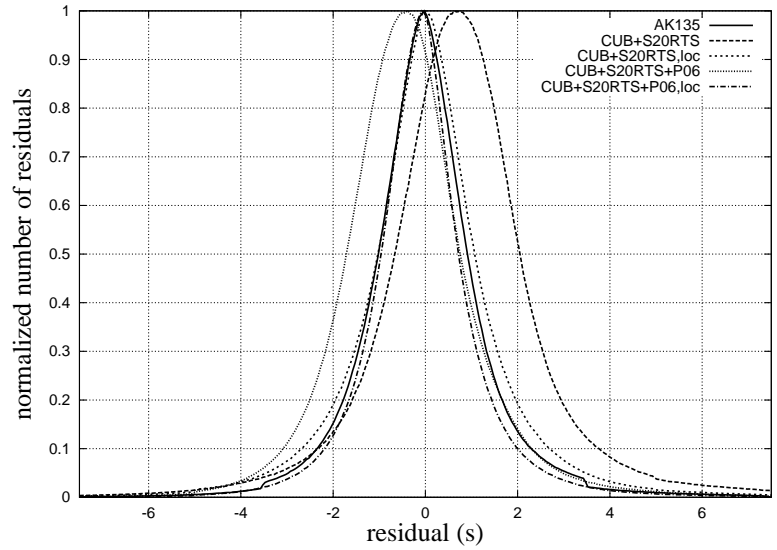
Figure 5.15: Histogram of the travel time residuals normalized to the maximum number versus the residuals computed with respect to AK135, CUB+S20RTS with/without a priori relocation and CUB+S20RTS+P06$^+$ with/without a priori relocation.
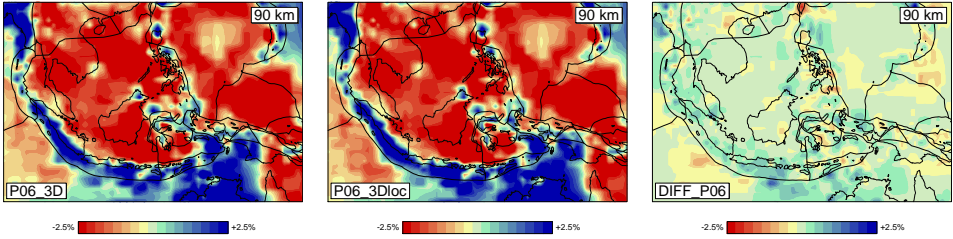

Figure 5.16: Section at 90 km depth beneath southeast Asia of the model P06_3D (without relocation prior to inversion), the model P06_3Dloc (with prior relocation) and their difference DIFF_P06. Blue are areas in DIFF_P06 where the model with a priori relocation contains higher velocities than the model without relocation and red are the regions where it is slower.

88

Figure 5.17: Section at 1175 km depth beneath Australia of the model P06_CS (without relocation prior to inversion), the model P06_CSloc (with prior relocation), the according starting model CUB+S20RTS and the difference DIFF_CS between P06_CS and P06_CSloc. Blue are areas in DIFF_CS where the model with a priori relocation contains higher velocities than the model without relocation and red are the regions where it is slower.
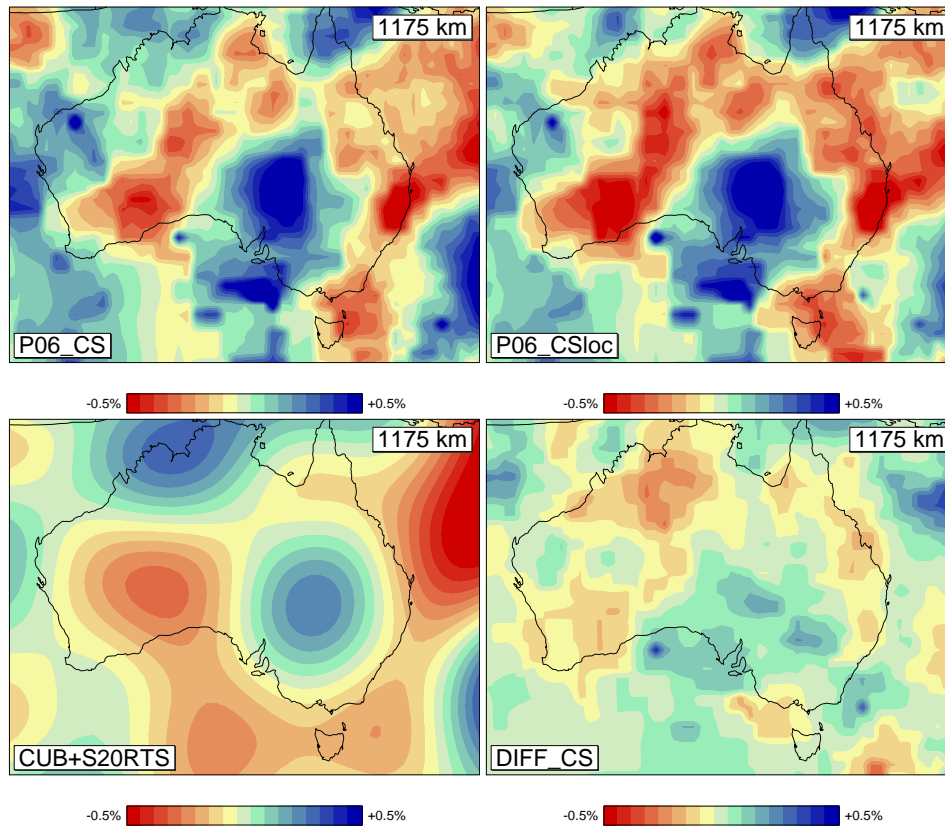
Chapter 6

Enhanced models of the European crust and mantle derived from travel time tomography

Seismic tomography has provided detailed images of the crust and mantle beneath Europe at both local and continental scale. The aim of this study is to improve imaging of the European mantle by combining arrival times from the International Seismological Centre (ISC) with additional arrival times from temporary experiments, data archives and bulletins incorporating also phase types which were not used before. As tomographic method, a regularized least squares inversion is performed for global mantle structure using an irregular grid parameterization. The inversions are performed both with a 1-D and a 3-D reference/starting model where the latter requires relocation of all earthquakes and 3-D ray tracing prior to the tomographic inversion. For the Europe-Mediterranean region, synthetic tests show that anomalies up to $0.5° \times 0.5°$ can be reconstructed in the best sampled regions of the uppermost mantle with resolution decreasing with depth. The added data sets are inverted separately to verify their quality showing that the obtained models contain velocity information also observed in other studies. The inversion results using the entire data set provide detailed velocity models of the mantle beneath Europe. Comparison with a previous model applying the same method shows that the new models image much more detail and enhance anomaly contrasts.

6.1   Introduction

The seismic velocity structure of the Europe-Mediterranean mantle has been subject of many tomographic studies both on local and regional scale (see Spakman and Wortel (2004) or Piromallo and Morelli (2003) for an overview).
Many of the global and regional high-frequency travel time tomography studies are primarily based on data from the International Seismological Centre (ISC) bulletins which provide the largest data collection available and is still expanding. For Europe, additional data are

available from various local experiments involving spatially dense station arrays which were placed in the field for at least several months. By incorporating these data, resolution can be improved locally below the temporary arrays and new information is provided for interpretation of tectonic processes.

Often, arrival times from those stations are only determined relatively. That means, not the arrival time of the phase onset is picked but the arrival time of a prominent part of the waveform relative to a reference waveform of the same event. This procedure has the advantage that observational errors due to a high noise level can be avoided but as a major disadvantage, the absolute arrival times remain unknown. Consequently, tomography provides only relative velocity variations with regard to the unknown average velocity below the array which cannot be converted to absolute velocities.

This may give the main reason why the relative delay time data from the individual experiments have, so far, not been combined to obtain a regional scale model of the European mantle. A consistent combination of the data from the different experiments would require repicking of the data to obtain absolute delay times. Another factor which hampers combining these data sets is that there is only little spatial overlap between the experiments. However, when absolute arrival time picks are consistently combined with a global data set of absolute delay times, a combined tomographic inversion may prove advantageous for improved imaging of mantle structure in the European region.

In this study we have taken this approach and reanalyzed the data of several experiments to obtain absolute arrival time picks. Subsequently, these high-quality data were combined with the global EHB data set (Engdahl *et al.*, 1998) updated until September 2004.

Additionally, seismological centers exist, which do not report their data to the ISC on a regular basis and therefore present a valuable source of complementary data. Absolute arrival times were picked from the ORFEUS (Observatories and Research Facilities for European Seismology) archive seismograms and the travel time data contained in the Euro-Mediterranean bulletin of the European-Mediterranean Seismological Centre (EMSC) were added.

In order to improve the model in the lower mantle, also core phases were included in the tomography.

6.2   The combination of data sets

6.2.1   EHB data set

The main data source for travel time tomography in this study is a reprocessed and updated version of the International Seismological Centre (ISC) bulletins extended with travel times from the National Earthquake Information Center (NEIC) of the USGS for the most recent events by Engdahl *et al.* (1998). This database will be referred to hereafter as EHB catalog. It now contains earthquake observations for the period 1964–2004 including over 445,000 events for 27.4 million first and later arriving phases. The processing of Engdahl *et al.* (1998) comprised a phase re-identification, theoretical travel time calculation in the Earth reference model ak135 (Kennett *et al.*, 1995) and a source relocation for well constrained events. For the global P tomography, 7.9 mill. regional P arrivals, 9.7 mill. teleseismic P, pP and pwP arrivals and 1.5 mill. PcP, PKP and PKiKP phases were selected. The selection criteria for

phase type	epicentral distance	residual range
P	$\leq 25°$	± 7.5 s
P	$> 25°$	± 3.5 s
pP, pwP (focal depth ≥ 35 km)	$25° - 100°$	± 3.5 s
PcP	$25° - 40°, 47° - 70°$	± 3.5 s
PKiKP, PKPdf	$110° - 140°$	± 3.5 s
PKPab, PKPbc, PKPdf	$\geq 150°$	± 3.5 s

Table 6.1: Selection criteria for the different phase types used for tomography.

epicentral distance and travel time residual range are given in Table 6.1. The updated catalog has approximately tripled in size compared to the original one and contains particularly more regional arrival times. The precision of the P phases was estimated following the method of Gudmundsson *et al.* (1990). This method uses ray bundles of teleseismic phases with decreasing width to extrapolate the standard deviation of ray bundles with zero width, which is presumed to be the upper limit of errors in the data. For the phases selected from the EHB catalog for $25° - 100°$ distance this error is estimated to be 0.65 s.

6.2.2 Euro-Mediterranean bulletin

The Euro-Mediterranean bulletin of the EMSC provides the second data set used in this study. Like the EHB data set, this bulletin contains a collection of arrival time observations from local networks in the Euro-Mediterranean region (Godey *et al.*, 2006). Well-constrained earthquakes in this catalog were relocated by the EMSC. However, instead of the EMSC locations, if existent, the corresponding EHB location is used or the events are relocated in ak135 for consistency with the EHB catalog. Also, since the EMSC uses locally varying 1-D reference models, all travel time residuals were recomputed using ak135 as reference model. The EMSC subset then consists of over 621,000 P and S travel times from 12,200 events for the period 1998–2003 for which EHB locations could be found and additionally 138,000 P and S travel times for 6,400 events for which an EMSC location exists. About 525,000 travel times are already contained in the EHB data set and therefore discarded from the data selection. New stations in the Euro-Mediterranean bulletin providing important information are situated, in particular, in Oman, Egypt, Morocco and Algeria (see Fig. 6.1). Using the same selection criteria as for the EHB data set, in total 155,000 P arrival times for 14,000 earthquakes were selected for tomography of the travel times not included in the EHB data set. However, only first arrivals were selected to minimize problems with phase misidentifications (e.g. in triplication zones). Following the method of Gudmundsson *et al.* (1990), the upper limit to random data errors was estimated to be 0.68 s.

6.2.3 Newly picked data for stations in Europe

Additionally, temporary experiments with spatially dense station arrays in Europe, the OR-FEUS archives and a collection of registrations for the UK, Ireland and part of northwestern

France which were not reported to the ISC (named Leeds data hereafter, provided to us by Arrowsmith (2003)) form another source of data for travel time tomography. The temporary experiment data comprise the SVEKALAPKO experiment in Finland (Bock et al., 2001), the TOR experiment in South Sweden, Denmark and North Germany (Gregersen *et al.*, 2002), the EIFEL experiment in the Eifel (Ritter *et al.*, 2000), the CALIXTO experiment in Romania (Wenzel *et al.*, 1998) and the MIDSEA project with a number of stations surrounding the Mediterranean Sea (van der Lee *et al.*, 2001). The data from these stations were obtained as waveforms, pre-processed and picked with the automatic picking method of Sandoval *et al.* (2004a). This procedure resulted in a total of 83,500 P-wave travel times (see Chapter 4 for a more detailed description of the data set). The picking errors were estimated within the picking algorithm to be approximately 0.15 s. The obtained arrival times were later on combined with the Euro-Mediterranean bulletin and EHB data set using the same selection criteria as before. Even though the number of additional travel times is comparatively small, the new data may have a considerable influence on the tomographic inversion as their quality is better than that of the average EHB or EMSC pick.

6.3 Tomographic method

In travel time tomography, travel times of seismic waves are compared to theoretical predictions computed from a reference model of the Earth's seismic wave speed. To avoid the limitations of using a strictly regionally defined model volume we include the entire Earth in our tomographic experiments. The EHB data set is used globally and for Europe we inserted the additional data from regional experiments and permanent networks. Our tomography code implements the following delay time equation for the forward problem of tomography (Spakman et al. 1993):

$$d = \int_{L_0} (s - s_0) \, dl_0 + (\mathbf{x} - \mathbf{x}_0) \cdot \nabla_0 T^0_{x_0} + \Delta t_x + \Delta t_s + \epsilon \tag{6.1}$$

where d represents the delay time/travel time residual, L_0 is the ray path in the reference model starting at the reference location x_0, dl_0 is the ray segment, s is the Earth's slowness (i.e. the reciprocal of the velocity) field and s_0 is the slowness field of the reference model. Δt_x contains the timing error due to source mislocation as a result of the slowness anomaly field $s - s_0$, Δt_s contains travel time effects due to station elevation and instrument response and ϵ describes the observational errors (e.g. picking errors or phase misidentification, remaining location errors).

In a tomographic analysis, a large set of delay time equations 6.1 derived from many source-station combinations is discretized and inverted for estimates of the slowness anomaly field $s - s_0$, the event mislocations $\mathbf{x} - \mathbf{x}_0$, origin time errors Δt_x and the station static terms Δt_s. Furthermore, this equation is valid for both 1-D and 3-D reference models of Earth structure as long as the data (delay times, ray paths and hypocenters) are consistent with the reference model used. Because travel time tomography is a nonlinear inverse problem and because the data have generally insufficient resolving power to obtain high and spatially uniform model resolution, the tomographic model is expected to depend on the reference model adopted. In this study we use two different reference models in order to define two distinctly different
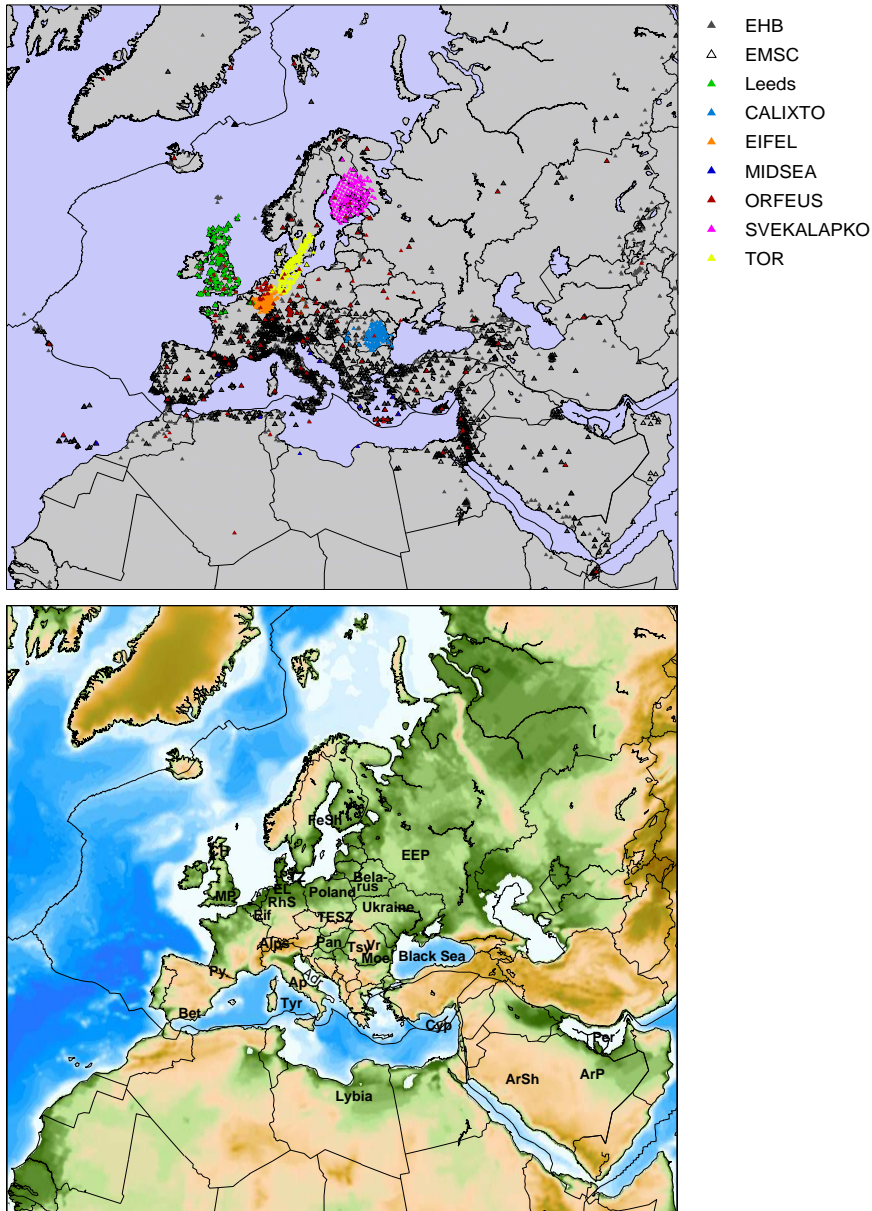
Figure 6.1: Top: Map of seismic station locations in the Europe-Mediterranean region. Different colours indicate the different data sources. Bottom: Map of the main tectonic units discussed in this study. Abbreviations: Adr – Adriatic basin, Ap – Apennines, ArSh – Arabian Shield, ArP – Arabian Platform, Bet – Betics, CH – Central Highlands, Cyp – Cyprus, EEP – East European Platform, Eif – Eifel, EL – Elbe lineament, FeSh – Fennoscandian Shield, Moe – Moesian Platform, MP – Midland Platform, Pan – Pannonian basin, Per – Persian Gulf, Py – Pyrenees, RhS – Rheic Suture, TESZ – Trans-European Suture Zone, Tsy – Transylvanian basin, Tyr – Tyrrhenian basin, TZ – Tornquist zone, Vr – Vrancea zone.

95

starting points for the tomographic inversion.

The first reference model is the radially symmetric model ak135 (Kennett *et al.*, 1995) to which the EHB data set and other data sets used pertain and which has been used before in global tomography studies (e.g. van der Hilst *et al.*, 1997; Bijwaard *et al.*, 1998). The inversion of all data with respect to ak135 leads to the tomographic model which we label P06.

The second reference model is a 3-D model of Earth structure. This model is a combination of three global tomographic models and is constructed in two steps:

In the first step, the P velocities of model CUB2.0 (Ritzwoller *et al.*, 2002a) are used for the uppermost mantle and combined with model S20RTS (Ritsema *et al.*, 1999) for the remainder of the mantle. The latter is converted to P-wave speed using the depth-dependent conversion factors as determined by Bolton and Masters (2001). These two models are blended through a depth-weighted linear average in the depth range 200 km to 300 km. The combination results in a relatively long wavelength model of the mantle primarily based on long period S data, surface waves and normal modes. A laterally heterogeneous crustal model (CRUST2.0, Bassin *et al.*, 2000) is implicitly included in model CUB2.0. In the second construction step, short wavelength mantle structure is blended in for which we use an amplified version of model P06. Because velocity anomaly amplitudes in travel time tomography are usually underestimated by 30%-50% in many mantle regions, the amplitudes of P06 are first amplified by a factor of two. Next, the null space shuttle of Deal and Nolet (1996) is used to remove those amplifications which are not supported by the travel time data. The remaining amplitude amplifications are in the null space of the travel time inverse problem of P06 which means that the travel time effects associated with amplitude enhancement cancel on average along the ray paths in ak135. The null space shuttle leads to model P06$^+$ which replaces CUB+S20RTS in regions well sampled by short period P data. In the Earth's core the 1-D model ak135 is used. For a more complete description of this reference model (CUB+S20RTS+P06$^+$) and how it is constructed we refer to Chapter 5.

The data set (event locations and delay times) is consistent with reference model ak135. It is, however, not consistent with the use of reference model CUB+S20RTS+P06$^+$ as starting point for tomography. To achieve consistency the entire global catalog of earthquakes is relocated in the 3-D reference model using a directed grid search method derived from the algorithm of Sambridge and Kennett (1986). The reference model travel times, feeding the grid search, are computed with 3-D ray tracing (Bijwaard and Spakman 1999) in the 3-D reference model. Also, the ray path geometry and delay times used for tomography are determined from 3-D ray tracing.

We use the procedure of Bijwaard *et al.* (1998) to solve the inverse problem. For the EHB and EMSC data, composite rays are used instead of single rays where a composite ray is built from single rays of the same phase type which originate from the same event cluster (defined by volumes of $0.3° \times 0.3° \times dz$ with volume thickness dz increasing from 15 km at the surface to 40 km at 660 km depth) and end at the same station. By using composite rays, the amount of data for inversion is reduced but at the same time the signal-to-noise ratio is increased. The data are weighted prior to inversion by the spread of the individual delay times within the respective ray bundle to account for the difference in ray bundle size. For the new data, this approach is not used as their quality is expected to be higher. Instead, single rays are used. The resulting data vector contains 10.4 mill. composite arrival times from originally

19.4 mill. single arrival times.

The Earth is parameterized by an irregular grid of non-overlapping cells according to the method of Spakman and Bijwaard (2001) where the cell size depends on the number of rays crossing a cell. The horizontal cell size varies in crust and mantle between $0.5° \times 0.5°$ and $10.0° \times 10.0°$. The layer thickness increases from the crust (10 km) to the lower mantle (200 km) and the layer boundaries respect the discontinuities as contained in ak135 (at 35 km, 410 km, 660 km, 2891.5 km, 5153.5 km depth). The inner and outer core are both parameterized by a single layer with cells of $10° \times 10°$ to allow for core structure but simultaneously prevent large model variations. The irregular grid is constructed from 8 035 000 cells of $0.5° \times 0.5°$ which are projected onto 604 000 non-overlapping irregular cells using a hitcount-constraint. The irregular cell approach mostly reduces overparameterization thereby improving the conditioning of the inversion matrix while retaining the possibility to resolve structure at small scales ($0.5°$) where allowed by the data.

The tomographic inversion itself is performed iteratively with the LSQR algorithm of Paige and Saunders (1982). Simultaneously with the inversion for cell slowness anomalies, we invert for event cluster mislocations and station corrections (see eq. 6.1). A second-derivative damping is applied to regularize the solution of the inversion and to obtain a smooth model. Additionally, for inversion with the 3-D reference model an amplitude damping is applied to suppress particularly in the crust and directly beneath it large excursions from the reference model. The model parameters are scaled for inversion dependent on cell size and hitcount to emphasize small cells and weigh down cells with very high hitcounts in the lower mantle following the approach of Bijwaard *et al.* (1998):

$$
\begin{pmatrix} \mathbf{C}_d^{-1/2}\mathbf{A} \\ \lambda\mathbf{C} \end{pmatrix} \mathbf{S}^{-\frac{1}{2}}\mathbf{m}' = \begin{pmatrix} \mathbf{C}_d^{-1/2}\mathbf{d} \\ 0 \end{pmatrix}
\tag{6.2}
$$

where $\mathbf{A}$ contains the ray path segments, relocation and station coefficients, $\mathbf{C}_d$ represents the data covariance matrix, λ is a damping factor controlling the trade-off between data misfit and model norm/smoothness varying between 1000 and 7000, $\mathbf{C}$ the matrix of damping coefficients, $\mathbf{S}$ is the scaling matrix with $(S_{jj}) = h_j V_j$ and h_j and V_j are hitcount and cell volume respectively, $\mathbf{m}' = \mathbf{S}^{\frac{1}{2}}\mathbf{m}$ is the scaled model vector $\mathbf{m}$ and $\mathbf{d}$ the data vector consisting of the travel time residuals.

6.4 Results - Separate inversion of the experiment data and EMSC data

To investigate the signal content of the newly picked absolute travel time data, the data from each experiment were inverted separately with the method described in Section 6.3 using ak135 as reference model to see if the main features expected below the arrays can be imaged. We note beforehand that we cannot recover the local detail in the crust and uppermost mantle as seen in the original tomographic models derived from the individual teleseismic experiments. First, our model parameterization is generally coarser than used in the original tomographic investigations. Second, the individual experiments have occasionally allowed

for more detailed corrections for local crustal structure. Third, the model box in each experiment is confined laterally to the experiment region and in depth usually to the first few hundred kilometers while here we invert each data set using a global mantle model parameterization. Lastly, the tomographic experiment studies inverted relative residuals which in part compensates for effects of structure outside the assumed model box but have led to velocity anomaly models without relation to a background of absolute velocities. Each of these factors will complicate a detailed comparison with our results.

As displayed in Figure 6.2a, the subducted slab beneath the Vrancea zone resulting from convergence of Europe and Africa is retrieved with the CALIXTO data. Typical for this and the following models is the comparatively low amplitude of anomalies. Since a global tomography is performed, the rays are traced along their entire path and energy can be smeared into the deep mantle as a result of lack of resolution. Except for differences in amplitude, exact geometry and the depth extent, a high-velocity body is imaged in the Vrancea region as in the models of Weidle *et al.* (2005) and Martin *et al.* (2006) which are also based on CALIXTO experiment recordings but using different travel time data sets and a different tomographic method.

The inversion model of the EIFEL data (Fig. 6.2b) shows low velocities directly beneath the Eifel where a presumed mantle plume has fed volcanism in the Eifel until 11 000 years ago. The anomaly is seen clearly between 50 km and 200 km depth. However, compared to the P model of Ritter *et al.* (2001) or the S model of Keyser *et al.* (2002) the absolute amplitudes are weaker and decrease more with depth.

The Tornquist zone could be imaged as well with the newly picked TOR data (Fig. 6.2c). It separates the high-velocity Fennoscandian shield from the younger Phanerozoic region of Central Europe with its lower velocities (at approximately $5°$ horizontal distance in Fig. 6.2). Furthermore, high velocities could be imaged beneath the Elbe lineament (at $\approx 2° - 3°$ horizontal distance). The larger scale detected features of this model are in agreement with the models of Arlitt *et al.* (1999), Shomali *et al.* (2006) and Voss *et al.* (2006) even though these models vary in depth extent of anomalies and inclination of the lithosphere-asthenosphere boundary below the Tornquist zone.

The high-velocity Archean core of the Fennoscandian shield could be reconstructed with the SVEKALAPKO data (Fig. 6.2d). Lower velocities in this case appear where crustal structures as the Rapakivi granite below southeast Finland are smeared out into the mantle due to a lack of data. The boundary between lithosphere and asthenosphere is located between 300 km and 400 km depth according to this model. A comparison to the model of Sandoval *et al.* (2004b) shows that both models contain similar structures but that the high-velocity body here extends deeper and has lower amplitudes due to the applied method.

A horizontal section at 90 km depth is displayed for the inversion of the Leeds data (Fig. 6.2e). Among other features, high velocities are found below South England related to the Midland platform (consisting of undeformed Precambrian lithosphere) and beneath the Central Highlands, which relate according to El-Haddadeh (1986) to remnants of a subducted oceanic plate from the Grampian orogenesis. The elongated low-velocity anomaly northwest of Wales coincides with a region of Paleogene magmatism. The lateral variation of described anomalies matches that found by Arrowsmith (2003).

Inversion of the EMSC data which were not contained in the EHB catalog provides a model

of the crust and uppermost mantle sampling the upper 250 km. As displayed here at 50 km depth, the model shows features imaged before in various regional scale and global experiments such as negative anomalies under the Tyrrhenian and Aegean backarc basins, negative anomalies associated with the crustal roots of Alps and Apennines, lower velocities under Anatolia while positive anomalies are associated with the Eastern Mediterranean and Adriatic basins.

Summarizing, with the newly picked absolute travel times we can recover the signature of mantle structure as imaged before in the proper tomographic experiments associated with each field experiment and based (mostly) on relative residuals. We do not recover the high detail, nor the amplitudes reported due to a lack of (depth) resolution. We do, however, image similar structures with absolute delay times instead of relative delay times. We only performed our experiments to demonstrate a similar information content of the data. Lack of depth resolution is natural in these experiments and can only be improved by merging all data sets with the EHB data set. This is now possible because we (re)-picked the waveform data for absolute travel times.

6.5 Results - Inversion of the entire data set

6.5.1 Variance reduction and model quality

As all delay time data sets are determined in the ak135 reference model they can be merged without creating inconsistencies. Inversion led to a data variance reduction of 52.1% in the inversion using ak135 as reference model reducing the standard deviation of the weighted, composite residuals to 1.44 after inversion. The variance reduction is lower compared to 57.1% of Bijwaard *et al.* (1998) but decreasing to almost the same normalized standard deviation of error-weighted data (1.44 versus 1.42). This may indicate a poorer signal to noise ratio in our data set which incorporates a large number of regionally observed events.

Hitcount maps (Fig. 6.3) indicate regions of high and low ray coverage. For example, ray coverage at shallow depth is low beneath the oceans due to a concentration of the epicenters along the Mid-Atlantic ridge and a lack of stations within regional distance of the epicenters. Also for the East European platform there is a low ray coverage due to a low number of events and seismic stations. With depth, ray coverage becomes more uniform, increasing towards the mid-lower mantle and decreasing again in the lowermost mantle.

 As stations and events are not equally distributed over the investigated region, the resolution of the velocity models varies spatially but it cannot be computed formally due to the large number of parameters. Therefore, sensitivity tests are performed with synthetic models (e.g. Spakman and Nolet, 1988) to detect lack of resolution and to estimate the minimum size of anomalies that can be reconstructed. The synthetic models for these tests consist of spatially well separated spikes of $\pm5\%$ amplitude with respect to the 1-D reference model which are subsequently projected onto the irregular grid. Tests are performed with different spike sizes from $0.5°\times0.5°$ to $6.0°\times6.0°$. Theoretical travel times are then calculated using the ray distribution associated with the observed data and Gaussian noise with a standard deviation of ±0.5 s is added to the data. Subsequently, the resulting matrix equation is inverted using the same regularization parameters as in the actual data inversion. In Figure 6.4, examples of
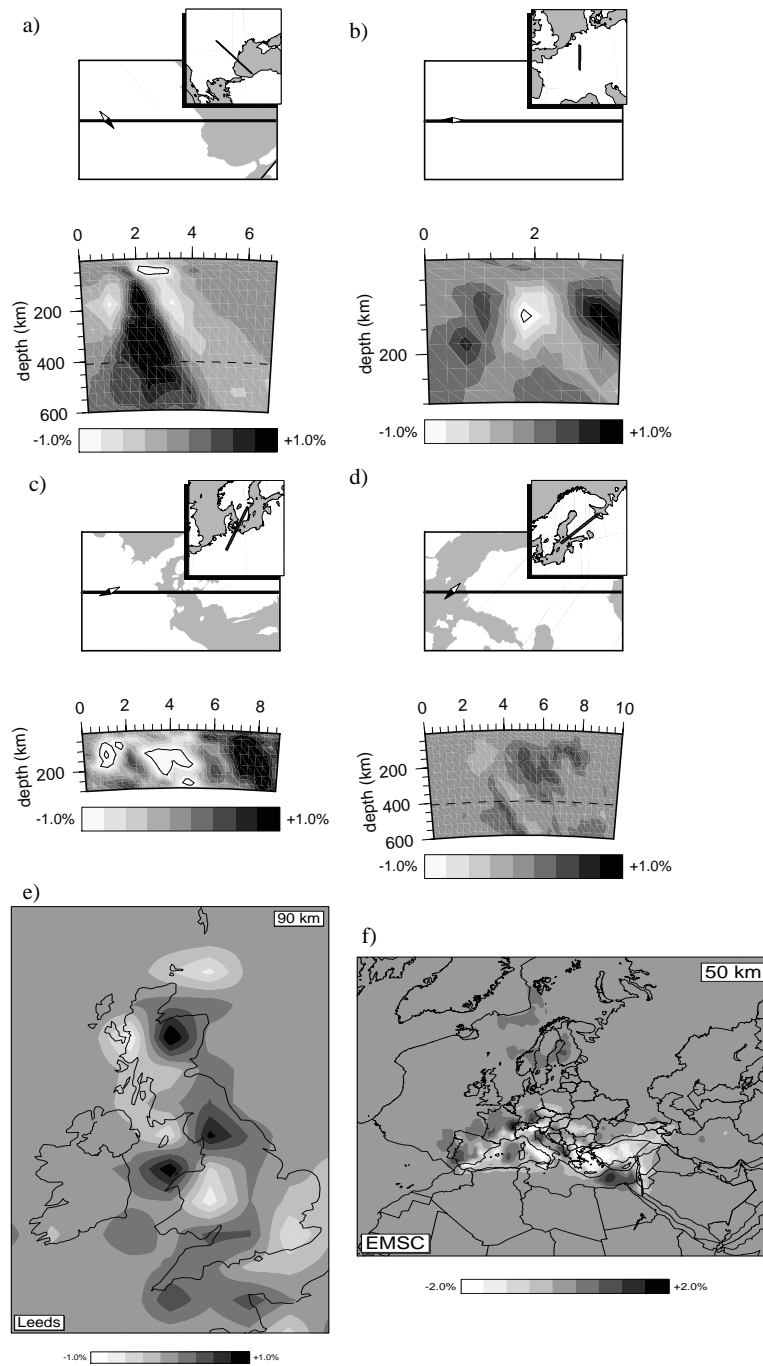
Figure 6.2: Results of the separate inversions of the CALIXTO (a), EIFEL (b), TOR (c), SVEKALAPKO (d), Leeds (e) and EMSC data (f).
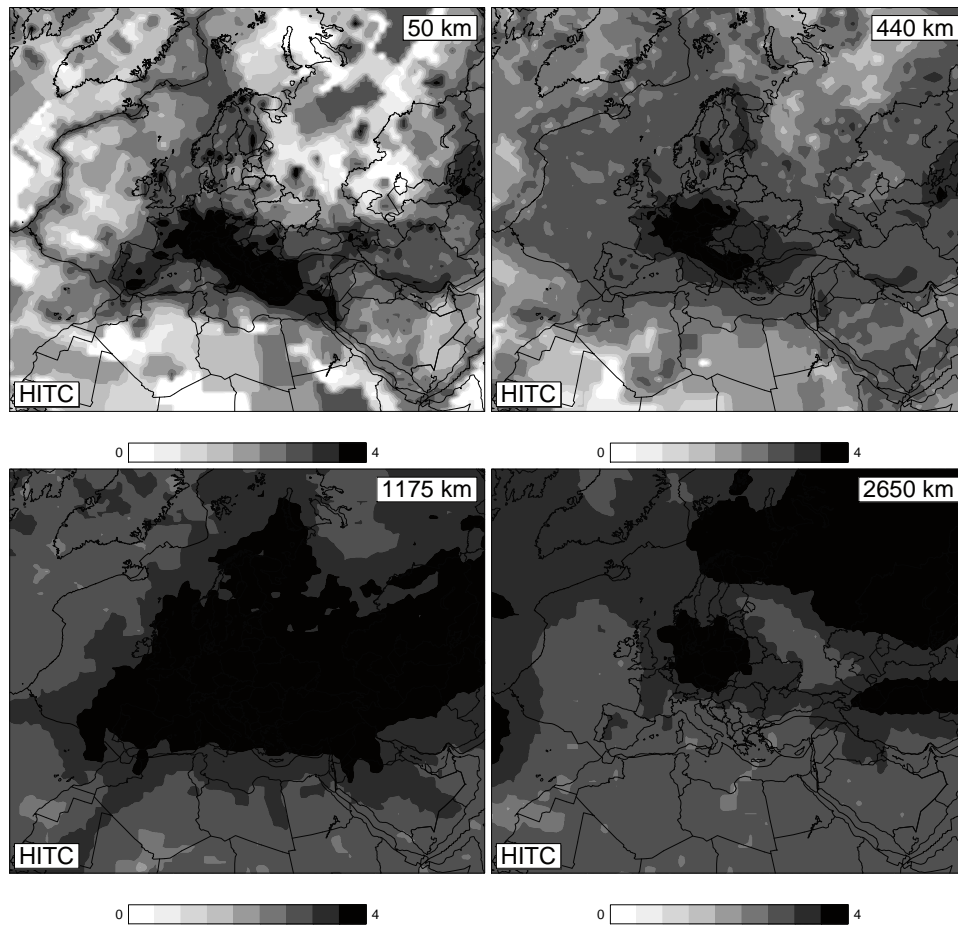
Figure 6.3: Logarithmic hitcount (i.e. number of rays crossing a cell) at various depths.
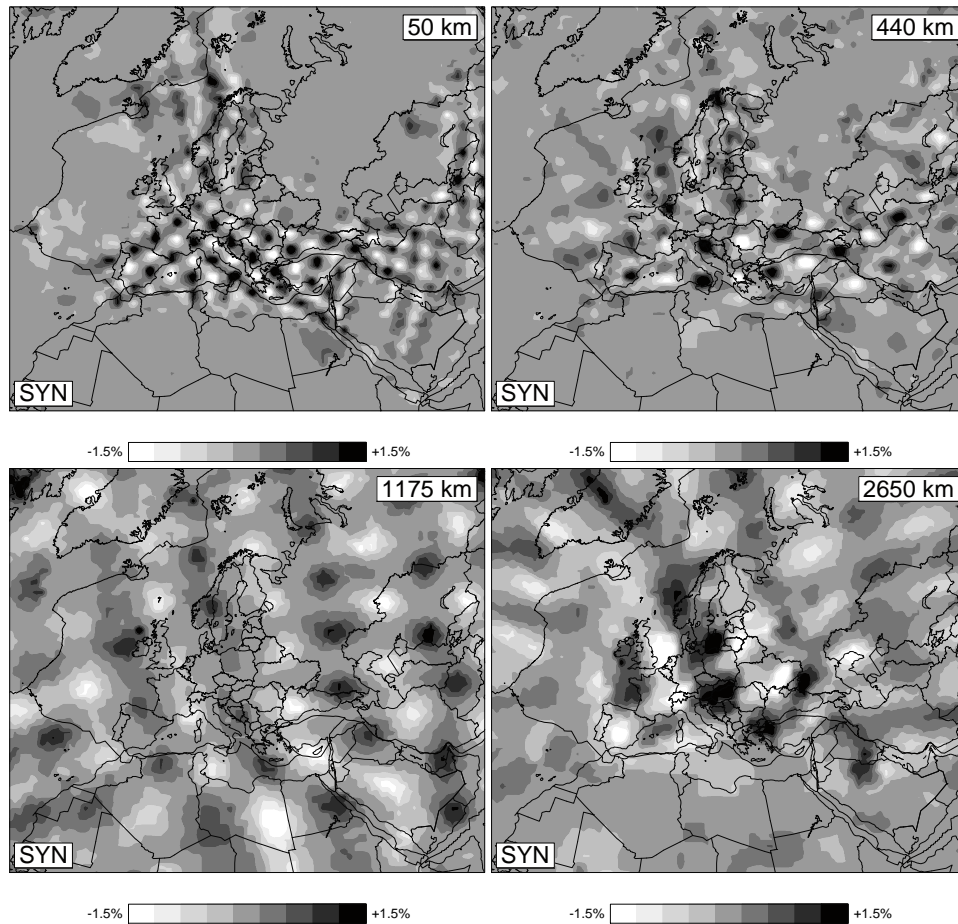
Figure 6.4: Spike tests for an anomaly size of $1° \times 1°$ at 50 km depth, $2° \times 2°$ at 440 km depth, $3° \times 3°$ at 1175 km depth, $3° \times 3°$ at 2650 km depth. The greyscales give the amplitude of the velocity anomalies.

such spike tests are shown for various layers with spikes of different sizes increasing with depth as the spatial resolution decreases with depth. In the uppermost mantle, anomalies of $1.0° \times 1.0°$ can be reconstructed (for instance, in the Aegean at 50 km even anomalies of $0.5° \times 0.5°$) whereas in the lower mantle, anomalies with a horizontal extension of $3.0°$ can be reconstructed.

To estimate the uncertainty of the velocity model caused by errors in the observed travel times, the data vector is permuted randomly before performing the inversion keeping the same inversion matrix as for the original data vector (Spakman, 1991). In general, a random

model with low amplitudes ($\approx 0.2-0.3\%$) is found in regions of good ray coverage as there is little correlation between data and ray paths (an example of such a test is given in Figure 5.4). Only poorly sampled regions, as for example the Northern Atlantic at 50 km depth, display systematic anomalies of higher amplitude ($\approx 1\%$). The mean velocity perturbations of the permuted data vector test are are close to 0% throughout the mantle. The root-mean-square values amount to $\approx 0.25\%$ at the top, reducing to $\approx 0.2\%$ in the upper mantle and to $< 0.1\%$ in the lower mantle and provide an upper bound for the amplitude errors since the data are treated as errors in this test while true data errors are smaller.

6.5.2 Model results - Comparison to the BSE model

Two models are computed: P06 with respect to reference model ak135 and P06_3Dloc with respect to reference model CUB+S20RTS+P06$^+$ as described in Section 6.3. Spatial resolution of these models is highly comparable although small differences in sensitivity test results exist. The significance of these differences is, however, difficult to quantify.

The newly picked data, the Euro-Mediterranean bulletin and the core phases provide additional information in different regions and depths. Therefore, to get a better impression of the new models (P06 and P06_3Dloc), they are compared in the following to the earlier model BSE of Bijwaard *et al.* (1998). BSE was obtained with the much smaller, original EHB data set of 1998 employing 7.5 million delay times and using ak135 as reference model. Also, the model parameterization used here is more detailed than the irregular cell grid used for BSE.

In Figure 6.5, all three tomographic models are displayed at various depths with respect to ak135 which allows for model comparison independent of the starting model used for inversion. The largest differences between BSE and the new models are found in the uppermost and lowermost mantle as particularly the number of regional travel times is increased and a large amount of core phases are used. Also, in the first 200 km another clearly visible difference between the tomography models is related to the reference models used. For BSE and P06 the reference model is ak135 and the results at e.g. 50 km and 185 km show large regions (north Africa, Atlantic, Siberia) where the inversion returns the reference model amplitude of 0% as a result of lack of data (ray paths). In model P06_3Dloc, these areas contain the velocity variations of the 3-D reference model CUB+S20RTS+P06$^+$ (see Fig. B.1 for the reference model). For instance, lateral heterogeneity at 50 km depth under Russia and Siberia results from crust-lithosphere structure as contained in the 3-D reference model, in particular, at this depth by the crustal model CRUST2.0 as embedded in the tomography model CUB2.0. In areas where ray paths sample mantle structure, the forward modeling procedure and subsequent inversion ensure that the resulting tomographic model is consistent with the travel time information and the 3-D background model. The current EHB data set has also been corrected for erroneous station coordinates (E.R. Engdahl, personal communication, 2001) which leads to removal of some spurious anomalies present in BSE. For example, a strong negative anomaly in crust and uppermost mantle in model BSE under the East European platform (see Fig. 6.5-50 km) proved to relate to incorrect coordinates for a station at this location, and has disappeared in P06.

At 50 km depth (below the crust in ak135), mountain ranges as the Alps, (southern) Pyrenees, Betics, Hellenides are imaged as low-velocity zones. In general, features now have finer outlines in P06 because of much more regional data and because cell sizes of the ir-

regular grid are smaller than in the BSE model which allows for imaging of more detail. The model P06_3Dloc is dominated by the reference model in regions of low ray coverage (e.g. East European platform, Africa), but is otherwise comparable in anomaly patterns to P06. However, P06_3Dloc generally shows higher amplitudes and local focusing effects (see Fig. 6.6). By construction, these higher amplitudes are partly in the null space of the travel time inverse problem and thus not inconsistent with the current data set. The local focusing effects basically result from 3-D earthquake location and 3-D ray tracing in the 3-D reference model prior to inversion.

The data picked from teleseismic experiments lead predominantly to local effects in the lithosphere below the station network. For instance, the SVEKALAPKO data enhance the outline of the thickest part of the crust (imaged by a low-velocity anomaly spot at 50 km) beneath Finland. The TOR data amplify and sharpen the change of velocities across the Tornquist zone. The Leeds data mainly increase velocities below the crust in the south of England and otherwise slightly amplify high velocities to the northeast of Scotland. Hardly any changes result from the inclusion of the EIFEL data from which can be concluded that these data are in good agreement with the EHB data for the region. The MIDSEA and ORFEUS data have a more distributed and untraceable effect on the tomographic models as the stations are distributed over a large region. Remarkable, however, is the effect at 50 km depth of a station in Lybia which provides a westward extension of the high velocities of the Tethyan margin lithosphere in the eastern Mediterranean basin. Another example can be found east of Belarus where the anomaly contrast across the Trans-European Suture Zone, separating the East European platform with its high velocities from the tectonically younger western part of Europe, is enhanced.

Since the Euro-Mediterranean bulletin contains mostly local and regional travel times, their main contribution to the tomography models is found in the crust and uppermost mantle ($<$ 250 km depth). For example, velocities below the southeast Arabian peninsula are decreased while they are increased beneath the Persian Gulf. Furthermore, various high-velocity regions below the Atlantic are amplified.

At 185 km depth, the effect of using more regional data can be noticed as the subduction of the African plate underneath Turkey close to Cyprus appears as a continuous high-velocity anomaly. Furthermore, with better ray coverage the Trans-European Suture Zone becomes a continuous structure along the western and southern borders of Poland and Ukraine. The low-velocity anomaly beneath the Arabian shield presumably caused by hot upwelling mantle material and associated volcanism (e.g. Debayle *et al.*, 2001) is now outlined better towards the east (also at shallower and deeper layers). Other noticeable improvements at 185 km depth are the enhancement of the high-velocity body beneath Finland as a result of the SVEKALAPKO data; amplification and sharpening of the change in velocities across the Tornquist zone by inclusion of the TOR data; a better outline of the western limit of the Trans-European Suture Zone due to inclusion of data from the ORFEUS archives; an increased lateral definition to the north of the Vrancea subduction system and higher amplitudes in the Vrancea slab as a result of the CALIXTO data, while the depth extent of the Vrancea slab is constrained by the combination of EHB data and CALIXTO data (Fig. 6.6). The additional information gained from the EMSC data around 185 km depth is limited. Yet, the high-velocity anomaly in the eastern Mediterranean region is slightly amplified and its boundary toward Egypt is

sharpened. Also, the high-velocity anomaly related to the stable part of the Arabian platform below Iraq and Kuwait is amplified. In P06_3Dloc many of these anomaly patterns are further focused, e.g. the Vrancea slab.

At 500 km depth, all models show the same pattern of high-velocity anomalies across the Mediterranean and southeastern Europe, even though details differ between models. These patterns have been associated with present lithosphere subduction and with past subduction resulting in flat-lying lithosphere slabs (Wortel and Spakman, 2000; Spakman and Wortel, 2004). Also differences between models can be observed, such as the positive anomaly below the Arabian plate which is hardly noticeable in BSE and P06 but appears in model P06_3Dloc. From 660 km depth downwards, minimum cell sizes are restricted to $1.0° \times 1.0°$ and below 1100 km depth to $1.5° \times 1.5°$ as the surface area of the cells becomes smaller with increasing depth. Main differences at 1175 km, occur beneath northeastern Africa and the southern half of the Iberian peninsula where the mantle is imaged now by low velocities in the new models. Furthermore, anomaly patterns under the Atlantic Ocean and positive anomalies associated with the Tethys subduction (Hafkenscheid *et al.*, 2006) are more enhanced and focused.

The core phases were added to better constrain the lower mantle. Among other studies which used core phases are those by Obayashi and Fukao (1997), Boschi and Dziewonski (2000), Kárason and van der Hilst (2001) and Lei and Zhao (2006) which indeed have shown that incorporation of core phases improves resolution in the lower mantle. As main contribution in this study, they improve the amplitudes and definition of anomalies in the lower mantle from 1900 km downwards while below Central Europe they lead to the imaging of new structure in the deepest mantle. At 1900 km, structures in P06 and P06_3Dloc are more focused compared to BSE while as an important difference we note the positive anomaly under the central Mediterranean (Italy and surroundings) and the low wavespeed anomaly to the southeast of it. The core phases also contribute to the low-velocity heterogeneity beneath western Europe and northwestern Africa.

In the lowermost mantle, around 2650 km depth, the additional information due to the core phases fills in a blank spot in the BSE model from beneath Sweden, across central-eastern Europe, to Greece. Indicative of a lack of data for the BSE model in the deepest mantle is also the fact, that the southern half of the displayed area is parameterized by much larger cells in that model. Also under the north Atlantic the pattern of positive anomalies has radically changed compared to BSE. P06 and P06_3Dloc also differ substantially with regard to positive and negative velocity patterns below Europe. The strong positive anomalies imaged under central and southeastern Europe, and flanked to the north by an east-west striking strong low-velocity zone are only partly present in the reference model CUB+S20RTS+P06[+]. These largely new anomalies can only result from a redistribution of ray paths and travel time signal (through 3-D ray tracing and event location prior to inversion) in the deepest mantle as a result of using a different reference model.

Agreements and differences between BSE and the new models, and between the two new models, can also be observed in many vertical cross-sections of which some are discussed in the following. Figure 6.6a shows a vertical low-velocity zone beneath Central Europe which has been interpreted by Goes *et al.* (1999) as a lower mantle upwelling and as the source for volcanism in that region (e.g. Eifel, Massif Central, Bohemian Massif). This hot upwelling
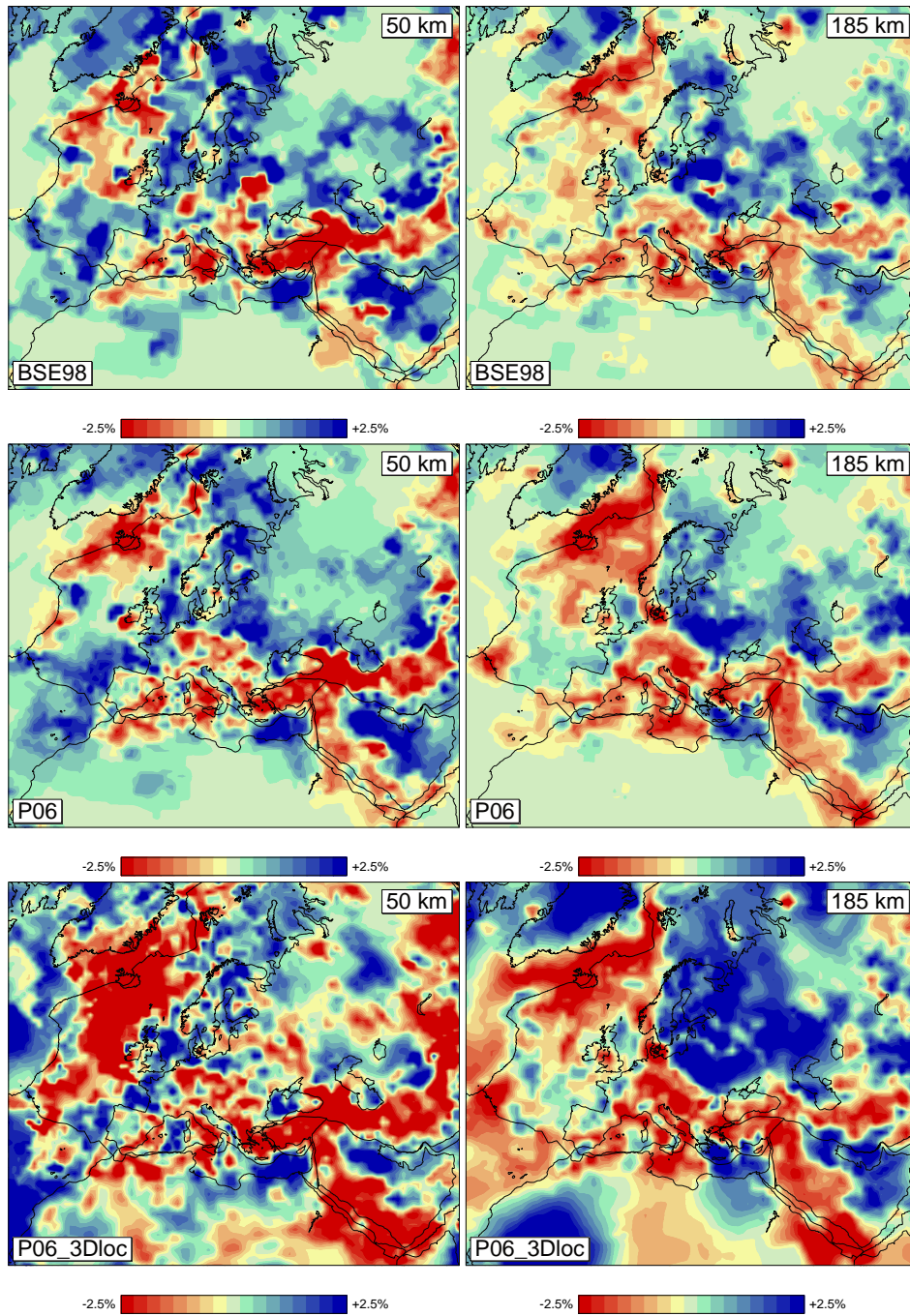
Figure 6.5: The new tomography models P06 (middle) and P06_3Dloc (bottom) with all the additional data incorporated compared to the BSE model by Bijwaard et al. (1998) (top) at 50 km and 185 km depth. All velocity variations are displayed with respect to ak135.
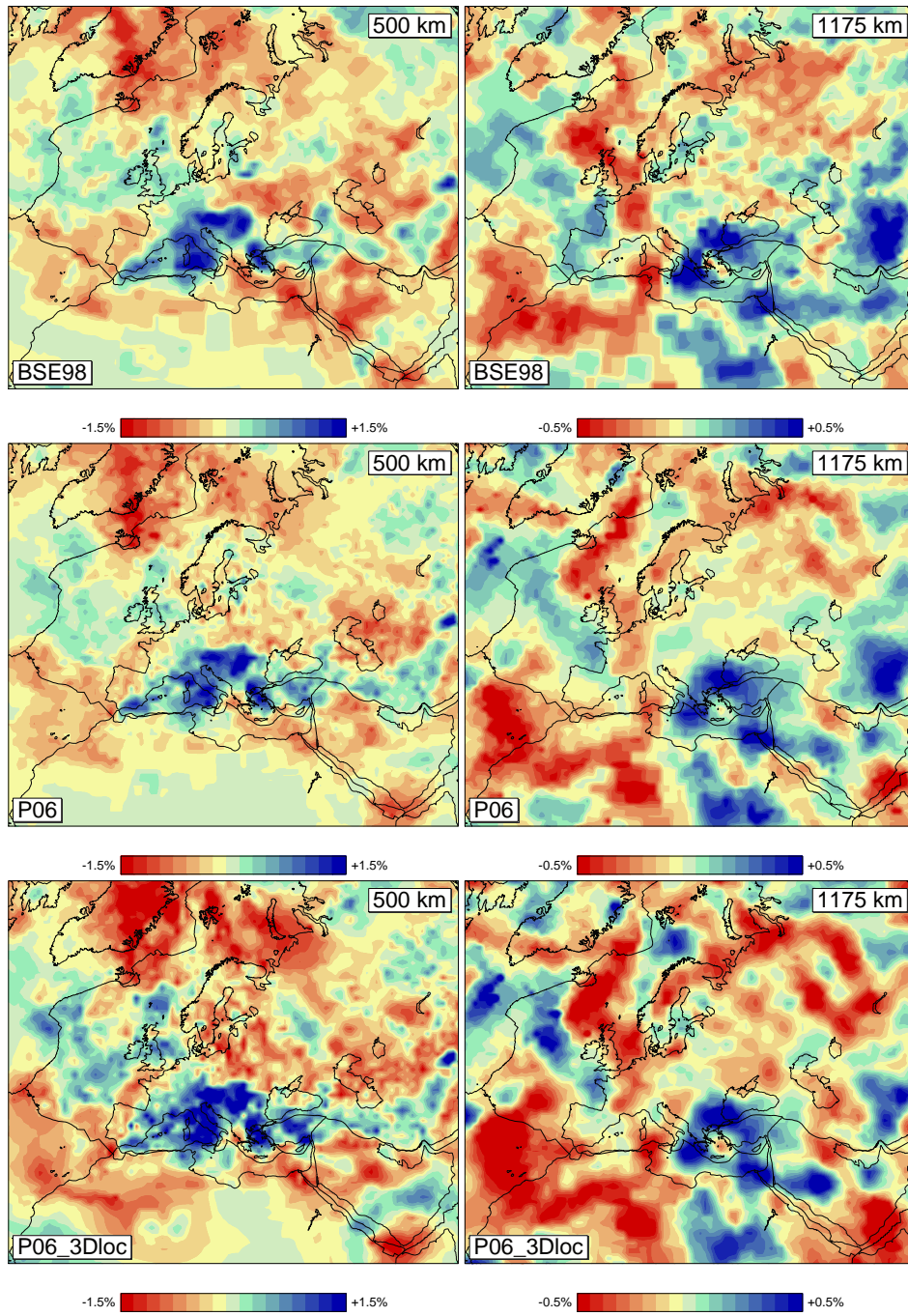
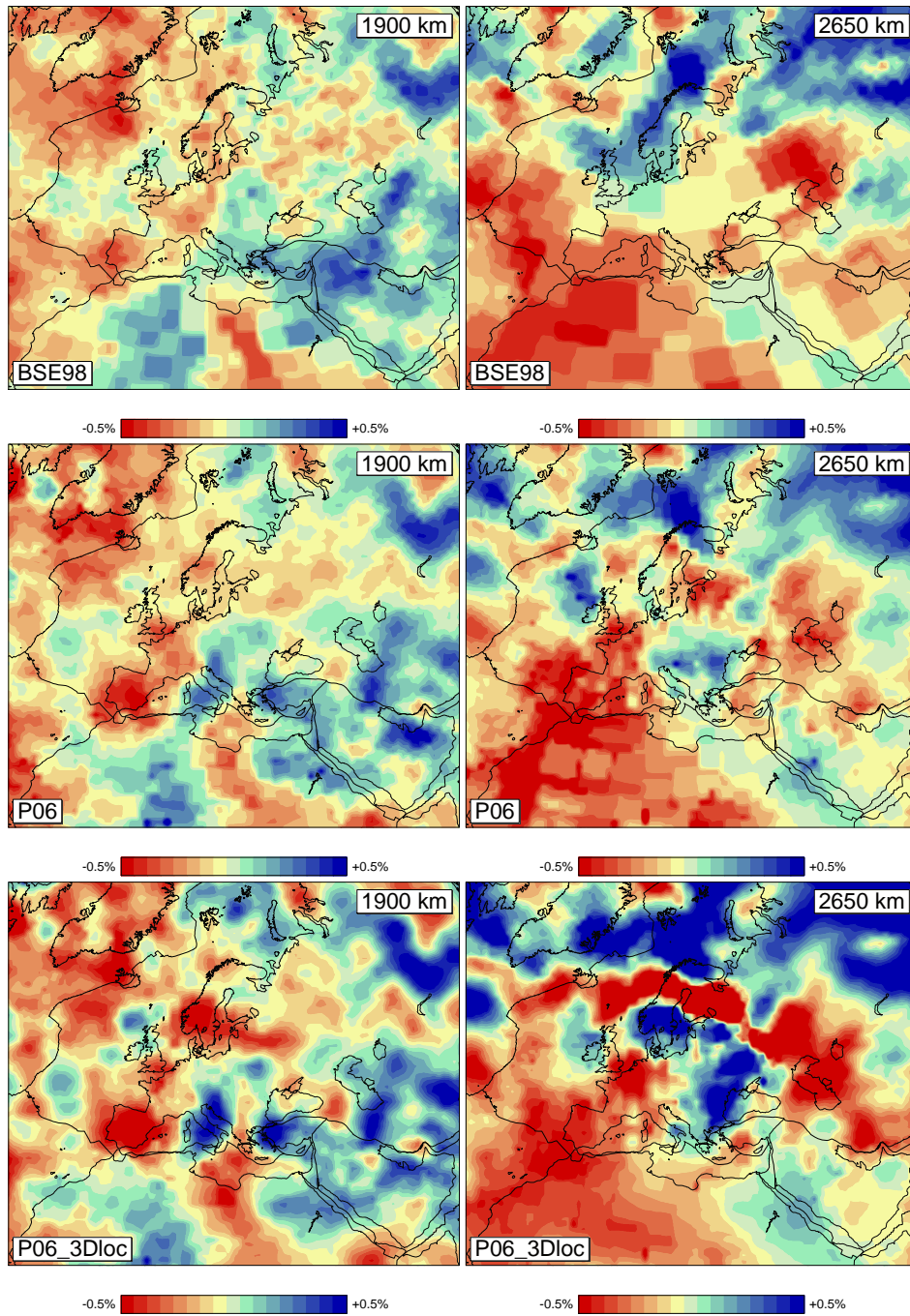**Figure 6.5:** (continued) The same models as before at 500 km and 1175 km depth.

Figure 6.5: (continued) The same models as before at 1900 km and 2650 km depth.

can now be imaged in greater detail and it becomes more evident (P06, P06_3Dloc) that this upwelling originates at the base of the mantle. Furthermore the connection between lower and upper mantle anomaly is enhanced (at 300–400 km and 18° geographical distance in the cross-section).

Cross-section (b) displays the high-velocity anomaly of the Fennoscandian shield in the upper mantle beneath Finland overlying a low-velocity mantle. The lithosphere-asthenosphere boundary is now found at approximately 300–350 km depth due to incorporation of the SVEKALAPKO data in particular, but also due to EMSC travel times and the addition regional travel times in the latest EHB catalog.

A "TOR" cross-section through the models is displayed in panel (c). While the image using the TOR data alone (Fig. 6.2c) is comparable to other studies which exclusively use TOR data (high velocities below the Elbe lineament, low velocities north of it and high velocities below the Fennoscandian shield), the addition of the EHB data, which contain many more regional phases, changes the model below the Elbe lineament (at approximately 2.5 ° horizontal distance in the figure). As main difference, the crust and uppermost mantle below northern Germany down to 110 km depth are imaged by a high-velocity anomaly. This anomaly coincides with a region identified as containing Avalonian basement (e.g. Shomali *et al.*, 2006) while south of it the Rheic Suture and Gondwanan basement follow. Below this anomaly, down to 310 km depth, a uniform low-velocity anomaly is observed limited to the north by the Tornquist zone while before (BSE) this negative anomaly was only weakly obtained below the Elbe lineament probably due to a lack of data there. Furthermore, now the Tornquist zone is imaged at approximately 0.5° further to the north than before.

Cross-section (d) shows the subducted lithosphere slab beneath the Vrancea region in the southeastern bend of the Carpathians. The new models, which contain the CALIXTO data and much more regional data from the EHB catalog, are consistent with BSE for this region and confirm the 3-D structure on which basis the interpretation was made that the Vrancea slab displays the final stage of subduction in which slab detachment has not yet occurred while north of it the subducted slab is detached (Wortel and Spakman, 2000). The Vrancea slab anomaly only differs in detail with the images obtained from other tomographic experiments using only CALIXTO data (Weidle *et al.*, 2005; Martin *et al.*, 2006).

Cross-section (e) shows a north-south section of the models across the Alps. As could be observed in the horizontal cross-sections (Fig. 6.5), the low-velocity anomaly in the crust and uppermost mantle follows the outlines of the Alps now very well, expressing the crustal wedge above the down-flexed European lithosphere (positive anomaly to the upper left) where the model was dominated before by high velocities. Furthermore, around 200 km depth, low-velocities are found in the new models below the European slab. All three models consistently show that the European plate dips southward under the Adriatic plate while the positive slab anomaly further south (at 6° geographical distance in Fig. 6.6e), results from southwestward subduction of the Apennine slab at an oblique angle to the section. Remarkable are the focusing effects obtained from the additional data (P06) and additional 3-D ray tracing and event location (P06_3Dloc).

Cross section (f) displays a south-north line through the eastern Mediterranean-Aegean region showing the Tethys slab which is still connected to the African plate. Owing to two additional stations in Libya and Egypt and 3-D ray tracing, the lithosphere beneath the east-

ern Mediterranean can be resolved better which results in a more continuous image of the African plate subduction.

The last two cross sections (g) and (h) display the Gibraltar slab and the Calabria slab, respectively. Focusing effects can observed in both sections. For the Gibraltar slab this concerns an improved delineation between the steeply east-dipping slab and the positive anomaly connected directly to the right which cuts the same slab more along-strike in this strongly curved subduction zone (Spakman and Wortel, 2004). Focusing effects for the Calabria slab occur predominantly in its flat lying portion which is thinner and of slightly higher amplitude (as for the flat lying anomaly in the Vrancea section (d)).

6.6   Discussion and Conclusions

We presented two new P-wave tomography models, P06 and P06_3Dloc, for the European region that were obtained from inversion of an extended EHB global data set combined with additional high-accuracy data from various European sources. The different European data sets were also inverted separately to check for informational content of the absolute travel times, we picked. Comparison with the published tomographic models derived from each data set (and inverting relative residuals) was hampered by the overall lack of depth resolution we observed as a result of using a global cell parameterization instead of a local model box as was used in the pertinent studies by others.

Overall, we found in our new models an enhanced focusing of structure with respect to the earlier BSE model while also important and sensible changes in anomaly patterns are observed such as the outline of the Trans-European Suture Zone. Furthermore, in some regions (e.g. Finland) an improved image of the lithosphere-asthenosphere boundary was obtained. New stations in regions with very low ray coverage (e.g. Lybia) prove to have a substantial impact on imaged structure while in some well sampled regions the additional European mostly only amplify anomalies observed earlier or confirm earlier findings (e.g. Vrancea zone, Eifel plume). In the lowermost mantle, due to the addition of cores phases, a redistribution of anomaly patterns is observed with respect to BSE while also a previously unsampled region below Central Europe could be imaged. Owing to the extended EHB data set, resolution improves greatly in the lowermost mantle of the European region which among other things provides new support for a deep mantle root for the central European upwelling.

A comparison between the two new tomographic models also demonstrates the positive effects of changing reference models for tomography. Particularly, P06_3Dloc resulted from inversions relative to a 3-D background model in which, prior to tomographic inversion, earthquakes were relocated and ray path geometry was determined by 3-D ray tracing to obtain consistency between the 3-D reference model, delay times, earthquake locations and origin time, and 3-D ray paths. As the same data set was used for inversion, differences between P06 and P06_3Dloc must be attributed to the non-linearity of the global tomographic inverse problem of travel times which has so far been neglected in most studies. Apart from many focusing effects and redistribution of anomaly patterns, also new structure could be imaged as a result of changing the reference model. We did not yet focus on the detailed accuracy of all these images which requires more work and analysis than only a few sensitivity tests.
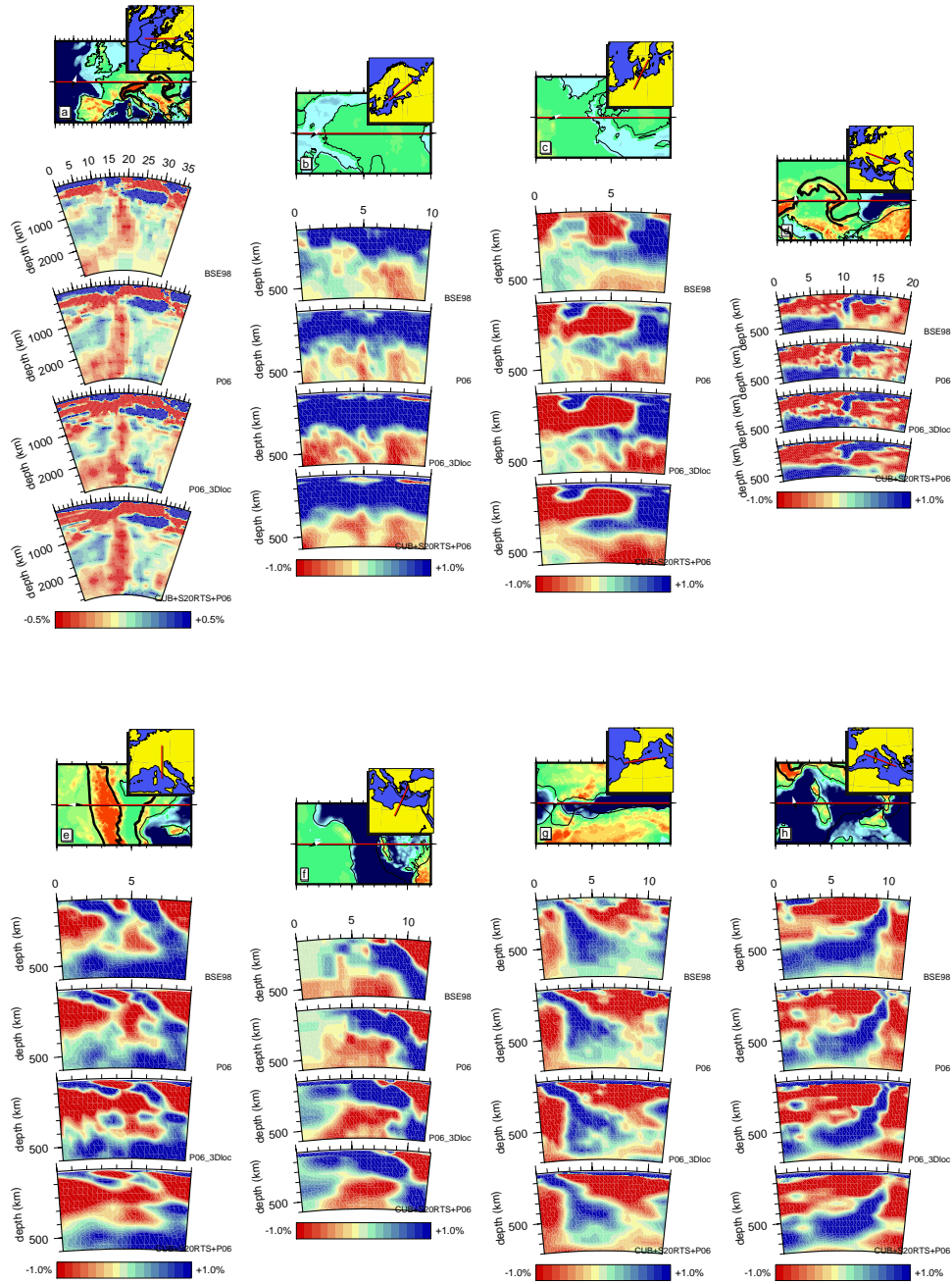
Figure 6.6: Vertical cross-sections through the BSE model and the new models P06 and P06_3Dloc beneath Central Europe (a), Finland (b), the TOR array (c), Romania (d), the Alps (e), the Hellenic arc (f), Gibraltar (g) and the Tyrrhenian basin (h). All velocity variations are displayed with respect to ak135.

In all, we conclude that the two new models provide enhanced images of European mantle structure which may prove useful for further geodynamic interpretation, for more accurate earthquake location and as a reference or starting point for forward and inverse model calculations in seismology and mantle dynamics.

6.7 Acknowledgments

Chapter 7

Travel time tomography of western North America with a new arrival time data set

7.1 Introduction

The west coast of North America has been, and still continues to be, a site of complex deformation due to its location near a major plate boundary. In Mesozoic and Cenozoic times, the Farallon plate (an oceanic plate west of the North American plate) was subducted eastward under the North American plate. In the Cenozoic (29 Ma ago), subduction of the Farallon plate beneath southern California was completed while subduction of the remaining northern part, called Juan de Fuca and Gorda plate (see Fig. 7.1), continued. With cessation of subduction in the south a transform fault between the northwestward moving Pacific plate and the westward moving North American plate was created (plate motions relative to Africa) and the Mendocino Triple Junction between Pacific, Juan de Fuca and North American plate formed. This triple junction started moving northward 25 Ma ago and was accompanied by an extinction of the arc volcanism along its way and initiation of volcanism in the northern Coast Range.

Tomography provides information which helps to reconstruct tectonic movements in that region. On a long-wavelength scale, surface wave tomography models exist, which image the upper mantle beneath the North American continent (e.g. van der Lee and Nolet, 1997; Godey *et al.*, 2003). However, in higher detail mostly local or regional models exist which do not image the entire region. For example, the subduction beneath the Cascades of Washington and Oregon was imaged by Michaelson and Weaver (1986), Rasmussen and Humphreys (1988) and Neele *et al.* (1993) and it was subject of the Cascadia 1993 experiment carried out across central Oregon to image the subduction of the Juan de Fuca plate under the North American plate. As part of this experiment, Rondenay *et al.* (2001) and Bostock *et al.* (2002) obtained a high-resolution image of the upper 120 km of the subduction zone. The Gorda slab and its

southern edge have been imaged by Benz *et al.* (1992) and Beaudoin *et al.* (1998) among other studies. The uppermost mantle beneath the southern Great Valley and the Sierra Nevada has been investigated by many authors with receiver functions, regional tomography and shear wave splitting (e.g. Benz and Zandt, 1993; Boyd *et al.*, 2004; Zandt *et al.*, 2004; Yang and Forsyth, 2006). In particular, many more crustal studies exist of northwestern America but as we focus on the mantle they will not be listed here.

In contrast to these local or regional studies, we will present here a comprehensive high-resolution tomography model of northwestern America based on new data combined with ISC (International Seismological Centre) and NEIC (National Earthquake Data Center) bulletin data.

7.2 Data

7.2.1 Newly picked data for stations in North America

For many recordings of the Advanced National Seismic Network (ANSS), the Incorporated Research Institutions for Seismology (IRIS), Canadian National Seismic Network (CNSN), Southern California Earthquake Data Center (SCEDC) and the NARS-Baja project arrival times were not determined and therefore not reported to the ISC. These recordings build the basis of the new, additional data set used here. Seismograms from these stations were obtained, pre-processed and picked by Sandoval *et al.* (2004a) with an automatic picking method to investigate the lithosphere and mantle beneath North America but so far, the data set has not been used for tomography. The data from that project were recorded from 2002–2004 and contain 120,000 P-wave picks for 486 events (event and station locations are given in Fig. 7.1).

7.2.2 EHB catalog

The main data source for travel time tomography in this study is a reprocessed and updated version of the International Seismological Centre (ISC) bulletins extended with travel times from the National Earthquake Information Center (NEIC) of the USGS for the most recent events by Engdahl *et al.* (1998). This database will be referred to hereafter as EHB catalog. It contains earthquake observations for the period 1964–2004 including over 445,000 events for 27.4 million first and later arriving phases. The processing of Engdahl *et al.* (1998) comprised a phase re-identification, theoretical travel time calculation in the Earth reference model ak135 (Kennett *et al.*, 1995) and a relocation of the events. From this data set, 19.1 mill. arrival times (P, pP, pwP, PcP, PKP and PKiKP phases) were selected for tomography.

7.3 Method

The method applied here is travel time tomography, which uses the difference between observed and predicted arrival times of P-waves to compute velocity variations within the investigated region with respect to a reference model. The theoretical arrival times are also
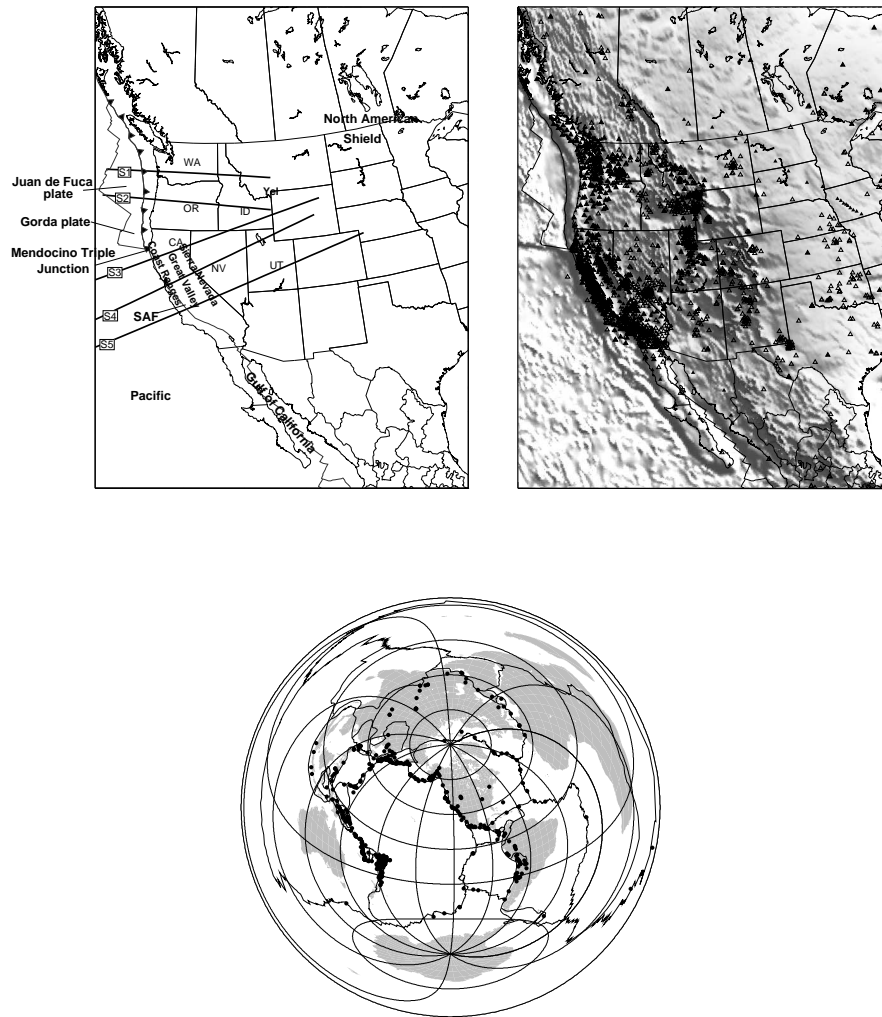
Figure 7.1: The lines S1-S5 on the top left give the location of model cross sections displayed later on (Fig. 7.4). Abbreviations: SAF – San Andreas fault, Yel – Yellowstone. In the map on the upper right, open triangles indicate the location of stations contained in the EHB catalog. Filled triangles show station locations of additional data. Illustrated in the bottom figure are the locations of the earthquakes contained in the new arrival time data set.

calculated with this reference velocity model, which is here the 1-D model ak135 by Kennett *et al.* (1995) and additionally for a later inversion a 3-D reference model. This 3-D reference model contains the global travel time tomography model obtained with respect to ak135 in regions of good ray coverage. The anomalies of the model are amplified up to a factor of 2 where allowed by the model null space as anomaly amplitudes are usually underestimated in travel time tomography in many mantle regions by 30%-50%. Otherwise, CUB2.0 (Ritzwoller *et al.*, 2002a), which is based on CRUST2.0 (Bassin *et al.*, 2000) in the crustal part, is used in the uppermost mantle and below that S20RTS (Ritsema *et al.*, 1999). For usage of the 3-D reference model, the earthquakes are relocated in that model to ensure consistency of source parameters and travel times. For more details on the use of 3-D reference models for travel time tomography see Chapter 5.

We use the method of Bijwaard *et al.* (1998) to solve the inverse problem. Even though focus is on northwestern America, a global tomography experiment is performed thereby avoiding all shortcomings of using a regionally defined model volume. Composite rays are used instead of single rays, where a composite ray is built from single rays of the same phase type which originate from the same event cluster and end at the same station. By using composite rays, the amount of data for inversion is reduced but at the same time the signal-to-noise ratio is increased. The data are weighted prior to inversion by the spread of the individual delay times within the respective ray bundle to account for the difference in ray bundle size. For the new data, this approach is not used as their quality is expected to be higher. Instead, single rays are used. The resulting data vector then contains 10.4 million residuals.

The Earth is parameterized by an irregular grid of non-overlapping cells following the approach of Spakman and Bijwaard (2001) where the cell size depends on the number of rays crossing a cell. The cell size varies in crust and mantle between $0.5°×0.5°$ and $10.0°×10.0°$ with an increasing layer thickness from the crust (10 km) to the lower mantle (200 km). The core is parameterized by a single layer for each, inner and outer core, with cells of $10°×10°$ to account for rays crossing through the core but to suppress strong model variations at the same time. Using such an irregular grid has the advantage of reducing the number of unknowns from 8 035 000 to 604 000, reducing the overparameteratization (and therefore the regularization needed during inversion) and retaining the possibility to resolve structure at small scales where allowed by the data.

The tomographic inversion itself is performed iteratively with the LSQR algorithm of Paige and Saunders (1982). A second-derivative damping is applied to regularize the solution of the inversion and to obtain a smooth model. Additionally, for inversion with 3-D reference models an amplitude damping is applied to suppress large excursions from the reference model.

7.4   Model recovery

As stations and events are not equally distributed over the investigated region, the resolution of the velocity model varies spatially. The uneven data distribution is clearly indicated in the hitcount map (Fig. 7.2) which gives the number of rays traversing a cell. For example, ray coverage at shallow depths is low beneath the Pacific due to a lack of earthquakes and stations. Also for the North American shield there is a lower ray coverage due to a low number of events and seismic stations. The new data increase ray coverage mainly along the

western part of the United States, in particular, beneath California and Washington.

As the computation of the resolution matrix is too time consuming due to the large number of parameters, tests are performed with synthetic spike models (e.g. Spakman and Nolet, 1988) of various spike sizes to estimate the resolution. These tests are performed with respect to ak135 and the synthetic models contain spikes of $\pm$ 5% amplitude which are projected onto the irregular grid. Theoretical travel times are then calculated using the ray distribution of the observed data and Gaussian noise with a standard deviation of ± 0.5 s is added to the data. Subsequently, the resulting matrix-vector equation is inverted. The result of spike tests with $0.5° \times 0.5°$, $1.0° \times 1.0°$ and $2.0° \times 2.0°$ spikes is displayed in Figure 7.2 at 50 km and 440 km depth. Spike anomalies are recovered in the western part of the United States where ray coverage is high with a minimum size of reconstructable spikes between at $0.5° \times 0.5°$ in the uppermost mantle and $3.0° \times 3.0°$ in the lower mantle (not shown).

7.5   Results

The tomography results are displayed in Figure 7.3 for inversion of the new data combined with the EHB data using ak135 as reference model (P06) and using a 3-D reference model (P06_3Dloc). To get a better impression of these models, they are compared to the model "BSE" of Bijwaard *et al.* (1998) which was obtained with a smaller data set but using the same method as here and applying ak135 as reference model. Consequently, P06 bears many similarities with BSE. Even though different reference models are used in the inversions, all models are displayed with respect to ak135 for comparison.

At 50 km depth, in model P06 the North American shield is imaged by high velocities. Beneath most of California except for the southernmost part, the San Andreas fault is resolved as boundary between the high velocities of the Pacific plate and the low velocities of the North American plate. The new data sharpen the velocity contrast between the Pacific and North American plate south of San Francisco. Furthermore, a comparison with the BSE model shows that the model is better resolved now with smaller grid cells beneath the North American shield as the latest EHB data set contains significantly more regional data. Differences in the tomography model using a 3-D reference model (P06_3Dloc) compared to P06 appear, in particular, where the ray coverage with short period P-waves is low and therefore mainly the 3-D reference model is re-obtained as beneath the Pacific or parts of the craton where low instead of high velocities are imaged as this region, at 50 km depth, is partly considered as crust in the reference model. Otherwise, anomaly amplitudes are mainly strengthened compared to P06.

At 185 km depth, the additional information of the new data is already reduced being still highest along the coastline. As main features in P06, a high-velocity anomaly parallel to the coastline could be imaged and low velocities beneath Yellowstone. The new data enhance the northern part of the high-velocity anomaly beneath Washington while in the south, the amplitudes of these anomalies are left unchanged but compared to the BSE model in the central part the velocities are decreased. Also, along the Gulf of California ridge, velocities are further decreased due to the new data. In the eastern half of the cross section other differences between BSE and P06 are found resulting in a better outlined boundary of the high-velocity anomaly in P06 beneath the shield towards the west. Usage of the 3-D reference
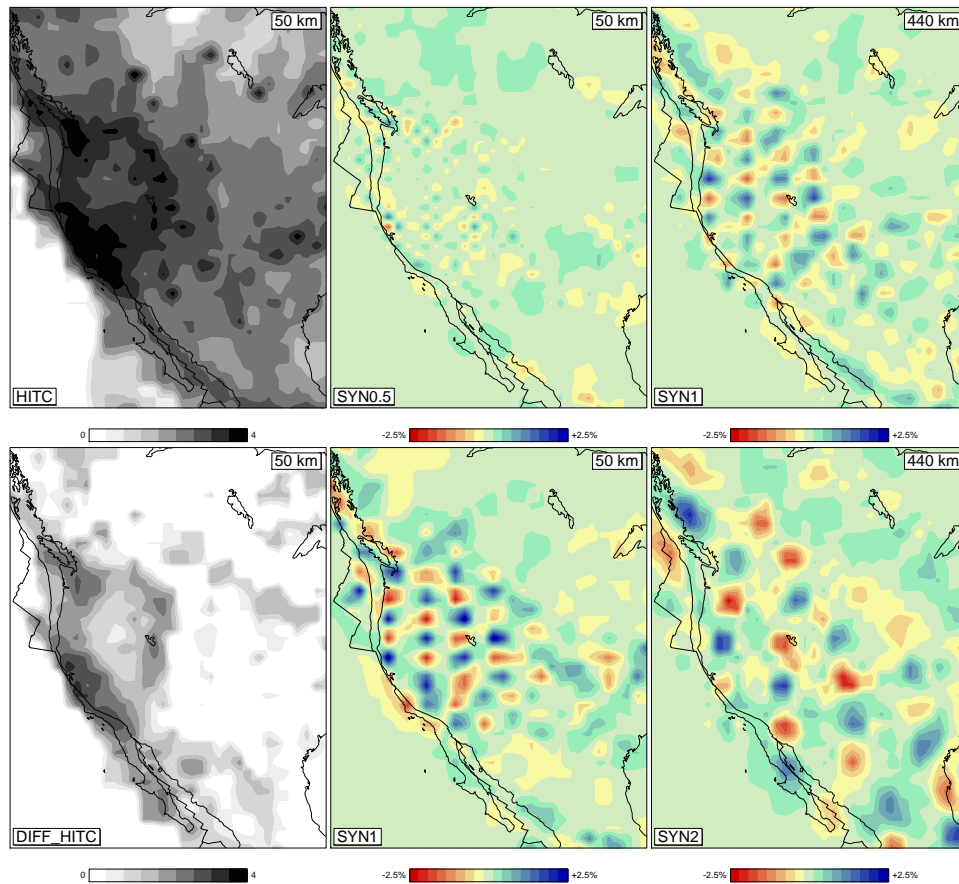
117

Figure 7.2: Displayed at 50 km depth is the hitcount of the combined data set (left, top), the addition of the new data to the hitcount (left, bottom), a $0.5° \times 0.5°$ and $1.0° \times 1.0°$ spike test using the combined data set (middle, top and bottom) and at 440 km depth a $1.0° \times 1.0°$ and $2.0° \times 2.0°$ spike test using the combined data set (right, top and bottom).

model provides again implicitly more realistic velocities beneath the Pacific and below the cratonic part of North America thereby enhancing the contrast to the tectonically active region of the North American Cordillera.

At 440 km depth in the upper mantle transition zone, P06 is dominated by low velocities beneath northwestern America but contains high velocities beneath Nevada, Utah and Idaho. Also, at this depth the signature of the North American shield has vanished and is replaced by a low-velocity anomaly. Differences with BSE are biggest in the eastern half of the section where P06 contains more data and therefore gives a more coherent image. The model using a 3-D reference/starting model is comparable to the model using a 1-D reference/starting model except for the Pacific where P06_3Dloc contains the low velocities of S20RTS.

To get a better impression of the distribution of high-velocity anomalies and their interchange with low-velocity anomalies, vertical cross sections through the models presented in Figure 7.3, are displayed in Figure 7.4. The exact location of the slices is given in Figure 7.1. Starting in the northern part of the model with a west-east trending slice (S1), the afore-mentioned high-velocity anomaly represents the subducted Juan de Fuca slab beneath North America. This slab is steep in the western part and flattens in the upper mantle transition zone. The new travel time residuals increase velocities particulary in the uppermost and lowermost section of the slab. The BSE model contains also above the 410 km discontinuity smeared out high velocities related to a lack of data.

Further south (S2), the slab is only observed with high velocities down to approximately 200 km depth with resolution being sufficient to reconstruct anomalies at this depth. The new data amplify the surrounding low velocites and compared to BSE, the high-velocity anomaly is more focussed.

Further south (S3), in P06 and P06_3Dloc the Gorda slab becomes again a more continuous feature lying flat in the top part of the transition zone. Compared to BSE the new data in combination with the latest EHB data set clearly improve the amplitudes of the slab anomaly. In the next slice further south (S4), a high-velocity anomaly cannot be found where it was seen before in the uppermost mantle while below 350 km depth it is detected. Again, the high-velocity anomaly in P06 and P06_3Dloc is more focused than in the BSE model.

Even further south (S5), this anomaly in the transition zone is observed again with weaker amplitudes. However, in the uppermost mantle a high-velocity anomaly east of the San Andreas fault is found in all models and the new data increase the velocities of that anomaly. Due to the different reference model, the connection of the high-velocity drip disappears in the model using a 3-D reference (P06_3Dloc).

7.6   Discussion and Conclusions

The new data clearly improve the tomographic model in the uppermost mantle and in regions that were sparsely sampled in previous global tomography studies (e.g. Bijwaard *et al.*, 1998). A subducted slab can be detected in the uppermost mantle from British Columbia to approximately 170 km south of the Mendocino triple junction and vanishing/weakening below $\sim$ 200 km depth beneath Oregon close to the boundary between Juan de Fuca and Gorda plate.

Earliest indicators of a high-velocity slab beneath southwestern Canada and the northwestern
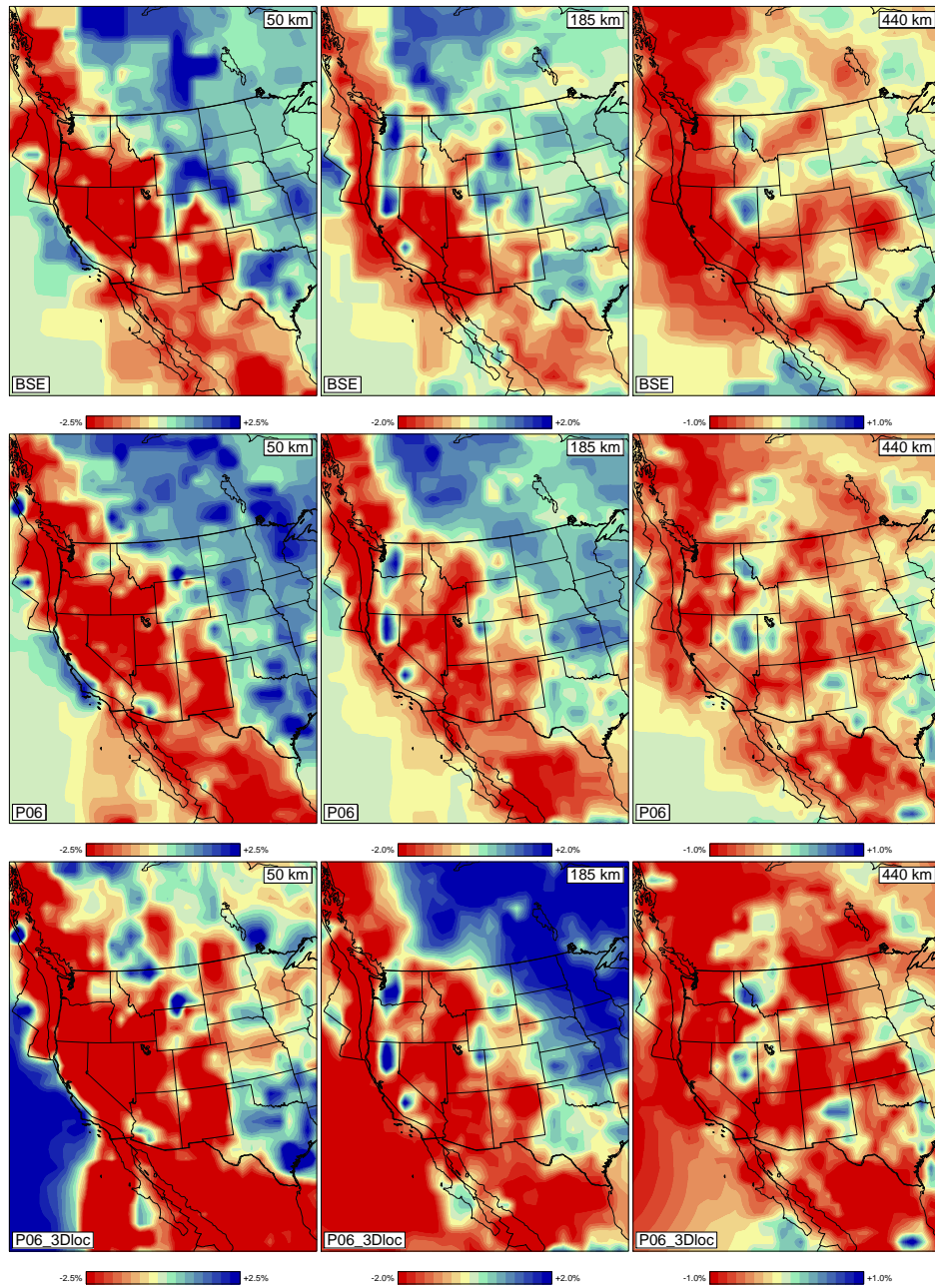
Figure 7.3: The BSE model of Bijwaard *et al.* (1998) (top row), the model using the newly picked data and EHB data with a 1-D reference model (middle row) and the model using the new data and EHB data with a 3-D reference model (bottom row) at 50 km (left), 185 km (middle) and 440 km depth (right). All velocity perturbations are displayed with respect to ak135 independent of the starting model used for tomographic inversion.
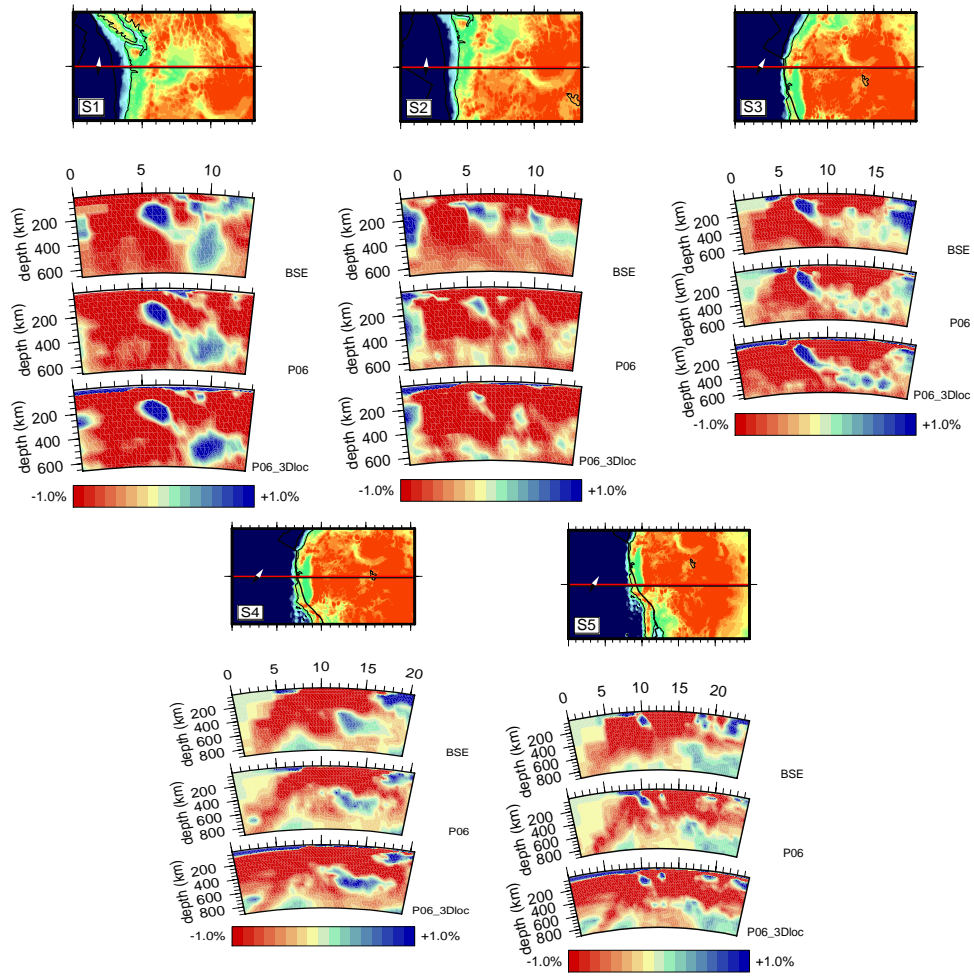
120

Figure 7.4: Vertical cross sections through the models as displayed in Fig. 7.3. The location of the cross sections is displayed in Fig.7.1. The velocity perturbations are given with respect to ak135 .

United States were observations of P travel times (McKenzie and Julian, 1971). The part of the slab beneath Oregon and Washington was also detected in an inversion of teleseismic P travel times by Michaelson and Weaver (1986), Rasmussen and Humphreys (1988) and Van-Decar (1991). The model of Rasmussen and Humphreys (1988) extends furthest south with a similar depth extent of the high-velocity to our model to at least 400 km in the northern part of their model (corresponding to S1) and 200 km in the southern part (corresponding to S2). However, our model continues further to the east and we are therefore able to image the flattening of the slab below 400 km depth.

The part of the Gorda slab (S3) beneath California was imaged earlier by Benz *et al.* (1992) with teleseismic P tomography. Its southern edge of the Gorda plate has been imaged by Beaudoin *et al.* (1998) with a seismic refraction-reflection profile being located at approximately $40°N$ beneath California, which is in good agreement with our model where the slab at 200 km depth extends to approximately $39°N$.

The low-velocity region at the southern end of the Gorda slab (S4) and the adjacent high-velocity anomaly beneath Central California (S5) have been subject of debate for many years. Ten Brink *et al.* (1999) suggest that the low-velocity anomaly (S4) represents a region of stretched slab material where thermal re-equilibration causes the observed low-velocity anomaly. As another possibility, Furlong *et al.* (1989), Benz *et al.* (1992) and Benz and Zandt (1993) interpret the low-velocity region as a slab window in which asthenospheric material is upwelling. According to our model, the low-velocity anomaly beneath Central California is caused by hot upwelling asthenosphere material that moved in after subduction ended and the slab sank into the mantle since remnants of this slab are still observable further to the east from 350 km depth onwards. Benz and Zandt (1993) suggest that the high-velocity anomaly at the southern end of the slab window below the southern Great Valley (S5) is caused by a fragment of the Farallon plate being left there after subduction ended. Zandt and Carrigan (1993) also interpret the slab window as a region where upwelling asthenosphere replaced the remnants of the Farallon slab after cessation of subduction in southern California. However, they interpret the high-velocity anomaly south of the slab window as a body dripping off the base of the lithosphere due to a small-scale convective instability. This theory was later on supported by a time-dependent simulation of the thermal evolution of the asthenosphere (Liu and Zandt, 1996) and Ruppert *et al.* (1998) and Saleeby *et al.* (2003) proposed the southern Sierra Nevada batholitic root as origin of the detached lithosphere. Also Zandt *et al.* (2004) come to the conclusion that this high-velocity anomaly represents either the root of the southern Sierra Nevada or a downwelling induced by foundering of the root. A recent seismic tomography study of the lithosphere beneath the southern Sierra Nevada with P and S wave travel times (Boyd *et al.*, 2004) confirms the existence of the high-velocity drip but dipping eastward beneath the southern Sierra Nevada. Boyd *et al.* (2004) conclude from analyses regarding composition and temperature that the anomaly represents stratified mantle lithosphere delaminated from the crust beneath the southern Sierra Nevada.

Our model does not allow for inferences on compositional and thermal aspects of the anomaly but unlike previous regional tomography studies, we are able to give a depth limit for the high-velocity anomaly confining it to a depth < 250 km. The obtained model agrees well with other studies that prefer removal of the Sierra Nevada root as cause of the high-velocity anomaly (instead of a Farallon slab fragment) and we observe the remnants of the Farallon

slab above the 660 km discontinuity further east of the high-velocity anomaly. Therefore, the most plausible explanation for the eastward dipping high-velocity anomaly below the southern Great Valley and Sierra Nevada is a drip of lithospheric root from the southern Sierra Nevada.

In summary, we have been able to image the P velocity structure beneath entire northwestern America in high detail with global travel time tomography. Newly picked arrival times have, in particular, improved the model in the uppermost mantle in region where ray density was low before thereby enhancing, for example, the outlines of subducted slabs.

7.7 Acknowledgments

Chapter 8

Relocation of a global earthquake data set with a 3-D velocity model

We have relocated a global earthquake data set of 450,000 events contained in the International Seismological Centre (ISC), National Earthquake Information Center (NEIC), Europe-Mediterranean Seismological Centre (EMSC) and regional network data bases. The initial earthquake locations were obtained using a standard 1-D Earth reference model while the earthquake relocations presented in this study were performed in a highly detailed 3-D velocity model based on travel time tomography using a directed grid search technique. Tests with well-located events show an improvement of the earthquake location errors using the 3-D model with respect to a 1-D Earth reference model. Furthermore, systematic source parameter shifts of the events in the global earthquake data set can be observed with respect to their initial location which are caused by 3-D Earth structure now accounted for in the earthquake location process.

8.1   Introduction

Accurate earthquake locations are important not only for seismo-tectonic and seismic hazard assessment but also for the Comprehensive Nuclear Test-Ban Treaty (CTBT) or for tomography studies investigating the velocity structure of the Earth's crust and mantle. The accuracy of event locations depends on many factors among which are the number of phases used for computation of the location, proper phase identification, the velocity model used for computation of reference travel times and the location method itself. Besides the ISC and NEIC, which provide global data sets of earthquake locations, the updated EHB catalog of Engdahl *et al.* (1998) provides a groomed version of the ISC and NEIC bulletins from 1964 to 2004 including improvements compared to other global catalogs. The earthquake locations in the EHB catalog were obtained using a 1-D Earth reference model adding regionally averaged travel time corrections for upper mantle structure. Furthermore, phase identification of depth phases in this catalog was improved using probability density functions of later-arriving phases. The 3-D velocity heterogeneities in the source regions and along the ray paths of the

observed phases are not routinely taken into account in any of the earthquake locations provided by the mentioned global catalogs as it is computationally expensive and requires a good 3-D velocity model of the Earth's interior.

In this study, a highly detailed 3-D model obtained from travel time tomography will be used in a directed grid search to find more accurate earthquake locations for a global earthquake data set.

8.2 The earthquake data set

8.2.1 EHB catalog

The main data source is the reprocessed and updated earthquake catalog of Engdahl *et al.* (1998) which is based on the ISC bulletins and extended with data from the NEIC of the U.S. Geological Survery for the most recent events. This database will be referred to hereafter as EHB catalog. It contains earthquake observations for the period 1964–2004 including over 445,000 events with 27.4 million first and later arriving phases. The processing of Engdahl *et al.* (1998) comprised a phase re-identification, theoretical travel time calculation in the Earth reference model ak135 (Kennett *et al.*, 1995) and a source relocation taking into account regionally averaged travel time corrections for teleseismic phases.

8.2.2 Euro-Mediterranean bulletin

The Euro-Mediterranean bulletin of the EMSC provides the second data set used here. This bulletin contains a collection of travel time observations from local networks in the Euro-Mediterranean region (Godey *et al.*, 2006). Well-constrained earthquakes in this catalog were relocated by the EMSC. However, if existent, the corresponding EHB location is used here instead of the EMSC locations. Otherwise, the events are relocated in ak135 including regional patch corrections for consistency with the EHB catalog using the relocation method described in Section 8.3. The resulting EMSC subset then consists of over 96,000 additional first-arriving P and S phases from 9,700 events for the period 1998–2003 for which EHB locations could be found and 138,000 P and S arrival times for 6,400 events for which an EMSC location exists. Depth phases (pP, sP, pwP) were not used to avoid problems with phase misidentifications.

8.2.3 Newly picked data for stations in North America

Sandoval *et al.* (2004a) obtained waveform registrations from the Advanced National Seismic Network (ANSS), the Incorporated Research Institutions for Seismology (IRIS), Canadian National Seismic Network (CNSN), Southern California Earthquake Data Center (SCEDC) and the NARS-Baja project (Trampert *et al.*, 2003). For 486 events registered between 2002 and 2004, for which an EHB location existed, 120,000 P arrival times were picked by Sandoval *et al.* (2004a) with an automatic picking method. For most of these stations, arrival times were not determined before.

8.2.4 Newly picked data for stations in Europe

Additionally, temporary experiments with spatially dense station arrays in Europe, the OR-FEUS (Observatories and Research Facilities for European Seismology) archives and a collection of registrations for the UK, Ireland and part of northwestern France provided to us by Arrowsmith (2003), form another source of data. The temporary experiment data comprise the SVEKALAPKO experiment in Finland (Bock et al., 2001), the TOR experiment in South Sweden, Denmark and North Germany (Gregersen *et al.*, 2002)), the EIFEL experiment in the Eifel (Ritter *et al.*, 2000), the CALIXTO experiment in Romania (Wenzel *et al.*, 1998) and the MIDSEA project with a number of stations surrounding the Mediterranean Sea (van der Lee *et al.*, 2001). The data from these stations were obtained as waveforms and arrival times were determined with the method of Sandoval *et al.* (2004a) resulting in a total of 86,600 P and S arrival times for 3100 events, for which an EHB location could be found.

8.3 Relocation method

From the EHB catalog, only events are relocated which are also relocated by Engdahl *et al.* (1998) and earthquakes which had a fixed EHB hypocenter depth are kept at fixed depth. Furthermore, we use only those P, S, pP, pwP, sP, PKPdf and PKiKP phases from the EHB data set, which were also used by Engdahl *et al.* (1998) for relocation and the additional phases from the other data sets for according EHB events. The additional EMSC events without corresponding EHB location are relocated using P and S phases. For all additional data, regional phases with absolute travel time residuals > 7.5 s and teleseismic phases with an absolute travel time residual > 3.5 s are not used. Also epicentral distances for P phases are limited to $< 100°$ and for S to $< 80°$.

The earthquake relocation is based on the method of Sambridge and Kennett (1986) which was implemented in an iterative grid search scheme. The hypocenter locations as given in the EHB catalog are used as initial locations around which a grid is set up of $0.2° \times 0.2° \times 20$ km with a node spacing of $0.02°$ and 2 km respectively. Theoretical travel times are computed for each node and observed phase arrival using ak135. Subsequently, theoretical travel times are computed in the 3-D reference velocity model for the corners of the grid with the 3-D ray tracing method of Bijwaard and Spakman (1999a) based on ray perturbation theory. The difference between the travel times using a 3-D and 1-D velocity model is determined at each corner and interpolated onto the other nodes of the grid. By adding the previously computed ak135 travel time to the difference afterwards, 3-D travel times are obtained at each grid node. The interpolation is performed to reduce computation time as 3-D ray tracing for each node and each observed arrival time would significantly increase the task. As criterion for the grid search, a misfit function is minimized, which is here the sum of the squared weighted arrival time residuals (observed arrival time - theoretical arrival time - corrections for ellipticity, station elevation, bounce point topography and water depth for depth phases) at each node. The weights differ by phase type as given in Table 8.1. First, within a time interval of ± 20 s around the origin time, the origin time that produces a minimum misfit is searched. The arrival times are then corrected for the new origin time and the spatial minimum of the misfit function is determined. If the minimum is located near the edge of the grid, the grid

phase type	weight^{-1}
P	0.3
S	1.5
pP, pwP, sP	1.0
PKPdf, PKiKP	1.0

Table 8.1: Weights applied for minimization of the misfit function.

is shifted with the new location as center and the thus found source parameters are used for the following iteration, otherwise the grid is refined to half the node spacing. The relocation procedure is repeated until the node spacing is reduced to $0.005°$ or when the maximum number of iterations (=6) is reached. On average a final location is found after 3 iterations and only 5% of the events require 6 relocation steps.

The relocations are accepted if the root-mean-square misfit of the residuals is less than the ak135 misfit + 0.5 s and if the epicenter shift is less than 50 km and the depth shift is less than 40 km for free-depth solutions.

8.4 Model

Relocation is performed with a 3-D velocity model obtained from global travel time tomography (named "P06_3Dloc" hereafter). The model was obtained in several processing steps: First, a travel time tomography was performed with travel time residuals from the EHB catalog, EMSC bulletins (Godey *et al.*, 2006) and seismic networks and experiments in North America (Sandoval *et al.*, 2004a) and Europe (Chapter 4) using ak135 as reference model. This model (named "P06") contains many features in the Earth's crust and mantle (e.g. subducting slabs, hot upwellings) in regions of good ray coverage.

Second, the amplitudes of this model were enhanced by doubling the anomaly amplitudes of P06. But in order not to affect the data misfit, only the part of the amplified model was used which lies in the null space. This null space model part was found by applying the null space shuttle of Deal and Nolet (1996). As the resulting model (named "P06$^+$") is a P velocity model, S velocity perturbations were derived using the depth-dependent $d \ln v_s / d \ln v_p$ values of Bolton and Masters (2001) which range from 1.345 in the upper mantle to 3.45 in the lowermost mantle.

Third, the model P06$^+$ was combined with the CUB2.0 model (Ritzwoller *et al.*, 2002b) in the uppermost mantle and the model S20RTS (Ritsema *et al.*, 1999) below that. The CUB2.0 model is based on broadband surface wave group and phase velocity measurements and uses a global crustal model (CRUST2.0, Bassin *et al.*, 2000) in the background. We used the P and S velocities as they are provided in this model. Between 200 and 300 km depth, the model S20RTS was smoothly blent in using a depth-weighted average of both models. S20RTS is based on Rayleigh wave phase velocity measurements, shear wave travel times and normal mode splitting measurements. Since it is a shear velocity model, it was converted to P velocities using the afore mentioned depth-dependent $d \ln v_s / d \ln v_p$ values of Bolton and Masters (2001). P06$^+$ is then combined with CUB+S20RTS applying a hitcount-dependent criterion

128

where hitcount is the number of rays crossing a model grid-cell. For cells with a hitcount bigger than 500/1000/2000 in the upper/mid/lower mantle P06[+] was used. A smooth transition from P06[+] to CUB+S20RTS was achieved by using a weighted hitcount-dependent average of both models in an intermediate hitcount range. For cells with a hitcount lower than 100/200/400 in the upper/mid/lower mantle CUB+S20RTS was used. The advantage of this approach is, that in regions of good ray coverage ray bending due to 3-D heterogeneities is accounted for according to P06[+] and otherwise according to CUB2.0 or S20RTS respectively which can be assumed to be more realistic models than a 1-D reference model.

Fourth, a final tomography inversion was performed using the extended global data set and CUB+S20RTS+P06[+] as reference model. Processing before inversion included a relocation of the earthquakes in the new reference model (similar to the relocation process presented here) to establish consistency between arrival time residuals and source parameters. The resulting model P06_3Dloc combines the long-wavelength structure as "seen" by long period seismic information with the detailed crust and mantle structure obtained from short period travel time data. The conversion to S-velocity anomalies was again performed using the $d \ln v_s / d \ln v_p$ values of Bolton and Masters (2001).

8.5 Location of ground truth events

To find improvements of relocation with the 3-D velocity model, tests with ground truth events are performed. These events are earthquakes and explosions whose source parameters are known exactly. Here, additionally events are considered with a location error up to 5 km. For Eurasia, events are selected from the reference event database of Bondár *et al.* (2004), which were not used for computation of the tomography model. For North America, only ground truth events are available to us, which were also used for tomography. Yet, these events are selected since most of them are located in regions with many stations and events and their influence on the obtained velocity model therefore is minor. For the entire ground truth data set, only events are selected that have a teleseismic secondary azimuth $< 180°$ (i.e. the largest azimuthal region centered around the event containing only one station) and which contain more than 10 teleseismic first arrivals.

8.5.1 Arrival time prediction

Assessment of arrival time prediction with a specific velocity model can indicate its ability to improve earthquake location. Therefore, theoretical arrival times are computed for 58,700 observed P phases of 306 ground truth events (using their exact location) with both ak135 and P06_3Dloc as velocity model. The closer the travel time residuals are to 0 s, the better the velocity model predicts the arrival times. As a summary of the computations, in Figure 8.1 the mean travel time residuals with respect to the epicentral distance are displayed together with their standard deviations. At distances up to approximately $69°$ the 3-D velocity model predicts the travel times better while between $69°$ and $76°$ ak135 gives better results and at greater distances the results are comparable for both models.
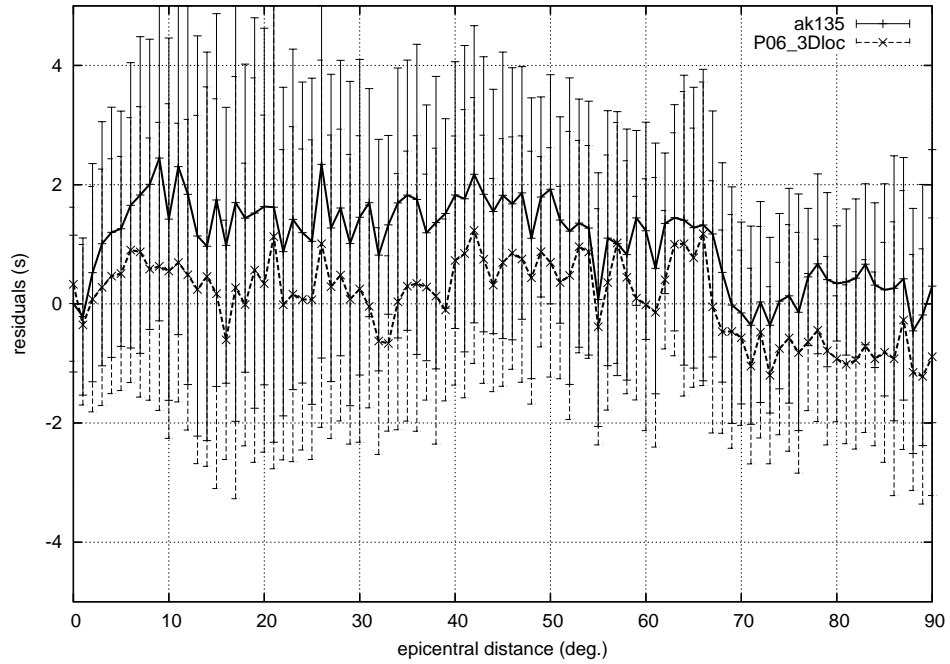
Figure 8.1: Mean travel time residuals and standard deviations computed with ak135 (solid line) and the 3-D velocity model (dashed line) with respect to the epicentral distances for ground truth events in North America and Eurasia.

	epicenter shift (km)	depth shift (km)	origin time shift (s)
fixed depth:			
ak135	9.9 ± 6.7	–	0.7 ± 0.7
3-D	6.4 ± 4.4	–	-0.4 ± 0.6
free depth:			
ak135	9.2 ± 4.8	-7.1 ± 6.9	1.6 ± 1.1
3-D	6.5 ± 4.7	-7.9 ± 6.0	0.8 ± 1.0

Table 8.2: Summary of the mislocations errors obtained for the ground truths events.

8.5.2 Hypocenter location

Mislocation errors are assessed here by relocating the ground truth events. The events are relocated with the method described in Section 8.3 using the 3-D velocity model and, for comparison, they are relocated using ak135 including a correction of the teleseismic travel times for average regional Earth structure below the stations (corrections are applied as provided by Engdahl *et al.* (1998)). Only the best constrained events are analyzed, which involve more than 250 phases for relocation and have a depth shift smaller than 40 km and a epicenter shift smaller than 50 km. The absolute origin time shift is restricted to 3.5 s to exclude events that do not contain sufficient depth-defining phases and therefore cause large trade-offs between depth and origin time shifts.

Thus, 226 events are relocated fixing the depth to the true location and 93 events are relocated allowing the hypocenter depth to shift. For the fixed-depth solutions using the 3-D velocity model and ak135 (including patch correction) respectively, relocation vectors are displayed in Figure 8.2. The relocation vectors are smallest in North America and parts of the Mediterranean region, which suggests that the events in those regions are well-constrained by travel time observations and/or that the 3-D model provides a good representation of Earth structure in those regions. As the event locations are known with an accuracy of 0-5 km, the source parameter shifts can be considered as mislocation errors. These mislocation errors are given in Table 8.2 for fixed- and free-depth solutions using ak135 and the 3-D velocity model. The fixed-depth solutions display epicenter shifts similar to the free-depth solutions and the mislocations are bigger for ak135 than for P06_3Dloc. The depth shift of the free-depth solutions is smaller for ak135 than P06_3Dloc but only suitable ground truth events with a focal depth < 35 km were found. Therefore, the depth mislocation might not be representative for deeper events. As can be expected due to a trade-off between origin time and event depth shift, the origin time shift is smaller for the fixed-depth solutions than the free-depth solutions and in both cases the origin time error is smaller for the 3-D model than ak135.

In summary, as arrival time prediction is improved due to the 3-D velocity model, relocation with that model reduces source location errors.

8.6 Results of relocating the global hypocenter data set

The relocation of 450,000 events took 2433 CPU-hours on an SGI Altix system using 8 Itanium-2 processors. It resulted in 203,000 events with a fixed-depth solution and 247,000
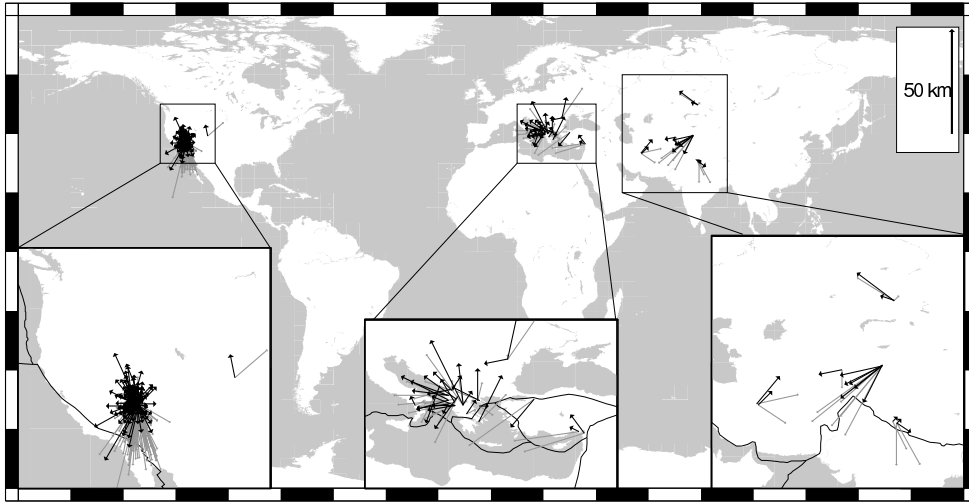
Figure 8.2: Relocation vectors of the ground truth events using the 3-D velocity model (black) and using ak135+patch correction (gray). The vector tails indicate the ground truth locations. The length of the relocation vectors is exaggerated with the length scale for the global plot as indicated.

events with a free-depth solution of which 187,000 and 232,000 relocations respectively were accepted. The rest was discarded as the event parameters were not well enough constrained by arrival time observations and therefore deviated too much from the initial location (constraints given in Section 8.3).

A summary of the source parameter shifts with respect to the original parameters using ak135 as velocity model for events with more than 10 travel time residuals is given in Table 8.3 and illustrated in Figure 8.3. For most of the accepted events the epicenter shift is less than 20 km and it amounts on average to 12.8 km. Also, the epicenter shifts for both fixed-depth and free-depth events increase with depth. For most of the free-depth events the depth shift is less than 15 km with an average shift of -3.1 km. The depth shifts are largest for shallow events and decrease with depth as model anomalies are largest in the crust and decrease with depth. Furthermore, the origin time shift is centered around 0.0 s and most events show an origin time shift of less than ± 2 s. The root-mean-square values of the travel time residuals after relocation with respect to the residuals obtained with ak135 are mainly unchanged or decrease by $\lesssim 0.5$ s with an rms misfit of less than 3 s for the majority of events (see Fig. 8.4).

In Figures 8.5 and 8.6 characteristic features of the relocations are illustrated by zooming in on the region where the Pacific plate is subducted to the west underneath the Eurasian and Philippine plates (top), the eastern plate boundaries of the Cocos and Nazca plates that are subducted underneath the Caribbean and South American plate (middle) and the plate boundary between Africa and Europe in the eastern Mediterranean Sea (bottom).

For East Asia only earthquakes with an EHB hypocenter depth $>$ 70 km are displayed to allow for better visualization. Along the western Pacific plate boundary, mainly negative ori-
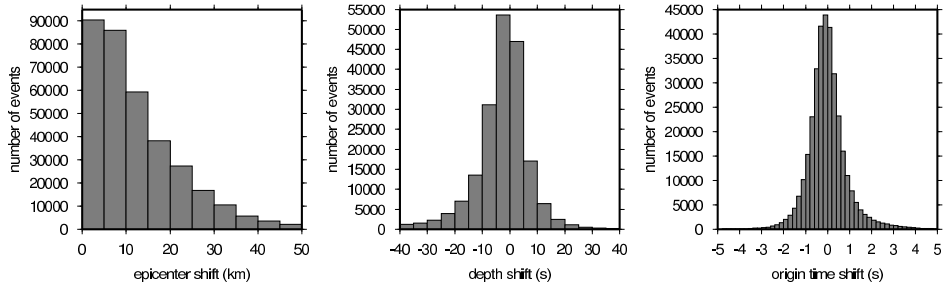
Figure 8.3: A histogram of the epicenter shifts with respect to the original ak135 locations (including patch corrections) for fixed- and free-depth events (left), a histogram of the depth shift for free-depth events (middle) and a histogram of the origin time shift for fixed- and free-depth events (right).
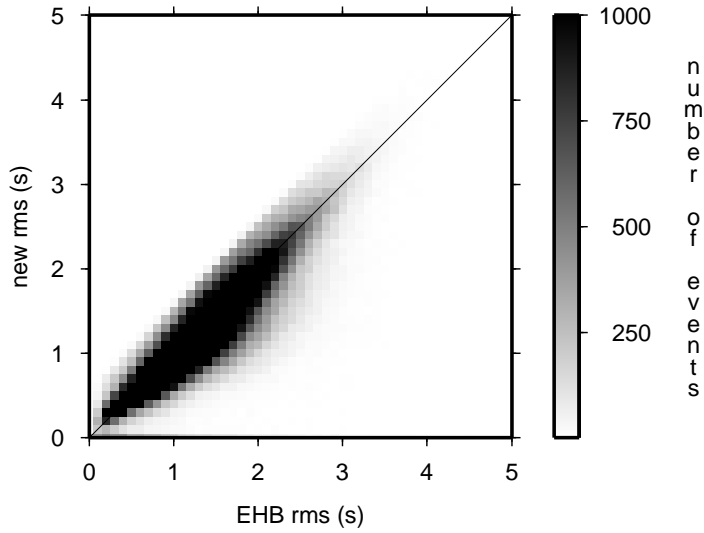

Figure 8.4: Density plot of the root-mean-square data misfit before (ak135 residuals) and after (3-D residuals) relocation.

133

gin time shifts can be observed. They compensate for remaining data misfit not accounted for by computation of travel time residuals with the 3-D reference model. Close to Japan and along the Mariana trench the epicenter shifts are comparatively small ($\approx$ 20 km) as the events are well-constrained and point towards the trench taking into account the existence of a high-velocity slab anomaly in the subduction zone.

Along the Andean subduction zone, origin time shifts are also mostly negative around -1 s in the southern Altiplano region decreasing significantly in the deeper parts of the subducted slab to $\pm$0 s while origin time shifts to the north are larger, between -2 s and -1 s. The epicenter shifts are on the order of 25–30 km in the Altiplano region pointing, like in the eastern Pacific subduction zones, towards the trench. North of the Altiplano plateau and at greater depth the relocation vectors are generally smaller, particularly the deep events have relocations of less than 10 km.

Along the southern part of the Middle American trench, the origin time shifts are generally negative and epicenter shifts are large moving the events northwestward in the northern part of the subduction zone while they shift the epicenters towards the trench in the southern part. In the eastern Caribbean origin time and epicenter shifts are mostly smaller relocating the earthquakes again towards the trench.

Relocation in the Aegean area shows many variations as the tectonic settings in which earthquakes occur are complex. Furthermore, most events in this region are located at shallow depth. In the Tyrrhenian basin, small negative origin time shifts are observed with small relocation vectors preserving the event clustering. Near Crete in the Aegean subduction zone, positive origin time shifts are found that change into small negative origin time shifts indicating the difference in source depth and model properties in this region. They are accompanied by small epicenter shifts showing that the locations are well-constrained by the travel time observations for these earthquakes. In the Vrancea region in Romania, where plate subduction took place along the Carpathian arc, negative origin time shifts indicate reduction of data misfit due to correction of the source parameters regarding the high-velocity slab there. Otherwise, epicenter and depth shifts in this region are small keeping the clustering of events within this very limited region.

As illustrated in Figure 8.6, in well-sampled regions as the subduction zone across Japan, depth and epicenter shifts are small leaving the locations almost unchanged. Also in South America, earthquake locations in the slab are only relocated over small distances. However, below 150 km depth the events are more clustered now narrowing the region in which seismicity is observed. In the Mediterranean where most earthquakes occur at shallow depth, events at less than 50 km depth are mainly located downwards building a layer of approximately 20 km thickness in which they cluster. Again, deeper events around 150 km depth are more focussed after relocation at the top of the slab.

8.7 Conclusions

We relocated a global earthquake data set with a 3-D reference model to account for local heterogeneities in the sources regions which could not be accounted for in the preceding relocation by Engdahl *et al.* (1998). As tests with ground truth events show, the 3-D reference model predicts travel times particularly at regional distances better than ak135. Furthermore,
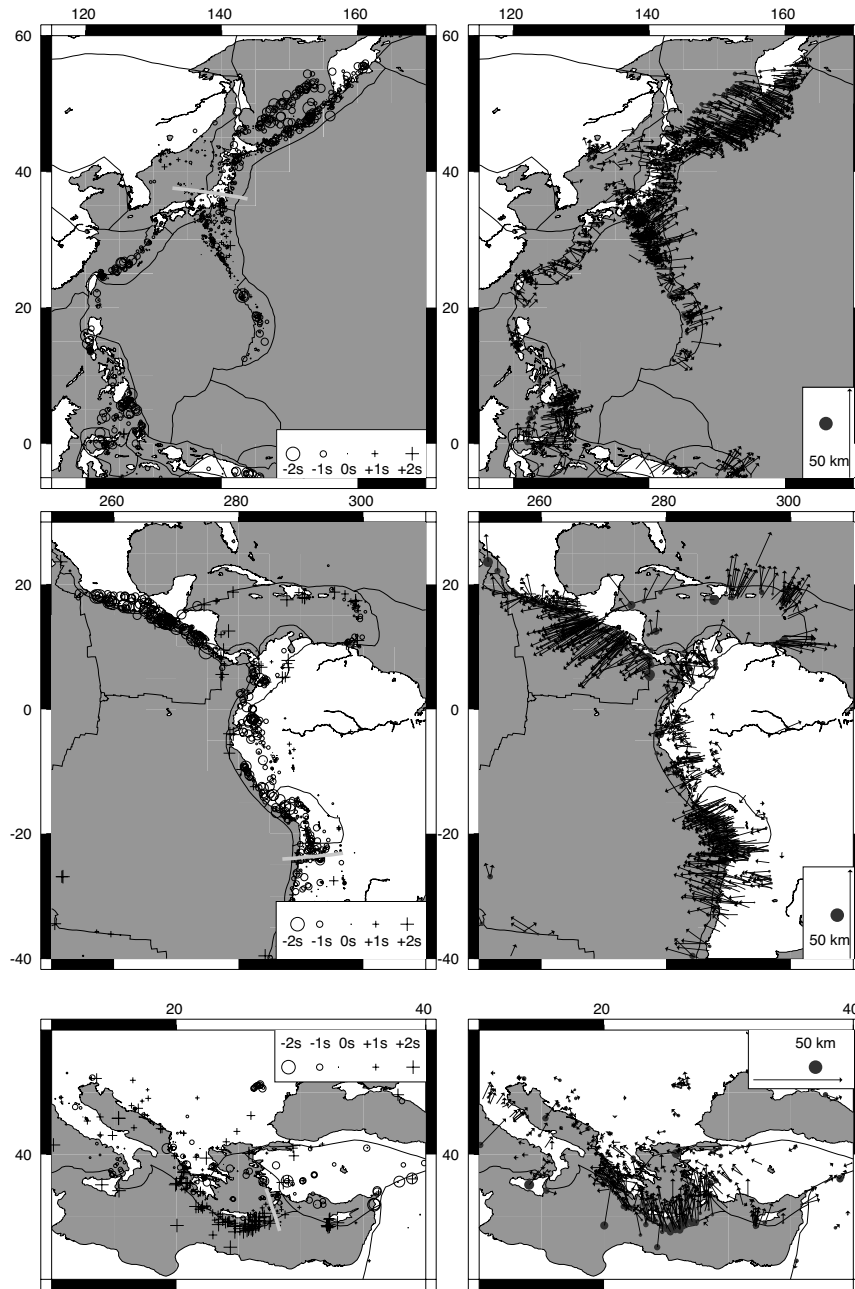
Figure 8.5: Source time shift (left) and epicenter shift (right) with respect to the original locations using ak135 as velocity model in the area of the Philippine plate (top), along the Cocos and Nazca plate subduction zones (middle) and in the eastern Mediterranean basin (bottom). For better visualization, in the top panels only events with more than 250 travel time residuals and an EHB focal depth > 70 km are displayed, in the other panels earthquakes at all depths are displayed but only those with > 250 travel time residuals in the mid panels and > 350 in the bottom panels.

135

Japan

South America

Eastern Mediterranean
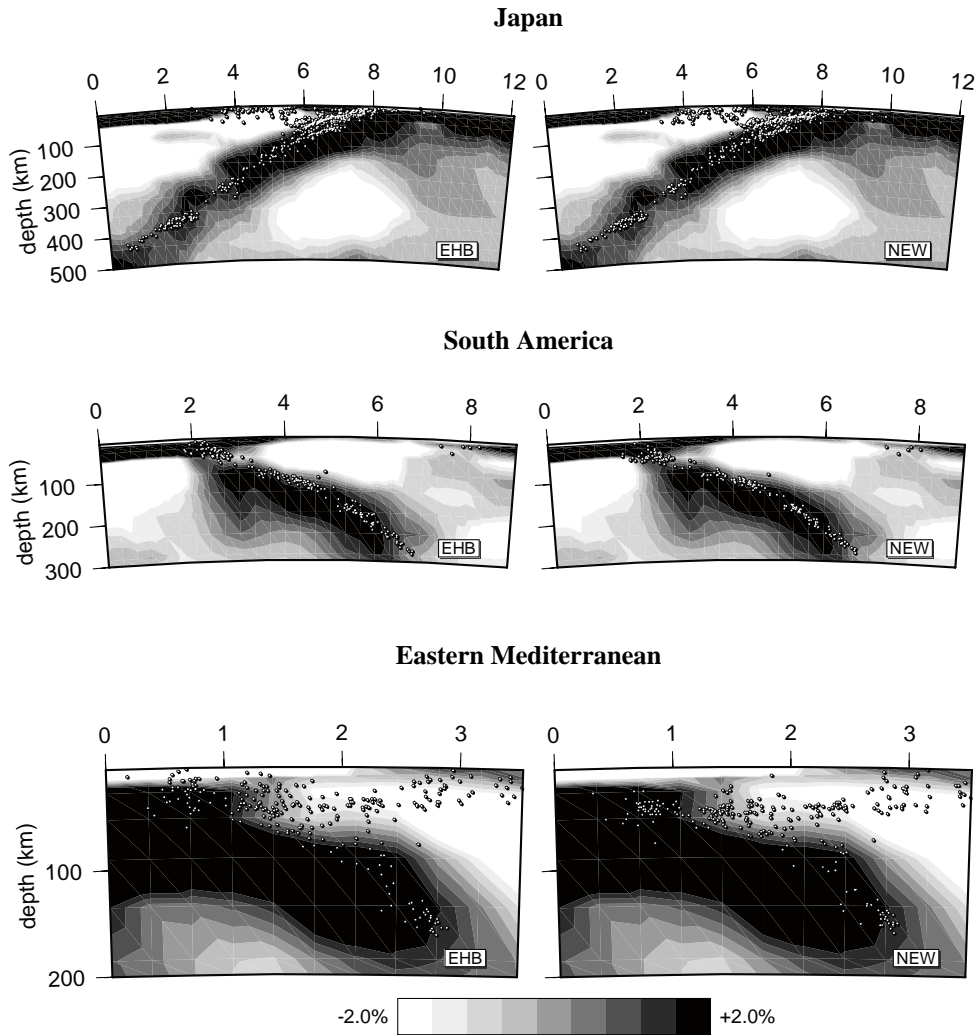
Figure 8.6: Vertical cross sections of three subduction zones. White dots represent the original locations using ak135 as reference model (left column) and new locations (right column). Displayed are free-depth events with more than 150 registrations for a slice of $\pm 2.0°$ width. The location of the slices is marked with gray lines in Figure 8.5. The grayscales in the background display the P06_3Dloc model anomalies along the cross section. Black tones represent velocities that are higher than the corresponding ak135 velocity at that depth and white tones indicate lower velocities.

	initial depth range			
	all	< 70 km	70 km–300 km	≥ 300 km
epicenter shift (km):				
fixed-depth events	12.8 ± 12.8	11.8 ± 12.7	17.4 ± 11.8	22.2 ± 9.7
free-depth events	12.8 ± 11.0	12.4 ± 11.6	12.9 ± 9.7	17.4 ± 9.3
all events	12.8 ± 11.8	12.0 ± 12.2	14.1 ± 10.5	19.1 ± 9.7
depth shift (km):				
fixed-depth events	–	–	–	–
free-depth events	-3.1 ± 9.4	-4.4 ± 9.8	-0.6 ± 7.9	-0.6 ± 8.2
all events	–	–	–	–
origin time shift (s):				
fixed-depth events	-0.1 ± 0.7	-0.1 ± 0.7	0.0 ± 0.6	-0.2 ± 0.5
free-depth events	0.1 ± 1.1	0.2 ± 1.2	-0.1 ± 0.7	-0.1 ± 0.7
all events	0.0 ± 0.9	0.0 ± 1.0	-0.1 ± 0.7	-0.1 ± 0.6

Table 8.3: Average source parameter shifts and rms-scatter of the accepted relocations with respect to the initial location for different depth ranges.

relocation with the 3-D velocity model gives smaller epicenter mislocations and the origin time errors are reduced, only the depth mislocations are slightly increased. However, for the estimation of the depth mislocation only surface and crustal ground truth events exist and relocation of the global hypocenter data set shows that depth shifts below the crust are significantly reduced suggesting that also the depth mislocation errors are reduced for deeper located events.

Besides that, the results show that relocation with theoretical travel times computed in the 3-D velocity model agree well with the computations using ak135 + regional patch corrections as the overall source parameter shifts are small. The relocations mainly account for 3-D velocity structure which could not be taken into account by the patch corrections in the computation of Engdahl *et al.* (1998) as systematic location changes indicate. Thereby, subduction-related epicenters are relocated towards the trench and remaining data misfit after consideration of the 3-D velocity model is accounted for by negative origin time shifts. At shallower depth, the earthquakes are mainly located downwards and origin time shifts vary as the crust of the 3-D model changes locally. Overall, more focussing of the earthquakes in clusters is obtained, particularly at depths greater than 150 km.

8.8   Acknowledgments

Chapter 9

Summary

In this study, global high-resolution P-wave velocity models were obtained for the Earth's crust and mantle using travel time tomography. Improvements to previous models were achieved by incorporating additional data and advancing the method to use 3-D reference models.

The newly compiled data set consists of a selection of travel times from the updated EHB catalog (Engdahl *et al.*, 1998), which forms a set of 445,000 events from the ISC bulletins and NEIC data up to September 2004. Compared to the original catalog of 1998 it has more than doubled and contains significantly more regional phases. From this catalog, 17.7 million first and later-arriving P phases and additionally 1.5 million core phases were selected. The selection was extended by 14,000 events from the EMSC bulletins for the period 1998-2003. Furthermore, over 200,000 newly picked, high-accuracy arrival times were incorporated originating from recordings of seismic networks and temporary experiments in Europe and North America which did not report arrival times to the ISC. The picking of the arrival times was performed with the automatic arrival time picker of Sandoval *et al.* (2004a) based on the adaptive stacking method of Rawlinson and Kennett (2004).

Methodologically, besides a standard 1-D Earth reference model, 3-D reference models were used based on a combination of tomography models that use travel time residuals and models that use independent observations from surface waves, normal modes and long period body waves. This approach was used, so far, only by Widiyantoro *et al.* (2000) for S tomography. But in addition, here the selected events were relocated in the respective 3-D reference model using a directed grid-search technique (Sambridge and Kennett, 1986) to establish consistency between travel times and event parameters.

The details and results of these improvements are described in Chapters 3 to 8:

In Chapter 3, the impact of the new regional data (up to the year 1998) contained in the EHB catalog was investigated in a regional Pn tomography study of the crust and uppermost mantle beneath Europe. This analysis showed that for P velocities in the crust and uppermost mantle anomalies of a minimum lateral extent of $0.4°$ can be resolved and for S velocities anomalies of $0.8°$ providing detailed images of the crust and uppermost mantle structure that could not be obtained in a previous study (Bijwaard *et al.*, 1998) using the original EHB catalog. Furthermore, in this study S travel times were used for tomography and tomographic inversions

were performed with a 3-D reference model (CRUST2.0 (Bassin *et al.*, 2000) and CUB1.1 (Shapiro and Ritzwoller, 2002)). These inversions show that the data have enough resolving power to change the reference model in regions of good ray coverage whereas otherwise the reference model is reobtained. Besides that, shortcomings of the 1-D Earth reference model ak135 (Kennett *et al.*, 1995) were observed which is too slow for upper mantle shear velocities.

Chapter 4 deals with the newly picked arrival time data of temporary and permanent seismic stations in Europe which did not report arrival times to the ISC and therefore were not used in previous studies. The high quality of these arrival times is revealed in station averages of teleseismic arrivals that reflect the velocity variations directly beneath the stations and is confirmed by lower station standard deviations of residuals than for the ISC data. As a by-product, the error of the ISC data could be determined to be on the order of 0.7 s.

In Chapter 5, the use of 3-D reference models was extended to global travel time tomography and investigated in more detail. In the crust and upper mantle ($<$ 300 km) the model CUB2.0 (Ritzwoller *et al.*, 2002b) was used. The crustal velocities of CUB2.0 are based on CRUST2.0 (Bassin *et al.*, 2000) but were modified in the surface wave tomography to fit the surface wave phase and group velocity observations. Furthermore, for the deeper parts of the mantle, S20RTS (Ritsema *et al.*, 1999) was incorporated as 3-D reference model. As inversions with this combined reference model showed, regions in the mantle exist where ray sampling is sufficient to obtain a tomographic model comparable to the one using ak135 as reference model. But where ray sampling is not sufficient to allow for larger deviations from the reference model, the small-scale Earth structure observed using a 1-D reference model is overprinted by the long wavelength 3-D reference model. Therefore, in a further tomographic inversion the long wavelength reference model was combined with the model obtained from travel time tomography using a 1-D reference model. However, before combining the models, the anomalies in the travel time tomography model were enhanced to correct for underestimation of model amplitudes due to regularization. The resulting model combines the long wavelength structure as "seen" by long period seismic information with the detailed mantle structure obtained from short period data. Using a 3-D reference model also has the advantage, that the inversion model now implicitly contains more realistic velocities in areas that were not well constrained by P travel times.

In Chapter 6, the influence of the newly picked data for seismic stations in Europe and additional information from core phases not used previously was studied. Due to the additional data, more detail is seen in the upper 400 km, particularly in regions with few seismic stations and/or earthquakes. Furthermore, features that were already observed earlier are enhanced. Besides that, the core phases help to constrain anomalies in the lowermost mantle and greatly improve imaging of the hot upwelling beneath Central Europe which is suggested to be the source of recent volcanism in the area (Goes *et al.*, 1999).

In Chapter 7, focus is on North America and the newly incorporated data for seismic stations in that regions. The Earth's structure is imaged in high resolution comparable to regional tomographic studies and due to the new data set the remnants of the Farallon plate, an ancient oceanic plate, could be located in the upper mantle transition zone.

Finally in Chapter 8, an application of the new high-resolution tomography model was presented. Tests with well-located events demonstrate that the new model predicts, particularly

at regional distances, arrival times better than a 1-D velocity model, and that consequently epicenter mislocations and origin time errors are significantly reduced due to the new model. The relocation of the global earthquake data set used in this study corrects earthquake locations for 3-D Earth structure not taken into account by the original locations obtained with ak135 as reference model. In addition, a better focussing of earthquakes in narrower clusters is achieved due to the new tomography model, particularly in the deeper parts of subducted slabs ($>$ 150 km depth).

References

Abers, G. G. and Roecker, S. W. (1991). Deep Structure of an Arc-continent Collision: Earthquake Relocation and Inversion for Upper Mantle P- and S-wave Velocities Beneath Papua New Guinea. *J. Geophys. Res.*, **96**, 6379–6401.

Alinaghi, A., Bock, G., Kind, R., Hanka, W., Wylegalla, K., and TOR and SVEKALAPKO Working Group (2003). Receiver function analysis of the crust and upper mantle from the North German Basin to the Archaean Baltic Shield. *Geophys. J. Int.*, **155**, 641–652.

Allen, R. M., Nolet, G., Morgan, W. J., Vogtfjörd, K., Bergsson, B. H., Erlendsson, P., Foulger, G. R., Jakobsdottir, S., Julian, B. R., Pritchard, M., Ragnarsson, S., and Stefansson, R. (2002). Imaging the mantle beneath Iceland using integrated seismological techniques. *J. Geophys. Res.*, **107**(B12).

Arlitt, R., Kissling, E., Ansorge, J., and TOR Working Group (1999). Three-dimensional crustal structure beneath the TOR array and effects on teleseismic wavefronts. *Tectonophysics*, **314**, 309–319.

Arrowsmith, S. J. (2003). *A tomographic investigation of upper mantle processes beneath the British Isles*. Ph.D. thesis, University of Leeds, UK.

Arrowsmith, S. J., Kendall, M., White, N., VanDecar, J. C., and Booth, D. C. (2005). Seismic imaging of a hot upwelling beneath the British Isles. *Geology*, **33**, 345–348.

Bassin, C., Laske, G., and Masters, G. (2000). The Current Limits of Resolution for Surface Wave Tomography in North America. *Eos Trans. AGU*, **81**, F897.

Beaudoin, B. C., Hole, J. A., Klemperer, S. L., and Tréhu, A. M. (1998). Location of the southern edge of the Gorda slab and evidence for an adjacent asthenospheric window: Results from seismic profiling and gravity. *J. Geophys. Res.*, **103**(B12), 30,101–30,115.

Beghein, C., Resovsky, J. S., and Trampert, J. (2002). P and S tomography using normal-mode and surface waves data with a neighbourhood algorithm. *Geophys. J. Int.*, **149**(3), 646–658.

Benz, H. M. and Zandt, G. (1993). Teleseismic tomography: lithospheric structure of the San Andreas fault system in northern and central California. In H. M. Iyer and K. Hirahara, editors, *Seismic Tomography: Theory and practice*. Chapman & Hall, London.

Benz, H. M., Zandt, G., and Oppenheimer, D. H. (1992). Lithospheric Structure of Northern California From Teleseismic Images of the Upper Mantle. *J. Geophys. Res.*, **97**(B4), 4791–4807.

Bijwaard, H. (1999). *Seismic travel-time tomography for detailed global mantle structure*. Ph.D. thesis, Universiteit Utrecht, The Netherlands.

Bijwaard, H. and Spakman, W. (1999a). Fast kinematic ray tracing of first- and later-arriving global seismic phases. *Geophys. J. Int.*, **139**, 359–369.

Bijwaard, H. and Spakman, W. (1999b). Tomographic evidence for a narrow whole mantle plume below Iceland. *Earth and Planetary Science Letters*, **166**(3-4), 121–126.

Bijwaard, H. and Spakman, W. (2000). Nonlinear global P-wave tomography by iterated linearized inversion. *Geophys. J. Int.*, **141**, 71–82.

Bijwaard, H., Spakman, W., and Engdahl, E. R. (1998). Closing the gap between regional and global tomography. *J. Geophys. Res.*, **103**, 30005–30078.

Bird, P. (2003). An updated digital model of plate boundaries. *Geochem. Geophys. Geosyst.*, **4**(3), 1027.

Bock, G. and the SVEKALAPKO Seismic Tomography Working Group (2001). Seismic probing of Archaean and Proterozoic Lithosphere in Fennoscandia. *Eos Trans. AGU*, **82**, 50,621, 628–629.

Bolton, H. and Masters, G. (2001). Travel times of P and S from the global digital seismic net-

143

works: Implications for the relative variation of P and S velocity in the mantle. *J. Geophys. Res.*, **106**(B7), 13,527–13,540.

Bondár, I., Engdahl, E. R., Yang, X., Ghalib, H. A. A., Hofstetter, A., Kirichenko, V., Wagner, R., Gupta, I., Ekström, G., Bergmann, E., Israelsson, H., and McLaughlin, K. (2004). Collection of a Reference Event Set for Regional and Teleseismic Location Calibration. *Bull. Seism. Soc. Am.*, **94**(4), 1528–1545.

Boschi, L. (2003). Measures of resolution in global body wave tomography. *Geophys. Res. Lett.*, **30**, 2–1.

Boschi, L. and Dziewonski, A. M. (1999). High- and low-resolution images of the Earth's mantle: Implications of different approaches to tomographic modeling. *J. Geophys. Res.*, **104**(B11), 25,567–25,594.

Boschi, L. and Dziewonski, A. M. (2000). Whole Earth tomography from delay times of P, PcP and PKP phases: Lateral heterogeneities in the outer core and radial anisotropy in the mantle? *J. Geophys. Res.*, **105**(B6), 13,675–13,696.

Boschi, L., Ekström, G., and Kustowski, B. (2004). Multiple resolution surface wave tomography: the Mediterranean basin. *Geophys. J. Int.*, **157**, 293–304.

Bostock, M. G., Hyndman, R. D., Rondenay, S., and Peacock, S. M. (2002). An inverted continental Moho and serpentinization of the forearc mantle. *Nature*, **417**, 536–538.

Boyd, O. S., Jones, C. H., and Sheehan, A. F. (2004). Foundering Lithosphere Imaged Beneath the Southern Sierra Nevada, California, USA. *Science*, **305**, 660–662.

Bruneton, M., Pedersen, H. A., Farra, V., Arndt, N. T., Vacher, P., Achauer, U., Alinaghi, A., Ansorge, J., Bock, G., Friederich, W., Grad, M., Guterch, A., Heikkinen, P., Hjelt, S.-E., Hyvonen, T. L., Ikonen, J.-P., Kissling, E., Komminaho, K., Korja, A., Kozlovskaya, E., Nevsky, M. V., Paulssen, H., Pavlenkova, N. I., Plomerova, J., Raita, T., Riznichenko, O. Y., Roberts, R. G., Sandoval, S., Sanina, I. A., Sharov, N. V., Shomali, Z. H., Tiikkainen, J., Wielandt, E., Wilegalla, K., Yliniemi, J., and Yurov, Y. G. (2004). Complex lithospheric structure under the central Baltic Shield from surface wave to-

mography. *J. Geophys. Res.*, **109**, B10303.

Buland, R. and Chapman, C. H. (1983). The Computation of Seismic Travel Times. *Bull. Seism. Soc. Am.*, **73**(5), 1271–1302.

Dahlen, F. A. (2004). Resolution limit to travel-time tomography. *Geophys. J. Int.*, **157**, 315–331.

Deal, M. M. and Nolet, G. (1996). Nullspace shuttles. *Geophys. J. Int.*, **124**, 372–380.

Debayle, E., Lévêque, J.-J., and Michel, C. (2001). Seismic evidence for a deeply rooted low-velocity anomaly in the upper mantle beneath the northeastern Afro/Arabian continent. *Earth Planet. Sci. Lett.*, **193**, 423–436.

Dercourt et al. (1986). Geological evolution of the Tethys belt from the Atlantic to the Pamirs since the Lias. *Tectonophysics*, **123**, 241–315.

Dziewonski, A. M. and Anderson, D. L. (1981). Preliminary reference Earth model. *Phys. Earth Planet. Int.*, **25**, 297–356.

Earle, P. S. and Shearer, P. M. (1994). Characterization of Global Seismograms Using an Automatic-Picking Algorithm. *Bull. Seism. Soc. Am.*, **84**(2), 366–376.

Ekström, G. and Dziewonski, A. M. (1998). The unique anisotropy of the Pacific upper mantle. *Nature*, **394**, 168–172.

El-Haddadeh, B. R. H. (1986). *Seismological investigations of the crust and upper mantle structure of the British Isles using teleseismic travel time data*. Ph.D. thesis, University of Leeds, UK.

Engdahl, E. R., van der Hilst, R. D., and Buland, R. P. (1998). Global teleseismic earthquake relocation with improved travel times and procedures for depth determination. *Bull. Seism. Soc. Am.*, **88**(3), 722–743.

Furlong, K. P., Hugo, W. D., and Zandt, G. (1989). Geometry and evolution of the San Andreas fault zone in northern California. *J. Geophys. Res.*, **94**, 3100–3110.

Godey, S., Snieder, R. K., Villaseñor, A., and Benz, H. M. (2003). Surface wave tomography of North America and the Caribbean using global and regional broad-band networks: phase velocity maps and limitations of ray theory. *Geophys. J. Int*, **152**(3), 620–632.

Godey, S., Bossu, R., Guilbert, J., and Mazet-

Roux, G. (2006). The Euro-Mediterranean Bulletin: A Comprehensive Seismological Bulletin at Regional Scale. *Seism. Res. Lett.*, **77**(4), 460–474.

Goes, S., Spakman, W., and Bijwaard, H. (1999). A Lower Mantle Source for Central European Volcanism. *Science*, **286**, 1928–1931.

Goldstein, P., Dodge, D., Firpo, M., and Minner, L. (2003). SAC2000: Signal processing and analysis tools for seismologists and engineers. In W. H. K. Lee, H. Kanamori, P. C. Jennings, and C. Kisslinger, editors, *The IASPEI International Handbook of Earthquake and Engineering*. Academic Press, London.

Gossler, J., Kind, R., Sobolev, S., Kämpf, H., Wylegalla, K., Stiller, M., and TOR Working Group (1999). Major crustal features between the Harz Mountains and the Baltic Shield derived from receiver functions. *Tectonophysics*, **314**, 321–333.

Grand, S. P. (2002). Mantle shear wave tomography and the fate of subducted slabs. *Phil. Trans. R. Soc. London.*, **360**, 2475–2491.

Grand, S. P., van der Hilst, R., and Widiyantoro, S. (1997). Global seismic tomography: a snapshot of convection in the Earth. *GSA Today*, **7**(4), 1–7.

Gregersen, S., Voss, P., and TOR Working Group (2002). Summary of project TOR: delineation of a stepwise, sharp, deep lithosphere transition across Germany–Denmark–Sweden. *Tectonophysics*, **360**(1-4), 61–73.

Grunewald, S., Weber, M., and Kind, R. (2001). The upper mantle under Central Europe: indications for the Eifel plume. *Geophys. J. Int.*, **147**, 1–17.

Gu, Y. J., Dziewonski, A. M., Su, W. J., and Ekström, G. (2001). Models of the mantle shear velocity and discontinuities in the pattern of lateral heterogeneities. *J. Geophys. Res.*, **106**, 11169–199.

Gudmundsson, O., Davies, J. H., and Clayton, R. W. (1990). Stochastic analysis of global traveltime data: mantle heterogeneity and random errors in the ISC data. *Geophys. J. Int.*, **102**, 25–43.

Hafkenscheid, E., Wortel, M. J. R., and Spakman, W. (2006). Subduction history of the Tethyan region derived from seismic tomography and tectonic reconstructions. *J. Geophys. Res.*, **111**, B08401, doi:10.1029/2005JB003791.

Hearn, T. and Ni, J. (1994). Pn velocities beneath continental collision zones: the Turkish-Iranian Plateau. *Geophys. J. Int.*, **117**, 273 – 283.

Ishii, M. and Tromp, J. (2001). Even-degree lateral variations in the earth's mantle constrained by free oscillations and the free-air gravity anomaly. *Geophys. J. Int.*, **145**, 77–96.

Jeffreys, H. and Bullen, K. E. (1940). Seismological Tables. *British Association Seismological Committee, London.*

Kárason, H. and van der Hilst, R. D. (2000). Constraints on mantle convection from seismic tomography. In M. A. Richards, R. Gordon, and R. D. van der Hilst, editors, *History and Dynamics of Plate Motion*, 121, pages 277–288. Am. Geophys. Union, Geophys. Monogr. Ser.

Kárason, H. and van der Hilst, R. D. (2001). Tomographic imaging of the lowermost mantle with differential times of refracted and diffracted core phases (PKP, P_{diff}). *J. Geophys. Res.*, **106**(B4), 6569–6587.

Kennett, B. L. N. and Engdahl, E. R. (1991). Traveltimes for global earthquake location and phase identification. *Geophys. J. Int.*, **105**, 429–465.

Kennett, B. L. N. and Gorbatov, A. (2004). Seismic heterogeneity in the mantle - strong shear wave signature of slabs from joint tomography. *Phys. Earth Planet. Int.*, **146**, 87–100.

Kennett, B. L. N. and Gudmundsson, O. (1996). Ellipticity corrections for seismic phases. *Geophys. J. Int.*, **127**, 40–48.

Kennett, B. L. N., Engdahl, E. R., and Buland, R. (1995). Constraints on seismic velocities in the Earth from traveltimes. *Geophys. J. Int.*, **122**, 108–124.

Kennett, B. L. N., Widiyantoro, S., and van der Hilst, R. D. (1998). Joint seismic tomography for bulk sound and shear wave speed in the Earth's mantle. *J. Geophys. Res.*, **103**, 12469–93.

Keskin, M. (2003). Magma generation by slab steepening and breakoff beneath a subduction-accretion complex: An alternative model for collision-related volcanism in Eastern Anatolia,

Turkey. *Geophys. Res. Lett.*, **30**(24).

Keyser, M., Ritter, J., and Jordan, M. (2002). 3D shear-wave velocity structure of the Eifel plume, Germany. *Earth Planet. Sci. Lett.*, **203**, 59–82.

Kissling, E. and Spakman, W. (1996). Interpretation of tomographic images of uppermost mantle structure: examples from the Western and Central Alps. *J. Geodynamics*, **21**(97-111).

Kissling, E., Ellsworth, W. L., Eberhart-Phillips, D., and Kradolfer, U. (1994). Initial reference models in local earthquake tomography. *J. Geophys. Res.*, **99**(B10), 19,635–19,646.

Landes, M., Fielitz, W., Hauser, F., Popa, M., and CALIXTO group (2004). 3-D upper-crustal tomographic structure across the Vrancea seismic zone, Romania. *Tectonophysics*, **382**, 85–102.

Lei, J. and Zhao, D. (2006). Global P-wave tomography: On the effect of various mantle and core phases. *Phys. Earth Planet. Int.*, **154**, 44–69.

Leveque, J.-J., Rivera, L., and Wittlinger, G. (1993). On the use of the checker-board test to assess the resolution of tomographic inversions. *Geophys. J. Int.*, **115**, 313–318.

Li, C., van der Hilst, R. D., and Toksöz, M. N. (2006). Constraining P-wave velocity variations in the upper mantle beneath Southeast Asia. *Phys. Earth Planet. Int.*, **154**, 180–195.

Li, X. D. and Romanowicz, B. (1996). Global mantle shear velocity model developed using nonlinear asymptotic coupling theory. *J. Geophys. Res.*, **101**, 22245–73.

Liu, M. and Zandt, G. (1996). Convective thermal instabilities in the wake of the migrating Mendocino triple junction, California. *Geophys. Res. Lett.*, **23**(13), 1573–1576.

Liu, X. F. and Dziewonski, A. M. (1998). Global analysis of shear wave velocity anomalies in the lowermost mantle. In M. Gurnis, E. Wysession, B. Knittle, and B. Buffet, editors, *The Core-Mantle Boundary Region*, volume 28, pages 21–36. Am. Geophys. Union.

Marone, F., van der Meijde, M., van der Lee, S., and Giardini, D. (2003). Joint inversion of local, regional and teleseismic data for crustal thickness in the Eurasia-Africa plate boundary region. *Geophys. J. Int.*, **154**, 499–514.

Marquering, H. and Snieder, R. (1996). Shear-wave velocity structure beneath Europe, the northeastern Atlantic and western Asia from waveform inversions including surface-wave mode coupling. *Geophys. J. Int.*, **127**, 283–304.

Martin, M. and Ritter, J. R. R. (2005). High-resolution teleseismic body-wave tomography beneath SE Romania - I. Implications for three-dimensional versus one-dimensional crustal correction strategies with a new crustal velocity model. *Geophys. J. Int.*, **162**, 448–460.

Martin, M., Wenzel, F., and CALIXTO working group (2006). High-resolution teleseismic body wave tomography beneath SE-Romania – II. Imaging of a slab detachment scenario. *Geophys. J. Int.*, **164**, 579–595.

Masters, G., Johnson, S., Laske, G., and Bolton, H. (1996). A shear-velocity model of the mantle. *Philos. Trans. R. Soc. London A*, **354**, 1385–411.

Masters, G., Laske, G., Bolton, H., and Dziewonski, A. M. (2000). The relative behavior of shear velocity, bulk sound speed, and compressional velocity in the mantle: implications for chemical and thermal structure. In S. Karato, A. M. Forte, R. C. Liebermann, G. Masters, and L. Stixrude, editors, *Earth's Deep Interior: Mineral Physics and Tomography from the Atomic to the Global Scale*, volume 117. Am. Geophys. Union.

McKenzie, D. and Julian, B. (1971). Puget Sound, Washington, Earthquake and the Mantle Structure Beneath the Northwestern United States. *Geol. Soc. Am. Bull.*, **82**, 3519–3524.

Mégnin, C. and Romanowicz, B. (2000). The 3D shear velocity structure of the mantle from the inversion of body, surface and higher mode waveforms. *Geophys. J. Int.*, **143**, 709–28.

Michaelson, C. and Weaver, C. S. (1986). Upper Mantle Structure From Teleseismic P Wave Arrivals in Washington and Northern Oregon. *J. Geophys. Res.*, **91**(B2), 2077–2094.

Montelli, R., Nolet, G., Dahlen, F. A., Masters, G., Engdahl, E. R., and Hung, S.-H. (2004a). Finite-Frequency Tomography Reveals a Variety of Plumes in the Mantle. *Science*, **303**, 338–343.

Montelli, R., Nolet, G., Masters, G., Dahlen, F. A.,

146

and Hung, S.-H. (2004b). Global P and PP traveltime tomography: rays versus waves. *Geophys. J. Int.*, **158**, 637–654.

Montelli, R., Nolet, G., Dahlen, F. A., and Masters, G. (2006). A catalogue of deep mantle plumes: new results from finite-frequency tomography. *Geochem. Geophys. Geosys. (G3)*, **7**.

Mooney, W., Laske, G., and Masters, T. (1998). CRUST 5.1: A global crustal model at $5° × 5°$. *J. Geophys. Res.*, **103**(B1), 727–747.

Neele, F., VanDecar, J., and Snieder, R. (1993). The Use of P Wave Amplitude Data in a Joint Inversion With Travel Times for Upper Mantle Velocity Structure. *J. Geophys. Res.*, **98**(B7), 12,033–12,054.

Nolet, G., Montelli, R., and Virieux, J. (1999). Explicit, approximate expressions for the resolution and a posteriori covariance of massive tomographic systems. *Geophys. J. Int.*, **138**(1), 36–44.

Nolet, G., Montelli, R., and Virieux, J. (2001). Reply to comment by Z. S. Yao, R. G. Roberts and A. Tryggvason on 'Explicit, approximate expressions for the resolution and a posteriori covariance of massive tomographic systems'. *Geophys. J. Int.*, **145**(1), 315–315.

Obayashi, M. and Fukao, Y. (1997). P and PcP travel time tomography for the core-mantle boundary. *J. Geophys. Res.*, **102**(B8), 17,825–17,841.

Paige, C. and Saunders, M. (1982). LSQR: An algorithm for sparse linear equations and sparse least sqares. *ACM Transactions on Mathematical Software*, **8**(1), 43–71.

Papazachos, C. and Nolet, G. (1997). P and S deep velocity structure of the Hellenic area obtained by robust nonlinear inversion of travel times. *J. Geophys. Res.*, **102**(B4), 8349–8367.

Paulssen, H., van der Lee, S., and Nolet, G. (1990). The NARS-Netherlands Project. *IRIS Newsletter*, **9**(4), 1–2.

Paulssen, H., Bukchin, B. G., Emelianov, A. P., Lazarenko, M., Muyzert, E., Snieder, R., and Yanovskaya, T. B. (2000). The NARS-DEEP project. *Tectonophysics*, **313**, 1–8.

Piromallo, C. and Morelli, A. (2003). P wave tomography of the mantle under the Alpine-Mediterranean area. *J. Geophys. Res.*, **108**(B2), 2065–2088.

Plomerova, J. and TOR Working Group (2002). Seismic anisotropy of the lithosphere around the Trans-European Suture Zone (TESZ) based on teleseismic body-wave data of the Tor experiment. *Tectonophysics*, **360**, 89–114.

Pulliam, J. and Snieder, R. (1996). Fast, efficient calculation of rays and travel times with ray perturbation theory. *J. Acoust. Soc. Am.*, **99**, 383–391.

Pulliam, R. J., Vasco, D. W., and Johnson, L. R. (1993). Tomographic Inversions for Mantle P Wave Velocity Structure Based on the Minimization of l^2 and l^1 Norms of International Seismological Centre Travel Time Residuals. *J. Geophys. Res.*, **98**(B1), 699–734.

Rangin, C., Spakman, W., Pubellier, M., and Bijwaard, H. (1999). Tomographic and geological constraints on subduction along the eastern Sundaland continental margin (South-East Asia). *Bull. Soc. Géol. Fr.*, **170**(6), 775–788.

Rasmussen, J. and Humphreys, E. (1988). Tomographic image of the Juan de Fuca plate beneath Washington and Western Oregon using teleseismic P-wave travel times. *Geophys. Res. Lett.*, **15**(12), 1417–1420.

Rawlinson, N. and Kennett, B. L. N. (2004). Rapid estimation of relative and absolute delay times across a network by adaptive stacking. *Geophys. J. Int.*, **157**, 332–340.

Resovsky, J. and Ritzwoller, M. H. (1999). A degree 8 mantle shear velocity model from normal mode observations below 3 mHz. *J. Geophys. Res.*, **104**, 993–1014.

Ritsema, J., van Heijst, H. J., and Woodhouse, J. H. (1999). Complex Shear Wave Velocity Structure Imaged Beneath Africa and Iceland. *Science*, **286**, 1925–1928.

Ritter, J., Jordan, M., Christensen, U., and Achauer, U. (2001). A mantle plume below the Eifel volcanic fields, Germany. *Earth Planet. Sci. Lett.*, **186**, 7–14.

Ritter, J. R. R., Achauer, U., Christensen, U. R., and the Eifel Plume Team (2000). The teleseismic tomography experiment in the Eifel region, Central Europe: Design and first results. *Seism. Res. Lett.*, **71**, 437–443.

Ritzwoller, M., Barmin, M., Villaseñor, A., Levshin, A., and Engdahl, E. (2002a). P_n and S_n tomography across Eurasia to improve regional seismic event locations. *Tectonophysics*, **358**, 39–55.

Ritzwoller, M. H. and Levshin, A. L. (1998). Eurasian surface wave tomography: Group velocities. *J. Geophys. Res.*, **103**(B3), 4839–4878.

Ritzwoller, M. H., Shapiro, N. M., Barmin, M. P., and Levshin, A. L. (2002b). Global surface wave diffraction tomography. *J. Geophys. Res.*, **107**(B12).

Röhm, A. (1999). *Statistical properties of travel time measurements and the structure of the Earth's mantle*. Ph.D. thesis, Universiteit Utrecht, The Netherlands.

Röhm, A., Trampert, J., Paulssen, H., and Snieder, R. (1999). Bias in reported seismic arrival times deduced from the ISC Bulletin. *Geophys. J. Int.*, **137**, 163–174.

Rondenay, S., Bostock, M. G., and Shragge, J. (2001). Multiparameter two-dimensional inversion of scattered teleseismic body waves 3. Application to the Cascadia 1993 data set. *J. Geophys. Res.*, **106**(12), 30795–30807.

Ruppert, S., Fliedner, M. M., and Zandt, G. (1998). Thin crust and active upper mantle beneath the Southern Sierra Nevada in the western United States. *Tectonophysics*, **286**, 237–252.

Saleeby, J., Ducea, M., and Clemens-Knott, D. (2003). Production and loss of high-density batholithic root, southern Sierra Nevada, California. *Tectonics*, **22**(6).

Sambridge, M. and Faletič, R. (2003). Adaptive whole Earth tomography. *Geochem. Gephys. Geosys.*, **4**(3).

Sambridge, M. and Kennett, B. L. N. (1986). A novel method of hypocentre location. *Geoph. J. R. astr. Soc.*, **87**, 679–697.

Sandoval, S., Kissling, E., Ansorge, J., and the SVEKALAPKO Seismic Tomography Working Group (2003). High-resolution body wave tomography beneath the SVEKALAPKO array: I. A priori three-dimensional crustal model and associated traveltime effects on teleseismic wave fronts. *Geophys. J. Int.*, **153**, 75–87.

Sandoval, S., Villasenor, A., Spakman, W., Benz, H. M., and Earle, P. (2004a). Automatic analysis of ANSS waveform data in near real time. *Geoph. Res. Abstr.*, **6**(00322).

Sandoval, S., Kissling, E., Ansorge, J., and the SVEKALAPKO STWG (2004b). High-resolution body wave tomography beneath the SVEKALAPKO array: II. Anomalous upper mantle structure beneath the central Baltic Shield. *Geophys. J. Int.*, **157**, 200–214.

Schmid, C., van der Lee, S., and Giardini, D. (2004). Delay times and shear wave splitting in the Mediterranean region. *Geophys. J. Int.*, **159**(1), 275–290.

Sengör, A. M. C., Özeren, S., Genc, T., and Zor, E. (2003). East Anatolian high plateau as a mantle-supported, north-south shortened domal structure. *Geophys. Res. Lett.*, **30**(24).

Shapiro, N. M. and Ritzwoller, M. H. (2002). Monte-Carlo inversion for a global shear-velocity model of the crust and upper mantle. *Geophys. J. Int.*, **151**, 88–105.

Shen, Y., Solomon, S. C., Bjarnason, I. T., and Wolfe, C. J. (1998). Seismic evidence for a lower-mantle origin of the Iceland plume. *Nature*, **395**, 62–65.

Shomali, Z. H., Roberts, R. G., Pedersen, L. B., and TOR Working Group (2006). Lithospheric structure of the Tornquist Zone resolved by non-linear P and S teleseismic tomography along the TOR array. *Tectonophysics*, **416**, 133–149.

Snieder, R. (1988). Large-Scale Waveform Inversions of Surface Waves for Lateral Heterogeneity. *J. Geophys. Res.*, **93**(B10), 12067–12080.

Snieder, R. and Sambridge, M. (1992). Ray perturbation theory for travel times and ray paths in 3D heterogeneous media. *Geophys. J. Int.*, **109**, 304–322.

Spakman, W. (1991). Delay-time tomography of the upper mantle below Europe, the Mediterranean, and Asia Minor. *Geophys. J. Int.*, **107**(2), 309–332.

Spakman, W. (1993). Iterative strategies for non-linear travel time tomography using global earthquake data. In H. Iyer and K. Hirahara, editors, *Seimic Theory. Theory and practice*, pages 190–226. Chapman and Hall.

Spakman, W. and Bijwaard, H. (2001). Optimization of Cell Parameterization for Tomographic Inverse Problems. *Pure and Applied*

148

Geophysics, **158**, 1401–1423.

Spakman, W. and Nolet, G. (1988). Imaging algorithms, accuracy and resolution in delay time tomography. In N. Vlaar, G. Nolet, M. Wortel, and S. Cloetingh, editors, *Mathmatical Geophysics*, pages 155–187. Reidel, Dodrecht, the Netherlands.

Spakman, W. and Wortel, M. J. R. (2004). A tomographic view on Western Mediterranean geodynamics. In *The TRANSMED Atlas: the Mediterranean Region from Crust to Mantle*, pages 31–52. Cavazza, W. and Roure, F. and Spakman, W. and Stampfli, G. M. and Ziegler, P. A.

Spakman, W., van der Lee, S., and van der Hilst, R. (1993). Travel-time tomography of the European-Mediterranean mantle down to 1400 km. *Phys. Earth Planet. Int.*, **79**(1-2), 3–74.

Su, W. J., Woodward, R. L., and Dziewonski, A. M. (1994). Degree 12 model of shear velocity heterogeneity in the mantle. *J. Geophys. Res.*, **99**, 4945–80.

Ten Brink, U. S., Shimizu, N., and Molzer, P. C. (1999). Plate deformation at depth under northern California: Slab gap or stretched slab? *Tectonics*, **18**(6), 1084–1098.

Trampert, J., van Wettum, A., Ritsema, J., Clayton, R., Castro, R., Rebollar, C., and Perez-Vertti, A. (2003). New Array Monitors Seismic Activity near the Gulf of California in Mexico. *Eos Trans. AGU*, **84**(4), 29.

van der Hilst, R. D. and Spakman, W. (1989). Importance of the reference model in linearized tomography and images of subduction below the Caribbean plate. *Geophys. Res. Lett.*, **16**(10), 1093–1096.

van der Hilst, R. D., Widiyantoro, S., and Engdahl, E. R. (1997). Evidence of deep mantle circulation from global tomography. *Nature*, **386**, 578–584.

van der Lee, S. and Nolet, G. (1997). Seismic image of the subducted trailing fragments of the Farallon plate. *Nature*, **386**, 266–269.

van der Lee, S., Marone, F., van der Meijde, M., Giardini, D., Deschamps, A., Margheriti, L., Burket, P., Solomon, S., Alves, P., Chouliaras, M., Eshwehdi, A., Suleiman, A., Gashut, H., Herak, M., Ortiz, R., Davila, J. M., Ugalde, A., Vila, J., and Yelles, K. (2001). Eurasia-Africa Plate Boundary Region Yields New Seismographic Data. *Eos Trans. AGU*, **82**(51).

van der Meijde, M., Marone, F., Giardini, D., and van der Lee, S. (2003). Seismic evidence for water deep in Earth's upper mantle. *Science*, **300**, 1556–1558.

van der Sluis, A. and van der Vorst, H. A. (1987). *Numerical solution of large, sparse linear algebraic systems arising from tomographic problems*, chapter 3, pages 49–83. D. Reidel Publishing Company.

van der Voo, R., Spakman, W., and Bijwaard, H. (1999). Tethyan subducted slabs under India. *Earth Planet. Sci. Lett.*, **171**, 7–20.

VanDecar, J. C. (1991). *Upper mantle structure of the Cascadia subduction zone from nonlinear teleseismic travel time inversion*. Ph.D. thesis, University of Washington, Seattle.

Vasco, D. W. and Johnson, L. R. (1998). Whole Earth structure estimated from seismic arrival times. *J. Geophys. Res.*, **103**(B2), 2633–2671.

Villaseñor, A., Ritzwoller, M. H., Levshin, A. L., Barmin, M., Engdahl, E. R., Spakman, W., and Trampert, J. (2001). Shear velocity structure of central Eurasia from inversion of surface wave velocities. *Phys. Earth Planet. Int.*, **123**, 169–184.

Voss, P., Mosegaard, K., Gregersen, S., and TOR Working Group (2006). The Tornquist Zone, a north east inclining lithospheric transition at the south western margin of the Baltic Shield: Revealed through a nonlinear teleseismic tomographic inversion. *Tectonophysics*, **416**, 151–166.

Weidle, C., Widiyantoro, S., and CALIXTO Working Group (2005). Improving depth resolution of teleseismic tomography by simultaneous inversion of teleseismic and global P-wave traveltime data – application to the Vrancea region in Southeastern Europe. *Geophys. J. Int*, **162**, 811–823.

Wenzel, F., Achauer, U., Enescu, D., Kissling, E., Russo, R., Mocanu, V., and Musacchio, G. (1998). Detailed look at final stage of plate break-off is target of study in Romania. *Eos Trans. AGU*, **79**, 589, 592–594.

Widiyantoro, S., Gorbatov, A., Kennett, B. L. N., and Fukao, Y. (2000). Improving global

shear wave traveltime tomography using three-dimensional ray tracing and iterative inversion. *Geophys. J. Int.*, **141**, 747–758.

Wilde-Piórko, M., Grad, M., and TOR Working Group (2002). Crustal structure variation from the Precambrian to Palaeozoic platforms in Europe imaged by the inversion of teleseismic receiver functions – project TOR. *Geophys. J. Int.*, **150**, 261–270.

Wolfe, C. J., Bjarnason, I. T., VanDecar, J. C., and Solomon, S. C. (1997). Seismic structure of the Iceland mantle plume. *Nature*, **385**, 245–247.

Wortel, M. and Spakman, W. (2000). Subduction and Slab Detachment in the Mediterranean-Carpathian Region. *Science*, **290**, 1910–1917.

Wylegalla, K. and TOR Working Group (1999). Anisotropy across the Sorgenfrei–Tornquist zone from shear wave splitting. *Tectonophysics*, **314**, 335–350.

Yang, Y. and Forsyth, D. W. (2006). Rayleigh wave phase velocities, small-scale convection, and azimuthal anisotropy beneath southern California. *J. Geophys. Res.*, **111**(B07306).

Yao, Z. S., Roberts, R. G., and Tryggvason, A. (1999). Calculating resolution and covariance matrices for seismic tomography with the LSQR method. *Geophys. J. Int.*, **138**(3), 886–894.

Yao, Z. S., Roberts, R. G., and Tryggvason, A.

(2001). Comment on 'Explicit, approximate expressions for the resolution and a posteriori covariance of massive tomographic systems' by G. Nolet, R. Montelli and J. Virieux. *Geophys. J. Int.*, **145**(1), 307–314.

Yliniemi, J., Kozlovskaya, E., Hjelt, S.-E., Komminaho, K., Ushakov, A., and SVEKALAPKO Seismic Tomography Working Group (2004). Structure of the crust and uppermost mantle beneath southern Finland revealed by analysis of local events registered by the SVEKALAPKO seismic array. *Tectonophysics*, **394**(1-2), 41–67.

Zandt, G. and Carrigan, C. R. (1993). Small-Scale Convective Instability and Upper Mantle Viscosity Under California. *Science*, **261**, 460–463.

Zandt, G., Gilbert, H., Owens, T. J., Ducea, M., Saleeby, J., and Jones, C. H. (2004). Active foundering of a continental arc root beneath the southern Sierra Nevada in California. *Nature*, **431**, 41–46.

Zhao, D. (2001). Seismic structure and origin of hotspots and mantle plumes. *Earth Planet. Sci. Lett.*, **192**, 251–265.

Zhou, H. W. (1996). A high resolution P wave model of the top 1200 km of the mantle. *J. Geophys. Res.*, **101**, 27,791–810.

Zielhuis, A. and Nolet, G. (1994). Shear-wave velocity variations in the upper mantle beneath central Europe. *Geophys. J. Int.*, **117**, 695–715.

Appendix A
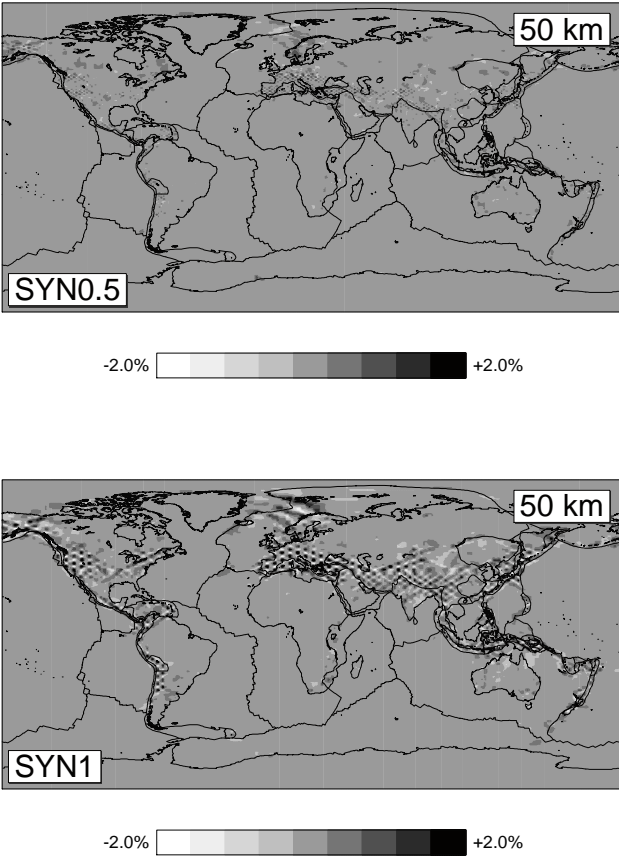
Figure A.1: Spike tests with spikes of $0.5° \times 0.5°$ at 50 km depth (top) and $1.0° \times 1.0°$ at 50 km depth (bottom).
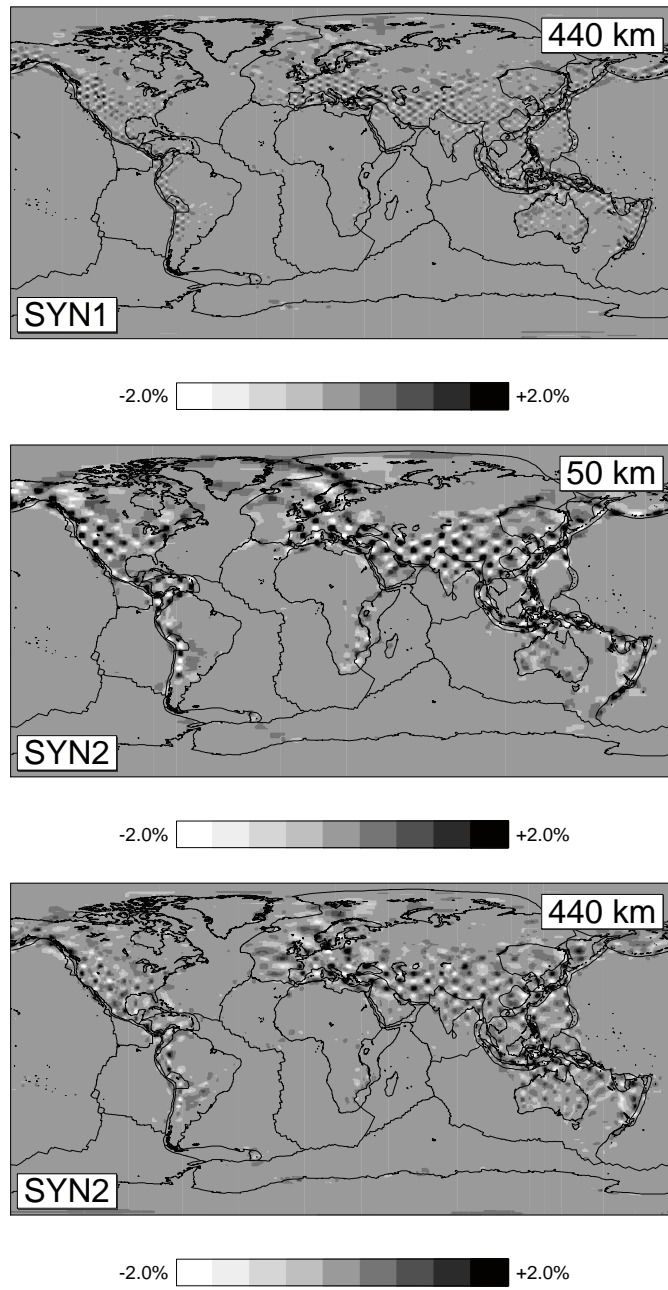
Figure A.2: Spike tests with spikes of $1.0° \times 1.0°$ at 440 km depth (top), $2.0° \times 2.0°$ at 50 km depth (middle) and $2.0° \times 2.0°$ at 440 km depth (bottom).
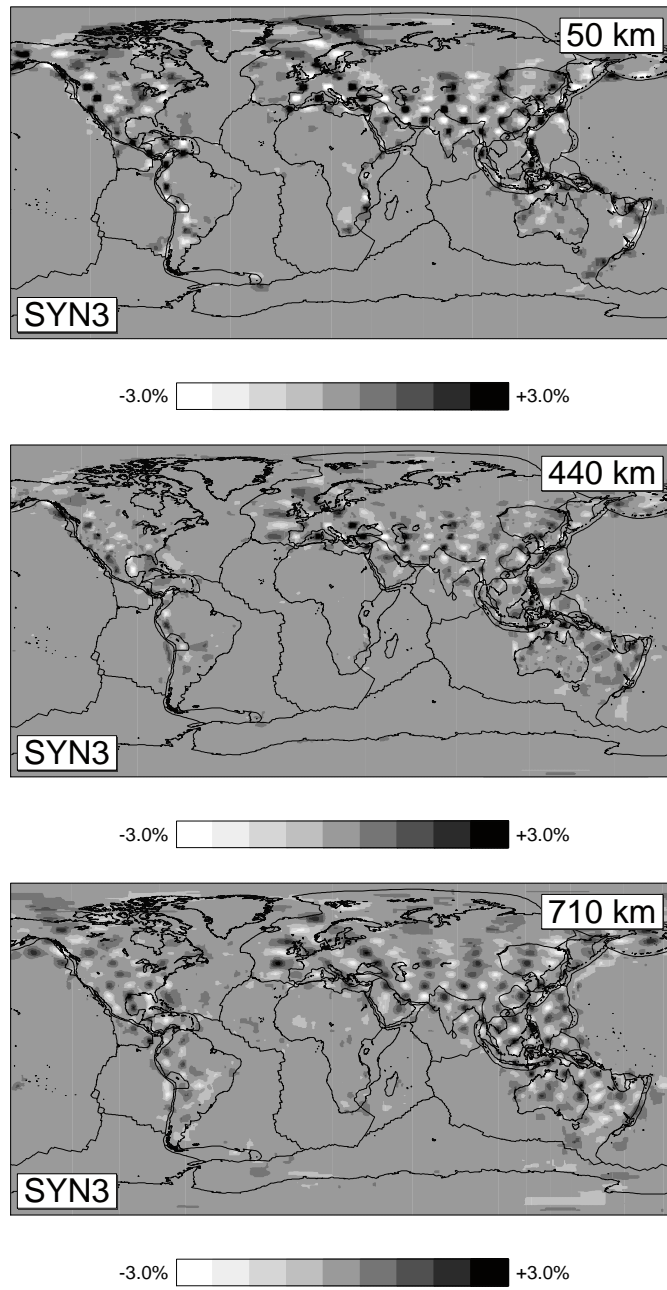
Figure A.3: Spike tests with spikes of $3.0° \times 3.0°$ at 50 km depth (top), $3.0° \times 3.0°$ at 440 km depth (middle) and $3.0° \times 3.0°$ at 710 km depth (bottom).
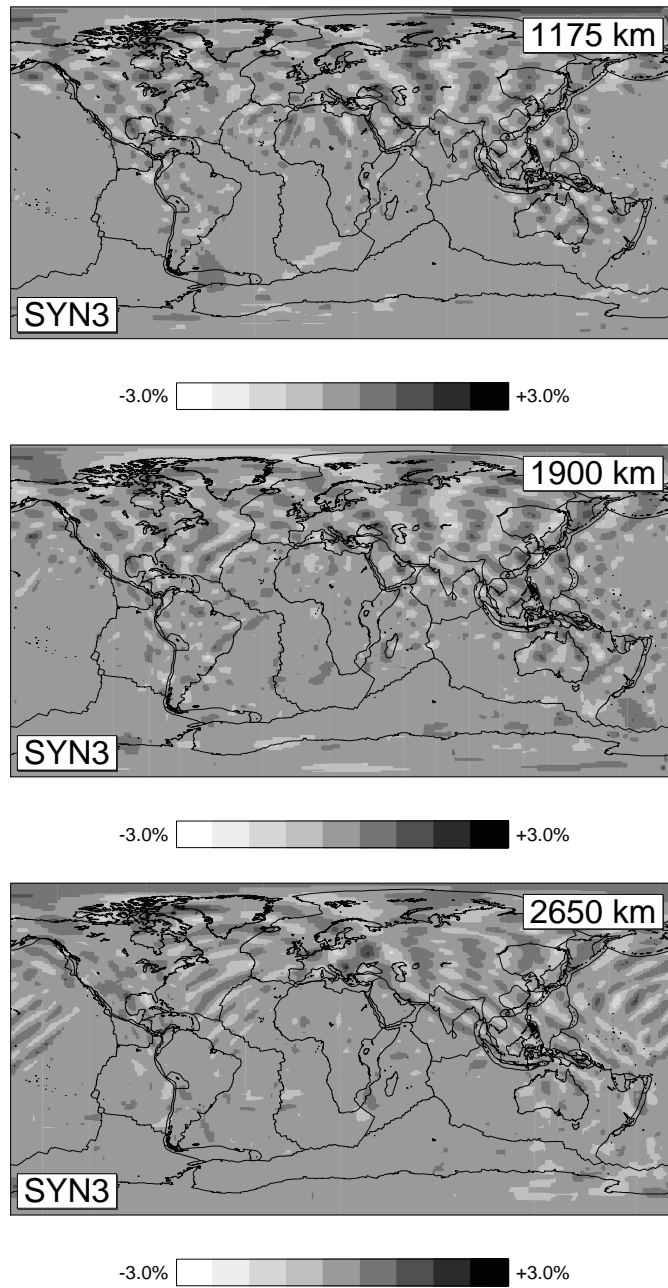
Figure A.4: Spike tests with spikes of $3.0° \times 3.0°$ at 1175 km depth (top), $3.0° \times 3.0°$ at 1900 km depth (middle) and $3.0° \times 3.0°$ at 2650 km depth (bottom).
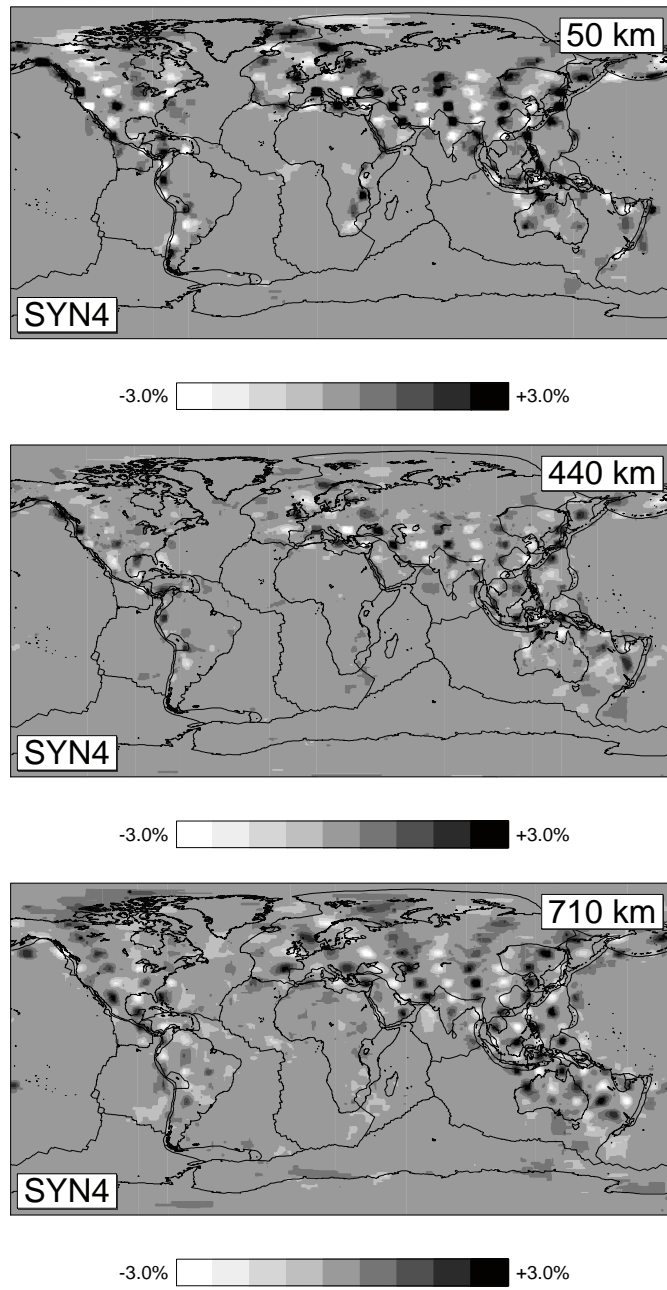
Figure A.5: Spike tests with spikes of $4.0° \times 4.0°$ at 50 km depth (top), $4.0° \times 4.0°$ at 440 km depth (middle) and $4.0° \times 4.0°$ at 710 km depth (bottom).

-3.0% +3.0%

-3.0% +3.0%

-3.0% +3.0%
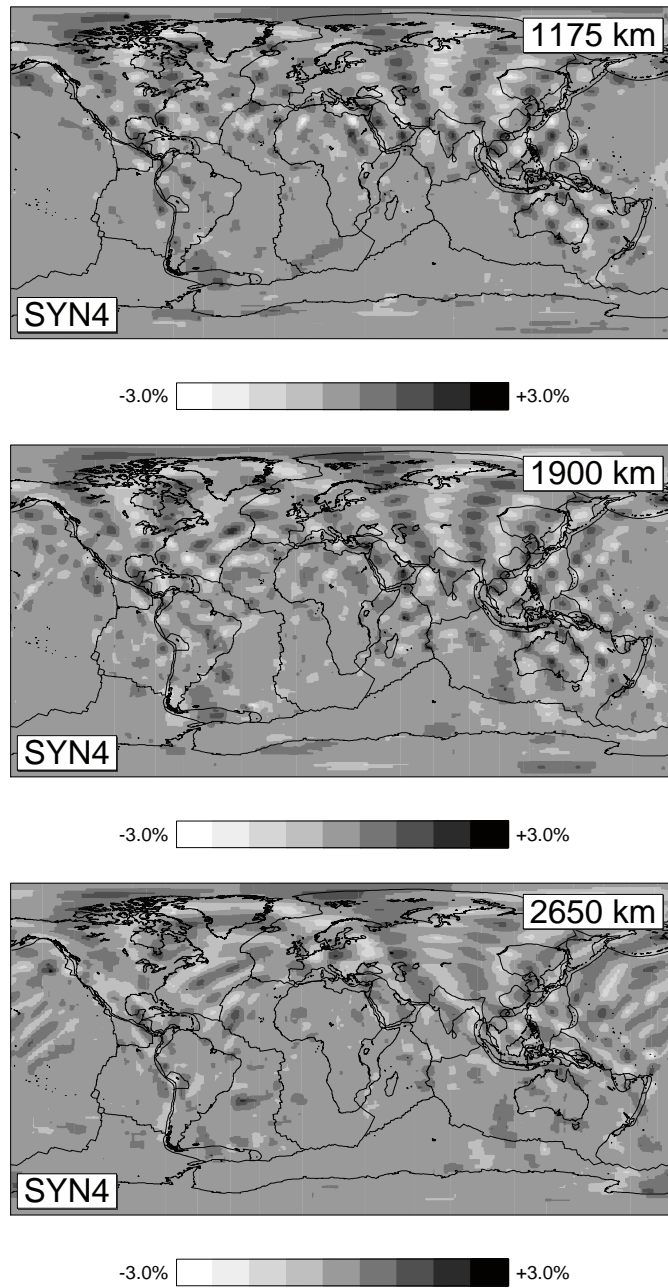
Figure A.6: Spike tests with spikes of $4.0° \times 4.0°$ at 1175 km depth (top), $4.0° \times 4.0°$ at 1900 km depth (middle) and $4.0° \times 4.0°$ at 2650 km depth (bottom).
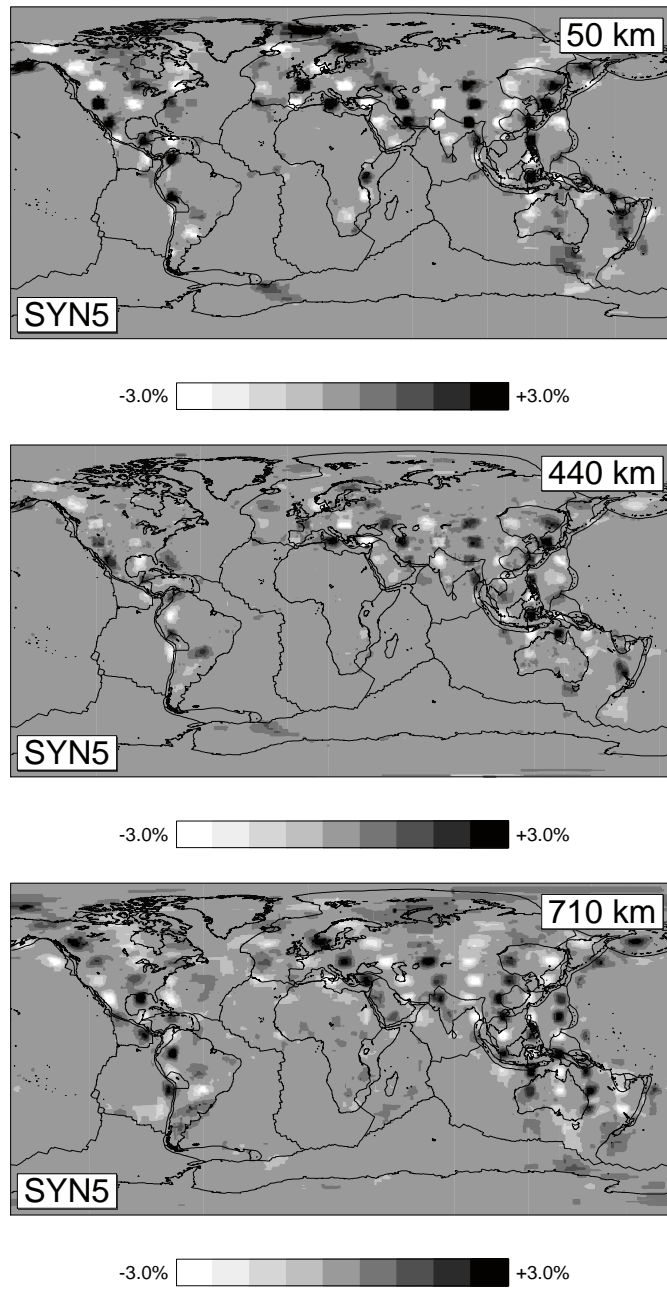
Figure A.7: Spike tests with spikes of $5.0° \times 5.0°$ at 50 km depth (top), $5.0° \times 5.0°$ at 440 km depth (middle) and $5.0° \times 5.0°$ at 710 km depth (bottom).
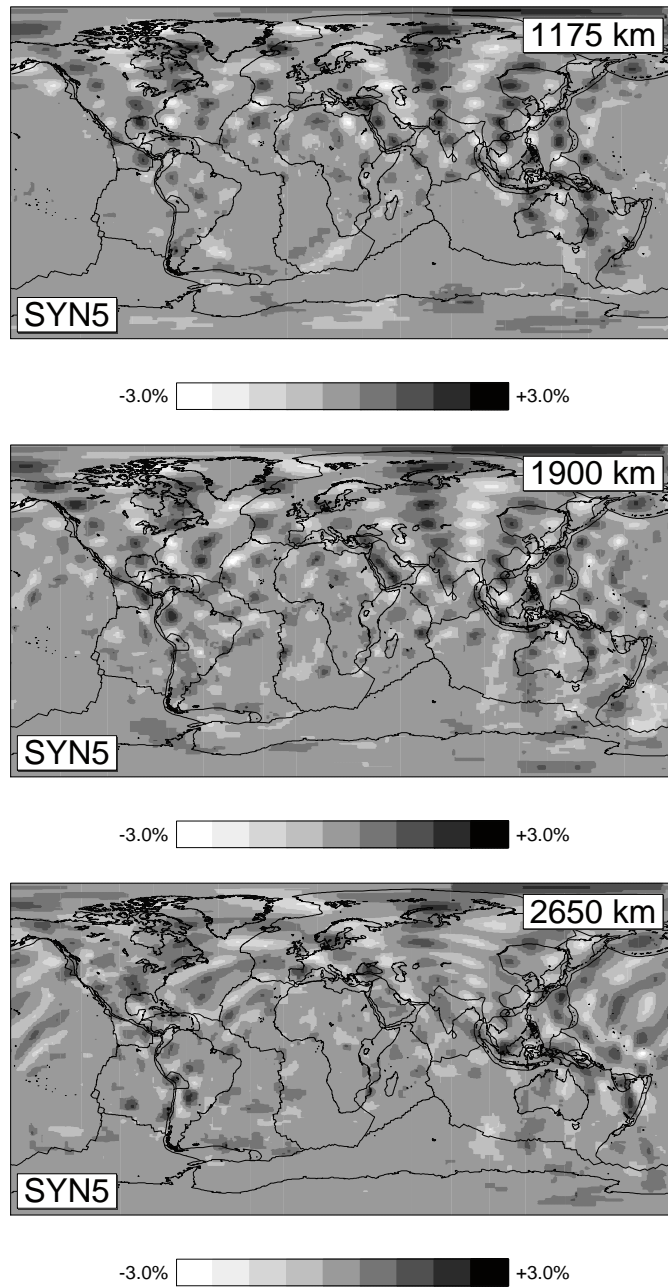
Figure A.8: Spike tests with spikes of $5.0° \times 5.0°$ at 1175 km depth (top), $5.0° \times 5.0°$ at 1900 km depth (middle) and $5.0° \times 5.0°$ at 2650 km depth (bottom).
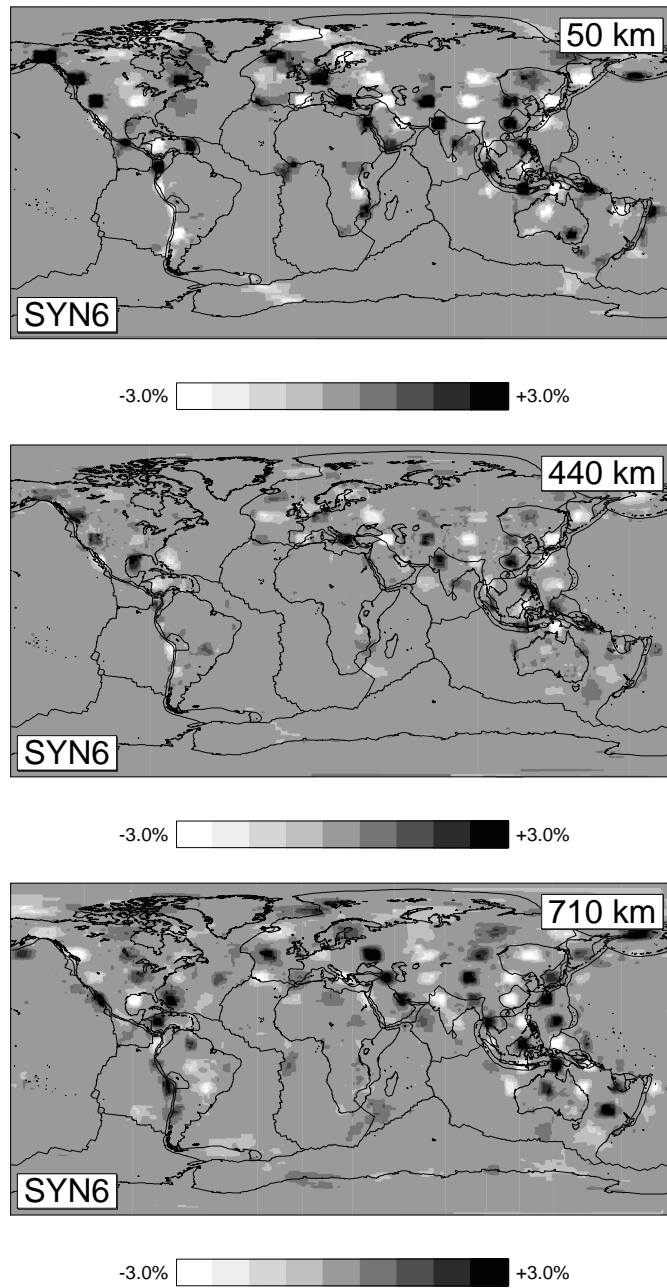
Figure A.9: Spike tests with spikes of $6.0° \times 6.0°$ at 50 km depth (top), $6.0° \times 6.0°$ at 440 km depth (middle) and $6.0° \times 6.0°$ at 710 km depth (bottom).
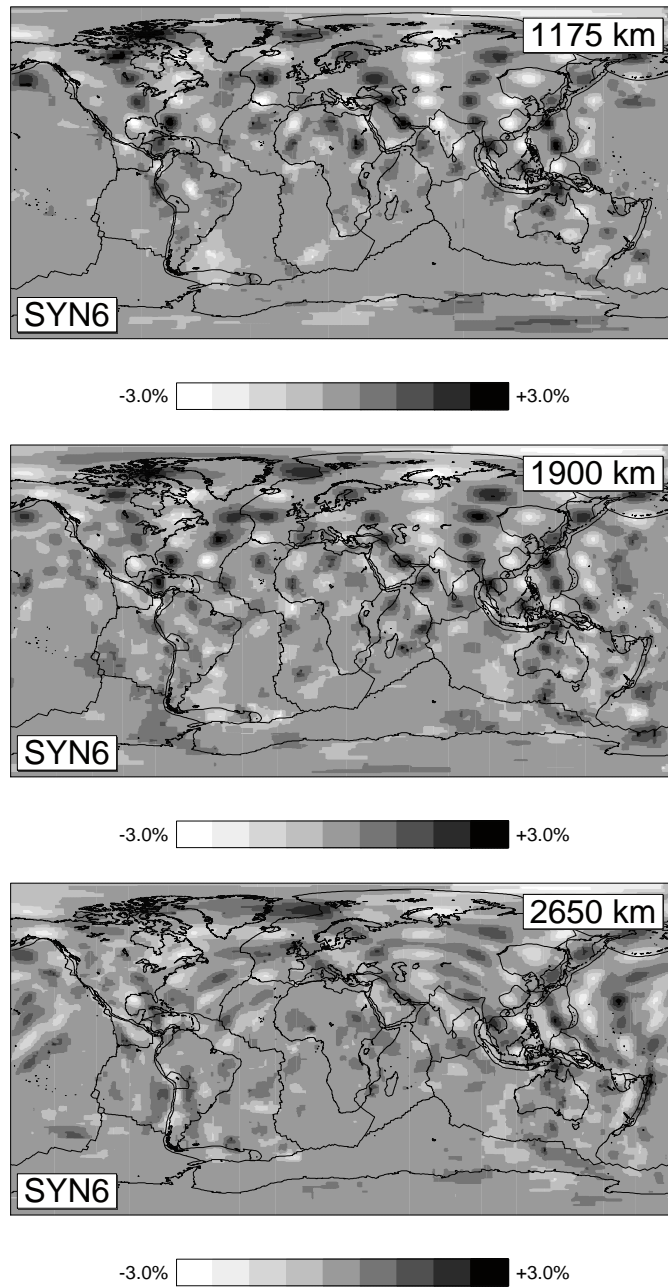
Figure A.10: Spike tests with spikes of $6.0° \times 6.0°$ at 1175 km depth (top), $6.0° \times 6.0°$ at 1900 km depth (middle) and $6.0° \times 6.0°$ at 2650 km depth (bottom).

Appendix B
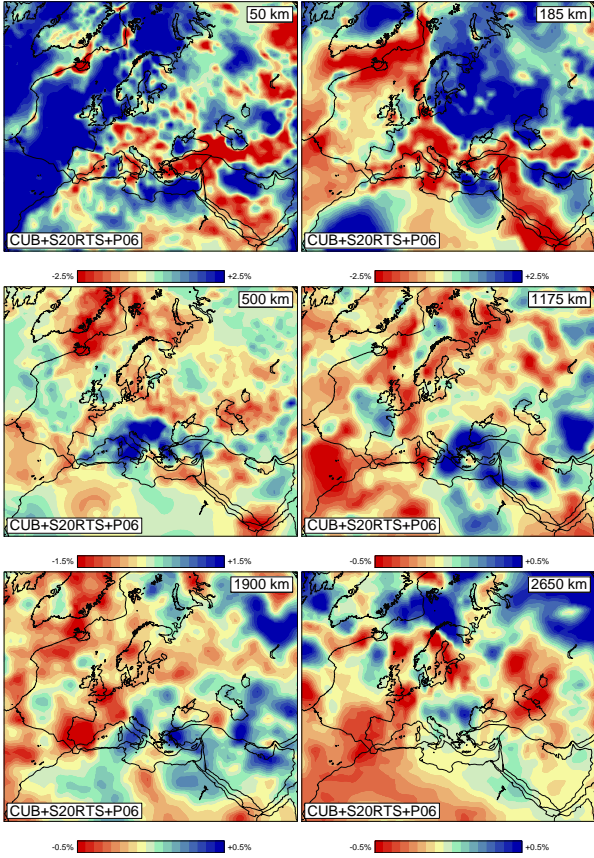
Figure B.1: Velocity variations of the 3-D reference model CUB+S20RTS+P06$^+$ displayed with respect to ak135 at various depths beneath Europe.

Samenvatting (Summary in Dutch)

In dit proefschrift werd met behulp van reistijdentomografie een globaal ruimtelijk hoogop-
gelost P-golven snelheidsmodel van de aardkorst en -mantel opgesteld. Verbeteringen in
vergelijking met vorige modellen werden bereikt door het toevoegen van nieuwe data en het
uitbreiden van de methode voor het gebruik van 3-D referentiemodellen.

De nieuw opgestelde data-set bestaat uit een selectie van reistijden van de actuele EHB-
catalogus (Engdahl *et al.*, 1998), die 445.000 aardbevingen bevat uit de ISC-bulletins en
NEIC-data tot september 2004. In vergelijking met de oorspronglijke catalogus van 1998
heeft de grootte van deze data-set zich meer dan verdubbeld en bevat deze beduidend meer
regionale seismische fasen. Uit deze catalogus werden 17,7 miljoen verschillende P-fasen
en aanvullend 1,5 miljoen kernfasen geselecteerd. De selectie werd verder met 14.000 aard-
bevingen van de EMSC-bulletin voor de periode 1998-2003 uitgebreid. Bovendien werden
200.000 nieuw bepaalde, nauwkeurige looptijden opgenomen, die van registraties van seis-
mische netwerken en tijdelijke experimenten in Europa en Noord-Amerika stammen, die
geen data aan het ISC melden. De bepaling van de reistijden werd uitgevoerd met de automa-
tische reistijd-picker van (Sandoval *et al.*, 2004a), die op een adaptieve "stacking"-methode
gebaseerd is.

Methodologisch werd er naast een standaard 1-D referentiemodel van de aarde, gebruik
gemaakt van 3-D referentiemodellen. Deze modellen baseren zich op een combinatie van
tomografiemodellen die looptijdresiduen gebruiken en modellen die onafhankelijke obser-
vaties van oppervlaktegolven, eigentrillingen en langperiodische ruimtegolven gebruiken.
Deze aanpak werd tot nu toe alleen door Widiyantoro *et al.* (2000) voor een S-golven to-
mografiemodel gebruikt. Maar daarnaast werden de aardbevingen in dit proefschrift in het
respectieve 3-D referentiemodel met een gerichte grid-zoekmethode (Sambridge en Kennett,
1986) gerelokaliseerd om de reistijden met de aardbevingsparameters consistent te maken.

De details en resultaten van deze verbeteringen worden in de hoofdstukken 3 tot en met 8
beschreven:

In hoofdstuk 3 wordt het effect onderzocht van de nieuwe, regionale data (tot 1998) in de
EHB-catalogus met een regionale Pn-tomografiestudie van de korst en bovenste mantel bene-
den Europa. Dit onderzoek laat zien dat voor de P snelheden anomalieën met een minimale,
laterale uitbreiding van 0.4 graden en voor S snelheden anomalieën van 0.8 graden kunnen
worden opgelost. Aldus worden gedetailleerdere afbeeldingen van structuren in de korst en
bovenmantel verkregen dan in een eerdere studie (Bijwaard *et al.*, 1998) met de oorspron-
kelijke catalogus. Voorts werden in deze studie S reistijden voor de tomografie gebruikt en
bijkomend werden tomografische inversies met een 3-D referentiemodel (CRUST2.0 (Bassin
et al., 2000) en CUB1.1 (Shapiro en Ritzwoller, 2002)) uitgevoerd. Deze inversies tonen
aan dat de data voldoende oplossingsvermogen hebben om het referentiemodel in dichtbe-
monsterde gebieden te veranderen, terwijl anders het referentiemodel wordt teruggevonden.
Verder werden tekortkomingen van het 1-D referentiemodel ak135 (Kennett *et al.*, 1995)
waargenomen, dat voor S snelheden in de bovenste mantel te langzaam is.

Hoofdstuk 4 behandelt de nieuwbepaalde reistijden van tijdelijke en permanente seismische
stations in Europa, die geen reistijddata aan het ISC melden en daarom niet in eerdere stu-
dies werden gebruikt. De goede kwaliteit van deze aankomsttijden wordt door teleseismische

residuen geopenbaard, die per station gemiddeld de snelheidsvariaties direct onder het station weerspiegelen, wat ook door lagere standaardafwijkingen dan in de ISC-data wordt bevestigd. Als bijproduct kon de onzekerheid van de ISC-data op de orde van 0,7 s worden bepaald.

In hoofdstuk 5 werd het gebruik van 3-D referentiemodellen van de regionale op de globale tomografie uitgebreid en gedetailleerder geanalyseerd. In de korst en de bovenmantel (< 300 km) werd het CUB2.0 model (Ritzwoller *et al.*, 2002b) gebruikt. De korstsnelheden uit CUB2.0 zijn gebaseerd op CRUST2.0 (Bassin *et al.*, 2000) maar werden door de oppervlaktegolven-tomografie gemodificeerd om deze met de fase- en groepsnelheidobservaties van de oppervlaktegolven overeen te laten stemmen. Bovendien werd in het diepere deel van de mantel S20RTS (Ritsema *et al.*, 1999) als referentiemodel opgenomen. Zoals de inversies met dit gecombineerde referentiemodel tonen, bestaan er gebieden in de mantel waar de straalbemonstering voldoende is om een tomografiemodel te verkrijgen dat vergelijkbaar is met het model dat met ak135 als referentiemodel werd verkregen. Maar daar waar de straalbemonstering niet voldoende is om grotere afwijkingen van het referentiemodel mogelijk te maken, worden de kleinschalige structuren die in de tomografie met een 1-D referentiemodel worden waargenomen, door het langgolvige 3-D referentiemodel overschreven. Daarom werd dit langgolvige 3-D referentiemodel in een verdere tomografische inversie gecombineerd met het reistijdtomografiemodel dat met een 1-D referentiemodel werd verkregen. Echter, de anomalieën van het reistijdtomografiemodel werden vóór het combineren van deze twee modellen versterkt om de onderschatting van de modelamplituden vanwege regularisatie te corrigeren. Het resulterende model combineert de langgolvige structuren, zoals zij door langperiodische data worden gezien, met de gedetailleerde structuren, verkregen met kortperiodische data. Het gebruik van 3-D referentiemodellen heeft bovendien het voordeel dat het inversiemodel nu ook impliciet realistischere snelheden bevat in gebieden die niet voldoende door P-reistijden worden beperkt.

In hoofdstuk 6 wordt de invloed van de nieuwe data van seismische stations in Europa en de extra informatie van de niet eerder gebruikte kernfasen onderzocht. Op grond van de extra data worden meer details in de bovenste 400 km van de mantel afgebeeld, vooral in regios met weinig seismische stations en/of aardbevingen. Tevens worden reeds eerder waargenomen structuren versterkt. Daarnaast helpen de kernfasen de anomalieën in het onderste gedeelte van de mantel te beperken en de afbeelding van een warme opwaartse stroming onder Centraal-Europa, die een mogelijk bron van het recente vulkanisme in dat gebied is (Goes *et al.*, 1999), wordt duidelijk verbeterd.

In hoofdstuk 7 wordt Noord-Amerika en de integratie van nieuwe data van stations in dit gebied behandeld. De aardstructur wordt met hoge resolutie afgebeeld zoals in regionale tomografiestudies en op grond van de nieuwe data-set kunnen de resten van de Farallon-plaat, een oude oceanische plaat, in de overgangszone van de bovenmantel worden gelokaliseerd.

Tenslotte wordt in hoofdstuk 8 een toepassing van het nieuwe, hoogopgeloste tomografiemodel gepresenteerd. Tests met nauwkeurig gelokaliseerde aarbevingen en explosies laten zien dat het nieuwe model de aankomsttijden, in het bijzonder bij regionale afstanden, beter voorspelt dan een 1-D snelheidsmodel en dat derhalve de mislokalisatie van de epicentra en de onzekerheden van de begintijden van aardbevingen aanzienlijk worden gereduceerd. De relokalisatie van de globale data-set, die in dit proefschrift werd gebruikt, corrigeert de aardbevinglokalisaties voor de 3-D aardstructuur, waarmee geen rekening was gehouden bij de

oorspronkelijke lokaties, verkregen met ak135 als referentiemodel. Bovendien wordt door het nieuwe tomografiemodel een betere focusering van de aardbevingen in sterker beperkte clusters bereikt, vooral in de diepere delen van gesubduceerde platen (> 150 km diepte).

Zusammenfassung (Summary in German)

In dieser Arbeit wurden mittels Laufzeittomographie globale hochaufgelöste P-Wellen-Geschwindigkeitsmodelle für Erdkruste und -mantel erstellt. Verbesserungen im Vergleich zu früheren Modellen wurden durch das Einfügen zusätzlicher Daten und die Erweiterung der Methode zum Gebrauch von 3-D Referenzmodellen erreicht.

Der neu erstellte Datensatz besteht aus einer Auswahl von Laufzeiten aus dem aktualisierten EHB-Katalog (Engdahl *et al.*, 1998), welcher sich aus 445 000 Beben aus den ISC Bulletins und NEIC Daten bis September 2004 zusammensetzt. Im Vergleich zum ursprünglichen Katalog von 1998 hat sich die Größe des Datensatzes mehr als verdoppelt und der Datensatz enthält wesentlich mehr regionale Phasen. Aus diesem Katalog wurden 17,7 Millionen erst und später ankommende P-Phasen und zusätzlich 1,5 Millionen Kernphasen ausgewählt. Die Auswahl wurde ferner um 14 000 Beben des EMSC Bulletins von 1998 bis 2003 erweitert. Außerdem wurden 200 000 neu bestimmte, sehr genaue Laufzeiten eingefügt, die aus Registrierungen von seismischen Netzwerken und temporären Experimenten in Europa und Nordamerika, welche keine Daten an das ISC senden, stammen. Die Bestimmung der Phaseneinsätze wurde mit dem automatischen Laufzeitpicker von Sandoval *et al.* (2004a), der auf einer adaptiven Stapelungsmethode von Rawlinson und Kennett (2004) basiert, durchgeführt.

Die Methode betreffend wurden außer einem gängigen 1-D Referenzmodell der Erde zusätzlich 3-D Referenzmodelle benutzt. Diese basieren auf einer Kombination von Tomographiemodellen, die Laufzeitresiduen gebrauchen und Modellen, die unabhängige Beobachtungen von Oberflächenwellen, Eigenschwingungen und langwelligen Raumwellen verwenden. Dieser Ansatz wurde zuvor nur von Widiyantoro *et al.* (2000) für eine S-Wellen- Tomographiestudie benutzt. Zusätzlich dazu wurden in dieser Arbeit die Beben in dem jeweiligen 3-D Referenzmodell mit einer gerichteten Gittersuchmethode relokalisiert (Sambridge und Kennett,1986), um Konsistenz zwischen Laufzeiten und Herdparametern zu schaffen.

Die Details und Ergebnisse dieser Verbesserungen werden in Kapitel 3 bis 8 beschrieben:

In Kapitel 3 wird der Einfluss der neuen, regionalen Daten (bis 1998), die im EHB Katalog enthalten sind, in einer regionalen Pn-Tomographiestudie der Kruste und des oberen Mantels unter Europa untersucht. Diese Untersuchung zeigt, dass für P-Wellen-Geschwindigkeiten Anomalien mit einer lateralen Ausdehnung von 0.4° aufgelöst werden können und für S-Wellen-Geschwindigkeiten 0.8°-Anomalien. Somit werden detailliertere Abbildungen der Strukturen in der Kruste und im oberen Mantel erhalten als in einer früheren Studie (Bijwaard *et al.*, 1998) mit dem ursprünglichen EHB-Katalog. Des Weiteren wurden in dieser Studie S-Laufzeiten für die Tomographie verwendet und weitere tomographische Inversionen wurden mit einem 3-D Referenzmodell (CRUST2.0 (Bassin *et al.*, 2000) und CUB1.1 (Shapiro und Ritzwoller, 2002)) erstellt. Diese Inversionen zeigen, dass die Daten über genügend Auflösungsvermögen verfügen, um das Referenzmodell in Gebieten guter Strahlüberdeckung zu verändern, während ansonsten das Referenzmodell zurückerhalten wird. Ferner konnten Unzulänglichkeiten des 1-D Erdreferenzmodells ak135 (Kennett *et al.*, 1995) beobachtet werden, welches im obersten Mantel zu geringe S-Wellen Geschwindigkeiten aufweist.

Kapitel 4 beschäftigt sich mit den neu bestimmten Laufzeitdaten von temporären und perma-

nenten seismischen Stationen in Europa, die keine Laufzeitdaten an das ISC schicken und daher in früheren Studien nicht verwendet wurden. Die hohe Qualität dieser Laufzeiten wird anhand der Stationsmittelwerte teleseismischer Residuen nachgewiesen, welche die Geschwindigkeitsvariationen direkt unter den Stationen widerspiegeln, was durch niedrigere Standardabweichungen der Residuen als in den ISC-Daten bestätigt wird. Als Nebenprodukt konnte der Fehler der ISC-Daten mit einer Größenordnung von 0,7 s bestimmt werden.

In Kapitel 5 wurde der Gebrauch von 3-D Referenzmodellen von der regionalen auf die globale Laufzeittomographie erweitert und detaillierter analysiert. In der Kruste und dem oberen Mantel (< 300 km) wurde das CUB2.0-Modell (Ritzwoller *et al.*, 2002b) benutzt. Die Krustengeschwindigkeiten aus CUB2.0 beruhen auf CRUST2.0 (Bassin *et al.*, 2000), wurden aber durch die Oberflächenwellentomographie von Ritzwoller *et al.* (2002b) entsprechend modifiziert. Außerdem wurde in den tieferen Bereichen des Mantels S20RTS (Ritsema *et al.*, 1999) als Referenzmodell eingefügt. Wie die Inversionen mit diesem zusammengesetzten Referenzmodell zeigen, existieren Bereiche im Mantel, in denen die Strahldichte ausreicht, um ein Tomographiemodell zu erhalten, das mit dem Modell vergleichbar ist, welches mit ak135 als Referenzmodell bestimmt wurde. Jedoch werden in den Bereichen, in denen die Strahlüberdeckung nicht ausreichend ist, um größere Abweichungen vom Referenzmodell zu erlauben, die kleinskaligen Erdstrukturen, die in der Tomographie mit dem 1-D Referenzmodell beobachtet werden, durch das langwellige 3-D Referenzmodell überprägt. Daher wurde das langwellige 3-D Referenzmodell in einer weiteren tomographischen Inversion mit dem Laufzeittomographiemodell, das unter Verwendung des 1-D Referenzmodells entstand, kombiniert. Vor der Kombination dieser beiden Modelle wurden die Anomalien des Laufzeittomographiemodells jedoch verstärkt, um die Unterschätzung der Modellamplituden aufgrund der Regularisierung zu korrigieren. Das resultierende Modell kombiniert die langwelligen Strukturen, wie sie von langperiodischen Daten "gesehen" werden, mit den detaillierten Strukturen, wie sie mit kurzperiodischen Daten erhalten werden. Die Verwendung von 3-D Referenzmodellen hat außerdem den Vorteil, dass das Inversionsmodell nun auch implizit realistischere Geschwindigkeiten in Gebieten enthält, die nicht gut durch P-Laufzeiten bestimmt werden.

In Kapitel 6 werden der Einfluss der neuen Daten von seismischen Stationen in Europa und die zusätzlichen Informationen der zuvor nicht benutzten Kernphasen untersucht. Aufgrund der zusätzlichen Daten werden mehr Details in den oberen 400 km des Mantels abgebildet, v.a. in Regionen mit wenig seismischen Stationen und/oder Erdbeben. Des Weiteren werden bereits früher beobachtete Strukturen verstärkt. Außerdem werden mit Hilfe der Kernphasen die Anomalien im untersten Mantel besser abgebildet und die Darstellung des heißen Aufstroms unter Zentraleuropa, der eine mögliche Quelle des rezenten Vulkanismus in diesem Gebiet ist (Goes *et al.*, 1999), wird deutlich verstärkt.

In Kapitel 7 stehen Nordamerika und die Einbindung neuer Daten von Stationen in dieser Region im Mittelpunkt. Die Erdstruktur wird hochaufgelöst wie in regionalen Tomographiestudien abgebildet und aufgrund der neuen Datensätze können die Überreste der Farallon-Platte, einer alten ozeanischen Platte, in der Übergangszone des oberen Mantels lokalisiert werden.

Schließlich wird in Kapitel 8 eine Anwendung des neuen Tomographiemodells präsentiert. Tests mit genau lokalisierten Erdbeben und Explosionen zeigen, dass das neue Modell v.a. in regionalen Herddistanzen Ankunftszeiten besser vorhersagt als ein 1-D Modell und da-

her die Fehllokalisierung der Epizentren und Herdzeitfehler aufgrund des neuen Modells deutlich reduziert werden können. Die Relokalisierung des globalen Erdbebendatensatzes, der in dieser Arbeit verwendet wurde, korrigiert die Erdbebenlokalisierungen bezüglich der 3-D Erdstruktur, welche bei der ursprünglichen Lokalisierung mit ak135 als Referenzmodell nicht berücksichtigt wurde. Zusätzlich wird aufgrund des Tomographiemodells eine bessere Fokussierung der Erdbeben in stärker begrenzten Clustern erreicht, v.a. in den tieferen Bereichen (> 150 km) von subduzierten Platten.

Acknowledgments

Curriculum Vitae

June 2, 1977   Born in Neuwied, Germany

1987 - 1996   Secondary School, Städt. Gymnasium Lünen-Altlünen, Germany

1996 - 2001   Study of Geophysics, Westfälische Wilhelms-Universität Münster, Germany

2002 - 2007   PhD student at the Faculty of Geosciences, Utrecht University,
The Netherlands